AFRL-ML-WP-TR-2004-4026

LIFE PREDICTION METHODOLOGIES FOR AEROSPACE MATERIALS ANNUAL REPORT, 2002

N.E. Ashbaugh, R.A. Brockman, D.J. Buchanan, G.A. Hartman, A.L. Hutson, K. Li, and W.J. Porter

University of Dayton Research Institute
Structural Integrity Division
300 College Park
Dayton, OH 45469-0128

JUNE 2002

Interim Report for 25 May 2001 – 24 May 2002

Approved for public release; distribution is unlimited.

STINFO INTERIM REPORT

This work is the result of Department of Air Force contract number F33615-98-C-5214. The appendix contains numerous conference papers and journal articles. If published, the various publishers may assert copyright. If so, the United States has for itself and others acting on its behalf an unlimited, nonexclusive, irrevocable, paid-up, royalty-free worldwide license to use for its purposes.

MATERIALS AND MANUFACTURING DIRECTORATE
AIR FORCE RESEARCH LABORATORY
AIR FORCE MATERIEL COMMAND
WRIGHT-PATTERSON AIR FORCE BASE, OH 45433-7750

NOTICE

THIS TECHNICAL REPORT HAS BEEN REVIEWED AND IS APPROVED FOR PUBLICATION.

/s/

JAY R. JIRA, Project Engineer
Metals Branch
Metals, Ceramics & NDE Division

/s/

ROLLIE E. DUTTON, Chief
Metals Branch
Metals, Ceramics & NDE Division

/s/

GERALD J. PETRAK, Asst Chief
Metals, Ceramics & NDE Division
Materials & Manufacturing Directorate

REPORT DOCUMENTATION PAGE

Form Approved
OMB No. 0704-0188

1. REPORT DATE *(DD-MM-YY)*
June 2002

2. REPORT TYPE
Interim

3. DATES COVERED *(From - To)*
05/25/2001 – 05/24/2002

4. TITLE AND SUBTITLE
LIFE PREDICTION METHODOLOGIES FOR AEROSPACE MATERIALS
ANNUAL REPORT, 2002

5a. CONTRACT NUMBER
F33615-98-C-5214

5b. GRANT NUMBER

5c. PROGRAM ELEMENT NUMBER
62102F

6. AUTHOR(S)
N.E. Ashbaugh, R.A. Brockman, D.J. Buchanan, G.A. Hartman, A.L. Hutson, K. Li, and W.J. Porter

5d. PROJECT NUMBER
4347

5e. TASK NUMBER
52

5f. WORK UNIT NUMBER
01

7. PERFORMING ORGANIZATION NAME(S) AND ADDRESS(ES)
University of Dayton Research Institute
Structural Integrity Division
300 College Park
Dayton, OH 45469-0128

8. PERFORMING ORGANIZATION REPORT NUMBER

9. SPONSORING/MONITORING AGENCY NAME(S) AND ADDRESS(ES)
Materials and Manufacturing Directorate
Air Force Research Laboratory
Air Force Materiel Command
Wright-Patterson AFB, OH 45433-7750

10. SPONSORING/MONITORING AGENCY ACRONYM(S)
AFRL/MLLM

11. SPONSORING/MONITORING AGENCY REPORT NUMBER(S)
AFRL-ML-WP-TR-2004-4026

12. DISTRIBUTION/AVAILABILITY STATEMENT
Approved for public release, distribution is unlimited.

13. SUPPLEMENTARY NOTES
This work is the result of Department of Air Force contract number F33615-98-C-5214. The appendix contains numerous conference papers and journal articles. If published, the various publishers may assert copyright. If so, the United States has for itself and others acting on its behalf an unlimited, nonexclusive, irrevocable, paid-up, royalty-free worldwide license to use for its purposes.

14. ABSTRACT

Three types of models to predict behavior of gamma titanium aluminide (g-TiAl) alloys in a high temperature turbine engine environment were developed and have been refined: (a) a model to evaluate linear elastic response, (b) a crystal plasticity model, and (c) a computational model for analyzing stress variations within polycrystals of g-TiAl. Orientation-imaging microscopy (OIM) has been used to understand the role that crystallographic orientation plays with respect to fatigue crack initiation and growth.

Mechanical tests have been conducted on various ceramic matrix composites to determine their viability in applications such as exhaust wash structures, exhaust nozzle flaps and seals and combustor liners. Models have been developed for determining effective thermoelastic properties and creep and damage associated with anisotropy of the creep response in off-axis orientations.

Titanium, nickel and aluminum alloys used in fabricating engine components have been examined to assess their behavior under laboratory conditions designed to simulate fretting fatigue, in turbine engine blade attachments, foreign object damage, high-cycle fatigue, and high-cycle/low-cycle interactions under engine operation.

continued on back

15. SUBJECT TERMS
Titanium aluminides, ceramic matrix composites, nickle-base superalloys, turbine blade materials, high-cycle fatigue, fatigue crack growth, elevated temperatures, creep, thermal fatigue, thermomechanical fatigue, fretting fatigue, load interactions, mixed-mode, stress intensity factors, finite element analysis, nondestructive evaluation

16. SECURITY CLASSIFICATION OF:

a. REPORT	b. ABSTRACT	c. THIS PAGE
Unclassified	Unclassified	Unclassified

17. LIMITATION OF ABSTRACT:
SAR

18. NUMBER OF PAGES
252

19a. NAME OF RESPONSIBLE PERSON (Monitor)
Jay Jira

19b. TELEPHONE NUMBER *(Include Area Code)*
(937) 255-1358

14. ABSTRACT *(concluded)*

The ability to predict turbine-engine-materials behavior under operating conditions is an important facet of the Engine Rotor Life Extension (ERLE) and Phase 1 DARPA Prognostics programs. Various studies have been undertaken to assess: (a) baseline properties for virgin material and material extracted from retired turbine disks, (b) fatigue crack initiation and growth, (c) the role that material defects play in low cycle fatigue crack initiation, (d) periodic overloads on fatigue crack growth behavior, (e) fatigue crack growth under near-threshold conditions, and (f) fracture surface marking for crack location during spin-pit testing. Studies that lead to the incorporation of residual stresses into future damage-tolerance based life management programs have been started on retained component stresses due to surface enhancement procedures and material processing. Several experimental methods and systems have been developed that enhance the prediction of turbine-engine-materials behavior are new test software development, enhanced thermal imaging systems, and better crack length measurement techniques.

TABLE OF CONTENTS

SECTION **PAGE**

Foreword vi
1.0 EXECUTIVE SUMMARY 1
  1.1 γ-TiAl-BASE ALUMINIDES 1
  1.2 CERAMIC MATRIX COMPOSITES 1
  1.3 HIGH CYCLE FATIGUE INVESTIGATIONS 2
  1.4 COMPONENT DAMAGE ASSESSMENT PREDICTION 3
  1.5 LIFE PREDICTION WITH RESIDUAL STRESS 4
  1.6 PHYSICALLY-BASED CONSTITUTIVE MODELING 5
  1.7 INTEGRATION OF EXPERIMENTAL PROCEDURES AND ANALYSES 5

2.0 INTRODUCTION 6
  2.1 BACKGROUND 6
  2.2 PROGRAM OBJECTIVES 6
  2.3 REPORT ORGANIZATION 7

3.0 DAMAGE TOLERANCE STUDIES OF g-TiAl-BASE TITANIUM ALUMINIDES 8
  3.1 MICROSTRUCTURAL INFLUENCES IN TiAl INTERMETALLIC ALLOYS 8
    3.1.1 Effect of Microstructural Anisotropy on Fatigue Behavior of γ-TiAl Alloys [C1] 8
    3.1.2 Primary Melting Issues Related to γ-TiAl [C2] 9
    3.1.3 Macro-segregation in γ-TiAl [C3] 9
    3.1.4 Lamellar Colony Orientation Determination in γ-TiAl Using Orientation Imaging Microscopy [C4] 10
  3.2 MODELING EFFORTS OF STRESS STATES LEADING TO CRACK INITIATION 11
    3.2.1 Elastic-Plastic Stress Analysis of γ-TiAl Polycrystals [C5] 11
    3.2.2 Colony Property Determination in a γ-TiAl [C6] 11
  3.3 SMART CONCEPT DEMO 11

4.0 DAMAGE ACCUMULATION AND FAILURE OF CERAMIC MATRIX COMPOSITES (CMC) 13
  4.1 CHARACTERIZATION OF OXIDE/OXIDE AND MI SiC/SiC CMC 13
    4.1.1 In-Plane Shear Behavior of Oxide/Oxide Nextel™610/AS CMC at Room and Elevated Temperature [C7] 13
    4.1.2 Fracture and Creep Rupture Behavior of Notched Oxide/Oxide and MI SiC/SiC CMC [C8] 13
    4.1.3 Creep Rupture Behavior of Oxide/Oxide and MI SiC/SiC CMC with Effusion Holes [C9] 13
    4.1.4 Effect of Machining Technique and Hole Angle on Creep Rupture Behavior of Oxide/Oxide Nextel™720/AS CMC with Effusion Holes 14
    4.1.5 Retained Strength of Oxide/Oxide CMC Combustor Ring Specimens 14
    4.1.6 Retained Strength of Flight Tested CMC Divergent Flaps and Seals 15
  4.2 MODELING AND MECHANICAL DESIGN ANALYSIS OF OXIDE/OXIDE NEXTEL™720/AS CMC 15
    4.2.1 Effective Elastic and Thermal Properties of a Damaged Woven Oxide/Oxide Composite [C10] 15
    4.2.2 Elasticity/Damage/Creep Model for Oxide/Oxide Nextel™720/AS CMC 16

TABLE OF CONTENTS (Continued)

SECTION **PAGE**

4.2.3 Thermal Stress Analysis of Oxide/Oxide CMC Combustor Rings 16
4.3 HIGH CYCLE FATIGUE OF CVI AND MI SiC/SiC COMPOSITE 17

5.0 HIGH CYCLE FATIGUE AND FATIGUE CRACK GROWTH IN AEROSPACE MATERIALS 18
5.1 FRETTING FATIGUE UNDER HIGH CYCLE FATIGUE 18
5.1.1 Characterization of crack initiation processes in Ti-6Al-4V [C11]............... 18
5.1.2 Fretting Fatigue of Dissimilar Metals [C12].. 18
5.1.3 Observations of Micro-damage Mechanisms Resulting from Fretting Fatigue of Ti-6Al-4V [C13].. 19
5.1.4 Inclined Fretting Fatigue Crack K Analysis.. 20
5.1.5 A Study of a Revised Pad Geometry.. 20
5.1.6 Characterization of Fretting Fatigue Damage in 4th Stage Compressor Section From the F100 & F110 Engines 21
5.1.7 Extension of Cu-Ni Study.. 21

5.2 CHARACTERIZATION OF BALLISTICALLY IMPACTED FOD 22

6.0 COMPONENT DAMAGE ASSESSMENT PREDICTION 23
6.1 BASIC MECHANICAL PROPERTIES - BASELINE/QUALIFICATION AND USAGE...23
6.2 MATERIAL STUDIES OF NICKEL-BASE SUPERALLOYS 23
6.2.1 Effects of Defects on Crack Initiation on IN100 (P/M) Under Low Cycle Fatigue Conditions.. 23
6.2.2 A Mission-Element Approach for Crack Growth Under Turbine Engine Spectra 24
6.3 ENVIRONMENTAL EFFECTS ON FATIGUE CRACK GROWTH IN TURBINE ENGINE MATERIALS 24
6.3.1 The Significance of Air in Fatigue Load Interaction 24
6.3.2 A Synergistic Multi-Mechanism Model for Fatgue Crack Growth under Service Conditions... 25
6.3.3 Influence of Environment on Load Interaction Effects in Fatigue Crack Growth under Spectrum Loading 25
6.3.4 Environment-Related Load History Effects in Elevated Temperature Fatigue of a Nickel-Base Superalloy 25
6.4 FRACTOGRAPHY ASSESSMENTS OF CRACK GROWTH AND LOAD INTERACTION (Spin Pit Simulation)...26
6.5 F100 DISK MODELING 26

7.0 LIFE PREDICTION WITH RESIDUAL STRESSES..27
7.1 RELAXATION FOR PM IN100 DUE TO TEMPERATURE AND EXPOSURE TIME...27
7.1.1 Effect of Temperature and Exposure Time on Relaxation of Residual Stresses... 27
7.1.2 Effect of Prestrain on Creep... 27
7.1.3 Residual Stress Relaxation Modeling.. 27
7.2 INFLUENCE ON CRACK GROWTH 28
7.2.1 Incorporating Residual Stresses in Life Prediction of Turbine Engine Components[C14].. 28

TABLE OF CONTENTS (Continued)

SECTION PAGE

7.2.2 Incorporating Residual Stresses in Life Prediction of Turbine Engine Disks [C15] 28
7.3 BULK RESIDUAL STRESSES IN ROTORS........ 29
7.4 SHOT PEENING PROCESS SIMULATION........ 30

8.0 PHYSICALLY-BASED CONSTITUTIVE MODELING 31
8.1 MODELING OF DEFECTS IN Ni-BASED SUPERALLOYS 31
8.2 PROBABILISTIC MODELING 31

9.0 INTEGRATION OF EXPERIMENTAL PROCEDURES AND ANALYSES........ 33
9.1 WINMATE DEVELOPMENT SUPPORT........ 33
9.2 INFRARED DAMAGE DETECTION SYSTEM (IDDS) ENHANCEMENTS........ 33
9.3 HIGH-SPEED, HIGH-STABILITY DIRECT CURRENT POTENTIAL DIFFERENCE (DCPD) CRACK DETECTION SYSTEM 34

10.0 TEST FACILITY ACTIVITIES 35
10.1 MATERIAL BEHAVIOR........ 35
10.1.1 Tension Tests on Ti-45Al-1.2Cr-2.2Nb-.3Mo -.3C, Ti-46Al-1.2Cr-.3Mo-.3C,Ti-46Al-1.75Cr-3Nb-.17W-.18B 35
10.1.2 Fatigue Tests on Trimarc/Ti-6Al-4V MMC 35
10.1.3 Tensile Test on γ-TiAl Laser Deposited: Ti-46.5Al-2Cr-3Nb-2W........ 35
10.1.4 Aluminum-7.5 Mg Nanophase Material Tests........ 35
10.1.5 Prior LCF Effect on Subsequent HCF Life........ 35
10.1.6 Prior LCF Effect on Subsequent HCF Life........ 36
10.1.7 HCF at Negative R........ 36
10.1.8 Influence of Pre-strain and a Notch on Fatigue Behavior 36
10.2 LABORATORY ENHANCEMENTS........ 36
10.2.1 Upgrade Of Laboratory Test Automation Hardware and Instrumentation ... 36
10.2.2 HCF Laboratory LabView® Software and Hardware Implementation........ 37
10.2.3 Improvement in Load Frame Alignment Equipment and Procedures........ 37
10.2.4 Compression Testing on IN100 at 23°C........ 37
10.2.5 Upgrades to the LVDT Extensometer........ 38
10.3 DATA ARCHIVAL SYSTEM........ 38

11.0 REFERENCES........ 39

Appendix: Compilation of Manuscripts 41
List of Manuscripts 42
List of Symbols, Abbreviations, and Acronyms........ 242

FOREWORD

The work described in this report was performed at the Behavior and Life Prediction Section of the Metals Branch in the Metals, Ceramics & Nondestructive Evaluation Division of the Materials & Manufacturing Directorate, Air Force Research Laboratory (AFRL/MLLMN) under Contract No. F33615-98-C-5214, "Life Prediction Methodologies for Aerospace Materials." The contract is administered under the direction of AFRL by Mr. Jay Jira. The program is being conducted by the Structural Integrity Division, University of Dayton Research Institute, Dayton, Ohio with Dr. Noel E. Ashbaugh and Mr. Robert J. Andrews acting as the Principal Investigator and Program Manager, respectively. This report is an interim report on the progress of the 5-year contract effort.

In the fourth year of the contract, the investigations were developed and directed by Drs., Robert Brockman, Geoffrey Frank, and Kezhong Li and Messrs. Dennis Buchanan, George Hartman, James Konicki, David Maxwell, and W. John Porter and Mrs. Alisha Hutson. Mrs. Jacqui Hawkins was responsible for coordinating the input and typing of this document. This interim report covers the work performed during the period of 25 May 2001 to 24 May 2002.

1.0 EXECUTIVE SUMMARY

1.1 g-TiAl-BASE ALUMINIDES

Gamma titanium aluminide (γ-TiAl) alloys show considerable promise for structural application in USAF propulsion systems. To assist the introduction of γ-TiAl components into gas turbine engine application, a thorough understanding of material response to the challenging gas turbine engine environment and the ability to predict material behavior in this difficult environment are requisite. Our efforts have concentrated on the development of models that will eventually enable the prediction of the onset of fatigue crack initiation in components manufactured using intermetallic materials. Three types of models were developed and refined during this period. The first model focused on deducing elastic properties of individual large, lamellar grains. Using single grain alpha-2 and gamma properties reported in the literature as the baseline for the constituents in lamellar grains, a 3-dimensional finite element (3-D FE) model has been developed to predict elastic response of single, lamellar grains based on their orientation. The model has accurately predicted longitudinal and transverse elastic response for a variety of lamellar orientations. A crystal plasticity model utilizing both interlamellar (soft mode) and translamellar (hard mode) deformation of the lamellar colonies is being developed. Slip system information from published research on polysynthetically-twinned (PST) materials is being used to define the interlamellar behavior. Progress on fine-tuning the crystal plasticity model has been hampered by the lack of a consistent set of data describing the activation strength required to trigger slip in these materials. Finally, work continued on the development of a computational model for analyzing stress variations within polycrystals of γ-TiAl, including the effect of anisotropic yielding and small-scale plastic flow. The primary objective of this ongoing project is to better understand the role of local stress variations on crack initiation. Working in concert, the models described above will aid in our ability to predict the fatigue initiation behavior of γ-TiAl components in service.

Significant effort was also spent using orientation-imaging microscopy (OIM) to understand the role that crystallographic orientation plays with respect to fatigue crack initiation and growth. Efforts continued in the characterization of common defects in wrought γ-TiAl alloys, their effect on fatigue performance and methods for defect elimination.

1.2 CERAMIC MATRIX COMPOSITES

Ceramic matrix composites (CMC) are currently being evaluated as replacement materials in high-temperature environments, such as gas turbine engines. Many of the applications include exhaust wash structures, exhaust nozzle flaps and seals and combustor liners. The mechanical and thermal loads imposed on these structures produce multiaxial stress states. Room and elevated temperature tensile tests on ±45°

Nextel™610/AS are used to characterize the off-axis behavior. Typically structures require holes, fillets, and attachment points in their design. Specimen geometries with notches and effusion holes (cooling holes) are being used to investigate the material behavior of the CMC under service operating temperatures. Creep rupture behavior and damage progression in melt-infiltrated (MI) SiC/SiC and Nextel™720/AS CMC are under investigation. As-received and sustained load (creep) experiments on effusion hole specimens are used to determine how damage initiates and progresses. Thorough scanning electron microscope (SEM) investigation of as-machined twist drill and as-laser machined effusion holes specimens reveal an extensive state of damage.

In addition to investigating the as received mechanical behavior and damage progression in oxide/oxide and SiC/SiC CMC, several projects are in progress to evaluate the retained properties of CMC after exposure to high-temperature combustion environments. Oxide/oxide combustor rings and Nicalon/Si3N4 and Nicalon/NC flaps and seals were tested to determine the retained strength after long-term exposure.

Several of the experimental programs described above provide mechanical behavior data to support the analytic modeling efforts on oxide/oxide CMC. A model has been developed for determining the effective thermoelastic properties that incorporates the matrix constituents, the fiber properties, and the fiber architecture. A creep and damage model has been developed that accounts for the anisotropy of the creep response in off-axis orientations.

Software and hardware enhancements were made to support elevated temperature HCF testing of chemical vapor infiltrated (CVI) and MI SiC/SiC CMC.

1.3 HIGH CYCLE FATIGUE INVESTIGATIONS

Titanium, nickel and aluminum alloys used in fabricating engine components are being re-examined in an ongoing effort to assess their behavior under laboratory conditions designed to simulate engine operation. Among the types of loading conditions being simulated are fretting fatigue, as observed in turbine engine blade attachments, foreign object damage (FOD), high-cycle fatigue (HCF) and high cycle / low cycle interactions (HCF/LCF).

The ongoing fretting fatigue characterization effort focused on differentiating between detrimental damage and surface modification, investigating crack growth behavior of fretting-fatigue nucleated cracks, correlating observed damage modes among different experimental contacts and service components, and simulating service environments by incorporating contacts with coatings and dissimilar metals. A range of contact and loading conditions were investigated that are representative of those to which turbine engine blade attachments may be subject, disregarding the effect of the dovetail flank angle. Fretting fatigue nucleated cracks were identified as the only mechanism responsible for a marked decrease in residual material integrity. The threshold behavior of such cracks was determined to be independent of the stress field that nucleated the cracks.

A numerical analysis was begun to assess the effect of crack nucleation angle on the potential propagation of cracks initiated under the sharp stress gradients that characterize contact fatigue.

Wear-related and stress/strain related damage was identified on laboratory specimens tested under different contact geometries. Other observed features common to all specimens were fretting debris or scarring, concurrent propagation of multiple cracks, and debris presence in the wake of fretting fatigue-nucleated cracks. Little similarity was noted between laboratory specimens and retired blade attachment regions during a cursory inspection. Some experiments are being conducted to test laboratory specimens under more realistic conditions by incorporating different pad materials, coatings and pad surface profiles. From these experiments, fretting fatigue behavior has been determined to be insensitive to surface composition beyond the resultant changes in the coefficient of friction, but is somewhat sensitive to changes in surface profile.

Extensive characterization of laboratory simulated FOD damage was conducted using scanning electron microscopy. Both glass and steel beads were used with various impact angles and velocities to produce FOD, via ballistic impact, on simulated airfoil specimens with different leading edge radii. Damage sites were characterized based on changes to the surrounding material and on the overall size of the impact site. Correlation of the reduction of fatigue strength with FOD depth was dependent on the type of impact projectile. Microstructural damage, which characterized nearly all of the impact sites produced with both types of beads, was attributed to crack initiation in the specimens impacted with the steel beads. Fatigue strength of impacted specimens was reduced measurably. The results indicate the need to re-evaluate the use of non-ballistic methods of FOD introduction, as they may not fully represent the FOD found on service components.

Comprehensive lab support was provided for several investigations of HCF and HCF/LCF interaction under uniaxial fatigue conditions. One ongoing HCF study focused on the fatigue behavior of grooved, round dogbone specimens under fully reversed loading. A related investigation focused on the fatigue behavior of notched specimens subjected to two or five percent pre-strain prior to machining of the notch. The goal of this study was to determine the effect of pre-strain that occurs at a notch root during the first half of the first fatigue cycle. In the HCF/LCF experiments, initial LCF cycles, up to 25% of estimated LCF life, had no effect on subsequent HCF fatigue strength for $R = 0.5$ and 0.8. This work included a comparison of constant maximum stress and step loaded baseline test results from which no effect of prior loading blocks from the step loading procedure was identified.

1.4 COMPONENT DAMAGE ASSESSMENT PREDICTION

The ability to predict turbine-engine-materials behavior under operating conditions is an important facet of the Engine Rotor Life Extension (ERLE) program. Our efforts at achieving this understanding have focused on the measurement of baseline properties for virgin material and material extracted from retired turbine disks. Tensile and creep properties have received some attention, however the majority of our efforts have been in the area of fatigue crack initiation and growth. An investigation into the role that material defects play in low cycle fatigue crack initiation was undertaken. A study was performed to assess the beneficial effect of periodic overloads on fatigue crack growth behavior and thoughts on how to employ overload cycles and account for their positive effects were presented. An investigation exploring fatigue crack growth under near-threshold conditions revealed sensitivities related to stress ratio when testing in laboratory air. The stress ratios employed were all above where crack closure would be a factor ($R>0.64$). The stress ratio sensitivity dissipates as the applied stress-intensity levels increase. The stress-ratio effect disappears when testing is done in vacuum suggesting a strong environmental effect.

Considerable effort was expended in support of the Phase 1 DARPA Prognostics program in areas related to simulated spin-pit testing using uniaxially-loaded specimens and in modeling of an F-100 12th stage high pressure compressor disks to determine the feasibility of crack-monitoring sensors. The simulated spin-pit testing combined the application of relatively low frequency spectra for crack growth and fracture surface marking purposes with scanning electron microscope-based fractography to evaluate the results of the applied spectra. The information gained from these experiments was transferred to the original equipment manufacturers (OEM) to aid in the design of their spin-pit spectra.

1.5 LIFE PREDICTION WITH RESIDUAL STRESS

A technology development program known as Engine Rotor Life Extension (ERLE) has the goal of extending the useful life of turbine engine disks. Current damage-tolerance based life management programs do not incorporate residual stresses in the lifing of components that employ surface enhancement procedures such as shot-peening. This task is an initial assessment of the synergistic interactions of temperature, exposure time and applied stress/strain on the relaxation of residual stresses. A baseline study of the effects of temperature and exposure time on the relaxation of compressive residual stresses induced by shot-peening is complete. This data will serve as a valuable benchmark for evaluating residual stress relaxation models. Preliminary efforts on residual stress relaxation modeling have correlated the rapid decrease in residual stresses with the decrease in the yield strength that occurs with increasing temperature. Predictions for stress relaxation under long term exposure will require development of a creep and relaxation model.

Crack growth analysis show that a 30% retention of the as-shot-peened compressive residual stresses provides a factor of two increase in fatigue crack growth life in the threshold regime. The goal of future work is to show how shot-peening at life limiting features on disks can extended the useful life of these components.

Process simulations are in progress to predict the retained residual stresses of shot peening. One approach uses a numerical model from the literature and a second approach uses FEA to simulate individual shot peening events. Both models show reasonable comparisons to x-ray diffraction results. However, additional material behavior data at high strain rates could improve the predicted residual stress profiles.

1.6 PHYSICALLY BASED CONSTITUTIVE MODELING

This task addresses the development and application of improved methods for modeling the stress-deformation behavior of high-temperature materials. Particular emphasis is given to those details that have a strong influence on our ability to predict component life. The study of defects, including voids, inclusions, and variations in composition, in nickel-based alloys is intended to improve our understanding of the mechanisms leading to crack initiation, and how we can better predict initiation life. The characterization of defect sizes, shapes, and distributions in production materials also provides information about the degree of statistical variability present both in the effective properties of a volume of material and in the stress distributions computed using more idealized models of the material behavior. Probabilistic modeling techniques, also under development as part of this task, will provide a means for integrating this information into stress analysis and life prediction methods for turbine engine components. Even more importantly, these analytical methods will help to reduce the uncertainty in data used for predicting component life, which translates directly into sharper estimates and reduced cost.

1.7 INTEGRATION OF EXPERIMENTAL PROCEDURES AND ANALYSES

Integrating experimental and analytical results is critical in developing physics-based models of material behavior. A primary way of meeting this need is to enhance experimental methods in such a way that the results are more directly usable in the modeling effort. Maintaining a close relationship between the scales on which the experiments are run and the modeling is performed is one aspect of this activity. Developing new experimental capabilities that provide direct measurements of parameters in the models is another. The UDRI has developed and/or enhanced several experimental methods and systems that meet these specific requirements. These methods and systems include new software, enhanced thermal imaging systems, and better crack length measurement techniques.

2.0 INTRODUCTION

2.1 BACKGROUND

The U.S. Air Force (USAF) has various programs in place directed toward the advancement of new gas turbine engines and aerospace vehicle technology and the support of current gas turbine engines. These programs include Integrated High-Performance Turbine Engine Technology (IHPTET), National Turbine Engine Durability (NTED), and Engine Rotor Life Extension (ERLE). The primary goals are (1) extend safely the life of current/legacy rotors, (2) improve performance, i.e., maintain properties at higher service temperatures, and (3) reduction in weight, i.e., use of lightweight materials with high-temperature capability. The need to extend the life of a wide range of current aerospace components has resulted in programs such as ERLE, HCF initiative, Aging Aircraft, Propulsion Life, and DARPA Prognosis. These programs are directed toward conventional materials, such as Ni-base superalloys, titanium (Ti) alloys (near α and $\alpha+\beta$), and aluminum alloys. To apply the advanced materials effectively or to consider further applications of conventional materials that have experienced service conditions, a thorough understanding of the material behavior must be obtained and a methodology of life prediction for these materials must be developed or refined. Advanced materials such as gamma titanium aluminide (γ-TiAl) alloys, high-temperature intermetallics, and CMC are leading candidates to satisfy these needs for various engine components.

2.2 PROGRAM OBJECTIVES

The primary objectives of this program are to:

(a) evaluate the performance of advanced and conventional materials under simulated service conditions

(b) develop and/or adapt experimental techniques for characterization of deformation, damage evolution, and failure of advanced and conventional materials under typical service conditions

(c) develop an understanding of the mechanisms leading to deformation, damage accumulation, and failure of advanced and conventional materials under a variety of test conditions, including simulated mission cycles

(d) develop physically based deformation and life prediction models necessary to ensure in-service reliability and maintainability of advanced and conventional materials subjected to aerospace usage loading conditions

(e) transition the new technology to USAF suppliers and customers

(f) use and update the data for various aerospace materials in the current archival system and enhance the materials data archival procedure.

2.3 REPORT ORGANIZATION

This fourth interim report presents the research conducted on the material behavior and modeling of aerospace materials within the Behavior/Life Prediction Section (MLLMN) of the Metals Branch (MLLM) in the Metals, Ceramics & Nondestructive Evaluation Division of the Materials and Manufacturing Directorate at Wright-Patterson Air Force Base, OH. This effort was conducted over the period from 25 May 2001 to 24 May 2002. The investigations that have been completed and were in progress during the fourth year of the contract will be discussed in this report.

The investigations for γ-TiAl, CMC, HCF, Component Damage Assessment Prediction, Life Prediction with Residual Stresses, Physically Based Constitutive Modeling, Integration of Experimental Procedures and Analysis, , and are discussed in Sections 3, 4, 5, 6, 7, 8, and 9, respectively. The last four investigations are associated with ERLE and DARPA Prognosis Programs. Ancillary laboratory activities are presented in Section 10. Extended discussions of the work-in-progress are presented to provide as much information as possible about the current investigations. Copies of the manuscripts, which have been written on the completed efforts, are provided in an appendix, Compilation of Manuscripts, for the convenience of readers who wish to have more detailed information of the investigations readily available.

3.0 DAMAGE TOLERANCE STUDIES OF g-TiAl-BASE TITANIUM ALUMINIDES

3.1 MICROSTRUCTURAL INFLUENCES IN TiAl INTERMETALLIC ALLOYS

3.1.1 Effect of Microstructural Anisotropy on Fatigue Behavior of g-TiAl Alloys [C1]

Our previous work has demonstrated the presence of intrinsic defects in wrought γ-TiAl aluminides and their deleterious effects on material performance. Also, service-induced damage of aircraft engines by foreign particle impact is an unfortunate, but relatively common, occurrence. To ensure reliability in turbine engine systems incorporating intermetallic materials, the damage tolerance design for fracture critical rotating components may have to be based on the fatigue threshold ΔK_{th} due to a very steep exponent of the crack growth da/dN curve. However, ΔK_{th} depends on a number of factors including the microstructure, grain size, environment, temperature, and crack size. In titanium aluminide alloys, crack size is a particularly important consideration since the relatively low fracture toughness dictates a small critical crack size under realistic stress levels. Data from long cracks may not accurately represent the behavior of naturally initiated cracks in actual structures.

Fatigue crack growth near the threshold has been observed to be intermittent for all the materials studied so far (Al, Ti, and Fe alloys). For the fully lamellar (FL) microstructure common in many γ-TiAl, the intermittent nature of crack advance was more exaggerated than has been observed for any other materials. This fact indicated that the fatigue crack growth mechanics of FL microstructure is significantly affected by the interaction between the crack tip and local microstructure. In general, the FL microstructure with a long crack showed a greater fracture toughness and fatigue growth resistance compared to duplex microstructure. It also showed a higher degree of anisotropy due to its intrinsic structural nature and relatively larger grain size. Thus, the crack size dependence of ΔK_{th} of γ-TiAl with a lamellar microstructure is closely related to the anisotropic nature of the structure. Prior studies of the effect of lamellar orientation on fatigue crack-growth rates have indicated that growth rates are faster when cracking is coplanar with the lamellar interface particularly at low ΔK levels. Finite element analysis revealed that only the mechanical properties of duplex microstructures with small grain size approach isotropic conditions.

The fracture toughness of notched specimens of polysynthetically-twinned (PST) TiAl materials strongly depends on the notch orientation with respect to the lamellar interface. In the threshold regime of long fatigue cracks, the direction of crack growth was greatly influenced by the orientation of lamellar interface relative to the loading axis and crack growth was delayed by the presence of colony boundary. Small-crack growth rates in lamellar microstructure were found to be faster than those of corresponding long cracks at the same applied ΔK levels; moreover, small cracks are found to propagate at applied ΔK levels below the long-crack ΔK_{th}. Thus, it is critical to define the lower-bound threshold values of FL microstructures in the presence of short fatigue cracks. However, when performing short crack tests of polycrystalline material using a four point bending specimen the correlation of crack growth rate with the colony orientation is difficult. The use of round fatigue specimens with multiple small notches under axial loading conditions allows for a correlation of the fatigue strength with respect to the lamellar colony orientation and determination of ΔK_{th}.

Our recent efforts have focused on the fatigue behavior of cylindrical specimens having small electro-discharge-machined notches within a lamellar microstructure. The relative orientation of the lamellar colony to the notch where fatigue crack initiated was determined using OIM. A correlation between the fatigue stress and lamellar colony orientation was derived and the notch sensitivity of FL γ-TiAl was determined.

3.1.2 Primary Melting Issues Related to g-TiAl [C2]

As the maturation process continues for development of γ-TiAl alloys for application in USAF propulsion systems, the need for manufacturing processes capable of delivering near-defect-free product has intensified. While gamma alloys are readily processed with techniques and equipment used for conventional titanium alloys on a laboratory- and prototype-scale, large-scale melting of these alloys has not been fully implemented. Recent efforts at evaluating large-scale production of a wrought γ-TiAl alloy uncovered a number of issues pertaining to initial ingot quality. Problems such as centerline porosity and/or piping, grain-size disparities, and high- and low-density regions related to insufficient melt homogenization were encountered. Our efforts have focused on a thorough characterization of the defects and recommending possible solutions for lessening their occurrence.

3.1.3 Macro-segregation in g-TiAl [C3]

Two wrought, near-γ-TiAl alloys, Ti-46.1Al-1.73Cr-1.85Nb-0.5Mo (at.%, named 3-95M) and Ti-46.5Al-2.0Cr-2.8Nb-0.1B-0.25W-0.22C-0.18Si (at.%, named KD-CBS) were investigated for gross segregation of alloying constituents. X-ray radiography, scanning electron microscopy (SEM), x-ray energy dispersive spectroscopy (EDS) dot mapping and microprobe analysis were utilized to characterize gross segregation in these alloys.

X-ray radiography revealed high-density segregation (HDS) and low-density segregation (LDS) regions in 3-95M and KD-CBS, respectively. The macro-segregation regions were as large as 16.5 x 1.6mm in 3-95M and 7.6 x 0.4mm in KD-CBS.

Further investigation on 3-95M showed that the degree of HDS differs from location to location, as revealed by SEM imaging contrast difference, structural morphology and relative phase volume fraction. In addition, a substantial density gradient is present in some regions. In general, the abnormal microstructure of HDS was determined to consist of β plus γ phases and lamellar colonies, compared to a fully lamellar normal structure. The colony size in the segregation region is much smaller, with finely spaced lamellae with occasional cracking evident between the laths. EDS dot mapping revealed the general variation in composition of the micro-constituents (β, γ and lamellar colony) for each of the five following elements: Al. Ti, Nb, Cr and Mo. The results confirmed that the b phase was rich in Nb, Mo and Cr (all three elements are β-stabilizers in conventional Ti alloys) and lean in Al; conversely, γ phase and lamellar colony are high in Al and low in Nb, Mo and Cr.

The quantitative results of each phase obtained by micro-probe analysis were consistent with the EDS dot mapping observations. A HDS region with a very high Nb content showed a much higher vol. % of β phase and lower vol. % of lamellar colony. A noticeable gradient (Cr, Nb, Mo and Al) with a mix of high- and low-density segregation, the latter always is associated with porosity and inclusion.

The LDS regions in KD-CBS were characterized as being rich in boron (B) and deficient in Al, confirmed by Auger, EDS dot mapping, and microprobe analysis. The resultant microstructure showed a very high vol. % of small boride particles in the extremely B-rich region and a banding structure consisting of equiaxed γ and borides in the moderate B-rich region.

The large-scale macro-segregation present in both TiAl alloys apparently originated from the melting pass and survived subsequent processing steps. The segregation issues can be addressed through improvements in developing a homogeneous melt during initial ingot production.

3.1.4 Lamellar Colony Orientation Determination in g-TiAl Using Orientation Imaging Microscopy [C4]

OIM was applied to a lamellar γ-TiAl, Ti-46.5Al-2Cr-3Nb-0.2W (at. %), in order to characterize the 3-dimensional (3-D) orientation of the microstructural constituents. The OIM technique, based on the acquisition and analysis of electron-backscattered-diffraction patterns or Kikuchi patterns from a bulk sample, currently can only image one phase (γ) at a time. However, since γ and α_2 phases share a strict orientation relationship within a lamellar colony, the colony orientation can be determined based on the knowledge of the g lath orientation alone. Since no super-lattice Kikuchi lines of the γ phase could be detected, due to limitations of the equipment sensitivity, a face centered cubic (FCC, a = 0.400 nm) unit cell was assumed for the γ phase and employed by the OIM software - instead of its actual tetragonal structure (a = 0.397 nm, C = 0.405 nm).

The image quality map drawn from OIM data resolved the individual γ laths having projection widths as low as 0.2 µm. The α_2 lath regions were distinguished as having "zero" image quality. The confidence index (CI) of the analysis was also zero in the α_2 lath and α_2/γ interface regions compared to the gamma phase regions ($0 < CI < 0.9$). The orientation map further distinguished γ twins from γ laths based on the twin's 60° rotation about its <111> zone axis. The lamellar colony orientation was determined using the intensity pole figures that were drawn from the orientation distribution function calculated using the OIM software.

3.2 MODELING EFFORTS OF STRESS STATES LEADING TO CRACK INITIATION

3.2.1 Elastic-Plastic Stress Analysis of g-TiAl Polycrystals [C5]

A computational model was described for analyzing stress variations within polycrystals of γ-TiAl, including the effect of anisotropic yielding and small-scale plastic flow. Interlamellar (soft mode) slip behavior was controlled by a separate collection of slip systems whose properties were derived from measurements on PST specimens. When used to represent several hundred randomly oriented material grains, the model provides distributions and statistical data about the local stress, strain, and plastic deformation resulting from a prescribed macroscopic loading. The primary objective of this ongoing project is to better understand the role of local stress variations on crack initiation.

3.2.2 Colony Property Determination in a g-TiAl [C6]

γ-TiAl alloys have been under development for use in rotating components for gas turbine engines. Detailed 3-D colony-level FE models are being developed at the U.S. Air Force Research Laboratory to predict damage initiation and accumulation in γ-TiAl during service loading. These models require knowledge of the orthotropic nature of the deformation and fracture behavior of individual colonies. While the elastic properties of gamma and alpha-2 single-phase materials have been extensively studied, the elastic response of fully lamellar two-phase materials has not received the same degree of attention. Our efforts focused on developing and refining an integrated experimental and analytical approach to deduce the colony properties in a γ-TiAl. Samples with gage sections composed of specifically oriented individual lamellar grains were tested in tension to determine the elastic behavior of this two-phase structure. Preliminary 3-D FE analysis, using the constituent properties available in the open literature, showed general agreement between the model results and the experimental measurements.

3.3 SMART CONCEPT DEMO

Additional modeling is being performed to demonstrate the concept of synthesis of modeling and analysis in real time (SMART) under development at AFRL/MLLMN. Currently, detailed finite element analysis models are being developed for regions of a γ-TiAl specimen for which optical displacement mapping measurements have been made. The capability to model statistical strength variations in groups of lamellae has been added to the crystal plasticity model in an attempt to reproduce some of the localized shear strain variations observed in these detailed measurements.

We have also initiated activity in the area of interactive analysis and experimentation, with the ultimate goal of performing mechanics analysis in real (or near-real) time and incorporating corrections, property information, boundary condition details, and other experimental data into the analytical calculations as the experiment progresses. In principle, this kind of solution must involve an optimization process to minimize some measure or measures of disagreement between the analytical model and reduced data from the experiment as it unfolds.

4.0 DAMAGE ACCUMULATION AND FAILURE OF CERAMIC MATRIX COMPOSITES (CMC)

4.1 CHARACTERIZATION OF OXIDE/OXIDE AND MI SiC/SiC CMC

4.1.1 In-Plane Shear Behavior of Oxide/Oxide Nextel™610/AS CMC at Room and Elevated Temperature [C7]

The in-plane shear behavior of an oxide/oxide CMC was investigated at 23 and 950°C in laboratory air. Monotonic tensile tests were conducted on specimens with fiber reinforcement oriented at ±45° to the loading axis. Tensile tests were conducted on specimens 12.6, 25.4 and 38.1 mm wide to examine the effect of specimen width on the in-plane shear behavior at room temperature. No effect of specimen width was observed. Results of the in-plane shear tests showed that at 23°C, shear stress-shear strain response was nonlinear, with a gradual failure of the composite under displacement control. In contrast, shear stress-shear strain deformation behavior at 950°C was more linear with a brittle failure mode. Examinations of the fracture surface profiles showed that at 23°C, matrix disintegration during fracture allowed entire fiber tows to be pulled from the matrix. This disintegration resulted in a fibrous fracture surface. The slow fiber pullout was consistent with the nonlinear shear deformation behavior. The fracture profiles showed that at 950°C matrix had remained bonded to fiber tows during fracture, resulting in short fiber lengths extending from the fracture plane. The damage observed on fracture surfaces indicated a change in the fracture behavior with temperature as a result in the change of shear deformation behavior.

4.1.2 Fracture and Creep Rupture Behavior of Notched Oxide/Oxide and MI SiC/SiC CMC [C8]

The failure behavior of tensile and creep tests of unnotched and notched oxide/oxide Nextel™720/AS and SiC/SiC melt infiltrated (MI) HI-NICALON-S/SiC were investigated. Nextel™720/AS was tested at 1100°C and MI HI-NICALON-S/SiC at 1200°C in laboratory air. Room temperature tests show that Nextel™720/AS exhibits notch insensitive behavior, while MI HI-NICALON-S/SiC exhibits slight notch sensitivity under tensile loading. In contrast, at elevated temperatures the Nextel720/AS exhibits slight notch sensitive behavior while the MI HI-NICALON-S/SiC is notch insensitive. Although the ultimate tensile strengths of Nextel720/AS and MI HI-NICALON-S/SiC are different, 180 MPa and 200 MPa, respectively, the composites show the same unnotched creep rupture strength of ≈ 150 MPa. In the case of large notches, i.e., notch length greater than the average tow size, the notch-sensitivity increased significantly under sustained loading for both composites. For the notched Nextel™720/AS CMC the creep rupture strength is reduced to ≈ 85 MPa while the MI HI-NICALON-S/SiC CMC the creep rupture strength is reduced to ≈ 110 MPa.

4.1.3 Creep Rupture Behavior of Oxide/Oxide and MI SiC/SiC CMC with Effusion Holes [C9]

Many CMC targeted for high-temperature aerospace applications such as combustors, combustor liners, blade outer air seals, exhaust washed structures, exhaust nozzle flaps and seals contain stress concentration sites such as holes and attachment points. Components such as combustors may also include effusion holes, which introduce a boundary layer of cooling air on the component surface and protect the CMC from the hot combustion gases. The holes also cool the component by providing more internal surface area. The results from creep tests of unnotched, notched, and effusion hole geometries of Nextel720/AS and MI SiC/SiC were compared. Nextel720/AS was evaluated at 1100°C and SiC/SiC at 982°C and 1200°C in laboratory air. In the case of large notches, such as notch length greater than average tow size, the notch-sensitivity increased significantly under sustained loading for both composites. Under sustained loading, the effusion hole (diameter less than tow size) specimens also exhibited notch-sensitivity comparable to that of specimens with large notches.

4.1.4 Effect of Machining Technique and Hole Angle on Creep Rupture Behavior of Oxide/Oxide Nextel™720/AS CMC with Effusion Holes

The effects of machining method and hole orientation were evaluated under sustained loading (creep) conditions. Two common methods for machining the holes are drilling with silicon-carbide tipped twist drills and laser machining. Effusion holes with their holes axes oriented at 90° and 20° from the loading axis were machined. Twist drill machining effusion holes at a 20° angle were not included in this study. The twist drill bits used for this study (0.5 mm Dia.) are not long enough to drill through the CMC at a 20° angle. As-machined holes made by silicon-carbide twist drilling showed extensive tear out on the back surface of the specimen. Also, the back surface hole diameter was ≈ 20% larger than the front. The as-laser machined holes showed a large recast layer around the hole that was ≈ 40% of the diameter of the 0.5 mm hole. The recast zone had numerous cracks as a result of thermal stresses that developed during solidification. The results of the 1100°C creep rupture failure times showed that the laser machining of both the 90° and 20° angled holes had a reduction in rupture life similar to the previous studies on large notches, that are greater than the tow size. In contrast, the creep rupture lives of 90° twist drill machined holes showed no reduction in rupture life when compared to unnotched data.

4.1.5 Retained Strength of Oxide/Oxide CMC Combustor Ring Specimens

Tensile specimens were excised from CMC combustor rings that were exposed in an experimental compact combustor. After several hours of exposure to the combustion environment the rings were removed. Extensive carbon deposits and a permanently warped shape suggest that the combustor rings were exposed to high temperature combustion gases and temperature gradients. Specimens from two CMC rings made from Nextel720/AS and Nextel720/A were tested. Four specimens were excised per ring, each with a 0°/90° fiber orientation. Tensile results from the Nextel720/AS ring showed that when compared to witness samples that were not exposed to the combustion environment, only two of the four samples had a 10% drop in the ultimate strength. For the Nextel720/A ring, one of the four samples had a 28% drop in the ultimate strength, while the others had shown behavior similar to unexposed material. Results from a thermal stress analysis of the combustor rings, discussed in section 4.2.3, showed that the stresses in the regions of the rings from where the specimens were removed were above the proportional limit of the virgin material.

4.1.6 Retained Strength of Flight Tested CMC Divergent Flaps and Seals

Two divergent flap and seal CMC materials, Nicalon/Si3N4 by Dow Corning and Nicalon/NC by Hitco, have been flight-tested and removed from service to characterize the extend of component damage and the retained strength of excised tensile specimens. The flaps and seals were photographed and cut into approximately 200 straight-sided tensile specimens. Each tensile specimen was photographed and categorized according to the extent of visible damage, primarily delamination. The specimens were then sorted and group according to the extent of damage. Specimens with the least amount of visible damage were tested first. Some specimens had such extensive damage they could not be prepared for testing. Tensile results thus far have shown a large scatter in the retained tensile strength. The tensile testing is still in progress.

4.2 MODELING AND MECHANICAL DESIGN ANALYSIS OF OXIDE/OXIDE NEXTEL™720/AS CMC

4.2.1 Effective Elastic and Thermal Properties of a Damaged Woven Oxide/Oxide Composite [C10]

Predictions for orthotropic thermoelastic material properties of Nextel720/AS were obtained. The predictions incorporated the matrix constituents, the fiber properties and eight-harness satin weave (8HSW) fiber architecture of the 2-D textile reinforcement (Nextel720). The objective was to determine the effective elastic and thermal properties of this multiphase woven composite, in the presence of processing-induced damage. The analytical approach follows a building-block scenario in which the microstructure was homogenized and simplified at various levels. Damage modeling was demonstrated to be essential for effective property estimation. Modeling of transverse cracking alone lead to degradation of in-plane properties, such as E_{xx}, leaving the thickness modulus E_{zz} unaltered from the undamaged value. Additional damage mechanisms such as fiber-matrix interfacial debonding, delamination, or effective matrix degradation were necessary to consider, in order to obtain lower estimates of the E_{zz} in the present composite. Predictions for thermoelastic moduli show excellent agreement with the available experimental data.

4.2.2 Elasticity/Damage/Creep Model for Oxide/Oxide Nextel™720/AS CMC

A creep model has been developed for N720/AS that accounts for the anisotropy of the creep response in off-axis orientations. The creep rate equations are based on the potential function

$$f(\sigma) = \sqrt{\sigma_{11}^2 - \sigma_{11}\sigma_{22} + \sigma_{22}^2 + \frac{3}{k^2}\sigma_{12}^2},$$

in which the parameter k controls the degree of anisotropy (k = 1 for isotropic materials). The resulting creep strain rate components are

$$\dot{\varepsilon}_{ij} = \dot{\varepsilon}\frac{\partial f}{\partial \sigma_{ij}}.$$

Although recent experimental results will allow us to define precisely the degree of anisotropy, detailed creep calculations have been performed only for several hypothetical values of the anisotropy parameter which appear to bracket the rate of CMOD measured in similar notched specimens (k = 0.25-0.50).

In contrast to the response of an isotropic material, in which the stress concentration at the notch root tends to decrease during creep, the anisotropic creep results suggest that the stress in the notch root may actually increase during creep. This highly localized stress increase occurs because the variation in the creep compliance with orientation creates a sharp stress gradient along the surface of the notch. Away from the notch surface, the amount of stress relaxation that occurs is (in some regions) greater than that observed in isotropic materials.

4.2.3 Thermal Stress Analysis of Oxide/Oxide CMC Combustor Rings

Finite element analyses have been performed on combustor rings, described in section 4.1.5, to investigate thermal stresses generated in Nextel720/AS and Nextel720/A components. Temperatures have been taken from computational fluid dynamics (CFD) analyses and were assumed to vary linearly from the inner diameter to the outer diameter. Two linear temperature profiles were analyzed. The first profile had inner and outer diameter ring temperatures of 100 and 700°C, respectively. The second profile had inner and outer diameter ring temperatures of 260 and 700°C, respectively. The inner and outer ring diameters were nominally 83 and 121 mm, respectively. For the 100–700°C case, the maximum principal stresses in the rings were approximately 100 MPa using an aluminosilicate matrix and 160 MPa using an alumina matrix. For the 260-700°C case, the maximum principal stresses in the rings were approximately 84 MPa using an aluminosilicate matrix and 130 MPa using an alumina matrix. In all cases the computed maximum principle stresses are less than the ultimate tensile strength of the 0°/90° CMC and greater than the ultimate tensile strength of the ±45° CMC. Results from the thermal stress analyses will be used to guide future CMC component designs and applications.

4.3 HIGH CYCLE FATIGUE OF CVI AND MI SiC/SiC COMPOSITE

Experimental support was provided for high-frequency HCF testing of CVI and MI SiC/SiC CMC. Software modifications were made to the existing LabVIEW® test control and data acquisition software to monitor specimen temperature during testing and after specimen failure. These data were used to determine temperature changes in CMC from frictional heating of the material. Software modifications were also implemented to allow for test control at frequencies < 10 Hz. This control enabled comparisons to be made with previous test results conducted on servo-hydraulic test machines. Hardware modifications included implementation of a furnace controller into the HCF interlock system to enable elevated temperature testing capability.

5.0 HIGH CYCLE FATIGUE AND FATIGUE CRACK GROWTH IN AEROSPACE MATERIALS

5.1 FRETTING FATIGUE UNDER HIGH CYCLE FATIGUE

5.1.1 Characterization of Crack Initiation Processes in Ti-6Al-4V [C11]

A study was conducted to quantify fretting fatigue damage and to evaluate the residual fatigue strength of specimens subjected to a range of fretting fatigue test conditions. Flat Ti-6Al-4V specimens were tested against flat Ti-6Al-4V fretting pads with blending radii at the edges of contact. Fretting fatigue damage for two combinations of static average clamping stress and applied axial stress were investigated for two percentages of total life. Accumulated damage was characterized using full field surface roughness evaluation and scanning electron microscopy (SEM). The effect of fretting fatigue on uniaxial residual fatigue strength was quantified by interrupting fretting fatigue tests, and conducting uniaxial residual fatigue strength tests at R=0.5 at 300 Hz. Results from the residual fatigue strength tests were correlated with characterization results.

While surface roughness measurements, evaluated in terms of asperity height and asperity spacing, reflected changes in the specimen surfaces as a result of fretting fatigue cycling, those changes did not correspond to decreases in residual fatigue strength. Neither of the two means of evaluating surface roughness (via asperity height or asperity spacing) was able to identify cracks observed during SEM characterization. Residual fatigue strength decreased only in the presence of fretting fatigue nucleated cracks with surface lengths of 150 mm or greater, regardless of the contact condition or number of applied fretting fatigue cycles. No cracks were observed on specimens tested at the lower stress condition. Threshold stress intensity factors were calculated for cracks identified during SEM characterization. The resulting values were consistent with the threshold identified for naturally initiated cracks that had been stress relieved to remove load history effects.

5.1.2 Fretting Fatigue of Dissimilar Metals [C12]

An investigation was conducted to characterize the fretting fatigue behavior of Ti-6Al-4V specimens tested against pads of dissimilar metallic composition. The behavior had been assumed to be better than like materials in contact based on the results of fretting fatigue wear investigations in the literature. Recent work, discussed in section 5.1.3, suggests that the damage mechanisms in fretting fatigue differ from those responsible for fretting wear. Consequently, the effect of dissimilar metals in contact might also differ.

Experiments were conducted using IN 100, 7075 T6 Al and Ti-6Al-4V pads against Ti-6Al-4V specimens with average applied clamping stresses of ≈200 MPa and ≈650 MPa. In these tests fretting fatigue limit stresses, σ_{FF}, were determined for a 10^7 cycle fatigue life using a step loading approach under ambient laboratory conditions at 300 Hz and R = 0.5 for each combination of pad material and clamping stress. Results from these experiments seem to support the concept of different damage mechanisms for fretting fatigue and fretting wear. Fretting fatigue limit stresses identified for specimens tested against IN 100 and aluminum pads were nominally the same as those for specimens tested against Ti-6Al-4V pads. Of the two clamping stress conditions for this study, a slight increase in σ_{FF} was observed for only one of the conditions: the IN 100 pad tests at the higher clamping stress condition. Finite element analyses (FEA) of the six experimental conditions, in which the σ_{FF} values for the tests were incorporated, indicated an extreme sensitivity to the coefficient of friction, μ, between the material pair.

Some differences were observed during SEM, elemental analysis (EDS), and roughness characterization of the tested specimens. Less wear debris was observed with the aluminum pads; and more with the IN 100 pads – perhaps due to the rougher (2-3x) IN 100 pad surfaces than with the Ti-6Al-4V pads. In general, the softer material was transferred to the harder material during the wear process; however, some IN 100 constituents were found on specimen surfaces from the relevant tests. This transfer is likely due to the presence of oxidized titanium, which would be hard enough to wear away some of the IN 100 surface. The oxidation and wear processes working in concert would account for the large amount of oxygen present in the wear debris from the IN 100 pads.

5.1.3 Observations of Micro-damage Mechanisms Resulting from Fretting Fatigue of Ti-6Al-4V [C13]

Over the course of many investigations, different fretting fatigue micro-mechanisms have been observed that are not of profound significance in and of themselves, but when taken together, begin to form a more comprehensive picture of how fretting fatigue damage progresses. The mechanisms are divided into geometry-specific mechanisms and common mechanisms.

In the former category, two contact geometries are represented: a sphere-on-flat and a flat-on-flat with blending radii. Micro-notching that could be linked to crack initiation was observed in the sphere-on-flat geometry. This type of behavior would be consistent with fretting wear in which surface modifications in the slip zone provide locations favorable for crack nucleation. Persistent slip bands and cracks located in the slip zone, but in the absence of significant wear debris were observed in the flat-on-flat geometry. These mechanisms are more representative of uniaxial fatigue behavior and suggest a considerable stress concentration as a result of the clamping load on the contact.

Of the mechanisms common to all geometries, three different test systems are represented: a dovetail system in which both clamping and shear loads are varied in phase, a uniaxial fatigue system in which part of the load on the specimen is transferred to the fretting pads, and a uniaxial system in which all of the load on the specimen is transferred to the fretting pads. In all of these test geometries, fretting debris was generated and some of that debris found its way into the wake of cracks nucleated under the contact stress field. The presence of the debris would prevent the crack from closing thereby decreasing the effective ΔK at the crack tip and decreasing the crack growth rate. Multiple simultaneous crack nucleation was also observed in each of the test geometries. Such observations are expected in light of the sharp stress gradients that occur near the edge of contact region; however, the presence of these cracks and the debris in their wake significantly affect crack growth behavior.

Based on these observations, one may infer that cracks nucleate due to the extreme stress concentrations near the edges of contact. Prior efforts to model fretting fatigue behavior based on this assumption alone have resulted in predictions that were overly conservative. A more successful model would incorporate the effects of the micro-mechanisms observed here, including the effect of multiple cracks, the effect of fretting debris on crack propagation and fretting induced plasticity.

5.1.4 Inclined Fretting Fatigue Crack K Analysis

An analysis of stress intensity values for fretting fatigue nucleated cracks is being continued from last year for inclined fretting fatigue cracks. The previous work [Nicholas, et al, 2001] focused on perpendicular edge cracks. The current work is intended to address the issue of cracks nucleated at some angle to the surface other than 90°. This issue becomes relevant when cracks nucleate in the presence of a stress field induced near the edge of a component contact interface where one of the components is subject to a cyclic bulk stress.

Two clamping stress conditions were selected as the focus of this work: 200 MPa and 650 MPa. Experiments performed as part of a prior investigation indicated σ_{FF} at $R = 0.5$ corresponding to a 10^7 cycle fatigue life of ≈300 MPa and ≈250 MPa, respectively, for these clamping stresses. All modeling assumes Ti-6Al-4V against Ti-6Al-4V at room temperature and a coefficient of friction, μ, of 0.3.

A weight function code to allow calculation of K_I and K_{II} for inclined edge cracks has been developed. Stress solutions have been calculated using finite element analysis for maximum and minimum stress states corresponding to σ_{FF} in the fretting fatigue experiments identified above. K_I and K_{II} have been calculated for the maximum stress condition. In the remaining work, K_I and K_{II} for the minimum stress condition and the corresponding ΔK_I and ΔK_{II} will be calculated and correlated with metallurgic observations.

5.1.5 A Study of a Revised Pad Geometry

A series of experiments has begun using a new pad geometry designed to better simulate the actual contact geometry used in compressor blade/disk attachments. The overall pad dimensions are 25.4 mm wide by 12.7 mm high by 6.35 mm thick. The contact face of these pads, shown in Figure 1 is machined with a 3 mm flat centered vertically on the pad and blended to a plane tilted at 11° to the flat with a 3 mm blending radius. Clamping stresses from 400 to 700 MPa have been selected to allow duplication of prior results obtained using a nominally flat pad with a flat length of 6.35 mm and approximately the same blending radius. Experiments are being conducted using a step loading approach to determine the σ_{FF} for a 10^7 cycle fatigue life for the contact geometry and applied loading conditions. The tests are being conducted at 300 Hz using an electro-magnetic shaker system. Three tests have been conducted so far for R=0.5, for which the results indicated $\sigma_{FF} \tilde{}$ 220 MPa, which is slightly lower than the average obtained in previous work (250 MPa) but within a reasonable level of scatter of ±25 MPa on both values.

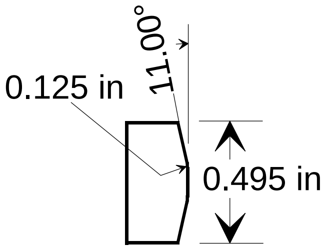

Figure 1: Schematic of Fretting Pad

5.1.6 Characterization of Fretting Fatigue Damage in 4th Stage Compressor Section From the F100 & F110 Engines

Extensive characterization of the fretting fatigue damage generated in service is being performed in order to assist in drawing conclusions about the validity or applicability of laboratory generated fretting fatigue damage and to determine why an engine from one manufacturer is more susceptible to fretting fatigue damage than from another. To address these issues, two retired compressor disks and matching blades have been acquired from two equivalent engines (equivalent engine location) manufactured by different companies. One disk was retired for fretting fatigue damage; the other was retired based on the applied number of cycles. The intent of this ongoing investigation is to compare the damage between the two components and compare the component damage to laboratory generated damage using a variety of characterization techniques including SEM, optical microscopy, and metalographic cross sectioning. Blades from each of the engines have been sectioned in the attachment root region and the sections have been characterized in the SEM, see [Calcaterra & Naboulsi, 2002] for preliminary results.

5.1.7 Extension of Cu-Ni Study

In 1998 an investigation was conducted to evaluate the fretting fatigue behavior of Cu-Ni coated fretting pads in the fretting fatigue apparatus used at AFRL Materials and Manufacturing Directorate in an effort to incorporate features that more closely simulate fretting fatigue as it occurs in turbine engine components. The results were less than conclusive, and so many of those experiments were repeated this year. Included in those tests were the “Series-of-5” tests, in which a single set of pads was used in testing five fretting fatigue specimens in sequence for the purpose of interrogating the wear behavior of the coating with repeated use. Both Cu-Ni coated and as-received pads were evaluated in this manner. In addition, the fretting fatigue limit stresses were re-evaluated for comparison to the original test results.

In the earlier work, the pre- and post-test pads were characterized in a variety of ways, including spectral analysis of the coating-substrate interface and coating composition, and alloy hardness of all materials concerned. Similar work is being conducted for the follow-on investigation in addition to extensive characterization of the post-test specimens to evaluate wear damage and cracking. Comparisons will be made of the behavior with and without the Cu-Ni coating. One paper has been published that documents the results of the experiments conducted in the earlier part of the investigation [Hutson, et al, 2002]. Another paper is planned for next year that will document the characterization results as well as the new experimental results.

5.2 CHARACTERIZATION OF BALLISTICALLY IMPACTED FOD

Specimens that simulate blades were ballistically impacted and then, fatigue tested using a step loading approach at 350 Hz under ambient lab conditions. SEM characterization revealed the presence of adiabatic shear bands on essentially all of the fractured surfaces. Shear bands in the serially sectioned specimens often had micro-cracks, tears, and occasionally shrinkage pores. These bands were present at, or very near, the fracture initiation sites of nearly all of the fractured surfaces. Fatigue fracture initiation always occurred at or near the exit side of the impact crater. The exit side is the deepest part of the crater and therefore has the larger stress concentration. A prediction of fatigue limit stress model was created using the effective stress concentration factor. Additional information on this effort can be found in [Birkbeck, 2002].

6.0 COMPONENT DAMAGE ASSESSMENT PREDICTION

6.1 BASIC MECHANICAL PROPERTIES - BASELINE/QUALIFICATION AND USAGE

In our efforts to understand the effects of real-world service on the retained mechanical properties of commonly-used, nickel-based superalloy disk materials, the development of baseline mechanical properties from materials that have not been exposed to service conditions, referred to as virgin materials, must be obtained. To date, IN100 has been the focus of our efforts due to a readily accessible source of virgin material. During the past year, stress-life fatigue (S-N) information has been collected at 538°C using a 1000 MPa maximum stress, a stress ratio of 0.05, and a frequency of 0.5 Hz. The goal of the S-N testing has been to measure the spread or difference in results under the same test conditions and to determine the mechanisms leading to fatigue crack initiation, through fractography. Section 6.2.1 elaborates on the efforts in understanding fatigue crack initiation. Testing to develop baseline properties for creep and creep rupture was also performed. Creep results at 704°C/ 565 MPa and creep rupture results at 732°C at 741 MPa were obtained and will be compared to properties from material that has seen actual service. Results from the baseline property testing will also be used in developing models developed to understand creep-fatigue interactions.

6.2 MATERIAL STUDIES OF NICKEL-BASE SUPERALLOYS

6.2.1 Effects of Defects on Crack Initiation on IN100 (P/M) Under Low Cycle Fatigue Conditions

It is well established that fatigue cracks typically initiate in structural components at stress concentrations wherein plastic deformation occurs within a nominally elastic component. These crack origins often include pre-existing defects, second phase particles and grain boundaries such as triple point and twin boundaries. We investigated the influence of defect and second phase particles as well as crystalline orientation on the fatigue crack initiation of nickel-base superalloys. Waspaloy, manufactured by cast and wrought processes, contained well-aligned carbon-nitride stringers and clusters. IN100, produced by the powder metallurgy technique, contained contrasting populations of pre-existing pores and nonmetallic inclusions (NMI). Furthermore, the super-solvus heat-treated IN100 produced a significant number of annealing twins. The twin-matrix boundary and triple point grain boundaries have a high orientation difference leading to high stress concentration due to plastic strain incompatibility.

The size, shape and statistical distributions of defects (e.g. pores, NMI, carbides and nitrides) in IN100 and Waspaloy were determined using optical image analysis techniques on prepared mounts. The contribution of these defects and grain orientation on fatigue crack initiation was examined in tests conducted on rectangular and cylindrical cross section specimens. Fatigue testing of the rectangular specimens was interrupted following crack initiation wherein the crack origins were identified using scanning electron microscopy and the orientations of the grains surrounding the initiated cracks were determined by orientation image microscopy (OIM). The initiation sites of the cylindrical specimens were identified from the fracture surfaces wherein the composition of the crack origins was determined using energy dispersive spectroscopy dot mapping. A correlation between the location of the crack initiation sites (sub-surface or internal) and the fatigue loading stress range was determined from the fatigue test results.

6.2.2 A Mission-Element Approach for Crack Growth Under Turbine Engine Spectra

The USAF is pursuing a technology development initiative to extend the useful lifetime of large, expensive, fracture-critical components in currently fielded gas turbine engines. A key element of this program is the development of improved methods for prediction of fatigue crack growth. Current approaches for life management of engine components tend to ignore potential benefits in crack propagation lifetime that may occur as the result of load interaction phenomena that occur under variable amplitude spectrum loading. Recent efforts have shown that periodic overload cycles in the midst of a typical turbine engine mission spectrum can result in significant reductions in crack growth rates, up to as high as 4X. Our goal in this work is to develop ideas for implementing the benefits of overload cycles into life prediction strategies aimed at extending the service lives of turbine engine components such as turbine disks.

6.3 ENVIRONMENTAL EFFECTS ON FATIGUE CRACK GROWTH IN TURBINE ENGINE MATERIALS

6.3.1 The Significance of Air in Fatigue Load Interaction

Fatigue crack growth experiments were conducted on notched Al-Cu alloy coupons under programmed loading conditions. The load programs were designed to induce microscopic marking of the crack formation and growth process under varying stress ratio and closure-free crack tip conditions. Control experiments were performed by switching between an air and vacuum environment. Notch-root natural crack formation and growth behavior was studied through high-resolution scanning electron microscopy. Varying the stress ratio from 0.74 down to 0.64 retarded crack growth by up to a factor of five. This significant ‘closure-free’ stress ratio history effect at intermediate down to threshold crack growth rates totally disappeared in vacuum. The results of this study suggest that as a consequence of the crack seeking the path of least resistance, load-sequence-sensitive-crack plane and front orientation may only induce retardation effects.

6.3.2 A Synergistic Multi-Mechanism Model for Fatigue Crack Growth under Service Conditions

Crack-tip advance under given applied cyclic load conditions is moderated by several mechanisms including crack closure, residual stress, crack front incompatibility and blunting. Experiments were designed to isolate the action of individual mechanisms using programmed variable amplitude load sequences. Fractographic observations from studies on three different materials indicated the synergistic action of at least three significant mechanisms. A model was proposed that incorporates these mechanisms to describe variable amplitude fatigue crack growth. Model response appears to be consistent with fractographic observations.

6.3.3 Influence of Environment on Load Interaction Effects in Fatigue Crack Growth under Spectrum Loading

Fatigue crack growth rate is sensitive to load history even in the absence of crack closure. A marginal reduction in stress ratio results in a degree of retardation that cannot be explained by constant amplitude correlation of growth rate with stress ratio. The effect appears to disappear in vacuum suggesting an environmental connection. This phenomenon was first observed in experiments on notched Al-Cu alloy coupons. Repeat experiments on a titanium alloy and nickel-base superalloy confirm the same effect in these materials. The latter was tested at elevated temperature in both air and vacuum. Further, the experiment included the action of both fatigue loading as well as dwell time, which resulted in fatigue combined with sustained load cracking. Transient retardation in crack growth, associated with the switch between fatigue and sustained load cracking, appears to be associated with their trans- and intergranular nature of cracking, respectively. The results of the study indicate the significance of load interaction effects in service loading that are traceable to environmental action.

6.3.4 Environment-Related Load History Effects in Elevated Temperature Fatigue of a Nickel-Base Superalloy

Near-threshold elevated temperature fatigue crack growth rates in nickel-base superalloy IN-100 are sensitive to load history effects that cannot be attributed to crack closure. The effects disappear in vacuum, suggesting operative mechanisms that are environment related. Experiments on compact-tension coupons under low amplitude loading show that programmed step-wise reduction in stress ratio causes noticeably retarded crack growth that cannot be explained from crack closure considerations. The effect rapidly diminishes with increasing stress-intensity range, indicating a near-threshold phenomenon. This effect is altogether absent in vacuum tests at elevated temperature. The experiments also indicate crack growth retardation when fatigue loading is mixed with hold-time. This appears to be caused by incompatible macro- and microcrack-front orientation associated with differences between the nature of sustained load and fatigue cracking.

6.4 FRACTOGRAPHY ASSESSMENTS OF CRACK GROWTH AND LOAD INTERACTION (Spin Pit Simulation)

Spin pit testing is an accepted method for determining how a component will behave when introduced to real-world gas turbine engine application. As part of the Phase I DARPA material prognostics effort, General Electric and Pratt & Whitney are organizing spin pit test programs using disks with electro-discharge machining (EDM) flaws in critical, high stress, locations. Our efforts have focused on developing conditions in which known features, or markers, are introduced to the fracture surface of cracks emanating from the EDM flaws. Marker cycles are usually accomplished by introducing a block of fatigue cycles with a different stress ratio or frequency than the majority of fatigue cycles in the test. Ideally, the marker cycles will result in a change in crack morphology from the previous or subsequent cycles. Marker bands need to be clearly visible on the fracture surface, using optical or electron microscopy, to be effective. Marker cycles are introduced at prescribed times and are used as reference sites to establish a timeline of events during a test.

To aid the engine companies in their fracture surface marking efforts, we conducted a series of tests using simulated spin pit loading conditions to determine how to best mark samples made from nickel-based superalloys. To date, we have been successful marking Rene88DT and Waspaloy and are presently working to mark IN-100.

6.5 F100 DISK MODELING

As part of the Phase I DARPA material prognostics effort, we have performed several modeling tasks dealing with the P&W F100 12th stage disk, which is a Waspaloy part. Three-dimensional finite element models of a typical 15° sector of the disk, and of half the disk, have been analyzed. Linear static analyses have been performed to determine:

- effect of bore boundary conditions on the stresses around bolt holes in the web
- stress concentrations and weight functions for K calculations, near the holes
- stress fields near machined notches near the rim of the disk
- the relationship of displacements in cut disks to the bulk residual stresses

We also are performing natural frequency analyses of the half-model of the F100 disk to determine the magnitude of frequency shifts associated with the presence of small cracks. This information is of interest in investigating the feasibility of crack monitoring techniques under consideration for use in spin pit tests of this and similar disks.

7.0 LIFE PREDICTION WITH RESIDUAL STRESSES

7.1 RELAXATION FOR PM IN100 DUE TO TEMPERATURE AND EXPOSURE TIME

7.1.1 Effect of Temperature and Exposure Time on Relaxation of Residual Stresses

The effects of temperature and exposure time on the residual stress depth profile of IN100 were studied. Plates of IN100 with dimensions 40mm x 49mm x 4mm were shot peened to specifications typical of turbine engine components. The plates were sectioned into nine smaller pieces 16mm x 13mm x 4mm by EDM for residual stress measurement via x-ray. Exposure temperatures of 427, 538, 650 and 704°C and exposure times ranging from 30 minutes to 300 hours were selected for this program. The elevated temperature exposures and x-ray measurements were subcontracted to Lambda Research Incorporated of Cincinnati, OH. Lambda provided residual stress and percent cold work results on twenty-four specimens. Each specimen had nine measurements at nominal depths of 0, 12, 25, 50, 75, 125, 175, 250 and 350 microns. The x-ray results show a large change in surface residual stresses change within the first half hour of exposure with small change for increased exposure while subsurface stresses show the opposite behavior.

7.1.2 Effect of Prestrain on Creep

A series of creep tests were conducted on prestrained specimens to guide the development of a constitutive model that would apply to the relaxation of residual stresses created by shot peening processes. The material was IN100 that was extracted from a rotor that had been used in service. Creep tests were conducted on round tensile specimens that had received prior elongation ranging from the as-received machined condition (0%) to 30%. The permanent elongations were applied at room temperature. Then, the specimens were subjected to creep stresses ranging from 600 to 1000 MPa at 704°C. For lower creep stress levels, the prestrain reduced the minimum creep strain rate and delayed the onset of tertiary creep compared to the as-received behavior. For higher creep stress levels, the prestrain increased the minimum creep strain rate and accelerated the onset of tertiary creep compared to the as-received behavior. In the use of these creep results in our constitutive model for relaxation of stresses associated with shot peening, the mechanisms for the cold work and relaxation associated with the shot peening processes are assumed to be similar to the mechanisms associated with prestraining and creep.

7.1.3 Residual Stress Relaxation Modeling

Analytical predictions have been performed to predict the relaxation of residual stresses observed in coupon tests performed at AFRL/MLLMN. The most significant experimental observation, based on x-ray diffraction measurements, indicates a sharp reduction in the largest residual stresses after relatively short thermal exposure (one to three hours) at 704°C.

Our models of this process include three steps. First, known (measured) values of the residual stresses and plastic strains (from XRD “cold work” data) are installed in the ABAQUS model through user-written subroutines, with the experimental data being mapped onto the finite element model by interpolation. Secondly, we simulate the heating process, which takes place relatively quickly but which introduces a significant drop in the yield stress of the material due to the elevated temperature. Finally, we analyze the creep behavior under the influence of the residual stress field for a specified period of time.

The first two steps in this analytical process have been completed very successfully, and seem to explain most of the effect that is observed experimentally. In other words, the primary reason for the quick reduction in the residual stress magnitude is the drop in yield stress that occurs as the material is heated. During the heating phase, the existing residual stresses become sufficient to cause a small amount of plastic flow, with an attendant redistribution of the stress field.

7.2 INFLUENCE ON CRACK GROWTH

7.2.1 Incorporating Residual Stresses in Life Prediction of Turbine Engine Components [C14]

The U.S. Air Force has initiated a technology development initiative known as Engine Rotor Life Extension (ERLE), which has the goal of extending the useful lifetime of major, fracture-critical components in currently fielded gas turbine engines, without increasing the risk of component failure. Full achievement of this goal will require improvements in a broad range of technologies, including life prediction and fracture mechanics, nondestructive evaluation, engine usage and health monitoring, and component repair. Surface treatments such as shot peening are extensively employed in the turbine engine components. However, current damage-tolerance-based life management practices do not explicitly account for the residual stresses induced by surface enhancement procedures. This study provided an assessment of the role of residual stresses in the durability of the component and identified critical issues to be addressed during implementation in life prediction methods.

7.2.2 Incorporating Residual Stresses in Life Prediction of Turbine Engine Disks [C15]

Successful incorporation of residual stresses in life management will require a good understanding of the surface and subsurface residual stress changes during service. Very limited data is available that documents the changes of surface and subsurface residual stresses under thermal and mechanical mission loadings. Data from legacy engines indicate that shot-peened induced residual stresses at critical locations are partially retained during service. This study assessed the influence of various levels or retained residual stresses on the threshold stresses, threshold crack sizes and crack propagation in Ti-6Al-2Sn-4Zr-6Mo. The results show that even retention of only 30% of the original residual stress distribution can yield greater than 2X increase in crack growth life compared to the baseline predictions excluding residual stresses. Combining residual stress data from disks from the field with detailed experiments, analysis and NDI techniques a life management practice can be implemented to extend life limited components.

7.3 BULK RESIDUAL STRESSES IN ROTORS

The evaluation and, hence, characterization of bulk residual stresses (BRS) is the purpose of this investigation. BRS and strains are pervasive throughout a body as compared to localized residual stresses and strains. BRS achieve equilibrium in the whole body while localized residual stresses achieve equilibrium over a smaller scale of dimensional characterization for the body. For a body such as an engine disk or rotor, where the thickness is usually small compared to other dimensions, the BRS will depend primarily on the coordinates in the plane of the disk. Shot peening around and in the bore of a hole in the rotor or in the web of the rotor would be an example of a local residual stress distribution.

Processing of the material for a rotor, machining the excess material from the processed shape and imposing service conditions on the rotor are assumed to be the predominate influences on BRS distributions in an engine rotor. One method that has been used to evaluate BRS in rotors has been to measure the circumferential displacements that occur across a radial cut between the outer rim and the inner bore. The number of these rotors that have been cut depended primarily on the need for test specimens that are obtained from these components.

Currently, the relative displacements across a radial cut have been evaluated for several rotors and sonic forgings. These displacement data are introduced as boundary conditions in a first order closed-form elasticity solution [Timoshenko & Goodier, 1951] and in finite element models (FEM) that contain detail geometric features of the rotor. Both analyses are based on linear elastic response of the material and symmetric stress distributions. The closed-form solution applies to a uniform thickness annulus. The predicted BRS from these two methods generally yield similar results if the component geometry is not complex. If the thickness of a rotor varies appreciably, applying the closed-form solution to multiple joined annuli of various uniform thicknesses has yielded stress distributions that are similar to the FEM results.

Future work will be directed toward measuring strain and changes in strain at a variety of locations on and in the rotors using X-ray diffraction, neutron diffraction, strain gages, and Moiré interferometry to improve the characterization the BRS in rotors.

7.4 SHOT PEENING PROCESS SIMULATION

Development of a model to predict the residual stress field from shot peening is proceeding along two fronts. The first approach is based on a numerical solution developed by French researchers. [Cao, et al, 1994] The numerical solution has been implemented within Excel and has been successfully correlated with published experimental data of shot peening-induced residual stresses for several different materials. Application of the numerical solution to the IN100 material of interest has shown the correct trends, but additional material property data are required to fully validate the solution. Efforts are in progress to identify or generate the required materials data. The second approach involves the application of finite element analysis techniques to the simulation of individual shot peening events and evaluation of the resulting residual stresses. A commercial explicit finite element analysis code, LS-DYNA, has been used to simulate a number of impact conditions on several different materials. These transient, elastic-plastic, impact analyses have been useful in developing a better understanding of the generation of the residual stress field between adjacent impact locations and the influence of multiple peening events near the same location. Finite element simulation of shot peening of the IN100 material exhibit the correct maximum residual stress magnitudes, but the depth of the predicted residual stress field is approximately half of that measured experimentally. Investigation of several issues that may affect the analytical predictions, such as rate-dependent plastic response and the nature of the boundary conditions used in the simulations, are in progress.

8.0 PHYSICALLY BASED CONSTITUTIVE MODELING

8.1 MODELING OF DEFECTS IN NI-BASED SUPERALLOYS

Imperfections of various types are the chief source of crack initiations leading to failure in IN100 alloys. Models of defects, including voids and inclusions, and associated plastic flow processes such as slip banding are being developed for use in both deterministic and probabilistic analysis of stresses in Ni-based materials. Thus far, we have focused on the analysis of voids, which are the primary form of defect encountered in PWA1106.

The construction of faithful mechanics models of voids occurring in forged parts depends upon the collection of geometric data describing the type, size, spacing, and shape of voids in manufactured parts. Data have been collected from images of sectioned PWA1106 samples, describing the mean diameter, aspect ratio, and average spacing of voids; the data collection and results are described in Section 6.2.1 of this report. These material data are being used both to define statistical parameters for probabilistic simulations, described in the following section, and to guide the development of parametric models of defects for use in elastic-plastic finite element analysis.

A rudimentary capability for generating detailed models of defects in IN100 is under development, based on the parametric analysis features recently introduced in the ABAQUS finite element code. Input variables are parameterized in terms of a few input variables describing the size, shape, and spacing of defects, and a detailed mesh is created in the vicinity of a defect of the specified shape and orientation. Thus far, the finite element models have been used only for elastic analysis, for comparison with elasticity solutions for ellipsoidal voids. The comparisons performed so far will provide valuable information about the mesh density required for acceptable accuracy for defects of various shapes and aspect ratios.

8.2 PROBABILISTIC MODELING

As additional data become available defining the statistical distribution of defects in the common variants of IN100, life prediction estimates can begin to incorporate this data to produce sharper estimates of the true service life of fielded components. As a first step in establishing probabilistic life estimation techniques for these alloys, an analysis of ellipsoidal defects with variable size, aspect ratios, and spacing has been implemented based on the elasticity solutions developed by Moschovidis [Moschovidis, 1975]. The portion of this computer code that performs and evaluates the actual elasticity solutions has been written and debugged by spot-checking with hand calculations and detailed finite element calculations for stress concentration factors for defects of various shapes. The resulting computer code is being embedded in a Monte Carlo simulation engine to demonstrate the basic strategy of the probabilistic life prediction process. The defect geometry data needed to drive the Monte Carlo simulation is currently being collected and analyzed at AFRL/MLLMN. Eventually, the probabilistic life prediction will incorporate additional analysis branches based on the finite element modeling techniques under development in other tasks described in this report.

9.0 INTEGRATION OF EXPERIMENTAL PROCEDURES AND ANALYSES

An important aspect of advanced material characterization is the close relationship between experiments designed to collect data under specific conditions and the analysis and modeling efforts to understand the associated material behavior. The UDRI has engaged in several efforts to help integrate these activities within the laboratory during the past year. The following paragraphs contain information on the specifics of these efforts and the results achieved.

9.1 WinMATE DEVELOPMENT SUPPORT

One of the hallmarks of contemporary material characterization testing is automation of the test control and data acquisition functions. The UDRI has been in the forefront of material mechanical test automation software for over two decades having developed various automation software packages leading up to the current WinMATE implementation. In the past year, much of this effort has been shifted to a separate contract; however, a number of the key elements of the development were still performed as part of the on-site effort. Specifically, these elements include laboratory debugging, user feedback, and certain enhancements done *in situ.*

A significant part of developing automation software is ensuring that the functions and interface meet the needs of the end users. In the case of the on-site contract, the end users are both the technical staff charged with performing the tests on a day-to-day basis as well as the project engineers and scientists who determine the test conditions and data to be acquired. The initial software design is developed, of course, with these needs in mind. Nevertheless, all the essential elements required by the end users are rarely possible to capture without their direct feedback after using a working version of the software. The on-site UDRI staff has participated on a regular basis in both using the code, providing suggestions for enhancements, and reporting errors. This feedback has resulted in over 100 changes to the code making it a substantially more usable tool.

9.2 INFRARED DAMAGE DETECTION SYSTEM (IDDS) ENHANCEMENTS

One of the ways in which we integrate experiments and analytical modeling is by providing experimental tools that can measure physical parameters corresponding to specific elements of the models. As we extend material models from the continuum mechanics to the microstructural realm, we require tools that allow us to experimentally study material response at the same reduced scale. The UDRI has therefore been developing an enhanced infrared damage detection system (IDDS) to detect highly localized damage regions on the scale of the microstructure.

In the case of cyclic applied loading, it is clear that damage accumulates over a large percentage of the life before a macroscopic crack finally appears and propagates to cause failure. For many multi-phase aerospace materials, the specifics of how and why a crack initiates at a specific location are not well understood. The IDDS developed by the UDRI allows detection of local damage regions very early in the damage accumulation process. It appears that this technique is capable of detecting damage prior to initiation of a crack of the size of the microstructure.

Most importantly, the IDDS precisely identifies the location or locations of local damage through the use of full-field imaging. This capability enables material scientists to employ powerful techniques like SEM, TEM, and others to study the phenomena and mechanisms of crack formation. Without knowing where to apply these techniques this task would be nearly impossible due to the large volume of material to be examined and the small features to be detected.

9.3 HIGH-SPEED, HIGH-STABILITY DIRECT CURRENT POTENTIAL DIFFERENCE (DCPD) CRACK DETECTION SYSTEM

Another way in which we more closely integrate experimental and analytical models is by making more precise experimental measurements. Thinking of this activity as simply an exercise in fine-tuning constants to the next decimal place would be a significant misjudgment. The improved measurement capability of the DCPD system developed by the UDRI is a clear case in point.

A widely used model of crack propagation in rotating turbine engine components relies on combining data from steady-state crack propagation tests under various test conditions. In previous work, the best available crack length measurement resolution was typically on the order of 250 mm. To obtain a sufficient number of data points for a reliable steady-state crack propagation rate might require that the crack be propagated as much as 10 or 20 mm. In addition, these previous tests were performed using a constant load amplitude so that the stress intensity factor varied throughout the test. This made interpretation of the results difficult.

The enhanced DCPD crack measurement system developed by the UDRI as part of the on-site effort has a resolution of 10 to 20 mm under typical test conditions. In addition, the associated software has the ability to control the load in such a way as to maintain a constant stress intensity factor range throughout the test. With these improvements we can now obtain the steady-state crack propagation rate for a given test condition by growing the crack only a few tenths of a millimeter in an order-of-magnitude less time than before. A whole range of test conditions can now be studied with a single specimen and details in the material behavior are revealed that were not previously evident. Thus, the improved resolution of the DCPD system has done much more than simply refine a few constants to the next decimal place. An entirely new material model is emerging based on the data being produced by this system.

10.0 ANCILLARY TEST FACILITY ACTIVITIES

10.1 MATERIAL BEHAVIOR

10.1.1 Tension Tests on Ti-45Al-1.2Cr-2.2Nb-.3Mo -.3C, Ti-46Al-1.2Cr-.3Mo-.3C, Ti-46Al-1.75Cr-3Nb-.17W-.18B

Fifteen tensile tests were performed at room and elevated temperature. The elevated temperature testing required setting up of special fixturing and a box furnace capable of 870°C.

10.1.2 Fatigue Tests on Trimarc/Ti-6Al-4V MMC

Two strain control fatigue tests of a double scarf joint between sections of Ti-6Al-4V and Trimarc1/Ti-6Al-4V MMC were conducted. These tests required the design and installation of special anti-buckling fixturing because of compressive loads seen during the tests.

10.1.3 Tensile Test of Laser Deposited Ti-46.5Al-2Cr-3Nb-.2W-0.15B

A tensile test of laser deposited Ti-46.5Al-2Cr-3Nb-.2W-0.15B Gamma TiAl at room temperature was conducted.

10.1.4 Aluminum-7.5 Mg Nanophase Material Tests

Tests were run to determine the critical stress intensity factor (K_{Ic}) in laboratory air at room temperature for an Aluminum-7.5Mg nanophase material. C(T) specimens with a width of 38 mm and a thickness of 6.3 mm were extracted from a billet approximately 68 mm diameter by 81 mm long. Specimens were extracted in both the radial and longitudinal orientation. Precracking for the K_{Ic} test was accomplished using a decreasing stress intensity load shedding routine that provided an approximate threshold stress intensity (K_{th}) value for the material. After precracking, the specimens were tested to obtain K_{Ic} values in accordance with ASTM E-399 “Standard Test Method for Plane-Strain Fracture Toughness of Metallic Materials.” The tests did not provide valid K_{Ic} values because the width to thickness ration was greater than allowed by ASTM E-399.

10.1.5 Prior LCF Effect on Subsequent HCF Life

A series of HCF tests using Ti-6Al-4V round dogbone specimens were conducted. The specimens were subjected to 25 % of life at a predetermined 10^5 fatigue limit stress. Then, they were step-loaded to determine an HCF limit stress for a 10^7 cycle fatigue life for stress ratios of 0.5 and 0.8. In addition, the lives from both constant P_{max} and step-loaded (for a 10^7 cycle fatigue life) baseline tests were compared to evaluate the load history effect of the step-loading procedure and to determine the effects on life from the prior 25%

LCF cycling. The comparison of lives from the step-loading tests to those from on constant P_{max} tests indicated that the prior HCF loading steps were negligible. The prior 25% LCF loading was found to have little or no effect on the subsequent HCF limit stress. Additional discussion can be found in [Mall, Nicholas, & Park, 2002].

10.1.6 Initiation of Cracks in Fretting Pads

Fatigue crack propagation was evaluated for cracks that had nucleated in fretting pads. The fretting pads were modified by hollowing out their backsides to form a C-shape. The "C" specimens were loaded in compression at the open end of the "C" to produce a tension load that would propagate any cracks that may be present on the fretted side. These specimens were tested under cyclic compression at 300 Hz using the step-loading technique to identify the stress at which the cracks would propagate.

10.1.7 HCF at Negative R

A series of experiments were conducted to evaluate the effect of notch radius in Ti-6Al-4V for R = -1 for a given Kt. UDRI conducted the experiments on smooth and notched dogbone specimens at 40 Hz. The results are compared [Lanning, Nicholas, Palazotto, 2002] to similar experiments conducted using positive stress ratios.

10.1.8 Influence of Pre-strain and a Notch on Fatigue Behavior

A series of experiments were conducted to evaluate the effect of prior pre-strain on fatigue behavior at the notch. A series of smooth dogbone samples were pre-strained to two or five percent strain and then submitted for machining of the notch. The applied pre-strain resulted in a minimization of the effect of the notch root strain that occurred in the first half of the first fatigue cycle. A discussion of these results is presented in [Ren & Nicholas, 2002].

10.2 LABORATORY ENHANCEMENTS

10.2.1 Upgrade Of Laboratory Test Automation Hardware and Instrumentation

About one-third of the servo-hydraulic test systems (eight) have been updated using the Windows based WinMATE software and seven of those systems use the large console for expanded instrumentation usage. In addition, there is one roll-around WinMATE system and one Mate system that are used for alignment and these systems could be used for test control if the need arose. Three horizontal test systems have been converted to vertical systems, this comes at the request of our sponsor to have more vertical test machines for ERLE testing.

10.2.2 HCF Laboratory LabView Software and Hardware Implementation

The software was changed to allow for frequencies less than 10 Hz. and to allow for stress/strain data to be acquired for the modulus verification of the test setup. In order to track temperature changes on CMC's from frictional heating of the material, the ability to keep acquiring data after specimen failed was included in the software.

A separate software package was developed to acquire up to eight channels of strain data for use in measuring the strain that was transferred to the fretting pads during tests conducted in the HCF lab. Also updates include the ability to manipulate data via user-entered equations to monitor calculated stress values in the dovetail-fretting fixture during the test.

The current software package was enhanced to allow for HCF/LCF testing on all systems. DC offset capabilities were added to AC circuitry (Amplifier) to allow for positioning of the armature for specimen loading/removal. Also, a DC offset interlock was added to the mean load (E-P Transducer) to keep fracture surfaces from coming in contact with each other. Self-tuning PID software was developed for 2 kHz and 20 kHz test systems.

The hardware for the 2 kHz system had a redesign of machine spring plate to extend the useful life of this loading mechanism. Also a "self-tuning" capacitor bank to maximize the loading capabilities of the 2 kHz test system was evaluated. New electro-pneumatic transducers were installed and evaluated to reduce the cost and improve the functionality of the existing mean load control system. Non-contact capacitance gages were evaluated and implemented for measuring the dynamic response of the shaker systems to replace strain gauging as a means of calculating the load correction factor. Modular furnace controllers originally developed for use in SH lab, it were modified and adapted to control furnaces and work with the interlock systems currently installed in the HCF Lab.

10.2.3 Improvement in Load Frame Alignment Equipment and Procedures

As our understanding of load line misalignment increases, our procedures for correcting the misalignment is evolving resulting in dramatic improvements in load frame alignment. The WinMATE alignment software is now being used as part of the alignment procedure both for fine alignment adjustments as well as verification of alignment for the fatigue hydraulic test frames. Currently alignment specimen geometry is being evaluated along with the installation of four additional strain gages to measure torsional misalignment.

10.2.4 Compression Testing of IN100 at 23°C

The compression testing had a dual purpose, first, to determine compression properties of IN100 and to determine the effect of shot-peen residual stress using compressive forces. Second, to use compression testing instead of tension testing since there was a limited supply of material, the compression testing required smaller samples (8mm diameter by 15 mm long) than tension samples so less material was used. The compression test used a LVDT extensometer to determine the strain data. We have conducted tests at 704 C using two 1kW quartz infrared lamps with type K thermocouples welded radially around the center of the sample at several locations, the results of these tests are inclusive.

10.2.5 Upgrades to the LVDT Extensometer

LVDT Extensometers were set up with a different body (V8) and longer coil (Schaevitz 025MHR) to allow for larger strain displacement. In addition, the inside of the coil was reamed to a larger diameter to further increase displacement capabilities. As a result of these adaptations, a strain displacement of more than +/-2mm was obtained.

In addition, a short gage length body (V7) was evaluated for use with large grain gamma and compression testing. A stable gage length of near 4mm was obtained for compression testing, and more testing is being scheduled.

10.3 DATA ARCHIVAL SYSTEM

The Data Archive is a central computer on which test data generated by AFRL/MLLMN are stored and indexed. Its purpose is to prevent the loss of valuable test data and provide local user access. During the past year the old server hardware was retired after generating a final backup of the data on DVDs. UDRI continues to support local administration of file access privileges and to work with computer services on global system administration. In addition, a large volume of test data was added to the archive, and the documentation provided to the users was updated to include modifications in nomenclature designed to accommodate specimens manufactured from retired engine components. Information documenting details of the data archival process is given to new users and to individuals as required.

11.0 REFERENCES

Birkbeck, J., “Effects of FOD on the Fatigue Crack Initiation of Ballistically Impacted Ti-6Al-4V Simulated Engine Blades,” PhD Thesis, University of Dayton School of Engineering, 2002.

Calcaterra, J.R. and Naboulsi, S., "Comparison of Analytical and Numerical Methods for Turbine Engine Dovetail Design," Proceedings of the 43rd SDM, Denver, CO, 22-24 April 2002.

Cao, W., R. Fathallah, J. Barralis and L. Castex, Residual stresses in shot peened metal components. SHOTPEEN: An interactive prediction software, Shot Peening (ICRS4), Society for Experimental Mechanics, Baltimore, Maryland, 1994.

Hutson, A.L., Niinomi, M., Nicholas, T., and Eylon, D., "Effect of Various Surface Conditions on Fretting Fatigue Behavior of Ti-6Al-4V," International Journal of Fatigue, vol. 24, no. 12, pp. 1223-1234, 2002

Lanning, D.B., Nicholas, T. and Palazotto, A.N., “HCF Notch Predictions Based on Weakest-Link Failure Models,” Int. J. Fatigue (submitted 10/02). presented at International Conference on Fatigue Damage of Structural Materials IV, Hyannis, MA, 22-27 Sept., 2002. Not reviewed yet.

Mall, S., Nicholas, T. and Park, T.-W., “Effect of Pre-Damage from Low Cycle Fatigue on High Cycle Fatigue Strength of Ti-6Al-4V,” Int. J. Fatigue (submitted 10/02).

Moschovidis, Z.A., Two Ellipsoidal Inhomogeneities and Related Problems Treated by the Equivalent Inclusion Method, Doctoral Dissertation, Northwestern University, 1975.

Nicholas, T., Hutson, A.L., Olson, S. and Ashbaugh, N., "In Search of a Parameter for Fretting Fatigue," Advances in Fracture Research, Proceedings of ICF-10, K. Ravi-Chandar, B.L. Karihaloo, T. Kishi, R.O. Ritchie, A.T. Yokobori Jr. and T. Yokobori, Eds., Paper # 0809, CD ROM, Elsevier, 2001.

Ren, W. and Nicholas, T., “Effects and Mechanisms of Low Cycle Fatigue and Plastic Deformation on Subsequent High Cycle Fatigue Limit in Nickel-Base Superalloy Udimet 720,” Mat. Sci. Eng., A332, 2002, pp. 236-248.

Timoshenko, S. and Goodier, J.N., Theory of Elasticity, 2nd ed. McGraw-Hill Book Co., Inc., 1951, pp. 66-69.

This page intentionally left blank

APPENDIX

COMPILATION OF MANUSCRIPTS

LIST OF MANUSCRIPTS

Paper Page

C1: Li, K., Rosenberger, A.H., Worth, B.D., Larsen, J.M., and Porter, W.J., “Effects of Microstructural Anisotropy on Fatigue Behavior of Gamma TiAl Alloys,” submitted to Fatigue & Fracture of Engineering Materials & Structures, July 2001. 43

C2: Porter, W.J., Li, K., Rosenberger, A.H., and Dimiduk, D.M., "Primary Melting Issues Related to Gamma Titanium Aluminides," Proceedings 3rd Int'l Symposium on Structural Intermetallics, Jackson Hole, WY, 23-27 September, 2001.. 68

C3: Li, K; Porter, W.J.; and Rosenberger, A.H., "Macro-segregation in Gamma Titanium Aluminides," submitted to Intermetallics, August 2002. 74

C4: Li, K., Porter, W.J., Rosenberger, A.H., and Larsen, J.M., "Lamellar Colony Orientation Determination in Gamma Titanium Aluminides Using Orientation Imaging Microscopy (OIM)," proceedings of the 11th AeroMat Conference & Exposition, ASM International, Bellevue, WA, 26-29 June, 2000.. 89

C5: Brockman, R.A., G.J. Frank, and S.E. Olson, "Elastic-Plastic Stress Analysis of Gamma Titanium Aluminide Polycrystals," Proceedings 3rd International Symposium on Structural Intermetallics, Jackson Hole, WY, 23-27 September 2001... 95

C6: John, R., Porter, W.J., Johnson, D.A., and Olson, S., "Colony Property Determination in a Gamma Titanium Aluminide," Proceedings 3rd International Symposium on Structural Intermetallics, Jackson Hole, WY, 23-27 September 2001... 103

C7: Kramb, V.A., Buchanan, D.J., John, R., and Zawada, L.P., “In-Plane Shear Behavior in Oxide/Oxide Ceramic Matrix Composites at Room and Elevated Temperature,” submitted for publication in Composites Science and Technology, October 2002. 111

C8: John, R., Buchanan, D., and Zawada, L.P., "Fracture and Creep Rupture Behavior of Notched Oxide/Oxide and SiC/SiC CMC," Proceedings of the 10th Int'l Congress of Fracture, Honolulu, HI, 3-7 December, 2001.. 125

C9: John, R., Buchanan, D.J., Kramb, V.A., and Zawada, L.P., “Creep Rupture Behavior of Oxide/Oxide Nextel®720/AS and MI SiC/SiC Composites with Effusion Holes,” Ceramic Engineering & Science Proceedings, 26th Annual Conf. on Composites, Advanced Ceramics, Matls., and Structures:A, The American Ceramic Society, Westerville, OH, 2002. Paper No.ECD2-L-02. 133

C10: Tandon, G.P., Buchanan, D.J., Pagano, N.J., and John, R., "Effective Elastic and Thermal Properties of a Damaged Woven Oxide/Oxide Composite," submitted to the Journal of American Ceramics Society, February 2002. 143

C11: Hutson, A.L.; Neslen, C.; and Nicholas, T., "Characterization of Fretting Fatigue Crack Initiation Processes in Ti-6Al-4V," accepted for publication by Tribology International, June 2002. 165

C12: Hutson, A.L.; Olson, S.; and Nicholas, T.; "Fretting Fatigue of Dissimilar Metals," proceedings of 7th National Turbine Engine High Cycle Fatigue Conference, West Palm Beach, FL, May 2002 195

C13: Hutson, A. L., Conner, B. and Chambon, L., “Observations of Fretting Fatigue Micro-damage of Ti-6Al-4V,” Proceedings of the 14th International Conference on Wear of Materials, Washington, DC, USA, 30 March – 3 April, 2003. submitted for review July 2002. 207

C14: John, R., Larsen, J.M., Buchanan, D.J., and Ashbaugh, N.E., "Incorporating Residual Stresses in Life Predication of Turbine Engine Components," Proceedings of Fatigue 2002, Stockholm, Sweden, 2-7 June 2002, p. 1063-1070. 220

C15: John, R., Larsen, J.M., Buchanan, D.J., and Ashbaugh, N.E., "Incorporating Residual Stresses in Life Predication of Turbine Engine Disks," NATO RTO Symposium on Monitoring and Management of Gas Turbine Fleets for Extended Life and Reduced Costs, 8-11 October 2001. 228

Effects of Microstructural Anisotropy on Fatigue Behavior of Gamma TiAl Alloys

Kezhong Li[*], Andrew H. Rosenberger, Brian D. Worth[†], James M. Larsen, and William J. Porter[*]

Air Force Research Laboratory, Materials and Manufacturing Directorate
AFRL/MLLMN, Wright-Patterson Air Force Base, Ohio 45433-7817, USA
[*] The University of Dayton Research Institute
Dayton, Ohio 45419-0128, USA
[†] Our friend and colleague Brian Worth, previously with The University of Dayton Research Institute, is deceased.

Abstract

This study investigated the sensitivity of the gamma titanium aluminide, Ti-46.5Al-2Cr-3Nb-0.2W (at. %) having a fully lamellar microstructure, to fatigue crack initiation and failure. Tests indicated a pronounced degradation in fatigue strength and an increase in scatter for artificially defected specimens as compared to smooth bars of the same geometry and material. Examination of the failure origin in the notched specimens found that crack initiation is dependent upon the orientation of the particular colony that cracked. The apparent fatigue crack growth threshold was substantially lower for these notched specimens than measured using conventional methods. The notches minimized the crack initiation period by promoting rapid mode I crack initiation in colonies oriented such that the α_2 and γ interface normal had a low angle to the loading axis. Given that individual colonies may crack, and the structural design philosophy should ensure that these cracks do not grow to failure under the anticipated service loading. This indicates that a uniform and refined microstructure is greatly preferred for the commercial implementation of this class of materials.

1. Introduction

Gamma titanium aluminide alloys, leading candidates for high temperature aircraft and automotive structural applications, are based on two ordered intermetallic phases: γ (TiAl, structure $L1_0$) and α_2 (Ti_3Al, structure DO_{19}). This class of materials has attractive mechanical properties which include high values of specific strength, specific modulus, and specific creep resistance, combined with good oxidation/hot corrosion resistance [1-3]. However, the relatively poor low-temperature ductility, fracture toughness and impact resistance typically exhibited by gamma alloys remain concerns [4], particularly when considering the presence of inherent defects in the materials or damage that occurs during service. In previous studies, the presence of intrinsic defects in cast and wrought γ-TiAl aluminides has been reported [5, 6]. Service-induced damage of aircraft engines by foreign particle impact or rough handling must also be considered [7-9]. To ensure reliability, damage tolerant design is required for fracture critical rotating components in gas turbine engines operated by the U. S. Air force. In addition, in some instances, component designs will probably need to consider fatigue crack growth threshold, ΔK_{th}, in order to accommodate the steep crack growth versus stress intensity range curves that are common for gamma alloys [7-10]. That is, a critical flaw size, a_0, should be defined (based on local stress levels) that will not lead to a propagating crack and component failure. However, ΔK_{th} depends on a number of factors including the microstructure, grain size, environment, temperature as well as loading and crack size. In this class of alloys, crack size is a particularly important consideration, since the relatively low fracture toughness dictates a small critical crack size under realistic stress levels [7-10]. It is well known that data from large cracks may not accurately represent the behavior of naturally initiated small cracks in actual structures [11-13].

Fatigue crack growth in the near-ΔK_{th} region has been observed to be intermittent in a wide range of materials (Al, Ti, and Fe alloys). For the fully lamellar (FL) microstructure of γ titanium aluminides, which typically exhibits relatively large lamellar colonies, the intermittent nature of crack advance is more exaggerated than has been observed for other materials [14]. This is due to the intrinsic nature of the FL microstructure, which shows a significant degree of plastic anisotropy. In a lamellar colony, the coherent γ and α_2 phases share a well-known, strict orientation relationship. As a result, each colony possesses a unique orientation with respect to its γ and α_2 phases. Mechanical properties obtained from polysynthetically twinned (PST) TiAl materials, which are pseudo –'single crystals' having parallel γ or α_2 laths [15,16], exhibit significantly anisotropy, especially in terms of plastic deformation. Fracture toughness of compact tension, C(T), specimens of PST crystals was found to be strongly depend on the notch plane orientation with respect to the lamellar interface normal [17,18]. Prior studies have demonstrated that the fatigue crack growth of polycrystalline γ-TiAl alloys was highly dependent on the lamellar orientation with respect to the crack propagation direction. The crack propagation resistance is highest when the crack propagates perpendicular to the lamellar interface, while resistance is lowest when the crack plane is at a low angle to the interface, particularly at low ΔK levels [14, 19-24s]. These studies imply that the "small-crack" behavior of the FL structure may be intimately related to the intrinsic anisotropy at the microstructural level, particularly when the crack size is smaller than the colony size.

The objective of the present work was to investigate the sensitivity to fatigue crack initiation and failure of FL gamma titanium aluminides, containing artificial defects,. Considerable variation in the fatigue strength of cylindrical specimens having multiple, small electro-discharge-machined (EDM) notches, was previously demonstrated [7]. The current work examines the influence of the relative lamellar colony orientation to the notch where fatigue cracking initiated and the apparent crack growth threshold. The correlation between the fatigue stress and lamellar colony orientation is discussed.

2. Experimental Procedure and Results

The gamma alloy employed in this study, developed by Kim [3], has the nominal composition Ti-46.5Al-2Cr-3Nb-0.2W (at. %) and is designated "K5". This material was forged and heat treated to achieve the nearly FL microstructure shown in Figure 1. The structure consists of large lamellar colonies, averaging approximately 700 μm in diameter, with occasional equiaxed gamma grains at the colony boundaries.

The fatigue specimens were nominally 5.0 mm in diameter, with a 25 mm long uniform gauge section. Specimens were electropolished, removing approximately 50 μm of surface, to reduce roughness and residual stress. In a previous study, fatigue tests were performed in air at 40 Hz at ambient temperature with a stress ratio R = 0.1 ($\sigma_{min}/\sigma_{max}$) on smooth specimens [8]. To examine the damage tolerance of the material, identical specimens containing small notches were tested under similar conditions [9]. On a given multi-notched specimen, three sets of four notches (for a total of 12 notches) were electro-discharge-machined (EDM) on the cylindrical surfaces at 90° intervals. Notches were 4 mm apart within the gauge section on adjacent cross sections of the cylindrical bars. Each notch was nominally semicircular having the approximate dimension 160 μm long, 75 μm deep and 25 μm wide. All the notch planes were nominally perpendicular to the loading axis, as shown in the schematic of the specimen, Figure 2.

The mechanisms of crack initiation at the notches were examined using a scanning electron microscope (SEM). Geometric measurements of the fracture initiation planes were performed using a confocal scanning laser microscope (CSLM). Here, a topographical map of the fracture surface near the initiation notch was obtained. With this data and an SEM image of the fracture initiation site, the orientation of initiation facets was determined with an accuracy of approximately ±1°.

2.1 Notch Sensitivity

The yield strength, σ_{YS}, and ultimate tensile strength, σ_{UTS}, of the unnotched K5 alloy is 375 MPa and 460 MPa, respectively, [8,9]. Figure 3 [9] shows the smooth bar S-N curve of maximum applied stress versus cycles to failure, which indicates fatigue strength (cycle number, $N = 10^7$) of 350 MPa. Also shown in Figure 3 are fatigue data from four multi-notched specimens (the numbers represent the specimen ID) revealing a substantial reduction in fatigue strength and a relatively high notch sensitivity in this material. In addition, there is significant scatter in the data of the notched specimen fatigue strength with one result (specimen #159) close to the smooth bar curve. These results imply that the sensitivity to fatigue crack initiation is considerably different among these specimens.

Table 1 summarizes the fatigue strength, number of cycles to failure and the apparent fatigue crack threshold, ΔK_{th}, for the multi-notched specimens. The number of cycles to failure ranges from 6×10^3 to 1.5×10^5. However, the S-N curve of the smooth specimen is rather flat, see Figure 3, when the cycle number is larger than 10^4. That is, the fatigue strength at 10^4 cycle ($\sigma_f = 375$ MPa) is only about 25 MPa higher than the 10^7 fatigue strength ($\sigma_f = 350$ MPa). Therefore, to simplify the analysis, these notched fatigue strength data were treated as the fatigue strength at 10^4 cycles. ΔK_{th} was calculated based on the assumption that the notches behaved as semicircular surface cracks having a depth of 75 μm. The two values represent the values of ΔK at the surface and depth of the notch, 0° and 90° respectively.

Table 1. Notched Specimen Fatigue Test Results

Sample ID	Fatigue Stress (MPa)	Number of Cycles to Failure	Calculated ΔK_{th} (MPa $\sqrt{m}$)		Number of Notches	Lamellar Orientation ϕ_i (°)*
			$K_{0°}$	$K_{90°}$		
159	350	148626	3.64	3.31	3	35
160	325	8808	3.38	3.07	1	13
161	300	65915	3.12	2.84	1	21
162	275	6068	2.86	2.60	2	11

* ϕ_i indicates the lamellar colony orientation with respect to fatigue crack initiation notch, which is indicated by an angle between lamellar interface normal and the loading axis.

2.2 Fractography

Fractographic observation revealed that at least one notch was contained on the fracture plane of the specimens. Table 1 summarizes the number of notches observed on each fracture surface and the orientation of the lamellar colony that appeared to initiate the failure. Predominately, the initiation event appeared to be the interlamellar fracture of a colony. The colony - notch orientation angle, designated ϕ, is defined to be the angle between the lamellar interface normal and the loading axis. Since the loading axis is always perpendicular to the notch plane, ϕ also indicates the angle between the lamellar interface and the notch plane.

2.2.1 Colony - notch orientation

The orientations of the twelve-notched colonies in each specimen were measured on the surface of the specimen in the SEM. When a notch was located at a colony boundary the orientations of the adjacent colonies were also measured. The orientation measured in this manner, termed ϕ_{2D}, gives only the 2-D orientation of the colony (not accounting for the inclination of the lamellar interface to the surface of the specimen) and is always less than or equal to the true 3-D “tilt” on the interlamellar plane. The orientation angle, ϕ_{2D}, of the colonies containing notches that did not initiate failure would be expected to be at higher angles than that of the initiation colony, ϕ_i, measured using the CSLM. However, when ϕ_{2D} was measured to be less than ϕ_i, the orientation of that colony was determined in 3-D using orientation imaging microscopy (OIM) [24]. The angle, $\phi_{3D,}$ measured by intensity pole figure using OIM software, indicates the colony lath inclination angle with respect to edged-on orientation. The OIM scan was conducted as the following: gun voltage, 20Kv, probe current, 7 nA and scanning step, 0.2 μm (see Reference 24 for the details of OIM operation and analysis). Table 2 is a summary of the SEM and OIM results.

Table 2 - Summary of the 2-D SEM and 3-D OIM Measurements.

Specimen ID	#159		#160			#161	#162
Initiation colony-notch angle, ϕ_i	35		13			21	11
Colony-notch angle, $\phi_{2D} < \phi_i$	24	5	10	10	5	4	None (min. = 19°)
Colony-notch angle, ϕ_{3D}	76	44	30	65	28	40	

2.2.2 Fatigue crack initiation in lamellar colonies oriented with lath plane nearly perpendicular to the loading axis

Among the four notched-specimens only one notch was associated with each fracture surface for specimens #160 and #161. The initiation colony orientation angles, ϕ_i, for these two specimens (#160 and #161) are 13° and 21°, respectively, indicating that the colonies that failed were predominantly in the orientations almost perpendicular to loading axis. Figures 4 (a-c) are SEM images of the fracture surface of the initiation site of #160. Figure 4(a) and (b) show the initiation region and a side view, respectively. Figure 4(c) is an enlargement of the initiation-notch region in 4(a). Likewise, Figures 5(a, b) show the initiation region and a side view, respectively, of the fracture surface of #161. These initiation sites reveal cleavage-like interlamellar fracture as the dominant crack initiation mode from a notch (#160 shows some small translamellar fractured colonies fractured at the notch, but the interlamellar failure dominates).

Careful examination of all the colony orientations associated with remaining eleven non-fractured notches of specimen #161, indicated that only one colony of the 2-D orientation angle (ϕ_{2D} = 4°) was smaller than the initiation colony orientation angle (ϕ_i = 21°), see table 2. The OIM analysis result indicated that the lath plane (ϕ_{2D} = 4°) actually inclined 40° to the edged-on colony lath plane. This result concluded that the initiation colony - notch orientation (ϕ_i = 21°) indeed had the smallest angle among the notched lamellar colonies.

For specimen #160, the situation was more complicated compared to specimen #161. The 2-D orientation angles of four colonies (ϕ_{2D} = 5°, 10°, 10° and 5°, respectively), were smaller than the initiation colony angle, ϕ_i = 13°. The lath plane inclination angles to the edged-on lath plane, ϕ_{3D}, were determined by OIM to be 44°, 30°, 65° and 28°, respectively (corresponding ϕ_{2D} in the same order), see Table 2. Again, the conclusion was that fatigue crack initiated from the colony, whose lath plane had the smallest angle with the notch plane.

SEM fractographic observation at low magnification revealed that multiple notches were present on the fracture surfaces of specimens #159 (3 notches) and #162 (2 notches). It was assumed that notches of each cross section were acting individually with respect to crack initiation since the notch size is much smaller (75 μm in depth) than their spacing. (The minimum spacing between notches is 3.5 mm). To simplify the analysis it was also assumed that there was only one initiation site for each specimen, i.e. the coincident notches that appear on the fracture surface are due to their locations on the same failure plane as the initiation notch. Thus, the analysis had to take into two steps. First, it had to be determined that, which notch on the fracture surface was initiation site and how big was the colony - notch orientation angle, ϕ_i. Second, it had to be inspected that if the orientation angles of the non-fractured notches were larger than the initiation angle, ϕ_i. To determine the initiation colony, the orientations of the colonies containing the notches on the fracture surfaces of #159 and 162 were compared. There are two notches (180° apart) on the fracture surface of specimen # 162. One of the two notches was located on the boundary of two colonies with 2-D orientation, $\phi_{2D} = 30^o$ and $\phi_{2D} = 58^o$, respectively. The fracture surface including the notch was characterized as translamellar fracture, making them unlikely crack initiation sites. The orientation of the other colony to the notch on the fracture surface was determined to be 11º by confocal scanning laser microscopy, see Table 2. Apparently, this colony was the crack initiation colony that showed a cleavage-like interlamellar facet, see Figure 6(a) and the side view, Figure 6(b). The minimum colony - notch angle among the remaining notched but non-fractured colonies was 19º. Thus, no OIM operation was necessary to determine lamellar colony orientations.

For specimen #159 two of the three notches on the fracture surface were both located on single colonies and the colony orientation angle, $\phi_{2D,}$ were measured 90º and 76º, respectively. The third notch on the fracture surface was located on the boundary of the triple colonies, the orientation angles of which were 35º, 45º and 65º, respectively. The colony of 35º orientation, which had the minimum orientation angle among the five colonies, was assumed to be the crack initiation site. The initiation colony (labeled as 'delamination colony' and $\phi = 35^o$) revealed a cleavage-like fracture, Figure 7(a), and clearly lines up with the notch as shown in Fig 7(b) and (c). The traces of the lamellar interfaces of the two of the three colonies ($\phi = 35^o$ and $\phi = 45^o$) on the cylindrical surface differ by almost 90 degrees. The impact of this particular intercolony lamellar morphology on the crack initiation will be discussed later.

For specimen #159 except the three notches present on the fracture surface seven notches were located in single colonies with colony orientation angles ranging from 53º to 88º. SEM back scattered images of the remaining two colonies showed very curved laths, see Figure 7(d). OIM scanning on one of the two colonies indicated the lamellar interface is almost perpendicular to the edged-on lath plane ($\phi_{3D} = 76^o$), which intersected the cylindrical specimen surface to form an elliptical shape.

2.2.3 Relationship between fatigue strength and colony–notch orientation

A carefully investigation of the values in Table 1 indicates that the fatigue strength of notched bars is dependent on the orientation of the lamellar colony in which a crack initiated. When the angle ϕ_i is less than 20° the fatigue strengths of notched bars are significantly lower than the smooth bars. The ϕ values of the three specimens (#160, 161 and 162) range from 11° to 21° (lamellar lath plane almost perpendicular to the loading axis) and their fatigue strengths (from 275 to 325 MPa) are lower than the smooth bar of σ_f =375 MPa at $N = 10^4$. However, when ϕ_i equals to 35° (#159) the fatigue strength, σ_f of 350 MPa, approaches that of the smooth bar. The reduction in fatigue strength when notches are present in lamellar colonies, whose lath planes are almost parallel to the notch plane, appears to be related to their lower fracture toughness. Fracture toughness data of a two-phase PST material (Ti-49.3Al) exhibit strongly anisotropic behavior [16, 17]. Table 3 lists the K_{IC} values with respect to the lamellar orientation relative to the crack plane, designated arrester (Type I), divider (Type II) and splitter (Type III), which is also shown schematically in Table 3. The minimum K_{IC} value of 4 MPa√m was obtained when the notch plane is parallel to the lamellar interface (Type III). This toughness is substantially lower than for either Type I or II orientations. Thus, the fatigue crack initiation behavior of the notched specimens may be expected to be largely dependent on the probability of a notch intersecting a type III oriented colony.

Table 3. Fracture Toughness K_{IC} of Ti-49Al PST Material [from ref. 17]

Type I (MPa√m)	Type II (MPa√m)	Type III (MPa√m)
15.7-25.7	8.7-23.4	4

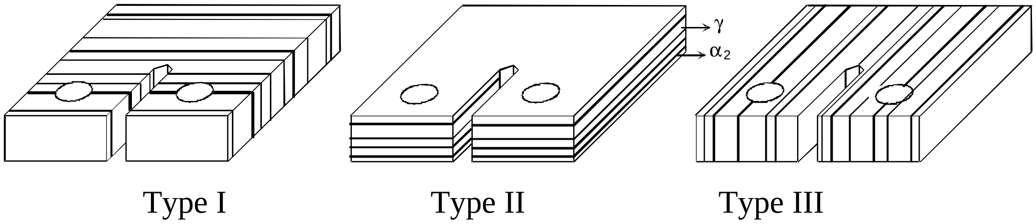

Significant deformation and secondary cracking was observed on the cylindrical surfaces near the notches that were in, or slightly offset from, the fracture surface – indicating that they did not initiate failure. Following initiation from a notch, the crack driving force likely increased significantly, as the crack “pop-in” size would be a significant fraction of the colony size.

Close correlation exists between the fatigue strength and the angle, ϕ_i, of the colony that initiated failure. Specimen #162 had the lowest colony orientation angle for the initiation plane, $\phi_i = 11°$, and the fatigue stress of 275 MPa was the lowest of the four notched specimens. In addition, the adjacent lamellar colony, to the left of the notch in Fig 6(a), deviated only 7° from the initiation colony, providing an easy fatigue crack propagation path. The initiation notch in specimen #159 was located in the boundary of triple lamellar colonies, which were orientated 65°, 45° and 35° from the notch plane, Fig 7 (a), (b) and (c) (without considering the inclination of lamellae with respect to specimen radial direction). The fracture surface shows translamellar fracture in the 65°- and 45°- oriented colonies and interlamellar delamination of the 35° - oriented colony, see Fig. 7(a). The other two notches on the fracture surface were located in highly inclined lamellar colonies. This observation may explain why the fatigue strength (350 MPa) of #159 is the highest of the four specimens and is only 25 MPa lower than the smooth specimen at 10^4 cycles. Fatigue cracks in specimens #160 and #161 initiated in lamellar colonies with $\phi_s = 13°$ and 21°, respectively. Both of these specimens had fatigue strength higher than #162. If initiation colony orientation alone was controlling fatigue strength, specimen #161 should have a higher fatigue strength than #160. However, the fact that #160 has a higher strength than #161, 325 MPa versus 300 MPa, indicates a more complicated crack initiation/propagation situation. The fracture surface of specimen #160, Figure 4(c), showed two small translamellar-fractured colonies located immediately in front of the initiation notch. Though small, they likely increased the resistance for crack initiation and resulted in the higher fatigue stress for specimen #160 compared to #161. There was no apparent colony toughening in specimen #161. Following initiation of the crack, propagation continued in the same lamellar colony.

Initiation of interlamellar fracture in the colony adjacent to the notch in specimen # 159 illustrates the influence of neighboring colonies on the deformation and failure of an individual colony. Kad, *et al*. [25] have produced 2-D simulations of anisotropic, polycrystalline gamma and have noted the influence of intercolony constraint on the development of large hydrostatic stresses at colony boundaries. These hydrostatic stresses, they conclude, are responsible some forms of crack initiation though generally Kad, *et al*. have examined this phenomena only at large plastic strains. The presence of three colonies in specimen # 159, with two colony orientations of $\phi \approx \pm 45°$ at the notch site, indicates that a competition between the two easy-slip colonies may have lead to the crack initiation. Localized slip would have had to occur in the colony containing the notch to initiate the crack in the neighboring colony [25]. This would depend on the relative sizes of the two colonies and the three dimensional constraint imposed by their neighboring colonies. The fact that this specimen exhibited the highest fatigue resistance of the four specimens indicates that this form of crack initiation is the least energetic. Thus the fatigue crack initiation sensitivity depends not only on the probability of notch intersects the mode III oriented colony, but also the constraint effects of the neighbor colonies.

3. Discussion

3.1 Fatigue Strength Differences in Smooth and Notched Bars

For the TiAl alloy studied, there was a significant difference in the fatigue strength of smooth and notched bars that is primarily related to orientation and size of the colonies containing notches. Apparently, the fatigue strength of a notched bar has a higher sensitivity to the local microstructural orientation than a smooth bar. A correlation appears to exist between orientation and crack initiation strength that is inverse to the known relationship between orientation and yield strength. The soft-mode ($\phi' = 30 - 60°$, ϕ' defined as the angle between the loading axis and lamellar lath plane) and hard-mode ($\phi' = 90°$) yield strengths for PST (49.3 at. % Al) material are about 100 and 500 MPa, respectively [14,15]. In polycrystalline γ-TiAl materials, σ_{ys} ranges from 380-500 MPa with grain sizes ranging from 230-2600μm [26]. This indicates that σ_{ys} of polycrystals is dominated by the aggregate of lamellar colonies and can approach the strength of the hard mode PST single crystals. The results in Table 1 indicate that the notched bar fatigue behavior of lamellar TiAl significantly depends on the angle between the notch plane or loading direction, and lamellar lath interface plane. In general, a soft mode lamellar colony associated with a notch, exhibits better crack initiation resistance than a hard mode orientation. That is, the fatigue strength of notched bars of polycrystalline materials follows the inverse of the yield strength / orientation of PST Gamma TiAl alloys.

The primary purpose behind the incorporation of twelve nominally identical notches in this experimental study was to increase the probability that a notch would fall on a relatively large colony in a specific orientation producing the minimum fatigue performance. Fatigue cracks generally initiate on the surface of a smooth specimen, if no substantial defect is present within the sample. Here crack initiation is strongly governed by the local plastic deformation at the surface. The formation of a deformation band in polycrystals is dictated by aggregate properties (e.g., the orientation of neighboring colonies and texture within the deformation bands) rather than by a single orientation [25]. However in a notched bar, initiation behavior can be governed by the anisotropic fracture toughness of the lamellar structure at the notch location. A minimum K_{IC} of 4.0 $MPa\sqrt{m}$, Table 2, was obtained from a type III C(T) specimen whose notch plane is parallel to the lamellar interface [17]. The fatigue crack growth threshold value of an identical C(T) specimen should be smaller than 4.0 $MPa\sqrt{m}$ and much smaller than ΔK_{th} of large crack C(T) specimen (8.6 $MPa\sqrt{m}$ for K5 - Lamellar) [8,10]. Thus, a type III notch-lamellar colony orientation could result in very low crack initiation strength. The resultant "pop-in" crack, which is on the order of the lamellar colony size, results in a significant increase in the crack driving force, ΔK, enabling continued propagation in a polycrystalline mode and corresponding a short propagation life. Therefore, the notches tend to minimize the number of cycles required for crack initiation and tend to change the mechanism of initiation from slip-induced to mode I crack opening, or fracture toughness. In summary, fatigue cracks can initiate and propagate from a notch located in a hard mode lamellar colony when the notch size is smaller than the nominal microstructural unit. This can have the effect of reducing the fatigue performance of a material over that of a smooth bar.

3.2 Critical Fatigue Crack Length, a_0

The work of Kitagawa and Takahashi [27] demonstrated a method of coupling the smooth bar fatigue strength with the crack growth threshold. A log-log plot of stress as a function of crack size relating these two properties results in two lines. Here a horizontal line representing the fatigue strength intersects a line having a slope of –1/2, representing the crack growth threshold at the "critical crack length". The application of ΔK_{th} as a "material property" was found to be limited to cracks equal to or slightly larger than the size, a_0, given by the intersection of the two lines.

A Kitagawa – Takahashi diagram for the notched fatigue data from this study was generated using the long-crack threshold (ΔK_{th}) of 8.6 $MPa\sqrt{m}$ [8,10] and a 10^7 fatigue strength range of 315 MPa, see Figure 8, with the resultant $a_0 = 443\mu m$. Some of the samples (#160, #161 and #162) show a significant deviation from the fatigue strength and crack growth threshold lines that could be a result of the notch depth, 75 μm, being much smaller than a_0. Thus, it seems that the problem regarding application of the fatigue crack growth threshold, ΔK_{th}, to the damage tolerance design is three folds. First, for isotropic materials it is expected that cracks or defects smaller than a_0 may exhibit "small-crack" effects, i.e. small cracks can propagate below the large crack threshold. Second, the dependence on the Kitagawa diagram when a_0 is smaller than the size of the dominant microstructural unit is likely to be anti-conservative due to the mechanisms of crack initiation and microstructural small-crack growth. Third, the intrinsic anisotropic nature of plastic deformation of lamellar gamma materials makes it probable that they will not follow the continuum behaviors used in the development of the diagram.

The "effective" fracture toughness of a Type III C(T) specimen (reduced to 3.6 MPa√m to account for the R = 0.1 fatigue loading) is also shown in Figure 8. Here the critical crack length, a_{III}, is 78 μm and the notch data lie much closer to this line. This indicates that the notches, produced by EDM machining, may act like cracks in terms of fracture toughness and could produce failure within the "safe" region of the Kitagawa diagram. Also shown in Figure 8 are conservative "pop-in" crack sizes that have been measured from the fracture surfaces of the notched specimens [7]. These are much closer to the long-crack threshold line and, depending on the level of crack closure in the pop-in cracks, could be within the finite life region of the Kitagawa diagram based on the effective threshold, $\Delta K_{eff,th}$. Alternatively, the initial crack size can be predicted using the crack growth rate data for the material [7], and the back calculated pop-in size can be determined, see Figure 8 and Table 4. Here, the crack sizes are larger than the approximate pop-in sizes determined from the fracture surfaces and all fall in the finite life region on the Kitagawa diagram. Here, a greater distance to the right of the ΔK_{th} line indicates a shorter life as discussed by Larsen, et al. [28]. The predicted pop-in size for specimen #162 is substantially larger than the average grain size. This is consistent with the sympathetic colony – notch orientation of initiation (ϕ_i = 11°).

Table 4. Predicted Pop-in Crack Sizes for Notched Specimens

Sample ID	Fatigue Stress (MPa)	Number of Cycles to Failure	~Pop-in Size (μm)	Propagation Life from Pop-in	Predicted Pop-in Size (μm)
159	350	148626	300	dnf *	460
160	325	8808	750	13150	840
161	300	65915	360	dnf	660
162	275	6068	600 **	dnf	1230

* Indicates that the crack did not propagate at this size.

** Size based on primary colony size – not including sympathetic colony.

The crack-size discussion presented here is not a rigorous analysis of the true crack sizes and shapes, which is beyond the scope of this work, but it clearly shows the influence of individual colonies on the fatigue behavior of a lamellar gamma alloy. The application of a threshold based life prediction scheme must incorporate the mechanisms of crack initiation in the material – in this case including the anisotropic fracture toughness and/ or fatigue crack growth threshold. "Small-crack" behavior is not conclusively ruled out in this material, which is an alternative explanation of the notched specimen behavior, however the mechanisms discussed here appear to have a stronger physical basis than a wholesale small-crack explanation.

3.3 Estimation of DK_{th}

At present no information is available regarding the fatigue crack growth threshold, ΔK_{th}, of PST materials with respect to lamellar orientations. Based on the low fracture toughness in the Type III orientation (i.e. the low delamination or cleavage stress) a similar anisotropic behavior in the fatigue crack threshold value would be expected. Also, ΔK_{th} should be lower than K_{IC} for the same lamellar orientation. Utilizing the notched fatigue specimen results, it is possible to estimate the lower bound of the fatigue growth threshold. Table 1 shows the calculated ΔK for the notched specimens, assuming the notches act as cracks, to be in the range of 2.6 to 3.6 $\mathrm{MPa}\sqrt{\mathrm{m}}$, which is clearly lower than the long-crack threshold of 8.6 $\mathrm{MPa}\sqrt{\mathrm{m}}$ [8,9]. The notch ΔK's are similar to, though generally lower than, the fracture toughness of the PST material in the Type III orientation when adjusted for the positive stress ratio ($K_{IC,\ eff}$ = 3.6 $\mathrm{MPa}\sqrt{\mathrm{m}}$). This indicates that the single colony ΔK_{th} is lower than the fracture toughness value, for the same orientation, and is on the order of 3.0 $\mathrm{MPa}\sqrt{\mathrm{m}}$ – possibly as low as 2.5 $\mathrm{MPa}\sqrt{\mathrm{m}}$ in the Type III orientation. This is lower than the threshold ($\Delta K_{th} \approx 3.5$ $\mathrm{MPa}\sqrt{\mathrm{m}}$) found when the crack size is smaller than the average lamellar colony size (145μm) of Ti-47Al-2Nb-2Cr-0.2B (at. %), having a corresponding long-crack threshold of 8.6 $\mathrm{MPa}\sqrt{\mathrm{m}}$ [18,23]. Also, an effective fatigue crack threshold (after correction closure), $\Delta K_{eff,th}$, of 4.5 $\mathrm{MPa}\sqrt{\mathrm{m}}$ was obtained from a near FL structure of Ti-48Al when the fatigue crack propagation direction is parallel to the lamellar interface [21]. The differences in these results could be due to several things. As a result of the strong anisotropy, the mechanical behavior of lamellar gamma is dependent on slight variations in the lamellar colony orientation [21]. The higher effective threshold, $\Delta K_{eff,th}$ = 4.5$\mathrm{MPa}\sqrt{\mathrm{m}}$, of the textured polycrystalline material compared to the others likely indicates the influence of constraint from neighboring colonies. The lowest values of threshold found in this study indicate the fatigue crack growth threshold that applies to a single colony in the type III orientation.

4. Summary and Conclusions

The apparent threshold associated with crack initiation is critically dependent on the orientation of the particular colony that cracks. The apparent fatigue crack growth threshold measured here is substantially lower than that measured in long fatigue cracks using conventional methods. This apparent threshold is also lower than the closure corrected or effective threshold, which would logically assume an absence of initial closure in the cracks emanating from the EDM notches. This indicates that in gamma structures the intrinsic defect size should be assumed to be on the order of the largest colony size. These colonies may crack, and may crack early in service, but the design philosophy should ensure that these cracks do not grow under the anticipated service loading. This indicates that a uniform and refined microstructure is essential for the commercial implementation of this class of materials.

Based on this study of crack initiation from intentional defects in a lamellar gamma titanium aluminide, the following conclusions ban be made:

1. The fully lamellar microstructure with a large colony size, having a high degree of plastic anisotropy, leads to scatter in the fatigue strength of bars having multiple notches.
2. When a notch is located in a type III orientation lamellar colony, the fatigue strength is much lower compared to a smooth specimen, as a result of the easy mode I crack initiation (toughness driven).
3. Though the polycrystalline fully lamellar microstructure has substantially greater crack growth resistance than duplex microstructure, this benefit can not be utilized in damage-tolerant structures due to anisotropic nature of ΔK_{th} when the colony size is large.
4. The lower bound of fatigue crack growth threshold should be utilized in design based on the knowledge of the microstructure size and uniformity, the influence of anisotropy on the mechanical behavior of the material and the critical crack length assessment from a Kitagawa diagram.
5. Colony boundaries are clearly beneficial in stopping the growth of an initiated crack; thus a fine colony structure is desirable to reduce the effective degree of anisotropy.

Acknowledgments

This research was performed in the Air Force Research Laboratory, Materials and Manufacturing Directorate, Wright-Patterson Air Force Base, OH and was supported in part by the Air Force Office of Scientific Research under Task 2302BW1. K. Li, B.D. Worth, and W.J. Porter gratefully acknowledge support of the Air Force Contract F33615-98-C-5214. The authors would like to acknowledge assistance of Chris Ahrens with some of the work.

References

1. Y-W. Kim, *JOM*, 1989, vol. 41 (7), pp. 24-30.
2. Y-W. Kim and D. M. Dimiduk, *JOM*, 1991, vol. 43 (8), pp. 40-47.
3. Y-W. Kim, *JOM*, 1994, vol. 46 (**7**), pp. 30-40
4. Y-W Kim, *Acta. Mater.*,1992, vol. 40 (6), pp. 1121-1134.
5. K. Li, W. J. Porter, A. H. Rosenberger and J. M. Larsen, in Fatigue '99 - Proceedings of the Seventh International Fatigue Conference, Beijing, P. R. China, 1999, X. R. Wu and Z. G. Wang, eds., Higher Education Press, Beijing, PRC and Engineering Materials Advisory Services Ltd., West Midlands, UK, 1999, pp. 1597-1602.
6. W. J. Porter, K. Li and A. H. Rosenberger, in Gamma Titanium Aluminides, Y-W. Kim, D. M. Dimiduk, and M. H. Loretto, eds., TMS, Warrendale, PA, 1999, pp. 587-593.
7. J. M. Larsen, A. H. Rosenberger, K. Li, W. J. Porter and R. John, in Fatigue '99 - Proceedings of the Seventh International Fatigue Conference, Beijing, P. R. China, 1999, X.R. Wu and Z.G. Wang, eds., Higher Education Press, Beijing, PRC and Engineering Materials Advisory Services Ltd., West Midlands, UK, 1999, pp. 1559-1566.
8. J. M. Larsen, B. D. Worth, S. J. Balsone and J. W. Jones, in Gamma Titanium Aluminides, eds. Y-W. Kim, R. Wagner & M. Yamaguchi, TMS, 1995, pp. 821-834.

9. J. M. Larsen, B. D. Worth, S. J. Balsone, A.H. Rosenberger and J. W. Jones, in Fatigue '96 - Proceedings of the Sixth International Fatigue Conference, Berlin, Germany, 1996, G. Luetjering and H. Nowack, eds., Tarrytown, N. Y. Pergamon, 1996, pp. 1719-30.
10. S. J. Balsone, J. M. Larsen, D. C. Maxwell and J. W. Jones, *Mater. Sci. Engr.*, A, 1995, vol. A192/193, pp. 457-464
11. R. O. Ritchie and J. Lankford, eds., Small Fatigue Cracks – Proceeding of the 2nd Engineering Foundation International Conference/Workshop, Santa Barbara, CA, US A, 1986, TMS, Warrendale, PA, 1986.
12. K. J. Miller and E. R. de los Rios, eds., Short Fatigue Cracks, Mechanical Engineering Publications Limited, London, 1992, UK.
13. D. L. Davidson and J. B. Campbell, *Metall. Trans.* A, 1993, vol. 24A, pp. 1555-1574.
14. M. Yamaguchi and H. Inui in Ordered Intermetallics - Physical Metallurgy and Mechanical Behavior, C. T. Liu et al, eds., Kluwer Academic Publisher, Netherlands, 1992, pp. 217-235.
15. H. Inui, Y. Toda and M. Yamaguchi, *Philosophical Magazine*, A, 1993, vol. 67(6), pp. 1315-1322.
16. T. Nakano, T. Kawanaka, H. Y. Yasuda and Y. Umakoshi, *Mater. Sci. and Engr.*, A, 1995, vol. A194, pp. 43-51.
17. S. Yokoshima and M. Yamaguchi, *Acta. Mater.*1996, vol. 44 (3), pp. 873-883.
18. J. P. Campbell, J. J. Kruzic, S. Lillibridge, K.T. Venkateswara Rao and R. O. Ritchie, *Scripta Mater.*, 1997, vol. 37(5), pp. 707-712.
19. P. Bowen, N. J. Rogers and A.W. James, in Gamma Titanium Aluminides, eds., Y-W. Kim, R. Wagner and M. Yamaguchi, TMS, 1995, pp. 849-865.
20. P. Bowen, R. A. Chave and A. W. James, *Mater. Engr.*, A, 1995, vol. A192/193, pp. 443-456.
21. S. Hirohisa, T. Keiro and O. Yasuhito, *Mater. Sci. & Engr.*, A, 1998, vol. A243, pp. 169-175.
22. D. J. Wissuchek, G. E. Lucas and A. G. Evans, in Gamma Titanium Aluminides, eds., Y-W. Kim, R. Wagner and M. Yamaguchi, TMS, 1995, pp. 875-882.
23. J. J. Kruzic, J. P. Campbell and R. O. Ritchie, *Acta Mater.*, 1999, vol. 47 (3), pp. 801-816.
24. Kezhong Li, William J. Porter and Andrew H. Rosenberger, “Lamellar Colony Orientation Determination in Gamma Titanium Aluminides Using Orientation Imaging Microscopy (OIM)”, to be submitted.
25. B. K. Kad, M. Dao and R. J. Asaro, *Philosophical Magazine* A, 1995, vol. 71(3), pp. 567-604.
26. Y-W. Kim, *Intermetallics,* 1988, vol. 6, pp. 623-628.
27. H. Kitagawa and S. Takahashi, in Proceedings of the 2nd International Conference on Mechanical Behavior of Materials, 1976, Boston, MA, USA. pp. 627-631.
28. J.M. Larsen, R. John, S.M. Russ, D.C Maxwell, B.D. Worth, A.H. Rosenberger, K.Li, and W.J. Porter, in Small Fatigue Cracks Mechanics: Mechanisms and Applications, eds. K.S. Ravichandran, R.O. Ritchie, and Y. Murakami, Elsevier, Oxford, 1999, pp. 131-142.

Figure Captions

1. Microstructure of fully lamellar alloy K5
2. Schematic of the multi-notched fatigue specimen.
3. Maximum stress versus cycles to failure for smooth and notched specimens (numbers represent the notched specimen IDs).
4. SEM images of specimen #160; (a) cleavage-like fracture surface associated with a notch where the fatigue crack initiated, (b) side view of the fracture surface, and (c) enlargement of notch region.
5. SEM images of specimen #161; (a) cleavage-like fracture surface associated with a notch where the fatigue crack initiated and (b) side view of the fracture surface.
6. SEM images of specimen #162; (a) cleavage-like fracture surface associated with a notch where the fatigue crack initiated and (b) side view of the fracture surface.
7. SEM images of specimen #159; (a) the fatigue crack initiated from a notch located close to the boundary of two lamellar colonies and (b), side view of the fracture surface. The delamination colony is labeled.
8. Kitagawa- Takahashi diagram of K5 lamellar microstructure showing Type III effective fracture toughness line and the notched data based on the notch depth, the conservative pop-in crack size and the crack size predicted using a life integration.

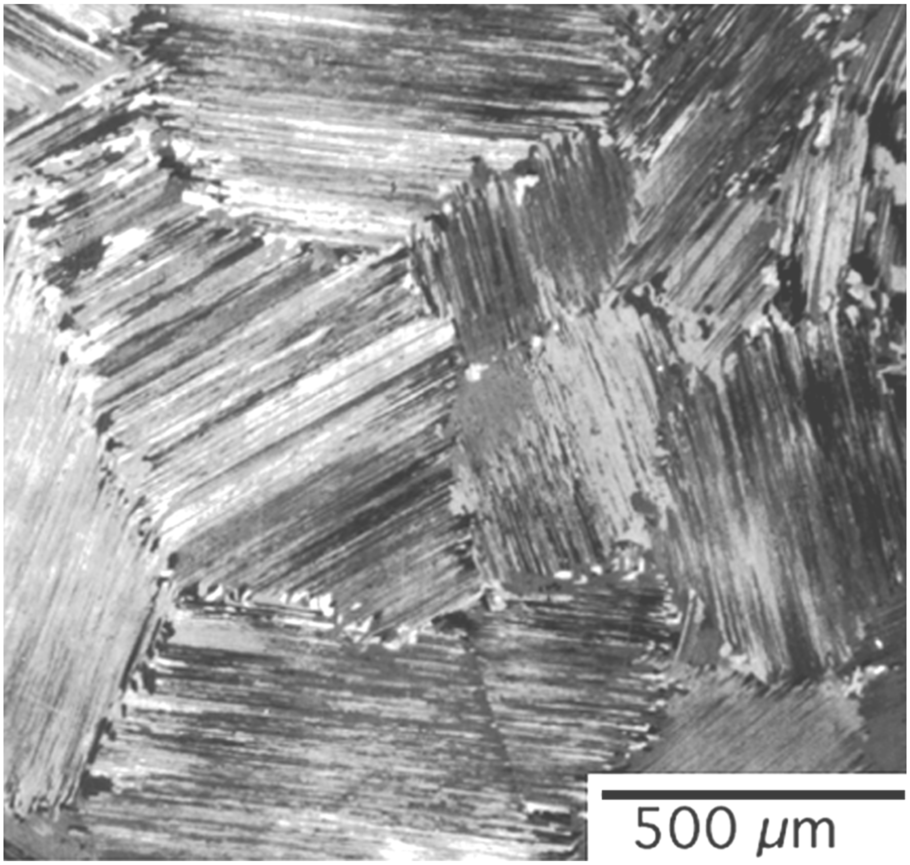
500 μm

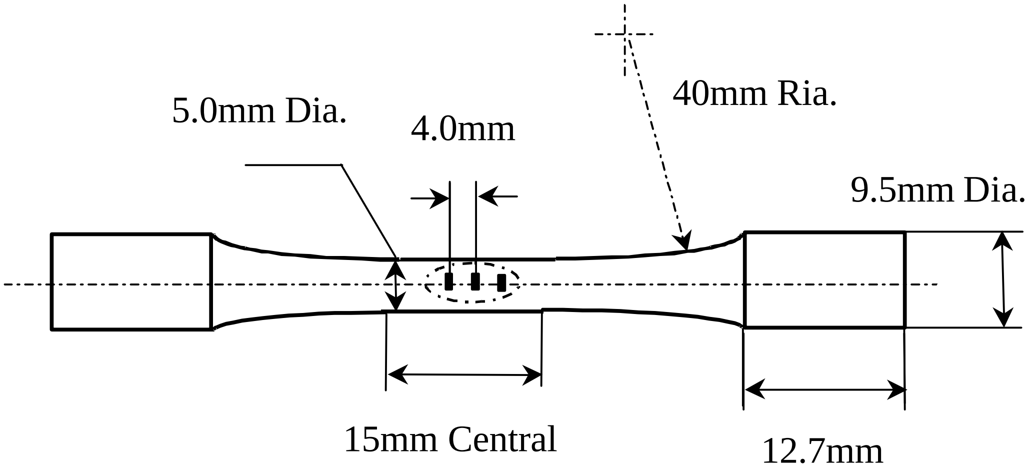

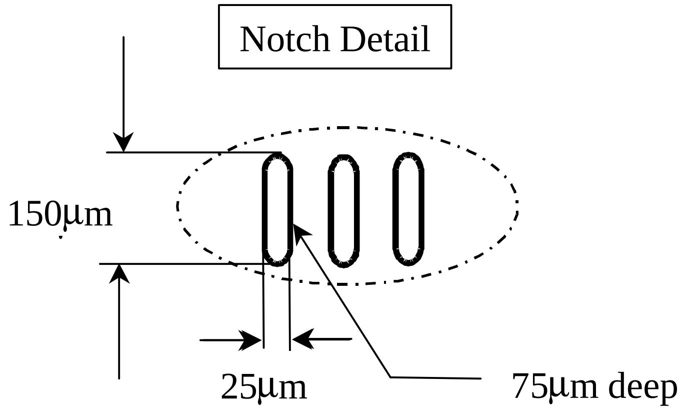

Note- Total length of specimen 85mm.
EDM (4) notches every 90° for total
12 notches per specimen.

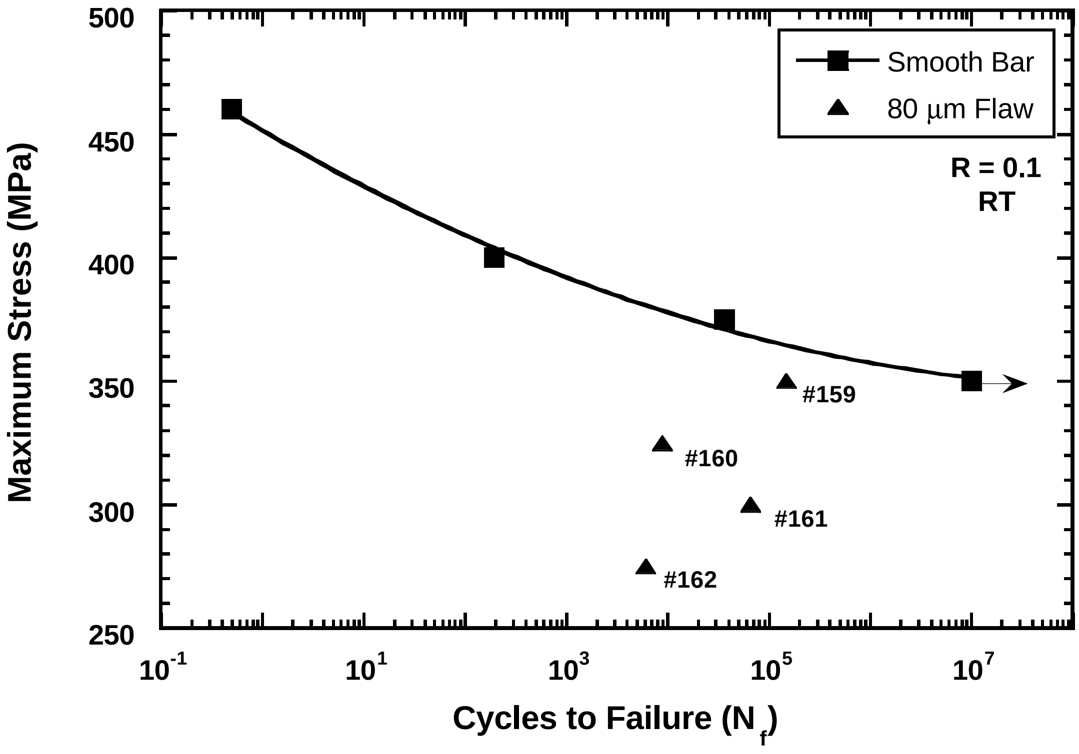
Maximum Stress (MPa)
500
450
400
350
300
250
10^{-1}
10^{1}
10^{3}
10^{5}
10^{7}
Cycles to Failure (N_f)
Smooth Bar
80 µm Flaw
R = 0.1
RT
#159
#160
#161
#162

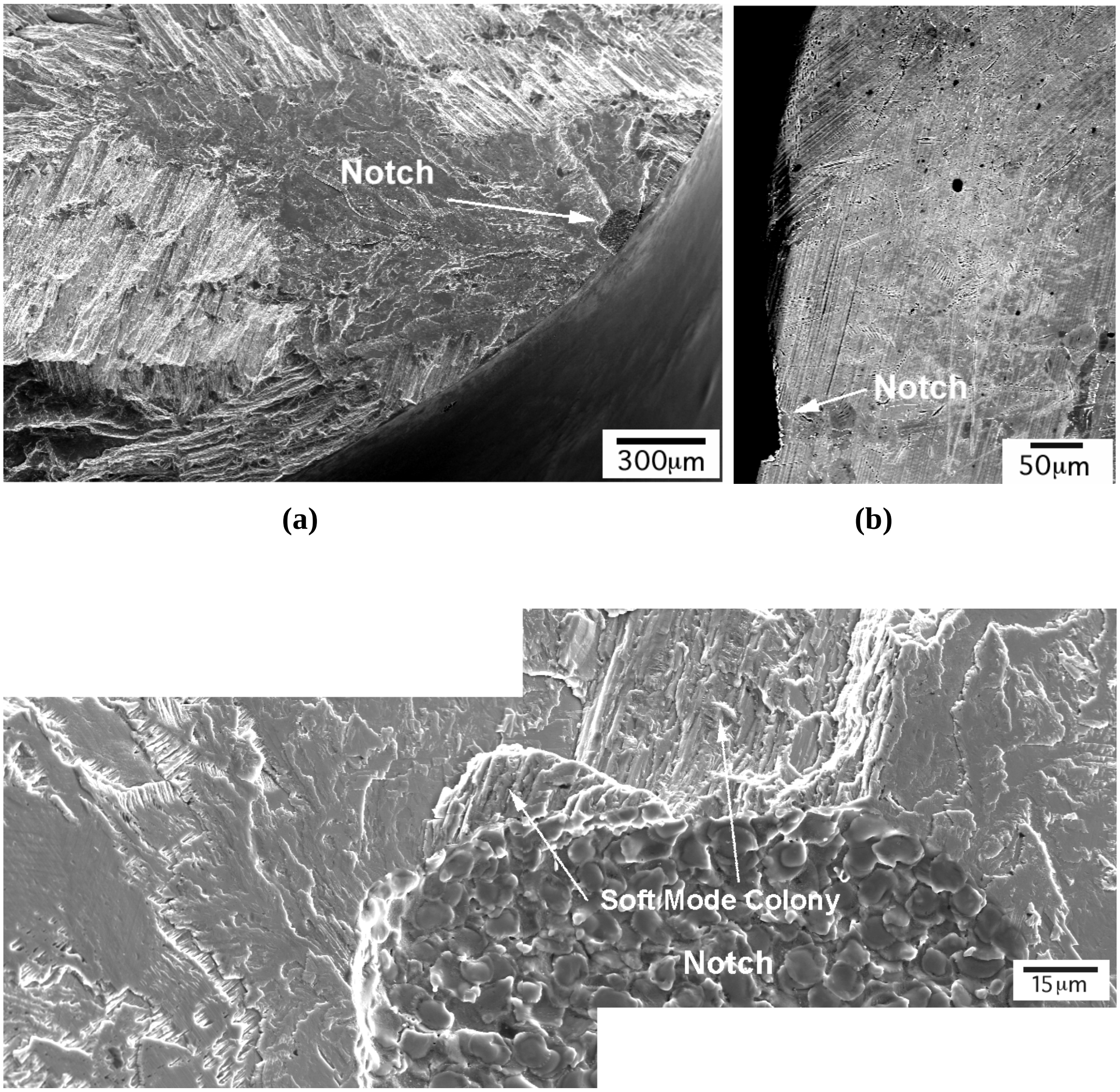

(a)

(b)

(c)

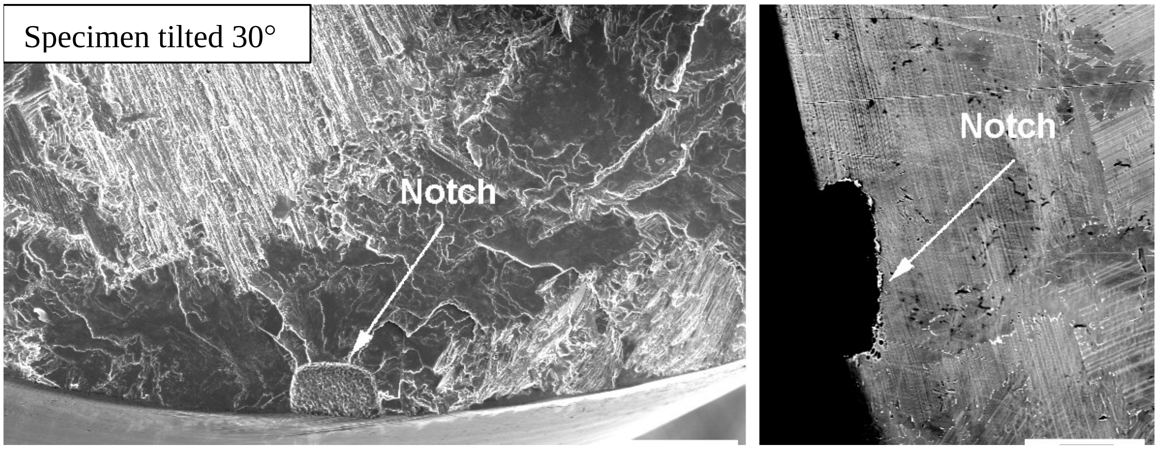

(a) **(b)**

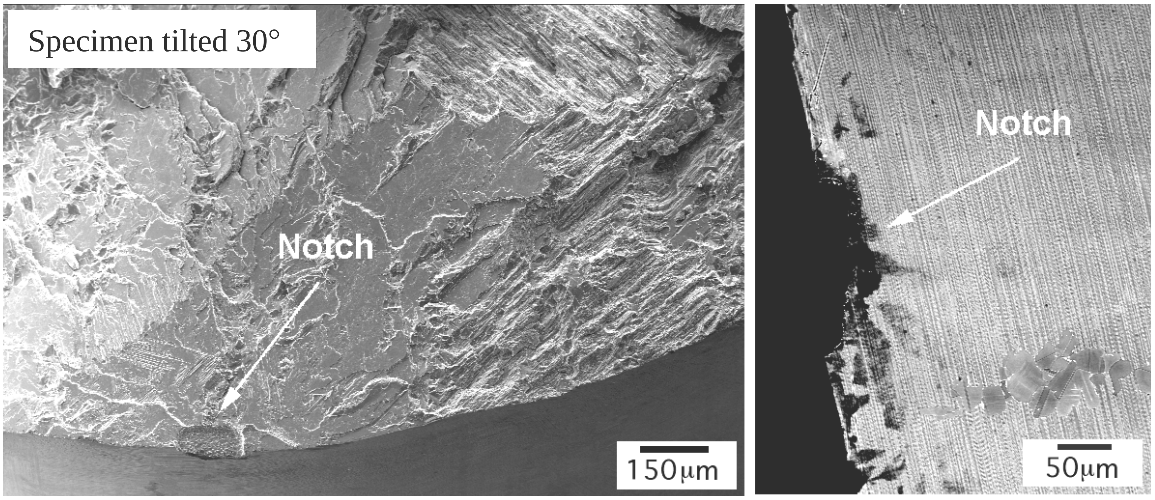
Specimen tilted 30°
Notch
150μm
Notch
50μm

(a) (b)

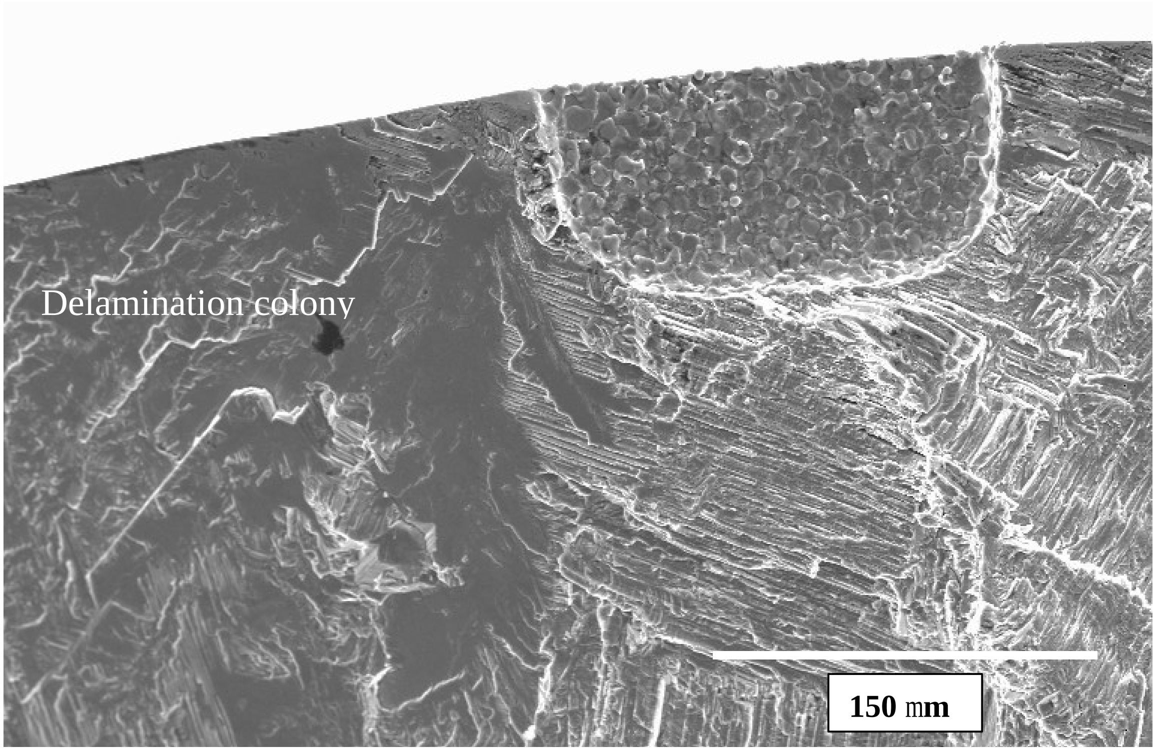
Delamination colony
150 mm

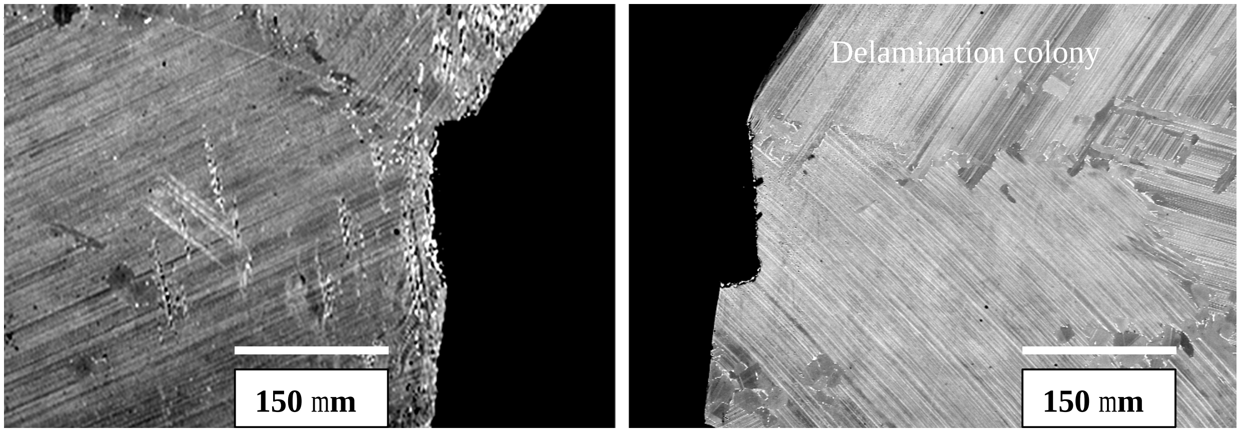
150 mm
Delamination colony
150 mm

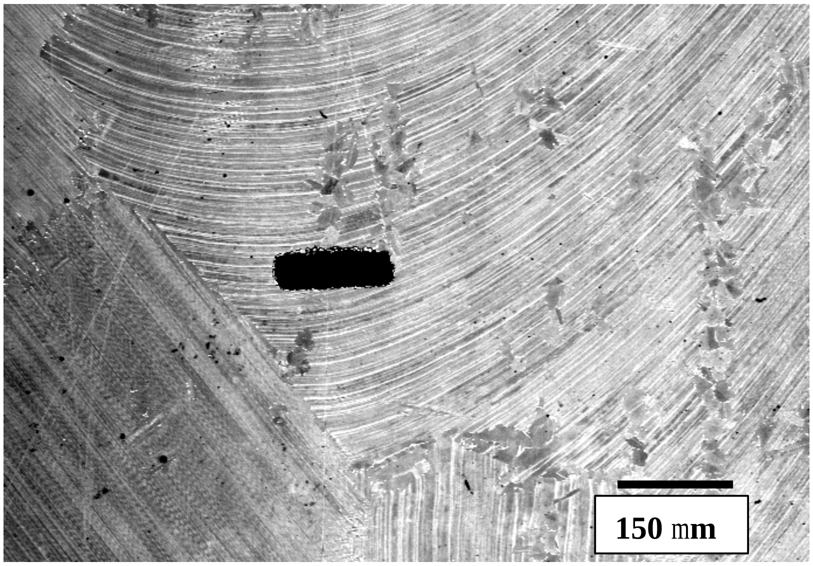
150 mm

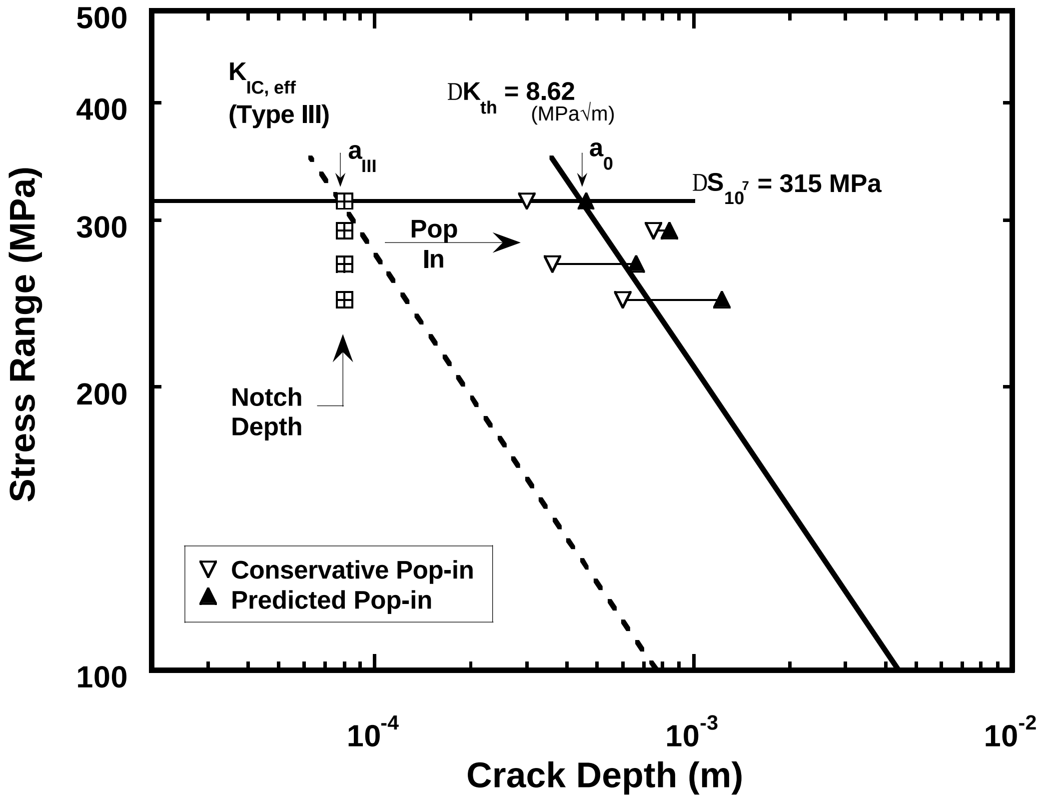
$K_{IC, eff}$
(Type III)
a_{III}
ΔK_{th} = 8.62
(MPa√m)
a_0
ΔS_{10^7} = 315 MPa
Pop
In
Notch
Depth
▽ Conservative Pop-in
▲ Predicted Pop-in
500
400
300
200
100
Stress Range (MPa)
10^{-4}
10^{-3}
10^{-2}
Crack Depth (m)

This page intentionally left blank

PRIMARY MELTING ISSUES RELATED TO GAMMA TITANIUM ALUMINIDES

W. John Porter, III[1]; Young-Won Kim[2]; Kezhong Li[1]; Andrew H. Rosenberger[3]; and Dennis M. Dimiduk[3]

[1]The University of Dayton Research Institute, 300 College Park, Dayton, OH 45469-0128 USA
[2]UES Inc., 4401 Dayton-Xenia Rd., Dayton, OH 45432 USA
[3]AFRL/MLLM, Air Force Research. Lab., 2230 Tenth St., Wright-Patterson AFB, OH 45433-7817 USA

Abstract

As gamma titanium aluminides mature into industrially-accepted structural materials, increased demand for manufacturing defect-free product is required. While gamma alloys can be processed using techniques and equipment currently used for conventional titanium alloys, large-scale melting of these alloys has not been fully implemented. In a program aimed at addressing large-scale production of a gamma titanium-aluminide alloy, a number of issues pertaining to initial ingot quality were discovered. Among these were centerline porosity and/or piping, grain-size disparities, and high- and low-density regions related to insufficient melt homogenization. This paper describes the assorted material quality issues and suggests solutions for their eradication.

Introduction

Gamma titanium aluminides (γ-TiAl), with their inherent light weight, oxidation resistance, and high-temperature property retention, continue to be investigated for various industrial and, in particular, aerospace applications [1-5]. As this class of material nears commercial utilization, issues pertaining to large-scale manufacturing require appropriate attention. Of particular importance will be the requirement to deliver high quality, nearly defect-free material. While laboratory and small-scale casting of γ-TiAl alloys is readily accomplished, it is often difficult to reproduce situations that may occur in a large industrial setting. Issues pertaining to input material variability (i.e. electrodes for vacuum arc remelting (VAR), compacts for cold-hearth techniques, etc.) and melt process control are, in many instances, beyond the capability of most laboratory practice.

For example, significant effort has gone into eliminating the presence, or reducing the severity, of defects in conventional titanium alloys [6-13]. Methods for improving alloy quality include triple-melt processes including triple VAR or replacing a VAR step with an intermediate cold-hearth melting step using plasma arc or electron-beam sources. Triple melting provides ample opportunity for sufficient mixing of alloying elements to minimize the chance of gross chemical segregation. The cold-hearth processes enable the practical elimination of high-density inclusions (HDI) such as fractured carbide tool bits mixed in with lathe turnings or other revert material by allowing the HDI to sink to the bottom of the melt and out of the melt stream. Importantly, the risk of low-density inclusions (LDI) such as titanium nitride surviving a cold-hearth melting process is reduced by the increased residence time of the LDI in the molten metal.

A systematic study to understand the intricacies of plasma arc melting γ-TiAl has found that ingot homogeneity increases with the use of homogeneous compacts, lower casting rates, and multiple melting steps (i.e. triple melt VAR) [14]. That study employed a dual-plasma-torch, cold-hearth unit to melt ingots having diameters of 10 or 15 cm [14]. An earlier study of a single-melt, 10 cm diameter ingot from the same furnace reported significant elemental variations and associated microstructural differences across the ingot [15]. Findings from those studies strongly suggest that the triple-melt approaches used in aerospace-grade conventional titanium alloys will aid in production of homogenous, large-diameter γ-TiAl ingots.

This paper discusses a variety of processing-related issues encountered in two single-melt, large-diameter γ-TiAl ingots. A short description of each type of defect and recommendations for improving the processes responsible for its presence will be discussed.

Experimental Procedure

The alloy characterized in this paper has a chemistry of Ti-46Al-1.5Cr-2Nb-0.5Mo-0.13B-0.27C (at%). Two ingots, 43 and 66 cm in diameter, respectively, were produced via plasma arc melting (PAM) on a four-torch, cold-hearth, production PAM unit (Allvac, Monroe, NC). The 43 cm diameter ingot was approximately 250 cm long and weighed nearly 1300 kg. The 66 cm diameter ingot was approximately 125 cm long and weighed 1680 kg. The feedstock for the ingots were puck-shaped compacts weighing nearly 2 kg. The compacts were composed of titanium sponge, aluminum pellets, TiO_2 powder, boron in the form of drawn and chopped Al-Ti-B rods, and small chunks of Cr-Al, Nb-Al and Mo-Al-Ti master alloys.

Following removal from the PAM unit, the ingots were soaked and slow cooled to prevent cracking due to thermal shock. The ingots were homogenized in vacuum for 5 hours at 1400°C and slow cooled to room temperature (Solar Atmospheres, Soudertown, PA). Extrusion was done using a start temperature of 1290°C and extrusion ratios of ~5:1 for the 43 cm ingot and 6.6:1 for the 66 cm ingot (Wyman-Gordan, Houston, TX). A two-step isothermal forging process at 1180°C was undertaken to produce both 2.8 and 7.6 cm thick by 42 cm diameter pancakes (Ladish Co., Cudahy, WI). The forgings were given a final heat treatment of 1370°C for 2 hours, slow cooled using helium to 870°C and then held at 870°C for 2 hours before furnace cooling.

Results and Discussion

The fully-lamellar, equiaxed microstructure of the cast+extruded+forged material following heat treatment is shown in Figure 1. The average grain size for this material was determined to be approximately 350 µm. Chemistries for the 43 and 66 cm diameter ingots, and for forgings taken from the 43 cm diameter ingot are shown in Table 1. The forgings used for the chemistry evaluation represent material from the bottom, the quarter-height, and the half-height of the 43 cm ingot.

Standard x-rays taken of 5 millimeter thick cross-sections electro-discharge machined (EDM) from the center of the forgings parallel to the forging direction (i.e. through-thickness plane) revealed a number of prominent features. An example of a cross-section x-ray is shown in Figure 2. Forging flow lines and centerline porosity are apparent in this figure. Elemental segregation during ingot solidification, as well as an inhomogeneous melt stream into the crucible, result in high-aluminum bands that persist through subsequent thermomechanical processing and final heat treatment. The high-aluminum bands are the light-contrast phase evident in the x-ray (Fig. 2).

Investigation of these regions using a scanning electron microscope (SEM) and backscattered-electron imaging (BEI) showed minimal differences between the banded areas when compared to the matrix microstructure. The centerline porosity is also a byproduct of the ingot solidification process that survived the extrusion and forging processes. Pores approaching 200 µm in length were observed. A series of pores distorted during the extrusion and forging processes are shown in Figure 3.

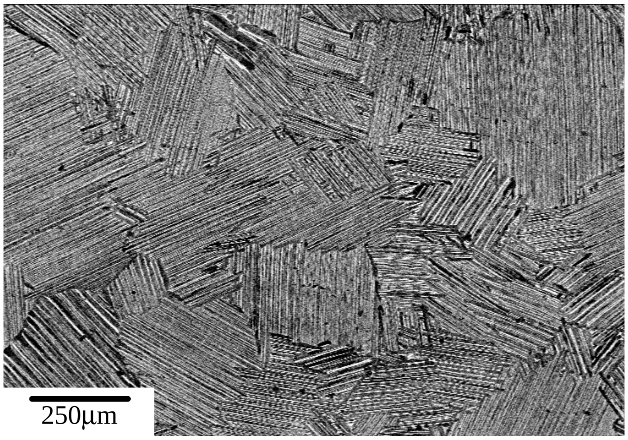

Figure 1: Microstructure of thermomechanically processed and heat treated Ti-46Al-1.5Cr-2Nb-0.5Mo-0.13B-0.27C (at%) (BEI)

X-rays of various cross sections revealed large spots or disk-shaped indications with distinct high-density contrast. Backscattered-electron imaging (BEI) was used to investigate some of these regions. One example is shown in Figure 4. This region measured approximately 16 mm long and 1.75 mm wide. The local microstructure consisted of a grain-boundary beta phase having small equiaxed gamma particles interspersed within. The grain-boundary phase surrounds a lamellar region highlighted by interlamellar cracking. The lamellar grains within the high-density region were approximately 50 µm in diameter and had a noticeably finer lamellar spacing than the matrix lamellar grains. The compositions of the individual phases, as determined by microprobe analysis, are indicated in the inset table. The aluminum-deficient beta phase has a particularly high level of chromium and molybdenum, indicating significant segregation upon cooling of the ingot. Also, gamma readily nucleates in the high-temperature, beta phase ($\beta \rightarrow \beta+\gamma$) upon during cooling in the solid state. .As shown in the upper left-hand corner of Figure 4, regions of lower-density material are often found encapsulated by the high-density material. An example of the low-density region is shown in Figure 5. An appreciable gradient in aluminum level is exhibited by the gradual increase in brightness as the distance from the central (dark) gamma grains is increased. The low-density areas also show evidence of microcracking within the surrounding fine lamellar microstructure (Figure 5b).

Table I: Composition Analyses from the 43 and 66 cm dia. ingots and from forgings taken from the 43 cm dia. ingot.

Aim Chemistry	***Element***/ location	**66 cm Ingot**	**43 cm Ingot**	**Forging A- middle of 43 cm ingot**	**Forging B- near bottom of 43 cm ingot**	**Forging C- bottom of 43 cm ingot**
		center of ingot	center of ingot	mid-radius	mid-radius	mid-radius
bal	***Titanium***	50.186	n/a	48.936	48.940	49.153
46.500	***Aluminum***	45.360	45.200	46.054	46.053	45.758
1.500	***Chromium***	1.408	1.500	1.617	1.730	1.639
2.000	***Niobium***	1.732	1.800	1.901	1.850	2.024
0.500	***Molybdenum***	0.445	0.500	0.495	0.481	0.500
0.125	***Boron***	0.109	0.130	0.147	**0.085**	0.151
0.260	***Carbon***	0.311	n/a	0.315	0.319	0.310
800-1000	***Oxygen (wppm)***	1300	1240	1260	1590	1310
	Nitrogen	0.020	n/a	0.101	0.011	0.017
	Vanadium	0.044	n/a	0.046	0.051	0.042
	Iron	0.077	n/a	0.072	0.079	0.079

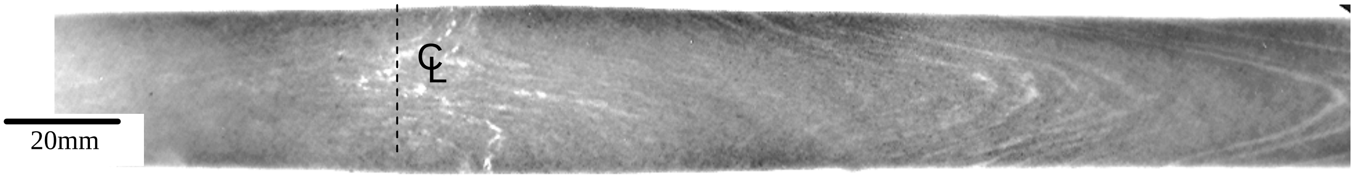

Figure 2: X-ray of 5 mm thick cross section from a fully-processed and heat-treated forging. Light contrast corresponds to porosity (centerline) and/or presence of light-element-rich phase(s) (forging flow lines).

A second type of high-density occurrence is shown in Figure 6. Unlike the high-density grain-boundary material shown in Figure 4, this form is globular in appearance. While the constituents are the same as described earlier, the volume fraction of the lamellar material within the defect is much lower while the volume fractions of beta-and gamma-phase material are higher than in the grain-boundary-type high-density regions.

While the average grain size was approximately 350 μm, many grains were found to be in excess of 800 μm. A grain having a diameter exceeding 800 μm is shown in Figure 7. This disparity in grain size may be due to inadequate distribution of boron throughout the ingot. Borides are potent grain-refining agents via the pinning mechanism in wrought gamma titanium aluminides [16]. Evidence of insufficient boron distribution is highlighted in the chemistry analysis (Table 1). Boron analysis of forged material from near the bottom of the 43 cm diameter ingot (Forging B) showed a low reading of 0.085 at% when compared to the boron aim of 0.125 at% (33% lower than aim). Boron readings from material from other locations in the ingot were consistent, highlighting the localized nature of inadequate boron dispersal. Rogue, large lamellar grains with unfortunate orientation have been shown to be likely locations for fatigue initiation [17]. Limiting the occurrence of similar grains is imperative to establishing fully-lamellar γ-TiAl alloys in fatigue-critical applications.

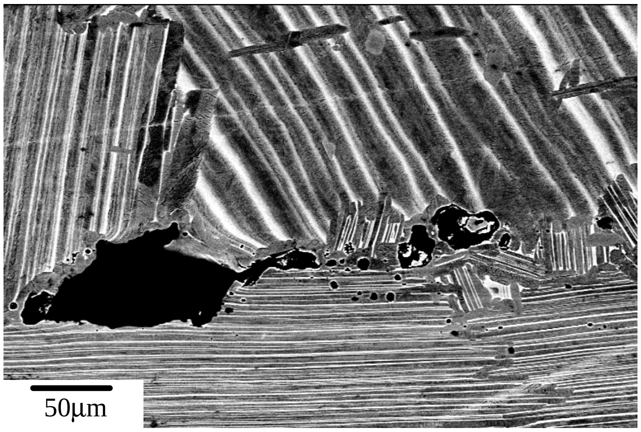

Figure 3: Residual casting porosity distorted during the extrusion and forging processes. (BEI)

Low density, lens-shaped regions were observed in forgings made using material from both ingots. Some of the low-density regions were as large as 2mm wide by 5mm long. The microstructure was composed of gamma grains having small flecks of beta phase in the center, gradually changing to a nearly-lamellar appearance with scattered, equiaxed gamma grains before reaching the fully-lamellar matrix. Boride particles were often associated with the low-density regions. Locally elevated boron levels are consistent with the observed fine gamma grain size [18].

The majority of the heterogenenities observed in these large ingots appear to be the byproduct of the solidification of an inhomogeneous molten material. While the localized or micro-level issues described in this paper differ from the macro-level heterogeneities of single-melt, 10 and 15 cm diameter ingot material discussed by Godfrey and Loretto [14], the remedies intended for lowering the probability of occurrence of each type of heterogeneity parallel one another. First, efforts must be taken to insure that the compacts comprising the feedstock or input material are as homogeneous as possible to reduce the risk of preferential melting of low-melting-point elements, in this case aluminum. Early, preferential melting of low-melting-point elements such as aluminum can lead to an inhomogeneous melt stream rich in these elements and obvious segregation issues within the ingot. Another issue pertaining to the feedstock is the use of sufficiently small diameter master-alloy additions that are able to fully melt and disperse their constituent elements. Ideally this would help to eliminate the high-density-type regions described previously.

The most significant way to effect ingot homogeneity issues would be to incorporate at least a second and preferably a third melting step in the ingot production process. Triple-melt conventional titanium alloys are required for disks, spools, shafts and other fatigue-critical aerospace applications. Many years of experience have shown multiple-melt approaches to yield homogeneous, high-quality ingots. The efforts of Godfrey and Loretto [14] have shown this to apply to medium-sized γ-TiAl ingots as well. It is safe to reason that the fabrication of high-quality, large-diameter γ-TiAl ingots is probable by utilizing homogeneous feedstock in concert with multiple-melting processes.

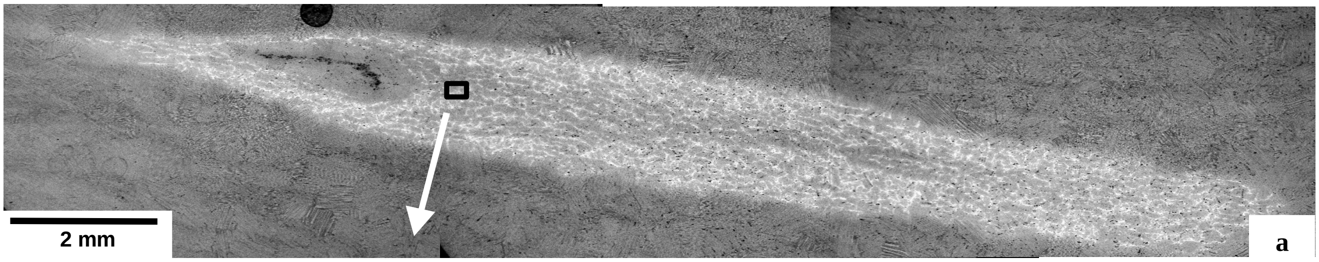

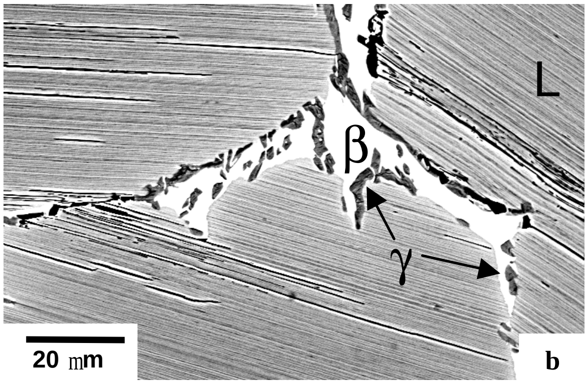

	Al	**Ti**	**Cr**	**Nb**	**Mo**	**Cr+Nb+Mo**
b	**34.9**	**57.1**	**4.0**	**2.5**	**1.5**	**8.0**
g	**47.9**	**48.9**	**1.0**	**2.0**	**0.3**	**3.3**
L- matrix	**46.1**	**49.8**	**1.5**	**2.1**	**0.5**	**4.1**
L- defect	**42.9**	**53.7**	**1.2**	**1.8**	**0.4**	**4.4**

c

Figure 4: Lens-shaped, high-density inhomogeneity. a) Low magnification; high-contrast region approximately 16 mm long and 1.75 mm wide (BEI), b) high magnification of continuous beta-rich grain-boundary phase, peppered with small gamma grains encompassing fine-spacing lamellar regions (BEI), and c) compositions of the individual phases as determined by microprobe analysis.

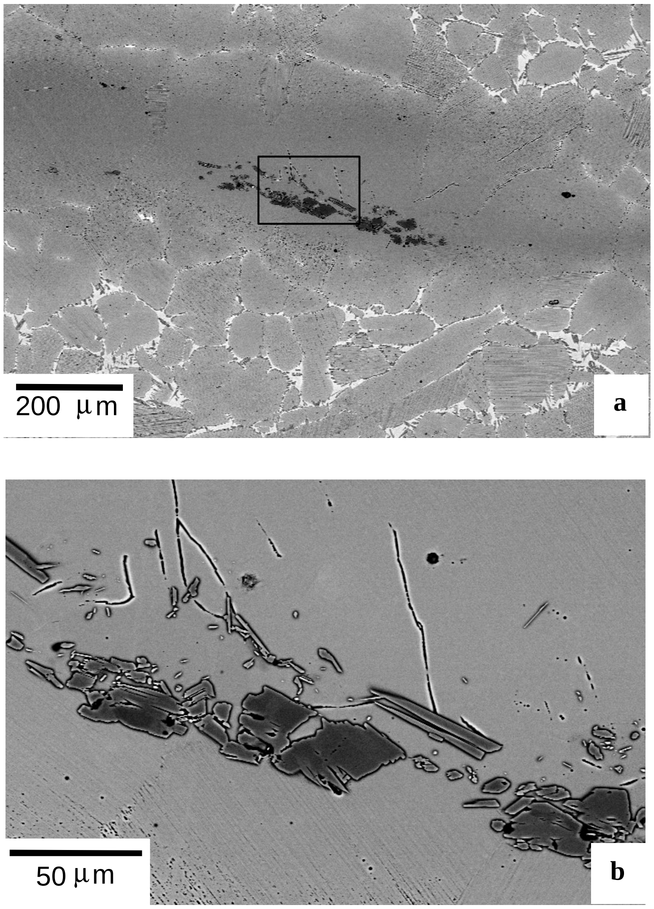

Figure 5: a) Lower-density gradient within grain-boundary-type high-density region (BEI), and b) microcracking within the surrounding fine lamellar microstructure (BEI).

Conclusions

Material from two single-melt, large-diameter, plasma arc melt ingots were evaluated to determine their homogeneity and relative occurrence of casting defects. Significant findings from this investigation include: 1) a variety of melt-related defects were identified and characterized, and 2) primary material quality concerns are related to elemental segregation and subsequent inhomogeneous microstructures. Porosity was also observed in these materials. Suggested approaches to improve ingot homogeneity include the use of multiple-melting campaigns as presently used in conventional titanium alloys, and increased homogeneity of feedstock material incorporating the use of smaller master-alloy particles in the initial compacts to insure complete melting of the input material.

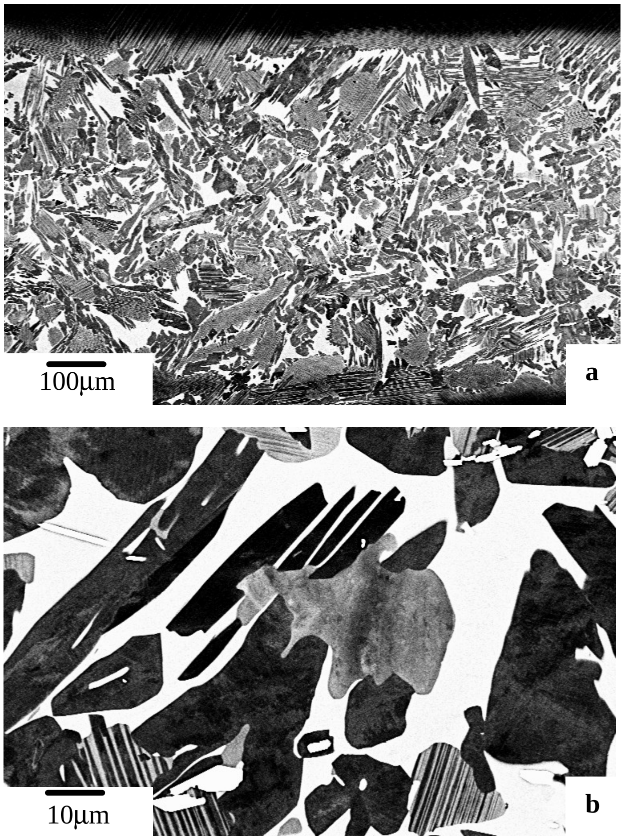

Figure 6: Regions containing globular-type high-density phases, a) Low magnification highlighting large amount of beta phase (BEI), and b) high magnification showing small volume fraction of lamellar phase within globular region (BEI).

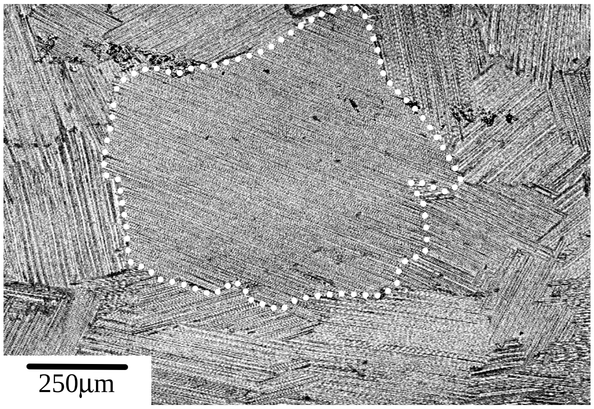

Figure 7: Representative large grain symptomatic of inadequate boron distribution during ingot casting (BEI). Large central grain has been outlined.

Acknowledgments

This research was performed at the Air Force Research Laboratory, Materials and Manufacturing Directorate, Wright-Patterson Air Force Base, OH. W. J. Porter and K. Li gratefully acknowledge the support of Air Force Contract F33615-98-C-5214.

References

1. Y-W. Kim, "Intermetallic Alloys Based on Gamma Titanium Aluminide," JOM, 41 (7) (1989), 24-30.

2. Y-W. Kim and D.M. Dimiduk, "Progress in the Understanding of Intermetallic Gamma Titanium Aluminides," JOM, 43 (8) (1991), 40-47.

3. P.L. Martin, C.G. Rhodes and P.A. McQuay, "Thermomechanical Processing Effects on Microstructure in Alloys Based on γ-TiAl," Structural Intermetallics, R. Darolia, J.J. Lewandowski, C.T.Liu, P.L. Martin, D.B. Miracle, and M.V. Nathal, eds., (Warrendale, PA, TMS, 1993), 177-186.

4. D.M. Dimiduk, P.L. Martin and Y-W. Kim, "Microstructure Development in Gamma Alloy Mill Products by Thermomechanical Processing," Materials Science and Engineering, A243 (1998), 66-76.

5. P.L. Martin and C.G Rhodes, "Microstructure and Properties of Refectory Metal Modified Ti-48at%Al-2at%Nb-2at%Cr", in Titanium '92, F.H. Froes and I.L. Caplan, eds., (Warrendale, PA, TMS, 1993), 399-406.

6. J.L. Henry, S.D. Hill, W.E. Anable and J.L. Schaller, "Source and Control of Nitride Inclusions in Titanium," Report of Investigations 7933, U.S. Bureau of Mines, (Washington, D.C., 1974).

7. W.H. Buttrill and C.E. Shamblen, "Hearth Melt Plus Vacuum Arc Remelt: Production Status," Titanium '95, Blenkinsop et al., eds, (London, UK, Institute of Materials, 1995), 1446-1453.

8. A. Mitchell, "Melting, Casting, and Forging Problems in Titanium Alloys," Materials Science and Engineering, A243 (1998), 257-262.

9. A. Mitchell, "Recent Developments in Specialty Melting Processes," Materials Technology, 9/10 (1994), 201-206.

10. J.P. Bellot, B. Foster, S. Hans, E. Hess, D. Ablitzer and A. Mitchell, "Dissolution of Hard-Alpha Inclusions in Liquid Titanium Alloys," Metals and Materials Transactions B, Vol. 28B (1997), 1001-1010.

11. Y. Honnorat, "Issues and Breaktrhough in the Manufacture of Turboengine Titanium Parts", Materials Science and Engineering, A213 (1996), 115-123.

12. A. Mitchell, "The Electron Beam Melting and Refining of Titanium Alloys", Materials Science and Engineering, A263 (1999), 217-233.

13. J.A. Van Den Avyle, J.A. Brooks and A.C. Powell, "Reducing Defects in Remelting Processes for High-Performance Alloys," JOM, 50 (3) (1998), 22-25

14. B. Godfrey and M.H. Loretto, "Origins of Heterogeneities in Plasma Melted Ingots of γ-TiAl," Materials Science and Engineering, A266 (1999), 115-122.

15. A.L. Dowson, T.P.Johnson, J.M. Young and M.H. Jacobs, "Microstructure and Chemical Homogeneity of Plasma-Arc Cold-Hearth Melted Ti-48Al-2Mn-2Nb Gamma Titanium Aluminide," Gamma Titanium Aluminides, Y-W. Kim, R. Wagner and M. Yamaguchi, eds., (Warrendale, PA, TMS, 1995), 467-474.

16. Y-W. Kim and D.M. Dimiduk, "Effect of Boron Addition on Grain Refinement and Lamellar Formation in Wrought-processed Gamma TiAl Alloys" this proceedings.

17. J.M. Larsen, B.D. Worth, S.J. Balsone, A.H. Rosenberger and J.W. Jones, "Mechanisms and Mechanics of Fatigue Crack Initiation and Growth in TiAl Intermetallic Alloys," Fatigue '96, Vol. III, G. Lütjering and H. Nowack, eds., (Oxford, U.K., Elsevier Science Ltd., 1996), 1719-1730.

18. K. Li, W.J. Porter, A.H. Rosenberger, and J.M. Larsen, "Defects in Wrought Gamma Titanium Aluminides," Fatigue '99, X.R. Wu and Z.G. Wang, eds, (Oxford, U.K., Elsevier Science Ltd., 1999), 1597-1602.

This page intentionally left blank

Macro-segregation in Gamma Titanium Aluminides

Kezhong Li[†], W. John Porter III[†], and Andrew H. Rosenberger[‡]

[‡] AFRL/MLLMN, Air Force Research Laboratory, Materials and Manufacturing Directorate, Wright-Pattern AFB, OH 45433-7817, USA

[†] The University of Dayton Research Institute, 300 College Park, Dayton, OH 45469- 0128, USA

Abstract

Two wrought, near gamma titanium aluminides, Ti-46.1Al-1.73Cr-1.85Nb-0.5Mo (at. %, material 3-95M) and Ti-46.5Al-2.0Cr-2.8Nb-0.1B-0.25W-0.22C-0.18Si (at. %, material KD-CBS) were investigated. X-ray radiograph, scanning electron microscopy (SEM), x-ray energy dispersive spectroscopy (EDS) dot mapping and micro-probe analysis were utilized to characterize of the gross segregation.

The x-ray radiograph revealed high-density segregation (HDS) and low-density segregation (LDS) regions in 3-95M and KD-CBS, respectively. The macro-segregation regions were as large as 16.5 x 1.6mm in 3-95M and 7.6 x 0.4mm in KD-CBS.

Further investigation on 3-95M showed that the degree of HDS is different from region to region as indicated by SEM imaging contrast, structural morphology and relative phase volume fraction. In addition, a substantial density gradient is present in some regions. In general, the abnormal microstructure of HDS was characterized to consist of β in addition to γ phase and lamellar colonies, compared to the normal fully lamellar structure. The colony size of the segregation region is much smaller, with finely spaced but occasionally cracked laths. EDS dot mapping showed the general variation in composition of the micro-constituents (β, γ and lamellar colony) for each of the following five elements: Al. Ti, Nb, Cr and Mo. The results confirmed that the β phase was rich in Nb, Mo and Cr (all three elements are β-stabilizer in conventional Ti alloys) and lean in Al; conversely, γ phase and lamellar colonies are high in Al and low in Nb, Mo and Cr.

The quantitative compositional results for each phase obtained by micro-probe analysis were consistent with the EDS dot mapping observations. A HDS region with a very high Nb content, showed a much higher volume fraction of β phase and lower volume fraction of lamellar colony. Severe concentration (Cr, Nb, Mo and Al) gradients also resulted in co-existence of high- and low- density segregation, the latter of which was always associated with porosity and inclusions.

The low-density segregation (LDS) region of KD-CBS was characterized as being rich in boron (B) and deficient in Al, confirmed by Auger, EDS dot mapping and micro-probe analysis. The resultant microstructure showed a very high volume of small boride particles in the extremely rich B region and a banding structure consisting of equiaxed γ and borides in the moderate B rich region.

The large-scale macro-segregation present in both TiAl alloys apparently originated from the melting pass and has survived the following processing. This tended to suggest that the problem could be eliminated if more homogeneously melted liquid can be poured into the crucible and cooled in a controlled manner.

I - Introduction

Gamma TiAl is a unique material having three distinct payoff areas for implementation in aircraft engines [1-4]: stiffness, high temperature strength and burn resistance. However, the implementation of gamma presents obvious challenges. The most serious issue is the small critical flaw size in damage tolerance design due to its low RT ductility, rapid fatigue crack growth and poor impact resistance [1-6]. For cast components large centerline shrinkage cavities and surface-connected shrinkage porosity are critical issues [1,2,7,8]. Wrought structures tend to be more homogeneous, thus, superior to cast structures due to the breakdown of the coarse ingot structure into smaller sizes.

Great attention has been given to the micro-segregation of γ-TiAl alloys, which occurs on the micro-scale between dendrite arms and within single grains [1,2,7-11]. The occurrence of dendritic segregation is due to a double cascading peritectic reaction during solidification. The reaction gives rise to dendritic core regions of α_2 and γ lamellae and interdendritic regions of normally single-phase γ, which are last to solidify from the melt [1,7-11]. However, gross segregation and unmelted raw materials sometimes observed in arc-melted ingots of conventional titanium alloys have not been reported [1]. This work reports the observation of macro-segregation observed in two wrought, near-gamma titanium alminide alloys, which included light element (boron) segregation and heavy element (Nb, Mo and Cr) segregation. The large scale and extent of the chemical inhomogeneity result in significant variations in structural morphology, phase composition and relative phase volume fraction, as well as formation of defects such as inclusions and porosity.

II - Experimental Procedure and Results

Two wrought γ titanium aluminides were investigated. Table 1 gives both nominal compositions in atomic percent.

Table 1- Composition (at. %)

	Al	Cr	Nb	Mo	Ti	B	W	C	Si
3-95M	46.1	1.73	1.85	0.5	48.9	0.085		0.32	
KD-CBS	46.5	2.0	2.8		48.0	0.1	0.25	0.22	0.18

The ingot of 3-95M, 43cm in diameter, was produced via triple hearth plasma arc melting (PAM). The ingot was approximately 250cm long and weighted 1300kg. The feed stock for the ingots were puck-shaped compacts composed of Ti sponge, Al pellets, TiO_2 powder, B in the form of drawn and chopped Al-Ti-B rods, and small chunks of Cr-Al, Nb-Al and Mo-Al-Ti master alloys. The ingot was homogenized in a vacuum furnace and slow cooled to room temperature. Extrusion was conducted with a reduction ratio of ~5.5:1. The resultant extrusion was cut into 11 mults which were converted with a two-step forging process at 1180°C and ~80% reduction (The forging investigated was the second from the bottom of the ingot). A super transus heat treatment was applied followed by stabilization.

The KD-CBS ingot was produced by single hearth PAM. The 35cm diameter ingot was then skinned to 32.5cm for canning and extruded with reduction ratio of ~6 to 1. The extruded billet was 13cm in diameter and 20cm tall, and subsequently isothermally forged at 1100°C to 3.1cm thick. The heat treatment was performed as following: 925°C/30min. + 1325°C/40min. + 1380°C/4min., furnace cooled to 900°C, held for 24 hours and finally air cooled to room temperature. The final pancake diameter was 24cm.

2.1- High-density elements segregation in 3-95M

Three pieces from cross-sectional slabs, 5mm thickness were electric-discharged machined (EDM) from the pancake, labeled as I, II and III, seen in Figure 1. Plate I was cut through approximately the diameter of the pancake (totally 44cm long). Plate II and III (next to each other) were about 38mm long, cut from the positions that were close to the pancake center and almost perpendicular to Plate I. All three plates were inspected by x-ray radiography. The x-ray operating parameters employed were the following: voltage 110kV, current 5mA and exposure time 2 to 3 minutes with a small focal spot 0.4mm and focal distance 102cm.

By placing a source of x-ray on one side of the plate and photographic film on the other, a shadow picture, or radiograph, can be made. The more dense portions of the objects allow a smaller portion of the radiation to pass through than the less dense, show lighter shade compared to the matrix, in the negative film of the radiograph. The operating parameters employed were able to show a brightness difference corresponding to 2% material density variation. Central pipe porosity appearing very dark in the negative film was within a 25mm radius of the center of the pancake. In all, five high-density segregation (HDS) regions were observed in the three plates of 3-95M. The centers of HDS regions were all located within 100mm in radius of the center of the pancake. The five HDS regions were designated: D_I of Plate I; D_{II-1} and D_{II-2} of Plate II; and D_{III-1} and D_{III-2} of Plate III. Apparently, D_{III-1} and D_{III-2} were extensions of D_{II-1} and D_{II-2}, respectively, since the corresponding defect sizes and locations relative to the pancake surface were similar. This indicated that D_{II-1} and D_{II-2} were disk shaped with the disk planes approximately parallel to the forging plane. The defects are about 7 – 17mm long and 1-2mm wide. The radiograph also reveled that a low-density band was inserted in the high density D_{III-1} defective region.

Although x-ray radiography can be employed to pinpoint defect locations, its application is limited in the detail it can resolve – on the order of 1 mm. The micro-structural characteristics of the defects were studied using SEM back-scattered electron (BSE) imaging. The elemental (Al, Ti, Cr, Nb and Mo) distributions of the defective regions were determined qualitatively using EDS dot-mapping and the quantitative composition of each constituent phase was determined by microprobe analysis.

The dimensions of the macro-segregation defects were measured in the low magnification BSE images: 12.8 x 0.8 mm (D_I), 16.5 x 1.6 mm (D_{II-1}), 7.6 x 1.6 mm (D_{II-2}), 16.5 x 1.3 mm (D_{III-1}) and 7.6 x 1.3 mm (D_{III-2}). All of the defect sizes are also shown in Figure 1.

Figures 2(a)-(d) are low magnification BSE micrographs showing predominant high-density segregation (HDS) regions from D_I, D_{II-1}, D_{II-2} and $D_{III-1,}$ respectively. All images were original SEM images without any computer enhancement. Concentration gradients were clearly visible in all images. In Figure 2(a), uniform, higher brightness of defect D_I was shown in the central part of the image but gradually decreased toward both ends. On the contrary the heavy element densities, of D_{II-1} and D_{II-2} and D_{III-1} were lower in the central region than the surrounding, Figure 2(b)-(d). As the gradient was significantly intense, isolated low-density segregation (LDS) regions with an island morphology were apparent, (dark image), Figure 2(b)-(d). The maximum size of the ellipse-shape island (D_{II-2} of Plate II) was as large as 2 x 1.5mm, Figure 2(c). Figure 2(d), which showed a partial image of D_{III-1}, revealed a LDS region inserted in the center and running parallel to the entire HDS defect of D_{III-1}. This observation is consistent with the defect image of D_{III-1} revealed by x-ray.

Figure 3(a) shows a BSE image of the normal microstructure of 3-95M, which was characterized as a fully-lamellar structure, $(\alpha_2+\gamma)_L$, with a typical colony size of 300 - 500µm. The BSE images of the HDS defective regions, shown in Figure 3(b)-(d), revealed a very different microstructural morphology compared to the normal structure. Three-phase structure was observed in the HDS regions including γ, β phase and $(\gamma+\alpha_2)_L$. This is owing to high concentrations of any or all of the elements: Cr, Nb and Mo, inevitably promoting the formation of β phase, a very bright phase in BSE imaging. As a consequence, the lamellar colony size and lath spacing decreased significantly as comparing Figure 3(b) and 3(c) to 3(a). However, differences in the extent of segregation resulted in differences in structural morphology and phase volume fraction. A higher volume fraction of the blocky β phase and a lower fraction of lamellar colonies were observed in region D_I, Figure 3(b), apparently due to the high concentration of the β-stabilizer elements. In the other HDS regions, including D_{II-1}, D_{II-2}, D_{III-1} and D_{III-2}, β phase appeared in lamellar colony boundaries forming discontinuous necklace structure, a representative seen in Figure 3(c). Although the lamellar colony is much smaller in the HDS regions, micro-cracks were occasionally observed in lath boundaries, Figure 3(d). On the other hand in the low density, island-like regions as seen in Figure 2(b-c), cracking (Figure 3(e)) and inclusions and pores (Figure 3(f)) were frequently observed. In Figure 3(f) lamellar lath bending and cracking are clearly visible. Apparently, substantial plastic deformation was impeded by inclusions during thermal processing, which resulted in cavitation and cracking.

To further investigate qualitatively the major element distribution (Al, Cr. Ti, Nb and Mo) EDS dot-mapping was performed in the HDS regions. That is, the BSE imaging and x-ray detector worked together to provide rapid analyses of both morphology and micro-chemical aspects in the microstructure.

The EDS x-ray detector is equipped in a Leica 360 field-emission SEM. The operating parameters of EDS dot mapping were the following: voltage 20kV, current 0.5nA, focal distance 25mm, dwell time 0.15 second and a resolution corresponding to 6.2 pixels per millimeter, which is identical to the SEM imaging resolution. The characteristic x-ray energies employed were: Al-K (1.49 keV), Cr-K (5.42 keV), Ti-K (4.51 keV), Nb-L (2.17 keV) and Mo-L (2.29 keV).

Figure 4(a)-(d) showed the EDS dot-mapping images with the corresponding BSE image of the HDS defect D_I, Figure 4(f). The microstructure consists of β phase (bright), lamellar colony (light gray), γ phase (embedded in β, dark gray) and unknown particles (very bright), seen Figure 4(f). The EDS dot maps of Al-K, Fig. 4(a) and Ti-K, 4(c), reveal the compositional phase contrast for β, lamellar colony, γ phase and the unknown particles. That is, for Al concentration from rich to lean (the EDS imaging intensity from the highest to lowest) the order is γ, lamellar and β phase. For Ti, the order is simply the opposite. Cr, Nb and Mo are richer in β phase but lean in γ and lamellar, Figure 4(b, c, e). The unknown particles are very lean (or absent) in Al, Ti, and Cr, but rich in Mo and contain some Nb.

Due to a difference in microstructural morphology and phase volume fraction between HDS region D_I and the other defective regions (D_{II-1}, D_{II-2}, D_{III-1} and D_{III-2}), EDS dot-mapping was also performed on D_{II-1}. The results were similar to the results from defect $D_{I.}$ That is, β phase was rich in Cr, Nb Mo and lean in Al. γ and lamellar phases were rich (γ is richer) in Al but lean in Cr, Nb and Mo.

To obtain quantitative contents of each constituent (α_2, γ, β and $(\alpha_2+\gamma)_L$ colony) microprobe analysis was performed using a Joel Superprobe 733. The operating parameters employed were the following: voltage 15kV, current 30nA and electron beam probe sizes (in diameter) 1μm or 10μm. All elements down to sodium (atomic number, Z = 11) can be detected. The compositions of the three constituents (γ, β and $(\alpha_2+\gamma)_L$) of the abnormal structures of the HDS regions were measured. For comparison α_2, γ and $(\alpha_2+\gamma)_L$ of the homogeneous microstructure were also measured. All the individual phases (γ, α_2 and β) were measured using 1μm probe size and the lamellar colony using 10μm probe size. A pure element intensity calibration was employed and each reported result was an average value of 3-5 measurements. The microprobe analysis was performed on defect region D_I and D_{II-1}. The results were summarized in Table 2.

The microprobe results confirmed that there is a significant variation in the Nb+Cr+Mo content of the lamellar colony in HDS regions (1.74 - 8.54, at. %) in addition to the presence of β phase, compared to normal structure (Nb+Cr+Mo = 3.94 %). Furthermore, much higher Nb contents are present in all three phases (γ, β and $(\alpha_2+\gamma)_L$) of region D_I compared to D_{II-1}. This result is consistent with the SEM and EDS dot-mapping observations: the β phase volume fraction is much higher in D_I than D_{II-1}. In addition, the lamellar structure is lean of Al (41.8-43.6%) and has a large variation of Ti content (47.8 –55.7%), comparing a normal structure of 46.2% Al and 49.8% Ti.

Table 2 - Composition for Constituent Phase (at. %)

Element		Al	Ti	Cr	Nb	Mo	Ti/Al	Cr+Nb+Mo
bulk content		46.10	48.90	1.73	1.85	0.5	1.08	4.08
Normal structureStructure, Fig. 3(a)	$(\alpha_2+\gamma)_L$	46.24	49.81	1.43	2.00	0.51	1.08	3.94
	γ	48.09	48.26	1.11	2.11	0.43	1.0	3.65
	α_2	40.09	55.00	2.27	2.00	0.62	1.38	4.89
HDS-D_{II-1}, see Fig. 3(c)	$(\alpha_2+\gamma)_L$	41.75	55.65	0.87	1.44	0.30	1.33	1.74
	β	34.87	57.11	4.0	2.52	1.50	1.64	8.02
	γ	47.85	48.89	0.97	2.03	0.27	1.02	3.27
HDS-D_I, see Fig. 3(b)	$(\alpha_2+\gamma)_L$	43.63	47.84	0.83	7.47	0.24	1.10	8.54
	β	34.84	52.56	2.24	9.79	0.59	1.51	12.62
	γ	46.75	44.47	0.60	8.03	0.15	0.95	8.78

2.2- Boron segregation observed in KD-CBS

The purpose of boron addition in the alloy was to reduce the lamellar colony size due to the formation of grain boundary pinning titanium borides. The gross segregation location of KD-CBS was also pinpointed by x-ray radiography, which showed a dark band in the negative film, compared to the surrounding matrix. The central part of the low-density segregation (LDS) region is about 3 cm from the edge of the pancake and is approximately 7 mm long by 0.4 mm wide, as measured by BSE imaging, see Figure 5. However, the BSE imaging technique could not determine if the lower average atomic number, or 'Z', was due boron, aluminum, or both. All elements down to carbon ($Z = 6$) can be detected by EDS equipped with a crystal spectrometer. However, the detection is very marginal for boron ($Z = 5$) and the detectability of the boron peak of x-ray spectrum heavily depends on the B content. Auger electron microscopy was employed to determine whether B or Al was responsible for the LDS, since light atoms (low Z) are more likely to eject auger electrons than to emit x-rays. The auger dot-mapping confirmed that B is rich in this region (referred to LDS-B afterwards) compared to the surrounding matrix. A BSE image, Figure 6(a), revealed a significant concentration gradient in this region. Figure 6(b), an enlargement of 6(a), showed an almost totally dark and featureless region. EDS dot mapping was performed at voltage 5kV and beam current 0.5nA, (x-ray characteristic energy: B-K = 0.185KeV, Al-K = 1.487 KeV), indicated that B was rich, Figure 6(c), and Al lean, Figure 6(d).

The normal as-forged microstructure showed a fine mixture of equiaxed γ and α_2 grains with no constituent larger than 20μm, a result due to dynamic recrystallization during forging, Figure 7(a). The alternating bright and dark banding structure of LDS-B was shown in Figure 7(b). The dark band consisted of very small (< 1μm) boride particles with a small volume fraction of α_2. The structure of the bright band consists of mainly equiaxed γ (however, of much smaller size compared to normal structure) plus a small amount of grain-boundary α_2. The phase identification work was supported by the microprobe analysis results using identical operating parameters as the high-density segregation study in 3-95M. Table 3 gives the compositions of each phase (γ, α_2 and boride) of the normal structure and dark and bright band of the LDS region.

Table 3 – Phase Composition of LDS-B (wt. %)

Structure	Phase	Al	Si	Ti	Cr	Nb	W	Total wt. %
Normal	γ	32.06	0.06	58.43	2.12	6.72	0.96	100.4
	α_2	21.66	0.19	58.79	7.00	6.76	5.03	99.4
Dark band	boride	10.10	0.03	60.00	1.60	5.73	0.93	76.1
Bright band	γ	32.88	0.03	57.59	2.39	5.70	0.95	99.5
	α_2	21.40	0.20	58.92	9.01	6.02	4.35	99.9

The current microprobe analysis can detect all elements down to sodium (Z = 11). The total weight % of the dark band of LDS-B was significant less than 100%, indicating, perhaps, the lack of boron detection. The dark band, consisting mainly boride particles, was very rich in Ti and lean in Al - consistent with results from other boron containing materials [12]. Microprobe analysis results also revealed that Cr and W prefer α_2 than γ phase, however, Nb seemed to equally partition in α_2 and γ.

III - Discussion

The large-scale gross segregation including both LDS in KD-CBS and HDS in 3-95M appears to suggest that the highly alloyed titanium aluminides are prone to severe segregation. Such substantial chemical and structural inhomogeneities are detrimental to mechanical properties. No aerospace component would be tested much less put into service containing such defects especially since most life-limiting mechanical properties are related to defects [1]. Thus, the successful implement of gamma alloys is dependent on development of processing routes which are capable of generating defect-free components, which are free from microstructural and compositional inhomogeneities [13].

The gross segregation severity, such as the segregation pattern and location with in a titanium aluminide forging is currently unclear without using destructive inspecting methods. The intensity of the transmitted x-ray beam is an inverse exponential function of the object thickness. Thus, when the incident x-ray beam is perpendicular to the forging surface of a pancake the intensity contrast is not great enough to resolve segregation-induced density differences. Techniques such as immersion ultrasonic inspection must be developed for titanium aluminides for their successful adoption by the aerospace industry. Nevertheless, there seemed to be a difference regarding the locations of macro-segregation in the 3-95M and KD-CBS materials. All of the observed high-density segregation regions in 3-95M obtained by random sampling were located within a 100mm radius of the disk center, whereas, the macro-segregation of the light element, boron, occurred very close to the edge of the pancake in KD-CBS. It seemed that the result of 3-95M is consistent with the general macro-segregation mechanism of beta-stabilizing elements in titanium alloys. For this class alloys macro-segregation generally occurs in the ingot center and head regions where solidification takes place under a high thermal gradient following remelting [14]. For KD-CBS the gross boron segregation was likely due to a single plasma hearth melting.

The association of segregation regions and their large size in 3-95M strongly indicates that the defects were due to insufficient mixing during melting. That is, heterogeneity originates from solidification of an inhomogeneous liquid, which consists of metallic ingredients with significantly different melting points [15], even following triple plasma arc melting.

Processing Alternative

Gamma alloys generally can be cast in a manner similar to conventional titanium alloys. The ingot can be processed via double or triple vacuum arc re-melting (VAR) to achieve chemical homogeneity [15,16]. Melt-related defects in titanium are typically classified as either low-density inclusion (type I, interstitial-stabilized hard α), aluminum-rich, α-stabilized regions (type II), or high-density inclusions (type III, β-stabilized) [17-20]. The triple VAR process is the current industry accepted specification for premium quality (rotor grade) titanium alloys. However, over the past 15 years, cold-hearth melting (CHM) has received significant attention in the titanium community since the concept is conductive to prevention or removal certain melt-related defects [17-22]. The two types of CHM are plasma (PCHM) and electron-beamed (EBCHM); the PCHM process uses a plasma torch in a protective atmosphere to heat the metal in the hearth, while EBCHM employs electron beams under a vacuum. The superiority of CHM to VAR comes from the fact that the molten metal must continuously transverse a horizontal, water-cooled hearth from the feed stock melting region to a collar mold where the ingot solidifies and is bottom-withdrawn. Separation of the melting and casting zones produces a more controlled molten metal residence time for eliminating inclusions by the recognized mechanisms of dissolution and density separation [17-20].

At present for industry practice one or more VAR may be replaced by electron- beamed or plasma cold hearth melting [22]. However, the requirement for disk and associated rotor components specifies CHM to be followed by a single VAR [19,21,22]. The final VCR step was required for chemical homogeneity (for EBCHM) and hydrogen removal (for PCHM) and ingot surface enhancement [19]. The introduction of the HM + VAR process replacing triple VAR began at GEAE in 1988. Over 8.2 million kg of titanium alloy ingots had been produced using the HM + VAR processes by the end of 1995. These processes have been shown to have the potential to produce materials with significantly reduced frequencies of melt-related inclusions, such as hard α and high-density inclusions, when compared to triple VAR process [19-21]. Hearth melting, used as a final melt step in the development of titanium aluminides (as in the ingot productions of 3-95M and KD-CBS), probably is the consequence of the hearth melt “only” technology development in 1993 in GEAE. The “only” after HM designated that it is at least the final, if not only, melting step [19]. The program has demonstrated that HM “only” processes are feasible for premium quality Ti alloys production. Nevertheless, producibility issues were encountered in making full-scale demonstration HM “only” heats; but all of these issues appear to be resolvable via enhanced process definition and control [19, 20].

Apparently, owing to much higher Al content compared to conventional titanium alloys, the demands for defect-free titanium aluminides are more challenging. Component cracking and surface connected porosity during solidification and cooling of cast γ TiAl alloys are major processing issues [1,2,7,8]. Dendritic segregation patterns (micro-segregation) resulting from the additions of Nb, Ta, W, are also well recognized [9-11,15]. Systematic investigation on the small-scale PCHM indicated that double melting or triple melting reduces the extent of heterogeneity; it suggested that the key to producing homogenous ingots is to have homogeneous liquid metal before pouring it into the crucible [15]. Nevertheless, the problem to be faced by the gamma community is the definition of the optimal melting processes.

No systematic work on the large-scale ingot melting has been reported. However, significant amounts of industry experimental and university lab work on titanium alloys have demonstrated that CHM is reaching new levels of enhanced process control. Successful application of advanced sensors has resulted in reduced variability and awareness of critical parameters for sustained refining performance. Hearth pool temperature, casting rate, chamber atmosphere in addition to equipment related parameters, all can be monitored [18-20]. As γ-TiAl alloys near the commercial utilization, the following issues pertaining to full-scale component manufacturing must be solved with emphasis on the large-scale ingot melting:

- Understand the mechanism of macro-segregation to allow development of improved melting process to minimize the occurrence.
- Modify master alloy purity, particle size and improve compact process.
- Optimize processes and develop scientific-based models of performance, integrate computational models and closed-loop controls to enable virtual prototyping of process.

Conclusions

Gross segregation including heavy elements (Cr, Nb and Mo, all beta stabilizers in Ti and its alloys) and light element, B, were observed in material 3-95M and KD-CBS, respectively. A significant variation in composition in the gross segregation regions compared to the bulk, resulted in the significant variations in microstructural morphology, phase formation, phase volume fraction and occasionally cracking. Since all the life-limiting mechanical properties of the rotation components in aircraft engines are related to defects, the large-scale gross segregation is not tolerable for the application. The defects were identified as being melted-related problems and suggestions have been made to manufacture defect-free materials.

References

1. C. M Austin and T. Kelly, Structural Intermetallics, R. Darolia, J. J. Lewandowski, C. T. liu, P. L. Martin, D. B. Miracle and M. V. Nathal, eds., TMS, Warrendale, PA, 1993, 143-150.
2. C. M Austin and T. Kelly, K. G. Mcallister and J. C. Chesnutt, Structural Intermetallics, M. V. Nathal, R. Darolia, C. T. Liu, P. L. Martin, D. B. Miracle, R. Wagner and M. Yamaguchi, eds., TMS, Warrendale, PA, 1997, 1997, 413-426.
3. Y-W. Kim and D. M. Dimiduk, JOM, 43(8), 1991, 40-47.
4. D. M. Dimiduk, P. L. Martin and Y-W. Kim, Materials Science and Engineering, A243, 1998, 66-76.
5. B. D. Worth, J. M. Larsen, and A. H. Rosenberger, Structural Intermetallics, M. V. Nathal, R. Darolia, C. T. Liu, P. L. Martin, D. B. Miracle, R. Wagner and M. Yamaguchi, eds., TMS, Warrendale, PA, 1997, 563-569.
6. A. H. Rosenberger, B. D. Worth and J. M. Larsen, Structural Intermetallics, M. V. Nathal, R. Darolia, C. T. Liu, P. L. Martin, D. B. Miracle, R. Wagner and M. Yamaguchi, eds., TMS, Warrendale, PA, 1997, 137-146.
7. K. Muraleedharan, L. L. Rishel, M. De Graef, A. W. Cramb, T. M. Pollock and G. T. Gray III, Structural Intermetallics, M. V. Nathal, R. Darolia, C. T. Liu, P. L. Martin, D. B. Miracle, R. Wagner and M. Yamaguchi, eds., TMS, Warrendale, PA, 1997, 215-224.
8. D. E. Larsen, Jr, Materials Science & Engineering, A213 (1996), 128-133.
9. P. L Martin & C. G. Rhodes, Structural Intermetallics, R. Darolia, J. J. Lewandowski, C. T. Liu, P. L. Martin, D. B. Miracle and M. V. Nathal, eds.,TMS, Warrendale, PA, 1993, 177-186.
10. S. L. Semiatin, J. C. Chestnut, C. Austin & V. Seetharaman, Structural Intermetallics, M. V. Nathal, R. Darolia, C. T. Liu, P. L. Martin, D. B. Miracle, R. Wagner and M. Yamaguchi, eds., TMS, Warrendale, PA, 1997, 263-276,
11. P. L. Martin, D. A. Hardwick, D. R. Clements, W. A. Konkel and M. A. Stucke, Structural Intermetallics, M. V. Nathal, R. Darolia, C. T. Liu, P. L. Martin, D. B. Miracle, R. Wagner and M. Yamaguchi, eds., TMS, Warrendale, PA, 1997, 387-394.

12 De Graef, D. A. Hardwick and P. L. Martin, Structural Intermetallics, 1997, 185-194.

13. A. L. Dowson, T. P Johnson, J. M. Young and M. H. Jacobs, ? Titanium Aluminides, Y-W Kim, R. Wagner, and M, Yamaguchi, eds., 1995, TMS, 467-474.
14. Alec Mitchell, JOM, 49(6), 1997, 40-42 and 69.
15. B. Godfrey, M. H. Loretto, Materials Science and Engineering, A266 (1999), 115-122.
16. Blair London, D. E. Larsen Jr., D. A Wheeler, and P. R. Aimone, Structural Intermetallics, 1993, 151-157.
17. A. D. Helms & C. M. O'Brien, JOM, 50(3), 1998, 12.
18. D. K. Melgaad, R. L. Williamson & J. J. Beaman, JOM, 50(3), 1998, 13-17.
19. C. E. Shamblen, Titanium ’95, P. A. Blenkinstop, W. J. Evans & H. M. Flower, eds., The Institute of Materials, London, UK, 1996, 1438-1445.
20. W. H. Buttrill & C. E. Shamblen, Titanium ’95, P. A. Blenkinstop, W. J. Evans & H. M. Flower, eds., The Institute of Materials, London, UK, 1996, 1446-1453.
21. W. R. Chinnis, Titanium ’95, P. A. Blenkinstop, W. J. Evans & H. M. Flower, eds., The Institute of Materials, London, UK, 1996, 1494-1499.
22. Timet website: www.timet.com

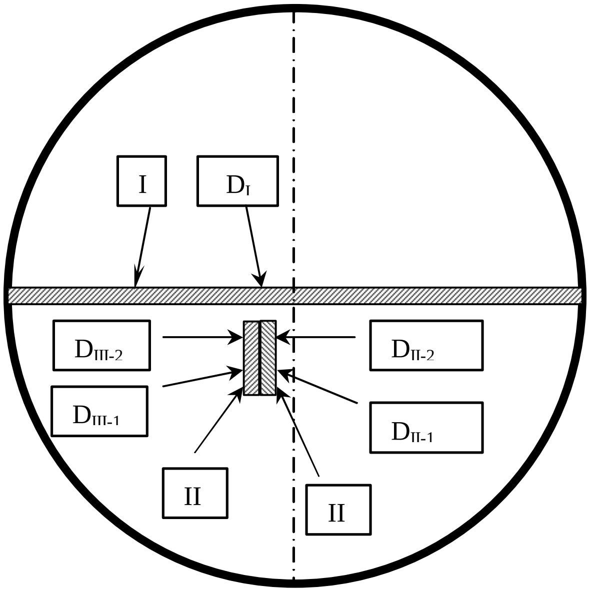

Defect	Dimensions (mm)
D_I	12.5 x 0.8
D_{II-1}	16.5 x 1.6
D_{II-2}	7.6 x 1.6
D_{III-1}	16.5 x 1.3
D_{III-2}	7.6 x 1.3

Figure 1, Position of the slabs examined in the 3-95M forging.

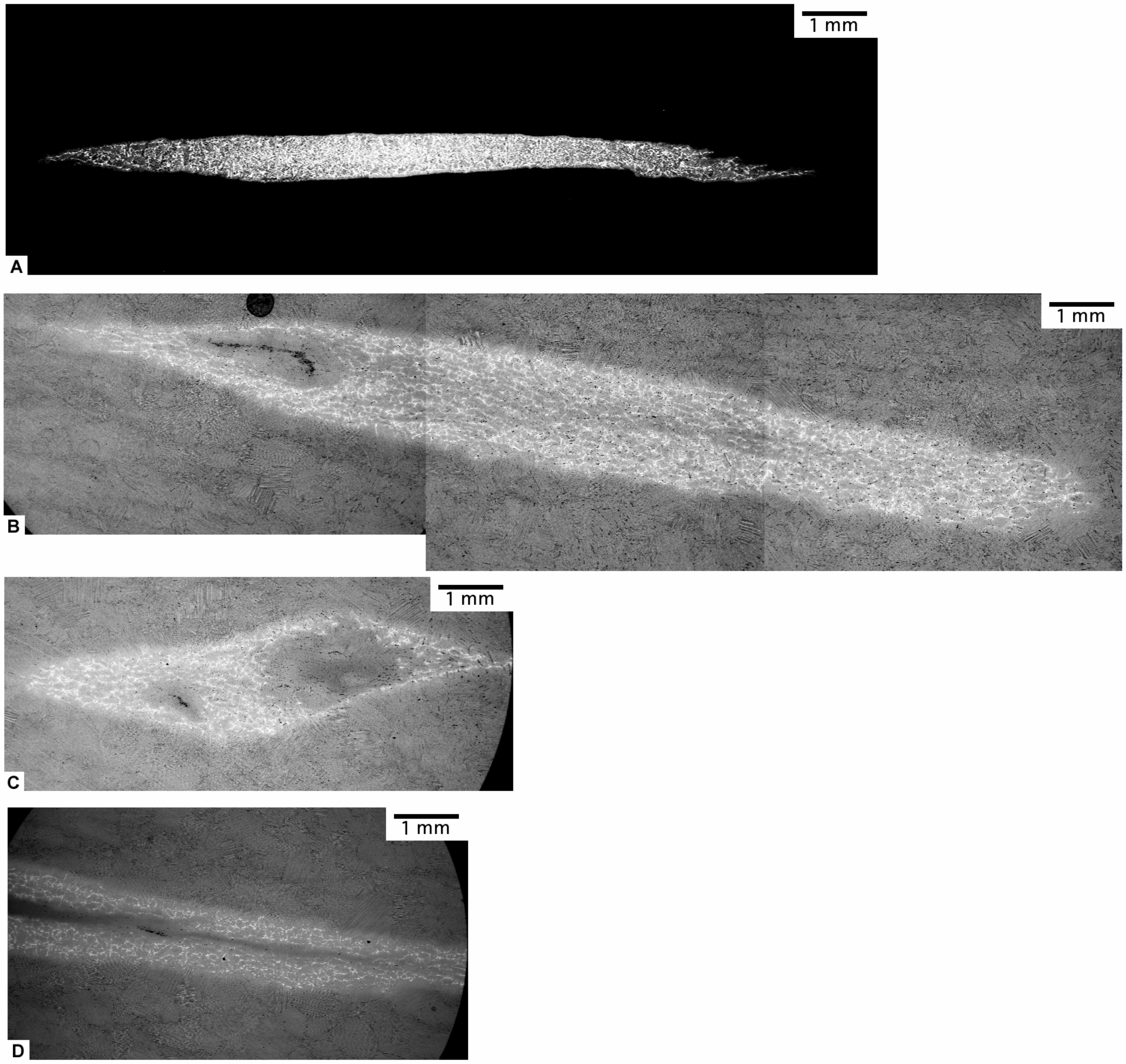

Figure 2, Defects found in 3-95M forging; a) defect D_{I}, b) defect $D_{II\text{-}1}$, c) defect $D_{II\text{-}2}$, and d) defect $D_{III\text{-}1}$.

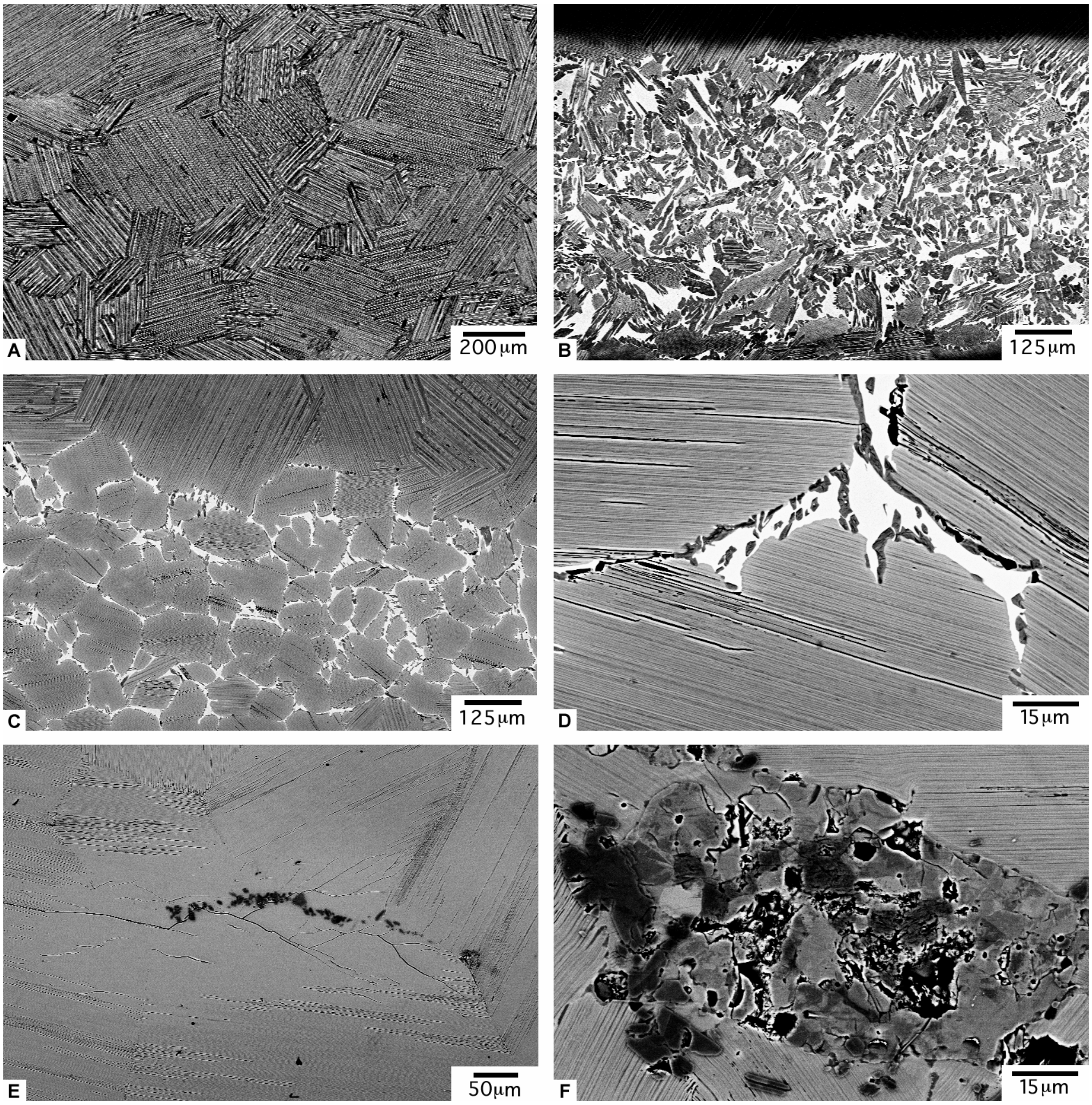

Figure 3, Details of defects found in 3-95M; a) BSE of typical, un-defected microstructure, b) blocky β phase of defect D_I, c) necklace β typical of D_{II-1}, D_{II-2}, D_{III-1} and D_{III-2}, d) interlamellar micro cracking often present in necklace β structure, e) low density, island defect with micro cracking, and f) large inclusion / pore defect.

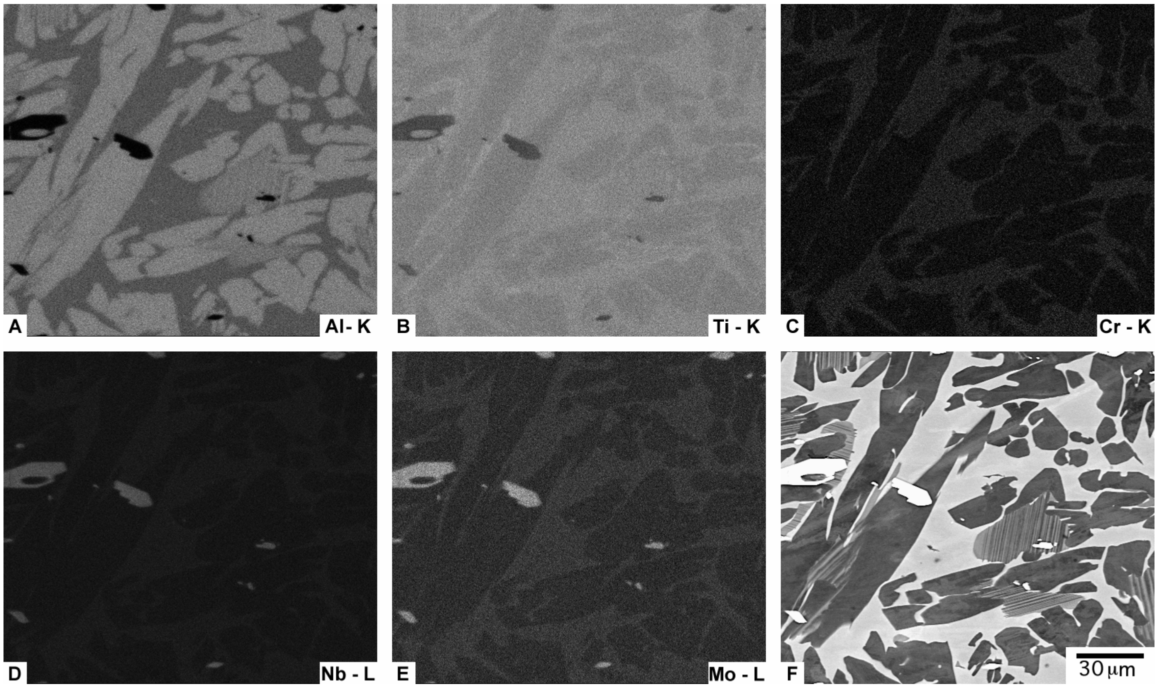

Figure 4, EDS dot-maps of defect structure in HDS defect D_I, showing; a) Al, b) Ti, c) Nb, e) Mo and f) back scattered SEM image.

Figure 5, Back scattered SEM image of a low density segregation defect in KD-CBS .

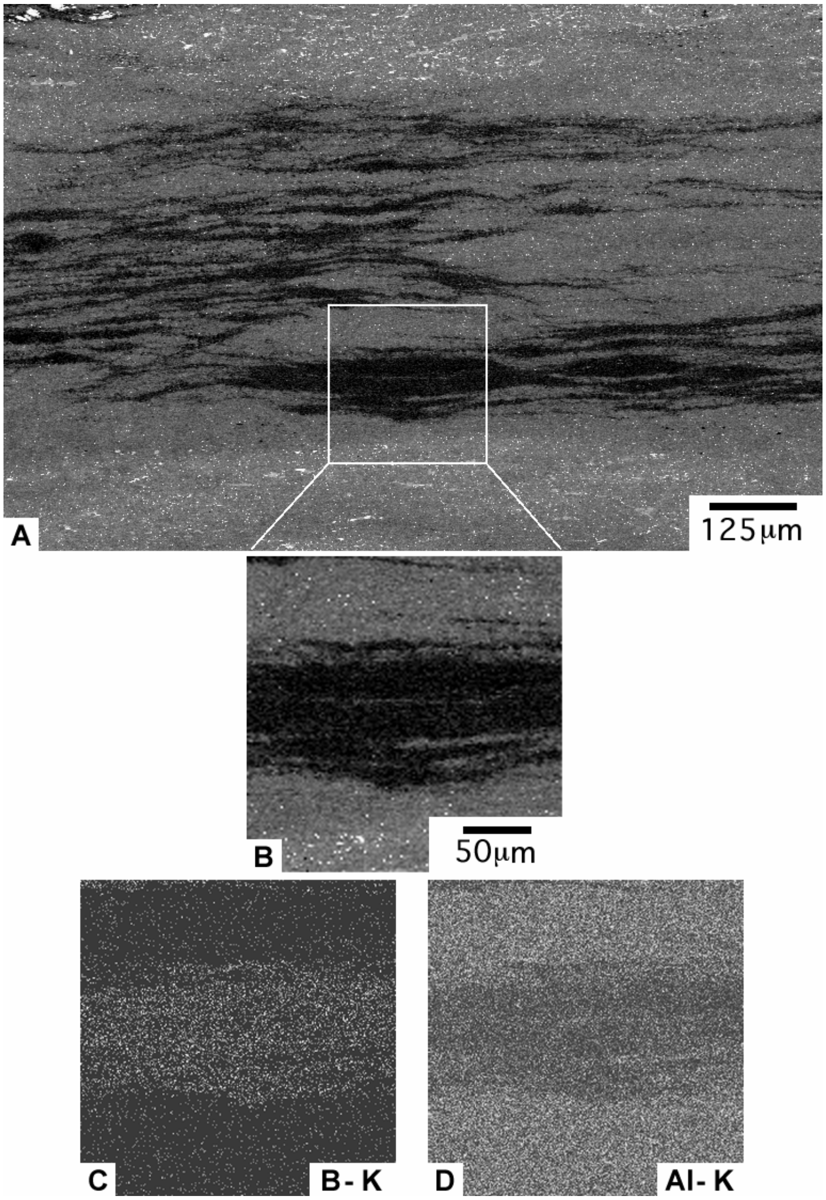

Figure 6, EDS dot-map of LDS defect in KD-CSB; a) back scattered SEM overview of defect region, b) details of EDS area, c) dot-map for boron, and d) dot-map for aluminum.

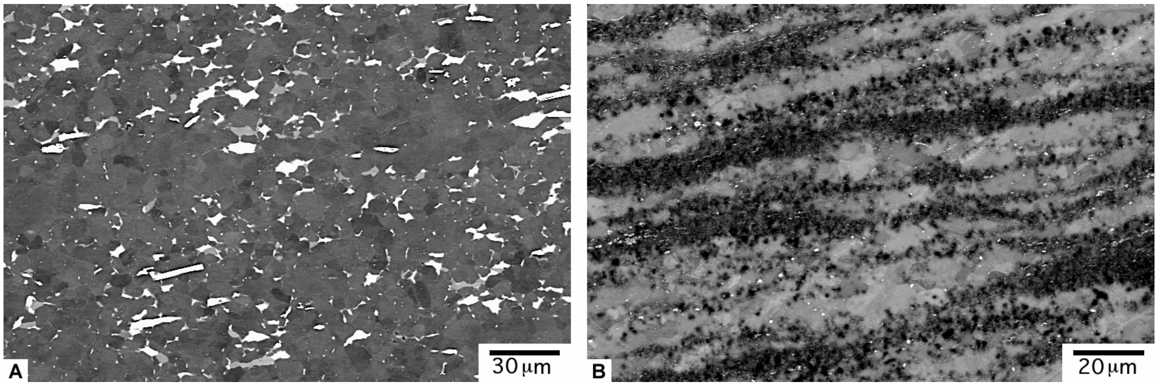

Figure 7, Details of the boron segregation, a) normal as forged microstructure in KD-CBS, b) banded structure of LDS defect.

Lamellar Colony Orientation Determination of Gamma Titanium Aluminides Using Orientation Imaging Microscopy (OIM)

Kezhong Li[†], William J. Porter[†] and Andrew H. Rosenberger
Air Force Research Laboratory, Materials and Manufacturing Directorate
AFRL/MLLN, Wright-Patterson Air Force Base, Ohio 45433-7817, USA
[†] The University of Dayton Research Institute, Dayton, Ohio 45419-0128, USA

Introduction

γ TiAl alloys have received considerable attention as candidate materials for elevated temperature aerospace applications [1]. The lamellar microstructure consisting of alternating γ ($L1_0$, a = 0.397nm, c = 0.405nm) and α_2 (DO_{19}, a = 0.579nm c = 0.467nm) laths in a colony, shows better creep resistance and higher toughness, as well as better fatigue crack growth resistance, than the duplex structure. However, the lamellar microstructure also shows significant crystallographic texture that results in anisotropic mechanical properties at the colony level [1-4].

Orientation Imaging Microscopy (OIM) technique, based on the acquisition and analysis of Electron Back-scattered Diffraction Patterns (EBSP), or Kikuchi patterns, from a bulk sample, currently can only image one phase (γ) at a time. However, since γ and α_2 phases in a lamellar colony share a strict orientation relationship of $(111)\gamma//(0001)\alpha_2$, $[1\bar{1}0]\gamma//[11\bar{2}0]\alpha_2$, the colony orientation can be described based on the knowledge of the γ lath orientation alone. Due to the modest tetragonity of γ-TiAl (c/a = 1.02) and limitation of the equipment sensitivity, a face centered cubic (FCC, a = 0.400 nm) unit cell was assumed for the γ phase and employed by the OIM software. The γ lath (or lamellar colony) orientation was determined using the intensity pole figures (IPF) and the point group symmetry of the assumed FCC unit cell of the γ phase.

2. Experimental Procedures

The alloy employed in this study was wrought Ti-46.5Al-2Cr-3Nb-0.2W (at. %), which was developed by Y-W Kim and designated K5. A fully lamellar microstructure was obtained by long-time exposure in the high temperature α-phase field. A rectangular-shaped specimen was machined with dimensions of 35 x 12 x 1.5mm, which also served as transverse direction (TD), radius direction (RD) and normal direction (ND), respectively. The specimen surface was manually ground, followed by mechanically polishing and finally electropolished.

The OIM apparatus, manufactured by TexSEM Laboratories, Inc., Draper, UT, was used on a Leica 360 field emission scanning electron microscope (SEM). The flat sample surface normal was tilted an angle of 70.5° from the vertical incident electron beam. The OIM operating parameters were the following: SEM focal distance, 25mm; probe current, 7nA; aperture size, 50μm and accelerating voltage, 25kV. Due to the very fine nature of lamellar laths in the colony, a scanning step of 0.2μm was employed.

3. Results

Figure 1 shows a normal (before tilting 70.5°) back-scattered SEM image of the lamellar colony that was subsequently scanned by OIM. In the image the γ lath traces (dark contrast) on the sample surface constituted a 45° angle with respect to the sample reference direction (RD). Figures 2(a)-(c) are orientation micrographs, which were obtained and 'corrected' by the OIM software to account for the tilting of the specimen (both RD and TD are in full scale). Figure 2(a) shows a gray-scale image quality (IQ) map where points with high IQ values are lighter shades of gray and low IQ values are darker. The actual IQ values range from 0 to 43.8. The dark gray bands with zero IQ appear to correspond to the α_2 laths while the lighter areas, with higher IQ values, are γ regions. The IQ map also resolves individual γ laths as noted by the light and medium gray regions. Figure 2(b) is a confidence index (CI) color map where the blank areas with zero CI indicated the locations of α_2 laths, the black points indicated CI < 0.10 and red points CI > 0.1. Apparently, the CI < 0.1 points were predominantly located in the γ/α_2 interface regions and some times extended to the internal γ laths. Figure 2(c) is a crystal orientation color map drawn with a 5° critical grain tolerance angle. Due to the assumption of an FCC unit cell of the γ phase employed in the OIM software, instead of its actual tetragonal structure, there are only two distinguishable orientations in γ laths: γ phase (green) and its twin (red). Since the OIM did not index the α_2 phase, the α_2 laths are left blank (white). The Euler angles of γ laths (110°, 9°, 334°) and γ twins (110°, 57°, 28°) were determined from diffraction patterns captured in SEM "spot mode". Figure 2(a)-(c), corrected for the specimen tilt, also show a 45° angle between the γ/γ or γ/α_2 interfaces and reference direction (RD). This result is consistent with the 45° angle measured between γ or α_2 laths and the vertical (RD) in Figure 1.

The lamellar colony orientation was determined using the intensity pole figure (IPF), drawn from the Orientation Distribution Function (ODF), calculated by the OIM software. Figure 3(a), (b) and (c) show the IPF under crystal directions [111], [110] and [100], respectively. Owing to the assumption of a FCC unit cell of the γ phase each intensity pole figure reflects the cubic crystal point group symmetry and can be used to determine the γ lath orientation. The projections of the four higher intensity [111] poles, seen in Figure 3(a), were marked by solid inverted triangles and indexed as $[111]$, $[\bar{1}\bar{1}1]$, $[1\bar{1}\bar{1}]$ and $[\bar{1}1\bar{1}]$ in Figure 3(d). Four great circles were drawn from these four $[111]$ poles and six $[110]$ poles were obtained from each intersection of two great circles. The six $[110]$ pole locations, marked with triangles in Figure 3(d) and 3(e), are consistent with the locations in the $[110]$ IPF, Figure 3(b). Of the four $[111]$ poles only $[1\bar{1}\bar{1}]$ pole constitutes a 45° angle with the sample RD, which is the angle measured in Figure 1. Apparently, the $[1\bar{1}\bar{1}]$ pole is the lamellar interface normal. The $[1\bar{1}\bar{1}]$ pole is 57° from the sample normal direction ND, measured using a Wulff net. If a zero rotation is defined as that $[0\bar{1}1]$ direction, which is on the great circle of the $[1\bar{1}\bar{1}]$ pole, is perpendicular to the sample normal, the point "S" results, Figure 3(d). The $(1\bar{1}\bar{1})$ plane rotation angle about its $[1\bar{1}\bar{1}]$ normal was measured as 8° counterclockwise. The zero rotation definition indicates that the $[0\bar{1}1]$ direction is parallel to the intersection between the $(1\bar{1}\bar{1})$ lamellar interface and the sample surface. Thus, the orientation of the lamellar colony can be described as the following: the γ/α_2 $(1\bar{1}\bar{1})$ interface normal is inclined at 57° to the specimen normal, ND, and is rotated 8° counterclockwise about its $[1\bar{1}\bar{1}]$ direction. The [010], [001] and [100] pole showing in Figure 3(e), which are the intersections of each two [110] type great circles, is consistent with locations of [001], [010] and [100] pole in Figure 3(c), respectively.

The angle between the trace of lamellar $(1\bar{1}\bar{1})$ interface and TD direction on the plane orthogonal to the sample surface (the TD-ND plane) was measured to be 42° in an SEM back-scattered image. The colony imaged by OIM was intentionally chosen to be on the corner of the sample to optically evaluate the accuracy of the orientation determination. Knowing that the lamellar interface constitutes a 45° angle to RD and a 42° angle to TD in the TD-ND plane, the inclination angle of the lamellar interface plane was determined to be 57° using a Wulff net. This indicates that the orientation determined by the OIM system is indeed accurate.

Figure 3(a), the [111] pole figure, shows seven poles, which originate from two sets of data. One set of data from the gamma matrix constitutes the four [111] poles with higher intensities. The other set of the data from the gamma twins constitutes three lower density [111] poles. Since the $[1\bar{1}\bar{1}]$ pole is the lamellar interface normal, this pole is the common one shared by the matrix and twins. The correlation of the poles between the matrix and twins can be indicated in either of the following two ways. Firstly, when all the seven [111] type poles rotated simultaneously so as to the $[1\bar{1}\bar{1}]$ pole is located on the ND great cycle and constitutes 45° to RD ($(1\bar{1}\bar{1})$ plane is perpendicular to the sample surface), the [111] poles of the matrix and twins in projection should show mirror symmetry. Secondly, the misfit orientation between the matrix and twin can be indicated as a 60° rotation, which is consistent with the FCC unit cell assumption.

4. Discussion and Conclusions

OIM is based upon quantitative and spatially specific crystallographic data, which can be manipulated and analyzed according to the research interest. In this study the method for the determination of lamellar colony orientation is similar to the conventional x-ray and neutron diffraction pole figure techniques. However, since OIM provides point-specific orientation measurements, this technique is capable of resolving the orientation of fine lath microstructures. The spatial resolution of BS imaging is typically about 0.05-0.1μm for a high resolution, field emission SEM, with variations depending on the accelerating voltage, beam current and atomic number of the material. The spatial resolution limit of EBSD is lower than that for imaging, because it depends on both the primary electron beam size and the spatial range of back-scattered electrons. It is believed that it is approximately 0.2μm [5]. In this work a scanning step of 0.2μm was proven to resolve very fine individual γ laths.

The results of the lamellar colony orientations can be used with SEM back-scattered images to accurately determine the actual lath-spacing distributions of the microstructure. The unique orientation of each lamellar colony can be determined using OIM, which gives the inclination angle, designated θ, of the γ/γ or γ/α_2 interface planes to the flat specimen surface. The distribution of γ and α_2 lath projection widths can be measured using SEM back-scattered imaging with the specimen normal to the electron beam. The actual lath spacing (the shortest distance in a lath) is the product of this projected spacing multiplied by a factor of $\cos\theta$. This eliminates the need to produce TEM foils of the material in order to obtain lath spacing information and could provide more representative distributions of the lath architecture through the interrogation of more colonies within a single sample.

The determination of lamellar colony orientations of a bulk sample using OIM will significantly benefits studies of the microstructural effects on the mechanical properties of materials. Mechanical properties including tensile, fatigue and creep strength are significantly affected by colony orientation and lath spacing [2-4]. A detail mapping of the macro-texture of lamellar structures and an analysis of the lath spacing distribution can serve as a reliable data base for accurate mechanistic-based modeling work to understand the elastic and plastic deformation, as well as fatigue and fracture mechanisms of this class alloys.

Orientation imaging microscopy can be utilized to map the 3-D colony orientation of a lamellar material having lath widths as fine as ~0.2μm. This technique allows for the accurate, rapid orientation measurement of electropolished flat bulk samples without the need for TEM. The orientation can be mapped to the sample reference coordinates – making this a powerful tool for analysis of the anisotropic nature of the lamellar structured materials. This knowledge of orientation (and consequently lath width) can form the basis for the experimental study of the effects of microstructural anisotropy on the mechanical behavior of these materials, especially deformation, fatigue, and fracture mechanisms.

Acknowledgments

This research was performed in the Air Force Research Laboratory, Materials and Manufacturing Directorate, Wright-Patterson Air Force Base, OH and was supported in part by the Air Force Office of Scientific Research under Task 2302BW1. K. Li and W. J. Porter gratefully acknowledge support of the Air Force Contract F33615-98-C-5214.

References

1. Y-W. Kim and D. M. Dimiduk, *JOM*, 1991, vol. 34 (8), pp. 40-47.
2. D. L. Davidson and J. B. Campbell, *Metall. Trans.*, 1993, vol. 24A, pp. 1555-1574.
3. S. Hirohisa, T. Keiro and O. Yasuhito, Mater. Sci. & Eng., 1998, vol. A243, pp. 169-175.
4. M. Yamaguchi and H. Inui, Ordered Intermetallics-Physical Metallurgy and Mechanical Behavior, C. T. Liu, et al. eds. Kluwer Academic Publisher, Netherlands, 1992, pp.217-235.
5. L. Adams, S. I. Wright and K, Kunze, Metall. Trans. A, 1993, vol. 24A, pp. 819-831.

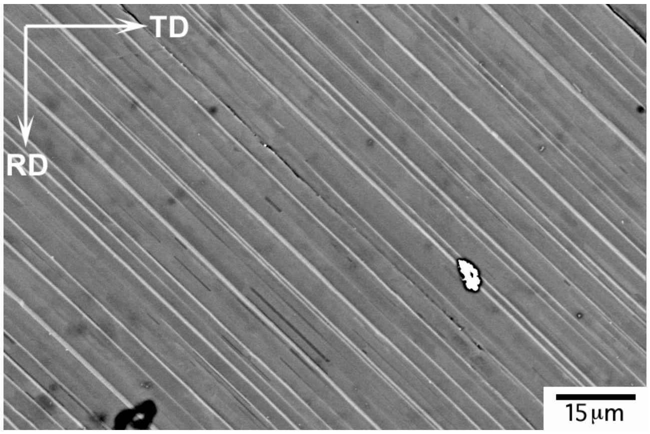

Figure 1- SEM back-scattered image of the lamellar microstructure.

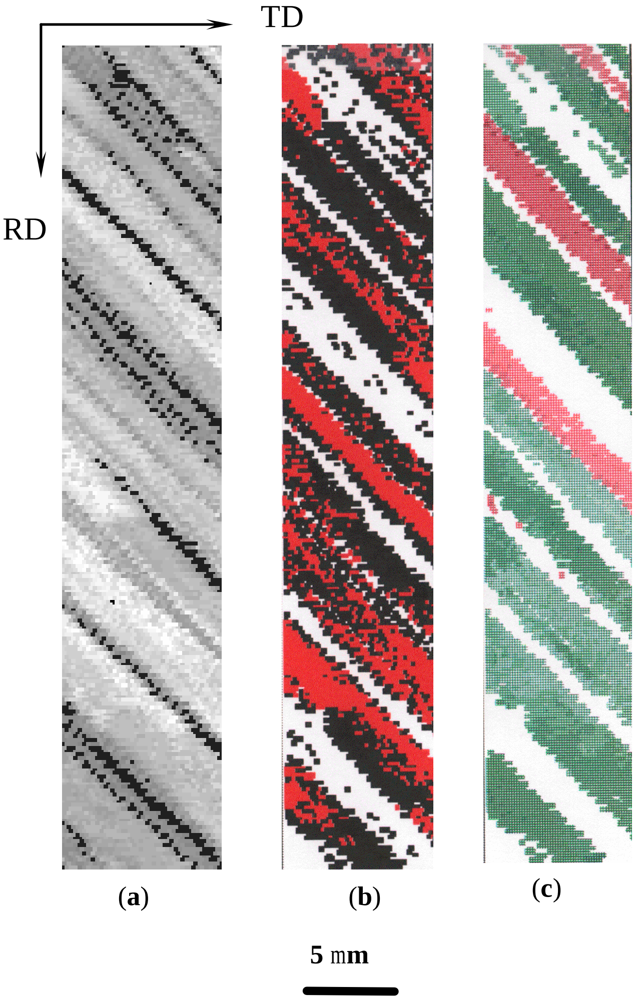

(a) (b) (c)

Figure2- Orientation micrographs, (a) Image quality (IQ) map (black: IQ = 0, white: high IQ), (b) Confidence index (CI) map (white: CI = 0, black: 0< CI < 0.1 and red: CI > 0.1), and (c) Crystal orientation map (white: α_2; green: γ and red: γ twin)

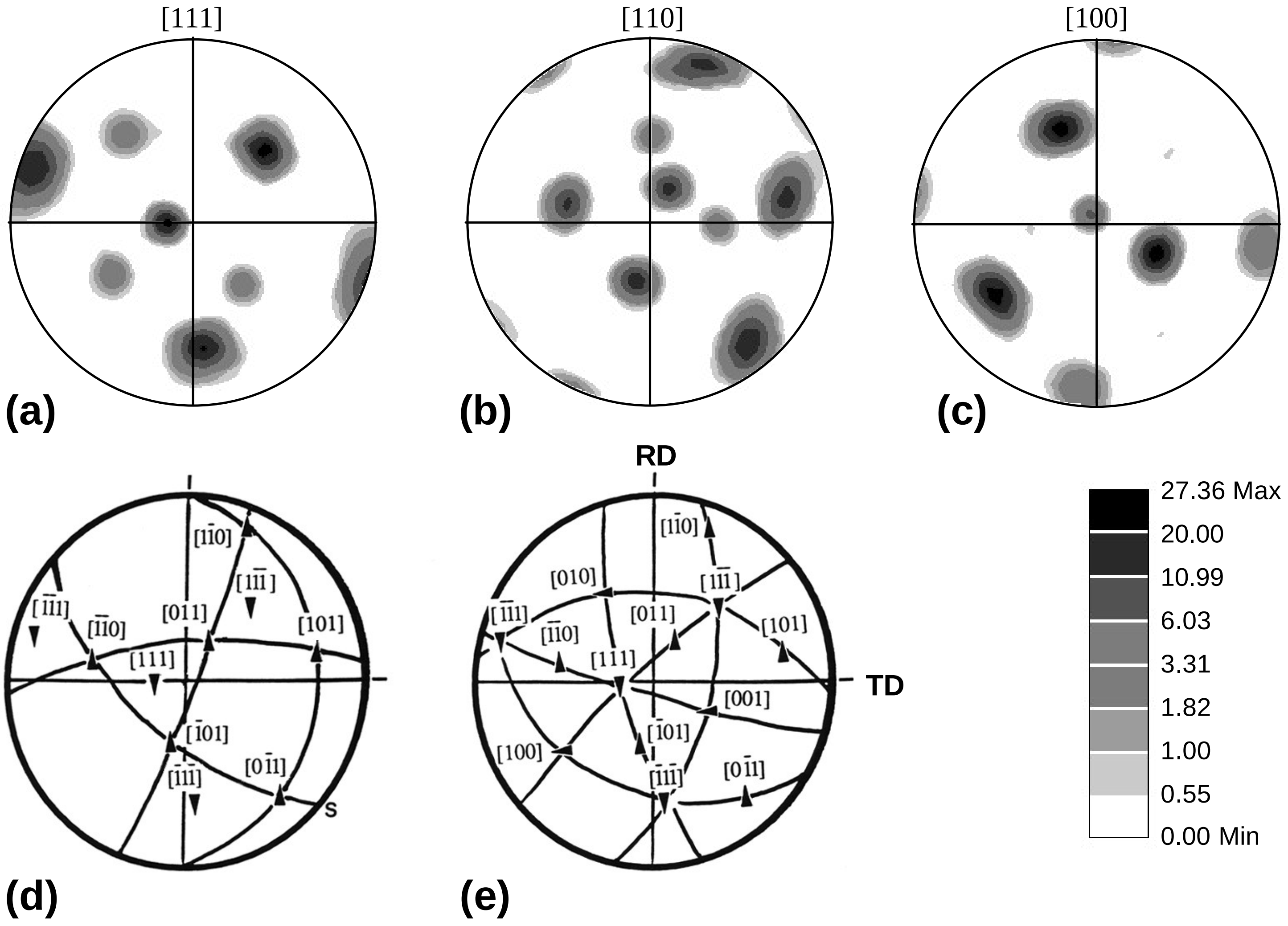

Figure 3- Intensity pole figure (IPF) and stereo projections; (a) [111] IPF, (b) [110] IPF, (c) [100] IPF, (d) Stereo projection showing [111] great circles and (e) [110] great circles.

This page intentionally left blank

ELASTIC-PLASTIC STRESS ANALYSIS OF GAMMA TITANIUM ALUMINIDE POLYCRYSTALS

Robert A. Brockman, Geoffrey J. Frank, and Steven E. Olson

University of Dayton Research Institute
300 College Park Ave.
Dayton, OH 45469-0110 USA

Abstract

A computational model is described for analyzing stress variations within polycrystals of γ-TiAl, including the effect of anisotropic yielding and small-scale plastic flow. Interlamellar (soft mode) slip behavior is controlled by a separate collection of slip systems whose properties are derived from measurements on polysynthetically twinned (PST) specimens. When used to represent several hundred randomly oriented material grains, the model provides distributions and statistical data about the local stress, strain, and plastic deformation resulting from a prescribed macroscopic loading. Our objective is to better understand the role of local stress variations on crack initiation.

Introduction

Titanium aluminide (TiAl) alloys are attractive for use in high-temperature structural applications, due to their low density, strength retention at high temperature, and potential for excellent fatigue resistance. The best combination of mechanical properties for many purposes is achieved with a small-grained lamellar microstructure, in which the material exists in lamellar colonies consisting of thin parallel layers of the γ (TiAl) and α_2 (Ti_3Al) phases. The lamellar microstructure exhibits some distinctive and complicated mechanical behavior, which presents some unique analytical challenges. The survey by Appel and Wagner (1) is a good introduction to microstructural details, processing issues, and microstructural behavior of this material.

The present work is an attempt to quantify the stress variations within polycrystals of γ-TiAl, to better understand the influence of factors such as anisotropy, localized plastic flow, and relative orientation of neighboring grains on crack initiation. The length scale represented in a typical stress model is a millimeter or more in each direction. As such, it is impractical to model the lamellae explicitly. The lamellar thickness, which is controlled by the cooling rate during processing, is between ten nanometers and a few micrometers. However, a representation of the localized response within individual lamellar colonies is needed to obtain a meaningful picture of the variations in stress throughout the polycrystal.

To accommodate the relatively large length scale of our problem, while allowing for the highly localized deformation patterns that commonly occur in lamellar TiAl, we adopt an approximation in which *the stress in the material mixture at a sampling point is uniform.* This idealization provides the correct macroscopic driving force for initiating plastic flow without representing layer-to-layer stress variations explicitly. At the same time, slip may occur in either phase of the lamellar microstructure in a “weakest link” fashion.

Much of the detailed numerical modeling of γ-TiAl that has been performed to date focuses on the individual phases (particularly the γ phase, which represents most of the material volume), or on the study of localized response within a single lamellar colony. Fischer, Schlögl, and co-workers have developed finite element-based micromechanical models of unit cells within a lamellar colony in both two and three dimensions (2-5). These and similar models use crystal plasticity models that represent the relevant slip systems explicitly, to capture anisotropic yielding, flow, and hardening behavior accurately. Lebensohn (6) has developed a simple model of a two-lamellae structure which represents the most important deformation mechanisms of a γ-TiAl PST crystal, and which may be extended to analyze polycrystal behavior through a mean-field approach..

Dao, Kad, Asaro and co-workers analyzed TiAl polycrystals in two dimensions in a series of papers (7-10). Planar projections of the three-dimensional crystallography are used in these works to investigate characteristics of the localized stress field while controlling the size of the numerical system to be solved. Even in two dimensions, analyzing the individual lamellae is impractical, and the authors employ effective properties that define the plastic flow behavior of a lamellar colony as a homogeneous entity. Similar calculations in three dimensions, which have not been reported heretofore, are the focus of this paper.

The interlamellar (soft mode) and translamellar (hard mode) deformation of lamellar colonies has been studied most extensively by experiments using PST (polysynthetically twinned) single crystals. While it seems clear that scale-related constraints are important in determining the yield strength in various orientations, the relative importance of lamellar spacing, lamellar colony size, and domain size within individual lamellae as scale parameters remains an open question.

It is interesting that a complete and definitive explanation of the mechanisms at work in the distinctive soft-mode yielding behavior has not emerged. Over a broad range of intermediate orientations, slip appears to occur almost exclusively on the (111) planes of the γ lamellae; that is, parallel to the interlamellar boundaries. However, the strengths associated with this mode of deformation are significantly lower than one expects based on the measured properties of the individual material phases (Figure 1). A key factor in this behavior is the fact that the chemical composition of the constituent phases, as they appear in the PST, is necessarily different from that of monolithic samples of the constituents.

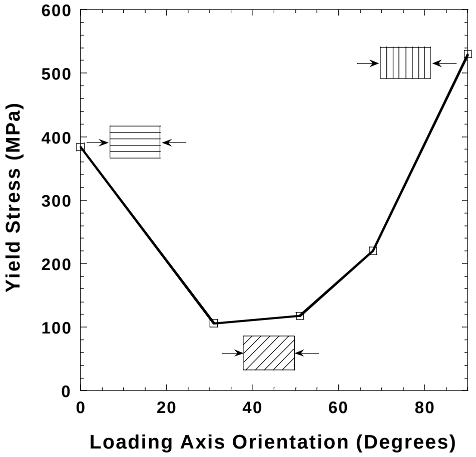

Figure 1: Dependence of yield strength on lamellar orientation; PST data in compression taken from Inui, et. al. (1992).

The distinctive nature of the soft mode deformation, which dominates the inelastic behavior of lamellar γ-TiAl in a wide range of intermediate orientations, has important implications in the construction of continuum models for this class of materials. While it is possible, given accurate data, to construct accurate plasticity models of the individual phases of the material, the process of extending these models directly to reproduce the anisotropic yield behavior of the lamellar microstructure is not possible without additional data that account for compositional variations.

In the modeling technique discussed herein, we adopt a phenomenological solution to this dilemma, in which additional data obtained from experiments on PST specimens is used to characterize the distinctive soft-mode slip response of the lamellar material. We introduce the interlamellar slip behavior explicitly in the form of additional systems having slip planes coincident with the interlamellar boundaries. While this approach is adequate for our immediate objective of modeling the stress variations in γ-TiAl polycrystals, the need for such an empirical device underscores the need for improving our understanding of the interlamellar slip behavior, and of the constituent strengths that control it. Methods for simulating this complicated response on a finer length scale than that adopted in the present model are needed, both to improve our understanding of the physical processes and to minimize the need for difficult and expensive laboratory tests in characterizing new materials.

In what follows, we outline the generic crystal plasticity model and associated numerical solution, followed by the definition of model parameters and assumptions for the γ phase (TiAl), α_2 phase (Ti_3Al), and the fully lamellar $\gamma+\alpha_2$ microstructure. Initial yielding and stress-strain curve predictions are made for TiAl PST specimens at various orientations and compared with experimental data. Finally, we present calculations based on a three-dimensional polycrystal model composed of fully lamellar γ-TiAl and a small volume percentage of equiaxed γ grains. This model comprises several hundred grains, and provides interesting data about the variation in stress and plastic strain throughout the sample for a given nominal strain or applied stress.

Plasticity Model

The anisotropic crystal plasticity model employed here is a rate-independent form similar to that described by Steinmann, et. al. (11). We assume a pointwise elasticity relationship of the form

$$\dot{\sigma}_{ij} = C_{ijmn}\left(\dot{\varepsilon}_{mn} - \dot{\varepsilon}^{p}_{mn}\right) \tag{1}$$

In our implementation, which works with the ABAQUS finite element code, material calculations are performed in terms of the material axis system, using the Cauchy stress and rate of deformation. Net rotations of the material are removed by transforming the stress and strain prior to applying the constitutive model, and restored afterward. Therefore, the coordinate system used is corotational in nature, and aligned with the (initial) principal material directions. It should be mentioned that our interest lies primarily in relatively small plastic deformation, so the discussion is limited to small deformations.

The yield function for each slip system (designated by upper-case indices) is expressed in terms of the stress components referred to the slip plane normal $\hat{\mathbf{n}}^{(I)}$ and the preferred slip direction $\hat{\mathbf{s}}^{(I)}$:

$$\tau^{sn(I)} = \sigma_{ij} s_i^{(I)} n_j^{(I)} \tag{2}$$

The yield condition for a specific slip system ($\hat{\mathbf{n}}^{(I)}, \hat{\mathbf{s}}^{(I)}$) is

$$F^{(I)}(\boldsymbol{\sigma}) - Y^{(I)}(\boldsymbol{\gamma}) = \left|\tau^{sn(I)}\right| - Y^{(I)} = 0 \tag{3}$$

The slip magnitudes $\gamma^{(I)}$ are the primary variables in the final constitutive equation system. The corresponding yield surface normal vectors may be written as

$$\nu_{ij}^{(I)} = \frac{\partial F^{(I)}}{\partial \sigma_{ij}} = \alpha^{sn(I)} \operatorname{sgn}\left(\tau^{sn(I)}\right) s_i^{(I)} n_j^{(I)} \tag{4}$$

The plastic flow rule assumes that slip occurs in the slip plane with normal $\hat{\mathbf{n}}^{(I)}$ along the preferred slip direction $\hat{\mathbf{s}}^{(I)}$. Summing the contributions from the set of all active slip systems, which we denote by *A*, gives

$$\dot{\varepsilon}^{p}_{ij} = \sum_{I\in A} \dot{\gamma}^{(I)} \mu^{(I)}_{ij} \qquad (5)$$

in which the Schmid tensor

$$\mu^{(I)}_{ij} = \tfrac{1}{2}\left(s^{(I)}_{i} n^{(I)}_{j} + n^{(I)}_{i} s^{(I)}_{j}\right) \operatorname{sgn}\left(\tau^{sn(I)}\right) \qquad (6)$$

defines the direction of the plastic strain rate for system I, and $\dot{\gamma}^{(I)}$ is its magnitude. Because the flow directions $\mu^{(I)}_{ij}$ reflect the sign of the shear stress, the slip rates $\dot{\gamma}^{(I)}$ are expected to be positive.

The strain hardening characteristics are assumed to be controlled by the accumulated plastic strain magnitudes, and may include interaction between slip systems. The hardening characteristics do not include local constraint effects that may lead to varying hardening behavior within a material grain, although it is possible to introduce this effect through property variations. Defining the hardening moduli $H_{IJ} = \partial Y^{(I)} / \partial \gamma^{(J)}$, we have

$$\dot{Y}^{(I)} = \sum_{J\in A} H_{IJ} \dot{\gamma}^{(J)} \qquad (7)$$

The consistency condition requires that the plastic flow rates be related to the stress rates via

$$\dot{\gamma}^{(I)} = \pi^{(I)}_{ij} \dot{\sigma}_{ij} \qquad (8)$$

with

$$\pi^{(I)}_{ij} = \sum_{J\in A} H^{-1}_{IJ} \nu^{(J)}_{ij} \qquad (9)$$

Model Parameters for TiAl Intermetallics

In this section we define specific constitutive model parameters for titanium aluminides in the form of pure γ (Ti-Al) and α_2 (Ti_3Al) phases, and for the lamellar microstructure formed from both phases arranged in a series of lamellar plates. Elastic properties for both pure phases have been published by several authors, and are in reasonable agreement with one another. Yield strengths have been reported in several publications, exhibiting somewhat less agreement. Properties of the lamellar material require additional information from PST experiments, since the composition of the constituents as they appear within the PST is invariably different from single-phase specimens.

Below we outline a collection of model parameters for the TiAl materials of interest, derived from a variety of sources. It should be noted that inconsistencies in the data are unavoidable because of differences in material composition, processing, and experimental techniques. Considerable work remains to define consistent and reliable properties for this class of materials, and to understand the relationship between key properties of the individual phases and that of the material in lamellar form.

Model Properties for γ (Ti-Al)

Elastic properties for the γ phase are based upon measurements reported by Yoo and Foo (13) for a composition of roughly Ti-56Al. In particular, we take

$E_1 = 140$ GPa $\nu_{12} = 0.2840$ $G_{12} = 78$ GPa
$E_2 = 140$ GPa $\nu_{13} = 0.2977$ $G_{13} = 105$ GPa
$E_3 = 135.4$ GPa $\nu_{23} = 0.2977$ $G_{23} = 105$ GPa

in which directions (1,2,3) correspond to the [100], [010], and [001] crystal directions, respectively. Yielding and hardening properties of the γ phase are similar to those used by Parteder, et al. (2). The crystalline structure is face-centered tetragonal (Ll_0) with aspect ratio 1.02. Here we employ the slip systems of an FCC lattice as a first approximation, with the preferred slip planes {111} and directions [110]. Parteder et al. further classify these systems as either pure (ordinary dislocations, involving Al atoms only) or mixed (superdislocations), noting that the mixed systems are more difficult to activate than the pure systems. The pure Al slip systems are: $(111)[\bar{1}10]$, $(\bar{1}11)[110]$, $(1\bar{1}1)[110]$, and $(11\bar{1})[\bar{1}10]$.

Figure 2 shows initial yield point predictions along various loading axis directions, for two values of critical resolved shear stress (CRSS). In the first case, a CRSS of 90 MPa is assumed for all slip systems; in the second calculation, an initial CRSS of 120 MPa is assigned to the superdislocation systems. The cusps in the upper curve are due to a change in the active slip system; near the 0° and 90° orientations, the ordinary dislocation modes with lower critical stress are active, while the superdislocation modes dominate for intermediate orientations. The initial yielding plots correspond to the lower bound obtained by plotting the inverse of the Schmid factor divided by the CRSS for all slip systems.

The assumed values of the hardening moduli are 800 MPa for the self-hardening terms (H_{II}) and for the latent hardening terms (H_{IJ}) for coplanar systems; for non-coplanar systems, $H_{IJ} = 1120$ MPa ($q = 1.4$). Obviously, our treatment of the hardening behavior is quite rudimentary, and refinement of the hardening models is an important area for future investigation.

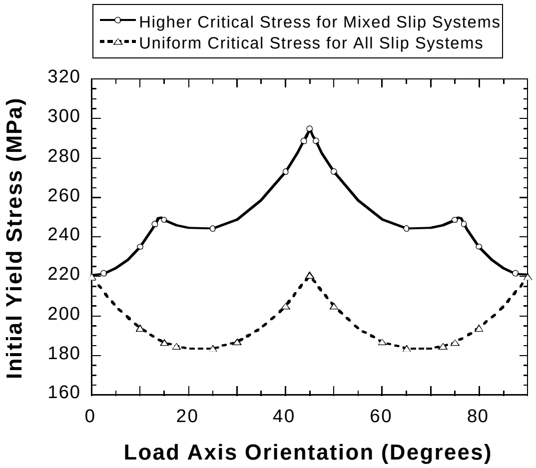

Figure 2. Initial yield predictions for gamma grains.

Model Properties for α_2 (Ti_3Al)

For the α_2 phase, the elastic constants again are based on measurements by Yoo and Foo (13). The α_2 crystal structure is hexagonal (DO_{19}); the '3' axis of our model is aligned with the 'c' crystal axis [0001], and the '1' axis is parallel to $[11\bar{2}0]$. Values of the orthotropic elastic constants are as follows:

E_1 = 125 GPa	ν_{12} = 0.4541	G_{12} = 43 GPa
E_2 = 125 GPa	ν_{13} = 0.1539	G_{13} = 62 GPa
E_3 = 190.9 GPa	ν_{23} = 0.1539	G_{23} = 62 GPa

The inelastic properties for α_2 are based on data collected by Yamaguchi and Inui (14) for Ti_3Al having approximately 36.5 at% aluminum. Data for the individual slip systems appear in Table 1. Details of the strain hardening characteristics of α_2 are not well defined at present. Assumed values of the latent hardening coefficients used in the present model are listed in Table 2. All hardening values are expressed in MPa.

Table 1. Slip system geometry and strengths for a_2-TiAl.

Slip System	Slip Planes and Directions	Yield Strength	Self Hardening Modulus
Prism	$\{1\bar{1}00\} < 11\bar{2}0 >$	100 MPa	500 MPa
Basal	$(0001) < 11\bar{2}0 >$	329 MPa	500 MPa
Pyramidal	$\{11\bar{2}1\} < \bar{1}\bar{1}26 >$	911 MPa	1500 MPa

Table 2. Hardening coefficients for a_2-TiAl.

	Prism	Basal	Pyramidal
Prism	800	1000	1000
Basal	1000	800	1000
Pyramidal	1000	1000	2000

Initial yield stress predictions for α_2 grains in various loading orientations are shown in Figure 3; in all cases the loading direction is the 'x' (horizontal) axis. Rotation in the basal plane causes only slight variations in the yield strength since the relevant slip systems all possess similar strengths, and each slip direction is only 30 degrees removed from the next. Rotation of the 'c' (hexagonal) axis toward the loading direction produces a very pronounced effect, as the higher-strength pyramidal systems eventually control the initial yielding behavior.

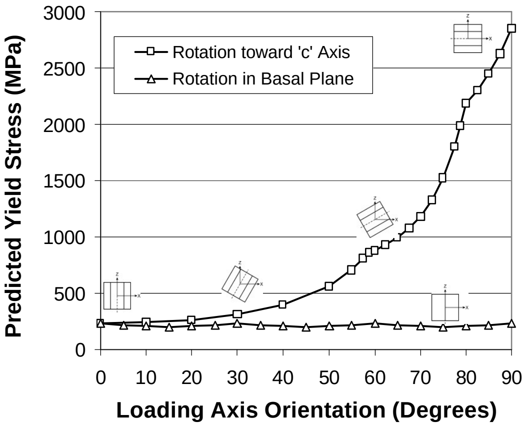

Figure 3. Initial yield predictions for α_2 grains.

Effective Model Properties for Lamellar $\gamma+\alpha_2$ TiAl

Our modeling approach represents individual γ grains and lamellar $\gamma+\alpha_2$ colonies, and their orientations, explicitly. However, our main interest lies in characterizing the stress variations among grains, and the stress or strain concentrations caused by changes in stiffness and orientation from grain to grain. Models with a sufficient number of grains to eliminate boundary effects typically consist of several hundred three-dimensional grains or lamellar colonies. In this setting it is impractical to model discrete lamellae, and we must resort to the use of effective properties and strengths for the lamellar TiAl microstructure.

Effective room temperature elastic properties for lamellar TiAl have been computed based on laminate calculations using the method described by Pagano (15). A summary of effective orthotropic constants for various proportions of α_2 and γ phases appears in Table 3. All moduli are given in GPa.

Table 3. Effective elastic properties of lamellar TiAl.

	a_2:g **Ratio**			
Property	**1:1**	**1:2**	**1:5**	**1:10**
E_{11}	160.3	171.3	182.1	186.8
E_{22}	160.1	171.5	181.9	187.2
E_{33}	206.4	211.5	216.6	218.9
ν_{12}	0.351	0.322	0.297	0.284
ν_{13}	0.155	0.153	0.147	0.147
ν_{23}	0.156	0.152	0.148	0.145
G_{12}	59.4	64.7	70.3	72.6
G_{13}	64.6	65.6	66.4	66.9
G_{23}	64.6	65.5	66.5	66.8

The potential slip systems of interest within a lamellar colony include those of both the γ and α_2 layers, as well as interlamellar slip modes. The coordinate system adopted for the α_2 phase is used also for the lamellar material, since the direction $(0001)_{\alpha_2}$ is aligned with the stacking direction of the lamellar planes. The slip geometry for the γ phase is transformed to a common coordinate system using the orientation relationships (16):

$$(111)_{\gamma}\,\|\,(0001)_{\alpha_2} \quad \text{and} \quad \langle 1\bar{1}0\rangle_{\gamma}\,\|\,\langle 11\bar{2}0\rangle_{\alpha_2} \qquad (21)$$

Considering the slip modes which may occur in the individual material phases, the mean free path of dislocation movement in the lamellar structure, for systems having components normal to the lamellar interfaces, is on the order of the lamellar thickness, which can be much less than 1 μm (17). Therefore, the strengths and hardening parameters associated with selected systems in the individual phases must be adjusted to reflect the differing constraint situation in the lamellar colony. We use a correction having the form

$$\tau_C = \tau_0 + \frac{k}{\sqrt{d_L}} \qquad (10)$$

in which d_L is the lamellar spacing. The slope of this correction is relatively small (k = 0.02 – 0.08 MPa-m$^{1/2}$), and depends upon the particular set of initial yield data selected for use. Although (10) has the form of a Hall-Petch correction, we hesitate to describe it as such. The variety of material data used in defining the model constants is great, and the primary function of the correction (10) has been to correct for variations between material strengths measured at different laboratories, using different variants of the material. The proper means of applying such a correction, even for a consistent body of material data, remains unresolved, since the controlling dimension for a given system may be related to lamellar spacing, domain size, colony size, or some combination of these lengths, depending on the geometry of the system.

As was mentioned earlier, the interlamellar slip behavior of γ-TiAl is not completely understood. Computation of appropriate properties and deformation characteristics in the neighborhood of the lamellar interfaces from first principles currently is infeasible. At the same time, experimental evaluation of meaningful continuum-level properties of the interface may not be possible because of the extremely small length scale at which the interface deformation mechanisms operate. Therefore, we employ the expediency of an independently defined interlamellar slip system, whose properties are derived from analyses of PST single crystal experiments. The alternative to this approach is to assume, for the lamellar microstructure, lower strengths than those indicated by experiments on the constituent material phases. Although we have chosen the former approach, the generic plasticity model described here can be applied using either set of assumptions.

The slip systems included in the lamellar material description are given in Table 4. The slip systems from the individual constituents are retained, and three additional interlamellar systems are introduced. The α_2 basal slip systems have been eliminated, since the slip planes coincide with the interlamellar slip planes; due to the much lower strength of the interlamellar modes, the basal slip systems in the α_2 phase would never be activated in practice.

Table 4. Slip systems for lamellar g+a$_2$ TiAl.

Slip System Description	Slip Planes and Directions	Yield Strength
γ	{111} [110]	90 MPa
α_2 Prism	$\{1\bar{1}00\} < 11\bar{2}0 >$	100 MPa
α_2 Pyramidal	$\{11\bar{2}1\} < \bar{1}\bar{1}26 >$	911 MPa
Interlamellar	$(0001) < 11\bar{2}0 >$	56 MPa

The use of both sets of constituent slip systems in the lamellar model corresponds to the assumption of an isostress condition in the lamellar microstructure in the neighborhood of a stress point; that is, both material phases are assumed to experience the same stress components, while their strains may differ. While more sophisticated constraint conditions between the phases can be imposed, the isostress assumption predicts the onset of macroscopic plastic flow with reasonable accuracy. This is possible because the moduli of the phases are similar, and because the yield behavior in virtually all material orientations is controlled by a limited subset of the slip systems.

For loading that is nearly aligned with the lamellar planes, yielding is controlled by the γ systems and the α_2 prism modes, which are activated at nearly the same time. Loading perpendicular to the lamellae involves the γ phase, followed by the α_2 pyramidal slip modes. Translamellar slip is controlled by the pyramidal slip system in the α_2 phase. In practice, the pyramidal modes are likely to be activated only as a result of dislocation pileup because of their high strength. In a wide range of intermediate orientations, the interlamellar behavior is the prevailing feature of the plastic flow behavior. Furthermore, within a polycrystal composed of lamellar colonies with random orientations, interlamellar slip in favorably oriented colonies dominates the initial stages of inelastic response.

Figure 4 shows a comparison of initial yield strength as predicted by the lamellar model, compared with experimental data collected by Parthasarathy, et al. (17) and Inui, et al., (16). A strength constant k = 0.02 MPa-m^{½} (eq. 10) provides the closest agreement with the data from (17) for the initial yield points, while a value of 0.07 MPa-m^{½} better matches the 0.2 percent offset data in (16). The predicted curves are identical at intermediate orientations, since the strength associated with interlamellar slip is a property of the lamellar microstructure, and is not subjected to the same correction as the constituent strengths.

Predictions of stress-strain curves for k = 0.02 MPa-m^{½} are shown in Figure 5, and compared with the microstrain measurements of Parthasarathy and coworkers. The strain scale is rather highly magnified, since the experimental conditions were limited to strains on the order of 0.5 percent; in this regime, a more sophisticated representation of the strain-hardening behavior would be desirable for improved accuracy.

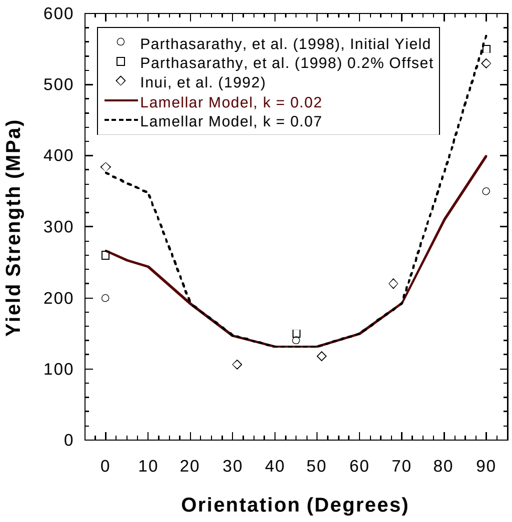

Figure 4. Predicted yield strength of lamellar colony at various orientations.

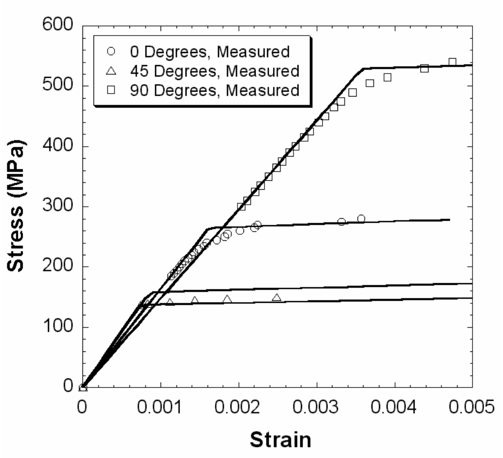

Figure 5. Predicted stress-strain curves for lamellar TiAl.

Polycrystal Analysis

The crystal plasticity model described above has been implemented in the form of a user-supplied material model (UMAT) for the ABAQUS finite element code. For each TiAl material variant, appropriate properties, including the relevant slip system geometry, are defined separately and used in the same solution algorithm.

Figure 6 shows a finite element model of a polycrystal composed of an equal number of lamellar colonies and equiaxed γ-TiAl grains. The volume fraction of lamellar TiAl is 0.96, with an assumed α_2: γ ratio of 1:5 within the lamellar colonies. Because of the relatively small fraction of γ grains present, filling the three-dimensional space with a regular pattern of both grain types is difficult. Here we use a geometric pattern in which cubic γ grains alternate with truncated rhombic dodecahedra representing the lamellar colonies. The width of the lamellar colonies is approximately 145 μm, and the overall length of the model in each direction is about 0.77 mm. The model contains a total of 512 grains, with the orientation of each grain being randomly generated. Fringe values in Figure 6 depict the orientation of each grain with respect to the loading direction, which is parallel to the global 'x' axis. Symmetry conditions are applied on the three rearward facing surfaces of the model. The remaining three faces are constrained to remain planar, but may expand or contract in response to the loading.

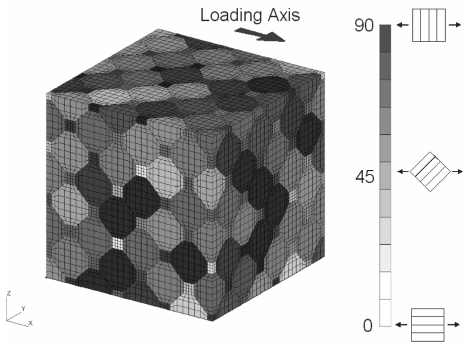

Figure 6. Polycrystal finite element model with randomly oriented grains.

In Figure 7, we compare a trace of macroscopic stress and strain under uniaxial compression loading with the measurements reported by Parthasarathy, et al. (17). The macroscopic response is quite reasonable. However, it is not clear why the prediction using k = 0.07 MPa-m$^{1/2}$ provides closer agreement with the experiment than k = 0.02. According to Parthasarathy, the polycrystals used in the experiment exhibited a more refined microstructure than the PST crystals from which properties were measured, but are otherwise similar.

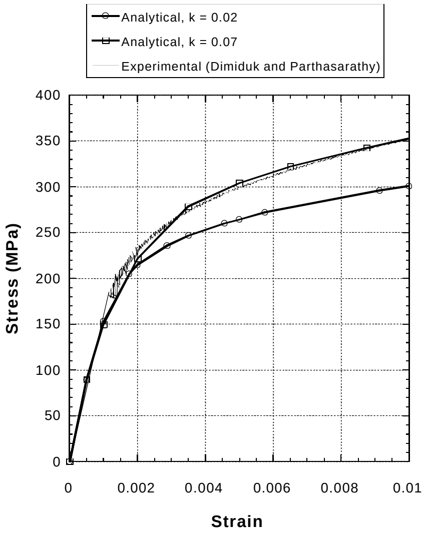

Figure 7. Predicted and measured stress-strain curves for TiAl polycrystal.

Figures 8 and 9 represent an attempt to separate the effect of local stress variations caused by anisotropy and differing orientations in adjacent grains from that due purely to crystal orientation. The Schmid resolved shear stress (SRSS) on the interlamellar planes,

$$\tau^{sn(IL)} = \overline{\sigma}_{ij} n_i^{(IL)} s_j^{(IL)} = \overline{\sigma}_{11} n_1^{(IL)} s_1^{(IL)} \tag{11}$$

in which $\overline{\sigma}_{ij}$ are the global (applied) stress components, is used to normalize the resolved shear stresses obtained from the finite element prediction. In the absence of localized stress concentrations, this normalized shear stress should equal one. Figure 8 depicts the ratio of the predicted shear stress to the SRSS for a nominal strain of 0.1 percent, where the response is predominantly elastic. The most variation in the shear stress occurs in lamellar colonies for which the SRSS is small (and in fact the stress ratios for some colonies are much larger than the range shown in the figure). However, the magnitude of the interlamellar shear stress for these extreme cases is quite small. A noticeable variation in the resolved shear stress from the SRSS is evident even in colonies that are favorably oriented for interlamellar slip (i.e., near 45 degrees to the loading axis). This fluctuation in the stresses is caused by local changes in the stress path resulting from elastic anisotropy, orientation differences in neighboring grains, and localized yielding.

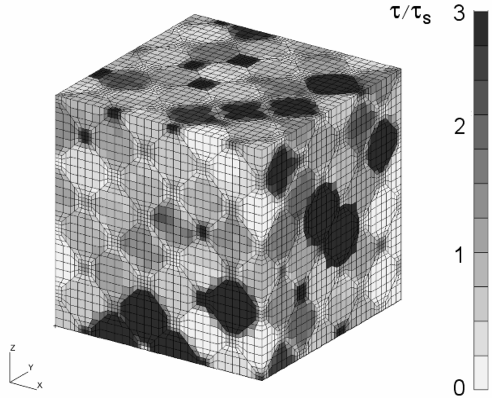

Figure 8. Predicted ratio of interlamellar resolved shear stress to Schmid stress in polycrystal finite element model. Ratios different from one reflect the influence of localized stress variations and orientation mismatch between adjacent grains.

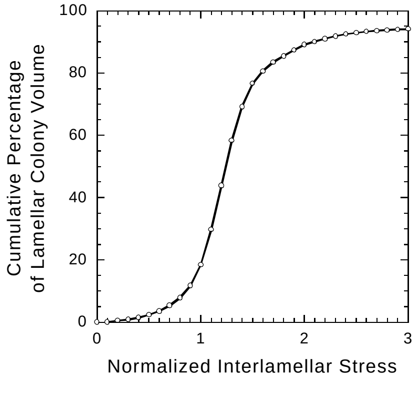

Figure 9. Distribution of interlamellar shear stresses in γ-TiAl polycrystal. Shear stresses within each grain are normalized with respect to the Schmid stress in that grain.

Figure 9 is a histogram relating the level of interlamellar shear stress (normalized by SRSS) to the cumulative fraction of material volume experiencing that shear stress or less. Only lamellar colonies are included in this data. The interlamellar stress is less than the SRSS only in about 20 percent of the material volume, while the interlamellar shear stress exceeds 2×SRSS only in about ten percent of the material. As was mentioned above, this latter population contains mostly material grains for which the absolute stresses are quite low compared with the interlamellar CRSS. Half of the material is subjected to interlamellar shear stress which is less than about 1.3×SRSS.

In Figures 10 and 11, the distribution of effective plastic strain,

$$\varepsilon_p = \int_0^t \frac{2}{3} \dot{\varepsilon}_{ij}^p \dot{\varepsilon}_{ij}^p dt \tag{24}$$

is shown at nominal strains of 0.2 and one percent, respectively. At a strain of 0.002, much of the polycrystal remains elastic; however, localized plastic strains exist which are 50 percent greater than the nominal strain. At one percent macroscopic strain, nearly all of the sample has yielded. Those grains containing unyielded material are oriented such that the loading is nearly normal to the lamellar planes. Localized effective plastic strains exist which are nearly four times as large as the nominal strain. Figure 12 contains this data in the form of a histogram.

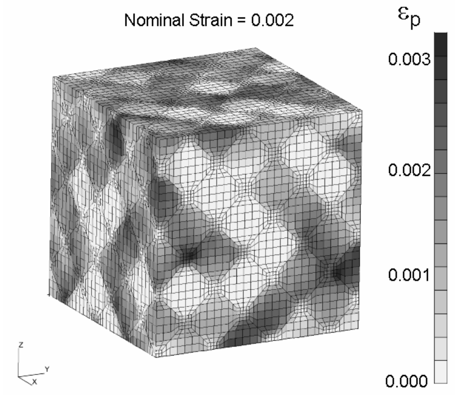

Figure 10. Effective plastic strains in TiAl polycrystal corresponding to a macroscopic strain of 0.2 percent.

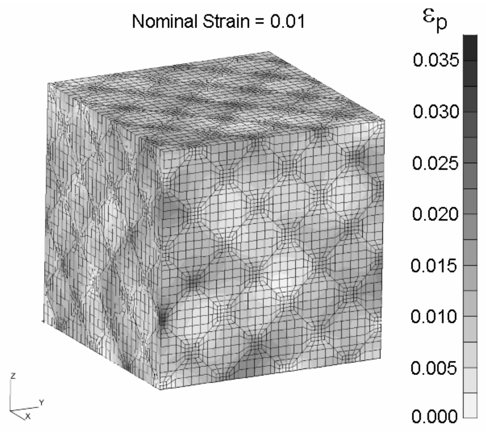

Figure 11. Effective plastic strains in TiAl polycrystal corresponding to a macroscopic strain of one percent.

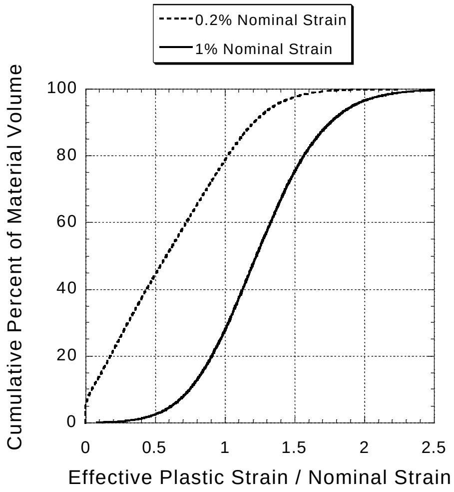

Figure 12. Effective plastic strain variation in polycrystal model. At 0.2% elongation, five percent of the volume remains elastic, and 20% experiences plastic strains larger than the nominal strain.

Summary

A crystal plasticity model suitable for small-deformation elastic-plastic analysis of localized stress variations in polycrystals of lamellar $\gamma+\alpha_2$ TiAl, as well as the individual phases of the material, has been presented. The modeling of the lamellar colonies introduces an averaged-stress approximation that eliminates the need for modeling individual lamellae explicitly, while capturing the most important features of the early plastic flow within a colony. The model has been implemented as a user material model subroutine (UMAT) for the ABAQUS finite element code. Three-dimensional stress analyses of polycrystals containing several hundred grains have been performed, and yield useful information concerning the local stress variations caused by elastic anisotropy, orientation differences among adjoining grains, and localized plastic deformation.

Acknowledgements

This work was performed at the Air Force Research Laboratory, Materials and Manufacturing Directorate, Wright-Patterson Air Force Base, Ohio, under DoD contract F33615-98-C-5214 and AFOSR Task 2302BW1. The authors gratefully acknowledge many fruitful discussions with Drs. James M. Larsen, Andrew H. Rosenberger, and Dennis M. Dimiduk of AFRL, Drs. Peter M. Hazzledine and Triplicane Parthasarathy of U.E.S., Inc., and Dr. Kezhong Li and Mr. W. John Porter of UDRI.

References

1. F. Appel and R. Wagner,. Microstructure and deformation of two-phase γ-titanium aluminides. Mat. Sci. Eng. R22 (1998) 187-268.

2. E. Parteder, T. Siegmund, F. D. Fischer, and S. Schlögl, Numerical simulation of the plastic behavior of polysynthetically twinned Ti-Al crystals. Mat. Sci. Engng. A 192-193 (1995) 149-154.

3. S. M. Schlögl and F. D. Fischer, Micromechanical modelling of TiAl intermetallics. Comp. Mat. Sci. 7 (1996) 34-39.

4. S. M. Schlögl and F. D. Fischer, The role of slip and twinning in the deformation behaviour of polysynthetically twinned crystals of TiAl: a micromechanical model. Phil. Mag. A 75(3) (1997) 621-636.

5. S. M. Schlögl and F. D. Fischer, Numerical simulation of yield loci for PST crystals of TiAl. Mat. Sci. Engng. A 239-240 (1997) 790-803.

6. R. Lebensohn,, H. Uhlenhut, C. Hartig, and H. Mecking, Plastic flow of γ-TiAl-based polysynthetically twinned crystals: micromechanical modeling and experimental validation, Acta Mater 46(13) (1998) 4701-4709.

7. B. K. Kad, M. Dao, and R. J. Asaro, Numerical simulations of plastic deformation and fracture effects in two phase γ-TiAl and α_2-Ti_3Al lamellar microstructures. Phil. Mag. A 71(3) (1995) 567-604.

8. B. K. Kad, M. Dao, and R. J. Asaro, Numerical simulations of stress-strain behavior in two phase $\alpha_2+\gamma$ lamellar TiAl alloys. Mat. Sci. Engng. A 192-193 (1995) 97-103.

9. B. K. Kad and R. J. Asaro, Apparent Hall-Petch effects in polycrystalline lamellar TiAl. Phil.Mag. A 75(1) (1997) 87-104.

10. M. Dao, B. K. Kad, and R. J. Asaro, Deformation and fracture under compressive loading in lamellar TiAl microstructures. Phil. Mag A 74(3) (1996) 569-591.

11. P. Steinmann, E. Kuhl, and E. Stein, Aspects of non-associated single crystal plasticity: influence of non-Schmid effects and localization analysis. Int. J. Sol. Struct. 35(33). (1998) 4437-4456.

12. ABAQUS User's Manual, Version 6.1, Hibbitt, Karlsson, and Sorensen, Inc., Pawtucket, Rhode Island, 2001.

13. M. H. Yoo and C. L. Foo, Physical constants, deformation twinning, and microcracking of titanium aluminide. Metallurgical and Material Trans. 29A (1998) 49-62.

14. M. Yamaguchi, and H. Inui, TiAl compounds for structural applications. In Dariola, R., Lewandowski, J.J., Liu, C.T., Martin, P.L., Miracle, D.B., Nathal, M.V. (eds) Structural Intermetallics. The Minerals, Metals, and Materials Society (1993) 127-142.

15. N. J. Pagano, Exact moduli of anisotropic laminates. In Sendeckyj, G.P. (ed.) Mechanics of Composite Materials. Academic Press, New York, 1974.

16. H. Inui, M. H. Oh, A. Nakamura, and M. Yamaguchi, Room-temperature tensile deformation of polysynthetically twinned (PST) crystals of TiAl. Acta Metall. Mater. 40(11) (1992) 3095-3104.

17. T. A. Parthasarathy, M. G. Mendiratta, M.G., and D. M. Dimiduk, Flow behavior of PST and fully lamellar polycrystals of Ti-48Al in the microstrain regime. Acta Mater. 46(11) (1998) 4005-4016.

COLONY PROPERTY DETERMINATION IN A GAMMA TITANIUM ALUMINIDE

R. John[†], W.J. Porter, III[*], and S. Olson[*]

[†] Air Force Research Laboratory, Materials and Manufacturing Directorate (AFRL/MLLMN),
Wright-Patterson Air Force Base, Ohio 45433, U.S.A.
[*] University of Dayton Research Institute (UDRI), Dayton, Ohio 45469, U.S.A.

Abstract

Gamma titanium aluminide (γ-TiAl) alloys have been under development for use in rotating components for gas turbine engines. Detailed 3-dimensional (3D) colony-level finite element (FE) models are being developed at the U.S. Air Force Research Laboratory to predict damage initiation and accumulation in γ-TiAl during service loading. These models require knowledge of the orthotropic nature of the deformation and fracture behavior of individual colonies. While the elastic properties of gamma and alpha-2 single-phase materials have been extensively studied, the elastic response of fully lamellar two-phase materials has not received the same degree of attention. This paper describes an integrated experimental and analytical approach to deduce the colony properties in a γ-TiAl. Samples with gage sections composed of specifically-oriented individual lamellar grains were tested in tension to determine the elastic behavior of this two-phase structure. Preliminary 3D FE analysis, using the constituent properties available in the open literature, showed general agreement between the model results and the experimental measurements.

Introduction

Gamma titanium aluminide (γ-TiAl) alloys are being developed for application in rotating components for gas turbine engines. Based on the intermetallic gamma (face-centered tetragonal) and alpha-2 ($D0_{19}$-modified hexagonal close-packed) phases, TiAl and Ti_3Al, respectively, these alloys are noted for their high temperature strength retention, lightweight, good oxidation resistance, and stiffness [1-3]. Recent studies by Larsen and Worth [4] showed that, during tension-tension fatigue loading of specimens with a single, artificial, semi-circular flaw, most of the γ-TiAl specimens did not fail at the location of the flaw. Damage initiation occurred at locations away from the machined notch, indicating that closely aligned and unfavorably oriented colonies were responsible for crack initiation. Detailed 3-dimensional (3D) colony-level finite element (FE) models are being developed at AFRL to predict such damage initiation. These models require knowledge of the orthotropic nature of the deformation and fracture behavior of individual colonies.

While the elastic properties of gamma [5-9] and alpha-2 [6,10,11] single-phase materials have been thoroughly investigated, the elastic response of fully lamellar two-phase materials has not received the same amount of attention. Limited data on the longitudinal modulus as a function of lamellar orientation based on tests conducted using PST specimens are shown in Fig. 1 [12,13]. Figure 1 highlights the need for a consistent set of data over a wide range of orientations. The relative lack of information on the elastic behavior of two-phase, lamellar titanium aluminides is contrasted by the extensive work reporting the deformation and fracture behavior of this material system [14-17]. Hence, a program was initiated at the U.S. Air Force Research Laboratory to characterize the elastic-plastic deformation and fracture behavior of individual colonies in a g-TiAl.

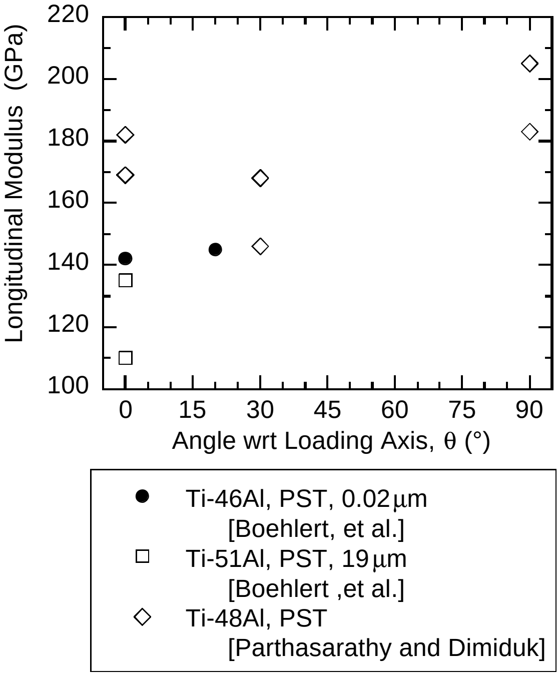

Figure 1: Effect of lamellar orientation on longitudinal modulus.

This paper describes an integrated experimental and analytical approach to deduce the colony properties in γ-TiAl. Specimens with gage sections composed of single lamellar grains were tested in tension to determine the elastic behavior of this two-phase structure. Preliminary 3D FE modeling results of the colony-level elastic behavior are presented and approaches for improving the model are discussed.

Material and Experimental Procedure

The alloy used in this study, nominally Ti-46.5Al-3Nb-2Cr-0.2W (at%), was developed by Kim [3] and designated as K5. To obtain the large grain microstructure required for this testing, the forged material (approximately 10x20x2cm) was heat treated in air at 1400°C for 24 hours and homogenized at 900°C for 24 hours and then air cooled. The heat treatment temperature is in the single-phase alpha field for the composition.

As discussed later, the specimens were machined from the central portion of the 20 mm thick forging. This region experienced the slowest cooling rates. The microstructure in this region was near-fully lamellar with an average grain size of approximately 7 millimeters in diameter and lamellar spacing in the 1 to 3 micron range. A photomicrograph of the microstructure is shown in Figure 2.

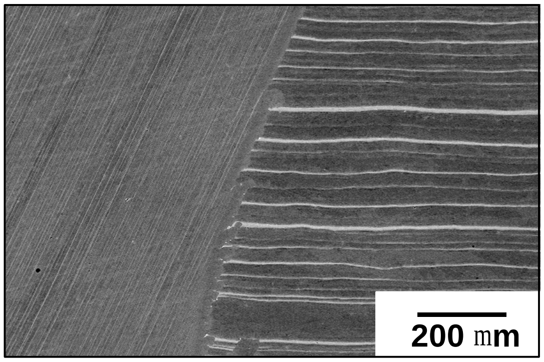

Figure 2: Microstructure of Ti-46.5Al-3Nb-2Cr-0.2W (a%) after 1400C/24hr heat treatment (SEM BSE image).

This image was obtained using a scanning electron microscope (SEM) in the backscattered-electron (BSE) mode. In this photo, the dark contrast phase is gamma and the light contrast phase is alpha-2. The material's chemistry was analyzed before and after heat treatment and the results are shown in Table I. Not surprisingly, the oxygen level was found to be significantly higher following heat treatment in air.

Table I. Pre-(as-cast) and post-heat treatment (HT) chemistries of Ti-46.5Al-3Nb-2Cr-0.2W (at%) used in this study.

Element	pre-HT (a%) as-cast	post-HT (a%) forged+HT
Al	46.38	46.46
Nb	3.00	2.98
Cr	2.17	2.05
W	0.20	0.21
Nb	0.10	0.12
Cr	0.05	0.05
Fe	0.05	0.05
O*	1112	3050
Ti	(bal)	(bal)

*wppm

Thin machining blanks (3mm thick), shown in Fig. 3, were sliced from the center of the forged material using an electro-discharge machine (EDM) and then polished. Figure 3 also shows the regions from which dogbone samples were EDM'd from the machining blanks such that the majority of the gage section of a specimen consisted of a single large grain with a specific surface orientation.

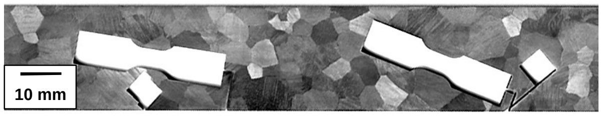

Figure 3: Machining blank. Note the large grain size of material used in specimen manufacturing.

As shown in Table II, three specimens designated 00-690, 00-692 and 01-254 were machined from the blank shown in Fig. 3. The photograph of a specimen cut-out from the machining blank is shown in Fig. 4 along with the dimensions.

Table II. Test Matrix and Specimen Orientation

Specimen Number	Gage Thickness B, (mm)	Gage Width W (mm)	Lamellar Orientation of Colony in Gage Section (°)		
			Surface[1] (θ)	Edge Front[2] (φ_F)	Through-thickness[3] (ψ)
00-690	2.190	3.500	-3.0	1.0	-18.5
00-692	2.310	3.375	42.0	-10.0	-11.0
01-254	2.397	3.650	84.5	20.0	2.0

[1] w.r.t. loading axis

[2] w.r.t. top surface

[3] w.r.t. bottom surface

In Fig. 4, the central grain is oriented nearly parallel to the loading direction. Due to the significant anisotropy of fully lamellar material, the surface and edge orientations of the gage section colony were carefully determined through metallography. Figure 5 shows the definitions of the various angles used to characterize the complete orientation of the colony. These details for each specimen are shown in Table II.

The deformation response of the central colony was measured using strain gages located on the top and bottom faces of the sample. The grid size of the strain gages was 0.381 x 0.508 mm. The gages were oriented parallel to the loading direction and located as close to the mid-face as possible.

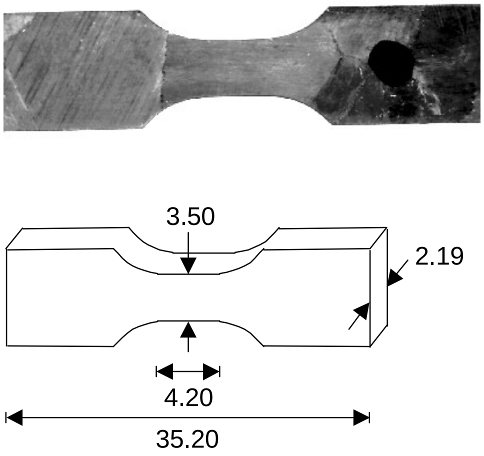

Figure 4: Specimen number 00-690. (All dimensions in mm)

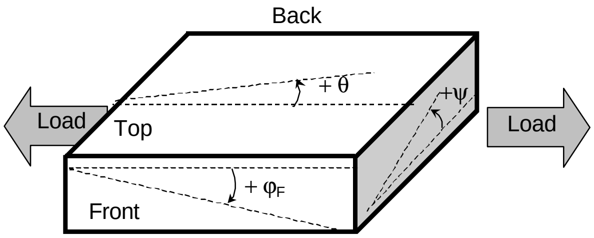

Figure 5: Schematic of lamellar orientation in the primary grain in the gage section.

The tests were conducted at room temperature on a servo-hydraulic machine in load control mode. A loading rate of 5 MPa/sec was employed. To insure that the samples were loaded in the elastic regime, the maximum stress applied was limited to 50 MPa for specimens 00-690 and 00-692, and 25 MPa for specimen 01-254.

As shown in Table II and Fig. 4, the experiments were conducted on small specimens. Hence, the test system was verified using instrumented Ti-6Al-4V specimens with dimensions similar to that of the γ-TiAl specimens. Small strain gages (0.381 x 0.508 mm grid size) were glued using standard procedures on all four sides of the specimen. Multiple load-unload cycles were applied and the modulus determined from the measured stress-strain response. The average modulus value (≈114 GPa) was nearly identical to that reported in the literature. The modulus values from the four strain gages were within ≈2% of the average indicating excellent alignment of the test system. All the verification load-unload tests using Ti-6Al-4V specimens were also devoid of hysterisis.

Results and Discussion

The measured stress-strain response for surface orientations, 3°, 42°, and 84.5° are shown in Figs. 6, 7, and 8, respectively. Figures 6 and 8 show that, for the 3° and 84.5° specimens, the stress-strain responses of the top and bottom faces are nearly identical. In contrast, in the 42° specimen (Fig. 7), there is a slight difference between the responses of the top and bottom faces. This difference in response was confirmed by rotating the specimen about the longitudinal and transverse axes, and retesting. In all the tests with multiple load-unload cycles, the stress-strain responses were devoid of hysteresis.

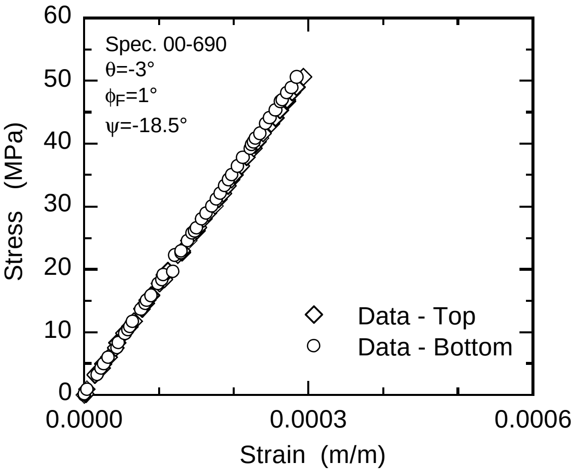

Figure 6: Experimental stress vs. longitudinal strain response for specimen # 00-690.

Following the measurement of strains within the central colony, detailed 3D FE analyses were conducted for each specimen. The FE analyses were conducted using ABAQUS. The detailed finite element model for specimen 00-690 is shown in Fig. 9. The different shades of gray correspond to the grains making up the sample. Each grain represented in the FE model was assigned properties based upon the metallographically determined orientation of the grain in the sample.

The FE models of the specimens contained a large number of nodes and elements. For example, specimen 00-690 contained 42,629 nodes and 38,390 elements. Most of the elements were 8-node brick elements with 6-node wedge elements used in limited regions. There were no wedge elements in the gage section. The typical mesh spacing was ≈ 0.15 mm. Individual grains were modeled based on grain mapping and orientations from SEM observations and metallography. In the grip section, only a region of ≈ 2.5 mm was modeled. One end of the specimen was fixed and the other end forced to remain planar with axial displacements, simulating clamped end conditions.

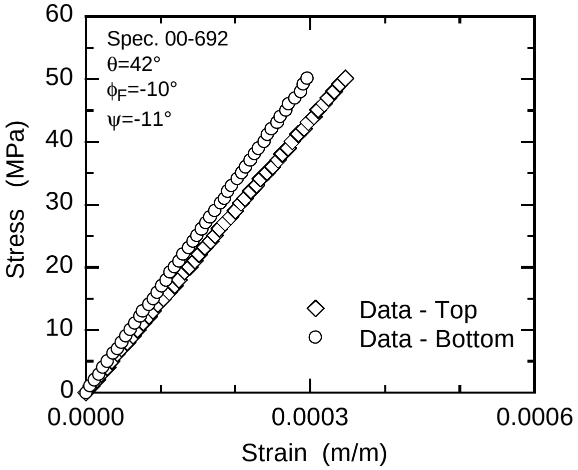

Figure 7: Experimental stress vs. longitudinal strain response for specimen # 00-692.

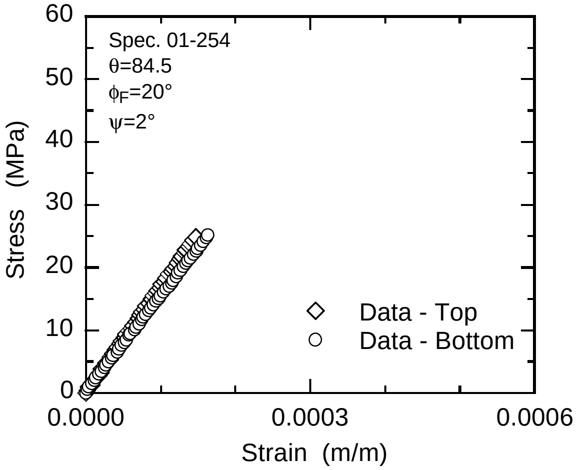

Figure 8: Experimental stress vs. longitudinal strain response for specimen # 01-254.

The elastic orthotropic properties used in the FE analyses are shown in Table III. The initial FE analyses were conducted using the properties identified as "FE-Initial". This set of elastic orthotropic properties was derived using constituent (gamma and alpha-2 phases) properties [18] and laminate models [19].

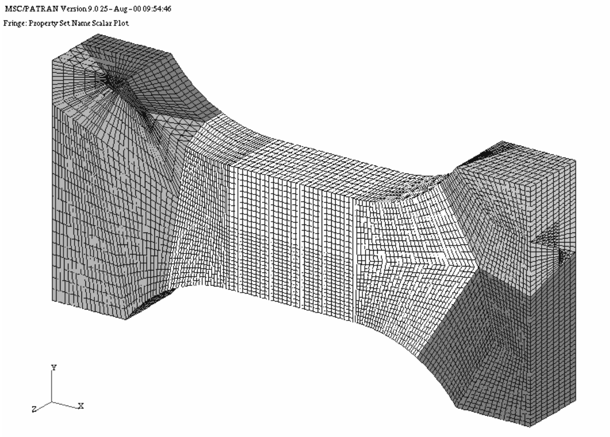

Figure 9: Finite element (FE) model of specimen number 00-690. The different shades of gray represent the grains in the sample. Specific properties were assigned to each grain based upon metallographically determined orientation.

Table III. Properties Used in Finite Element Analyses.

Property	FE-Initial	FE-Modified	Units
$E_1 = E_2 =$	186.2	172.4	GPa
$E_3 =$	218.6	195.9	GPa
$G_{12} =$	72.46	61.59	GPa
$G_{13} = G_{23} =$	66.85	66.85	GPa
$\nu_{12} =$	0.2872	0.2872	
$\nu_{13} = \nu_{23} =$	0.1458	0.1458	
Assumes composition = 90% γ + 10% α_2		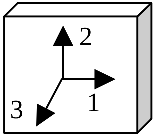	

The FE results based on the initial set of properties (FE-Initial) are compared with the measured responses for the 3° specimen in Fig. 10. The predicted stress-strain response was stiffer by ≈ 7.4%. Similarly, the predicted (Iteration 1) response was higher than the average measured response by ≈ 10.4% and by ≈19% for the 84.5° and 42° specimens, respectively. Based on these differences and some trial runs, E_1, E_2 and G_{12}, were decreased to better correlate with the data, as shown in Figs. 11, 12 and 13 for the 3°, 42° and 84.5° specimens, respectively. This new set of properties corresponds to "FE-Modified" in Table III. Note that the modified elastic moduli and shear values are within the range of published constituent properties.

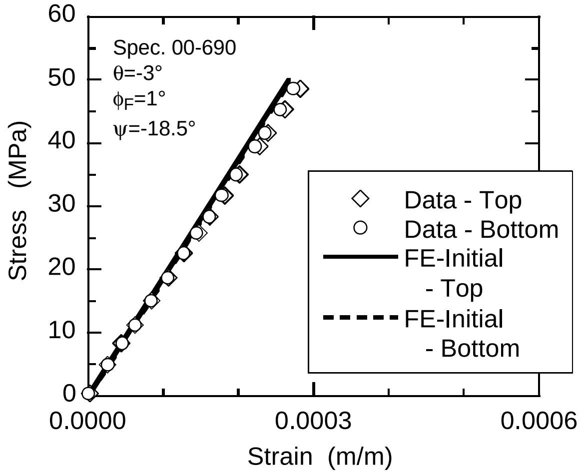

Figure 10: Comparison of predicted (FE-Initial) and measured stress vs. longitudinal strain response for specimen # 00-690.

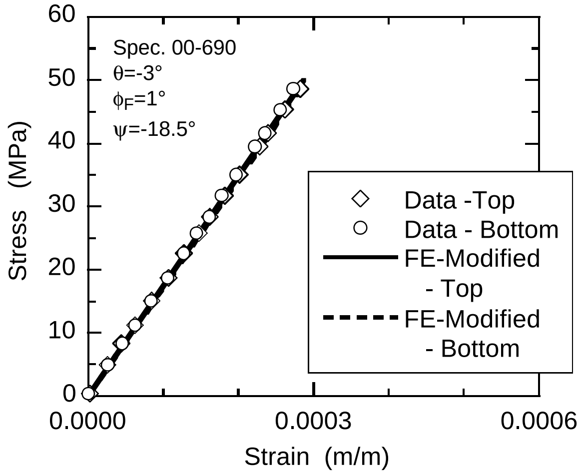

Figure 11: Comparison of predicted (FE-Modified) and measured stress vs. longitudinal strain response for specimen # 00-690.

The FE results are very close to the data for the 3° and 84.5° specimens (Figs. 11 and 13). Similar to the data, the FE results also indicate that top and bottom face responses are identical. However, for the 42° specimen (Fig. 12), the FE result is between the measured responses. The FE result does not show the difference in responses between the top and bottom faces. Additional measurements and analyses are in progress to understand this behavior for the 42° specimen.

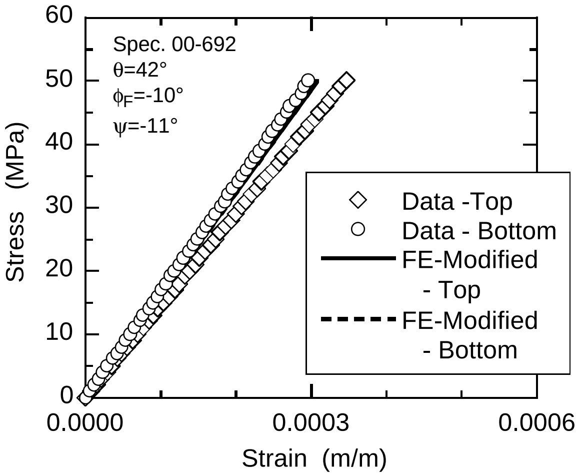

Figure 12: Comparison of predicted (FE-Modified) and measured stress vs. longitudinal strain response for specimen # 00-692.

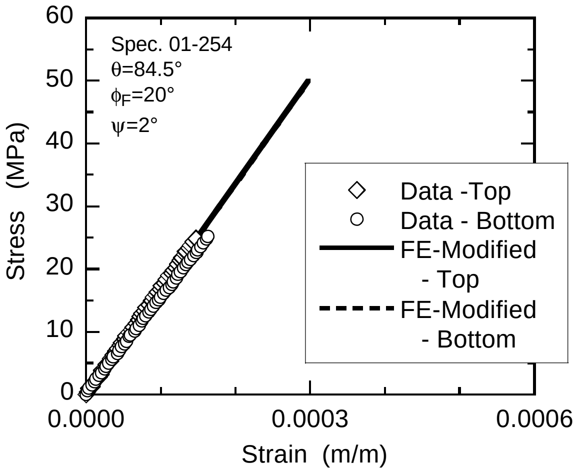

Figure 13: Comparison of predicted (FE-Modified) and measured stress vs. longitudinal strain response for specimen # 01-254.

Using the two sets of properties shown in Table III, the effective longitudinal modulus for a PST was predicted as a function of lamellar orientation and compared with the available data [12,13] in Fig. 14. The predicted trend agrees well with the values determined by Parthasarathy and Dimiduk [13].

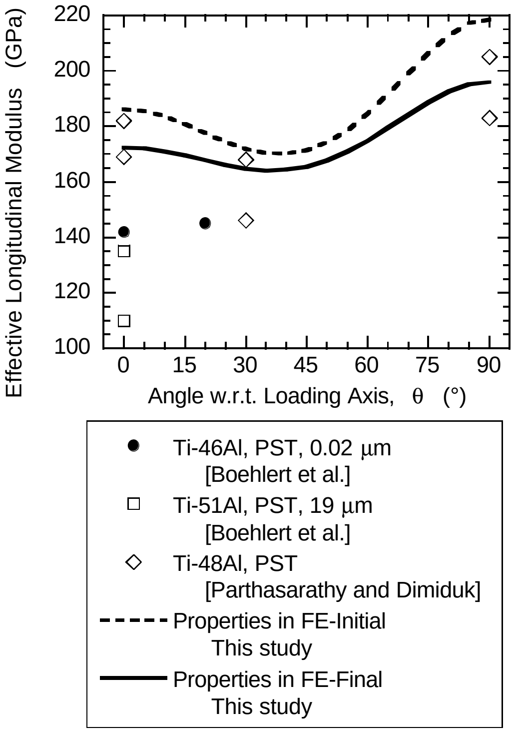

Figure 14: Effect of lamellar orientation on longitudinal modulus.

During this study, the specimens were machined based on the lath orientation in the central colony (θ in Fig. 5) as observed on the surface of the machining blank shown in Fig. 3. The other orientations (φ_F and ψ in Fig. 5) could not be controlled as desired unlike typical PST specimens. However, the exact orientation of the grains were modeled accurately during the FE analysis. Additional specimens are being prepared for determination of the modulus and Poisson's ratio at intermediate orientations. In addition, the specimens from this study will be tested to failure to determine the yield stress as a function of lath orientation.

The properties deduced during this study are based on a colony size of ≈5mm, which is ≈10X larger than that found in the K5 alloy. The influence of scale on the deduced properties needs to be investigated prior to application in colony-based 3D FE analysis of conventional γ-TiAl. Experiments using full field displacement techniques are being planned to address this issue.

Summary

In an effort to understand the elastic behavior of γ-TiAl with lamellar microstructures, an integrated experimental and analytical approach to deduce the colony properties in γ-TiAl was developed. Tensile samples with a single lamellar grain in the gage section were loaded in the elastic regime to determine the colony-level response. Strain was monitored by placement of strain gages within this central colony on the top and bottom faces of the sample. Detailed 3-dimensional finite element analysis was used to deduce the orthotropic elastic properties from the stress-strain response of these specimens. Initial results indicate that the orthotropic properties determined using constitutent properties give a reasonable estimate of the longitudinal modulus as a function of lath orientation.

Acknowledgments

This research was performed at the Air Force Research Laboratory, Materials and Manufacturing Directorate (AFRL/MLLMN), Wright-Patterson Air Force Base, OH 45433-7817 and was supported in part by the Air Force Office of Scientific Research under task 23061P10 (Program Manager: Dr. Craig Hartley). W. J. Porter and S. Olson gratefully acknowledge the support of Air Force Contract F33615-98-C-5214. The authors gratefully acknowledge the assistance of Mr. Dan Knapke in conducting the experiments. The authors also gratefully acknowledge numerous technical discussions with Dr. Robert Brockman (UDRI), Dr. James M. Larsen (AFRL/MLLMN), and Dr. Andrew H. Rosenberger (AFRL/MLLMN).

References

1. Y-W. Kim, “Intermetallic Alloys Based on Gamma Titanium Aluminide,” JOM, 41 (7) (1989), 24-29.

2. Y-W. Kim and D. M. Dimiduk, "Designing Gamma TiAl Alloys: Fundamentals, Strategy and Production," Structural Intermetallics 1997, ed. M.V. Nathal, R. Darolia, et al. (TMS, Warrendale, PA, 1997), 531-543.

3. Y-W Kim, “Ordered Intermetallic Alloys, Part III: Gamma Titanium Aluminides,” JOM, 46 (7) (1994), 30-40.

4. J.M. Larsen and B.D. Worth, Air Force Research Laboratory, AFRL/MLLMN, Wright-Patterson AFB, OH 45433, U.S.A., Unpublished results, 1997.

5. H. A. Lipsitt, D. Schechtman, and R. E. Schafrik, "The Deformation and Fracture of TiAl at Elevated Temperatures," Metall. Trans., 6A, (1975), 1991-1996.

6. R. E. Schafnik, "Dynamic Elastic Modulus of Titanium Aluminides," Metall. Trans., 8A (1977), 1003-1006.

7. Y. He, R. B. Schwarz, A. Migliori, and S. H. Whang, "Elastic Constants of Single Crystal γ-TiAl," J. Mater. Res., 10 (1995), 1187-1195.

8. K. Tanaka, T. Ichitsubo, H. Inui, M. Yamaguchi, and M. Koiwa, "Single-crystal Elastic Constants of γ-TiAl," Phil. Mag. Lett., 73 (2) (1996), 71-78.

9. M. H. Yoo, J. Zou, and C. L. Fu, " Mechanistic Modeling of Deformation and Fracture Behavior in TiAl and Ti_3Al," Mater. Sci. Eng., A192-193 (1995), 14-23.

10. H. A. Lipsitt, D. Schechtman, and R. E. Schafnik, "The Deformation and Fracture of Ti_3Al at Elevated Temperatures," Metall. Trans., 11A (1980), 1369-1375.

11. K. Tanaka, K. Okamoto, H. Inui, Y. Minonishi, M. Yamaguchi, and M. Koiwa, "Elastic Constants and Their Temperature Dependence for the Intermetallic Compound Ti_3Al," Phil. Mag. A, 73 (5) (1996), 1475-1488.

12. C.J. Boehlert, M. Zupan, D.M. Dimiduk, and K.J. Hemker, "Microsample Tension and Tension-creep Testing of Fully-lamellar TiAl Single Crystals," Gamma Titanium Aluminides 1999, Y-W. Kim, D.M. Dimiduk, M.H. Loretto, eds. (Warrendale, PA, TMS, 1999), 669-77.

13. T.A. Parthasarathy and D. Dimiduk, Air Force Research Laboratory (AFRL/MLLM), Wright-Patterson AFB, OH (1998), unpublished research.

14. H. Inui, M.H. Oh, A. Nakamura, and M. Yamaguchi, "Room-Temperature Tensile Deformation of Polysynthetically Twinned (PST) Crystals of TiAl," Acta Metall. Mater., 40 (1992), 3095-3104.

15. S. Yokoshima, and M. Yamaguchi, "Fracture Behavior and Toughness of PST Crystals of TiAl," Acta Mater., 44 (1996), 873-883.

16. M. Yamaguchi, H. Inui, S. Yokoshima, K. Kishida, and D.R. Johnson, "Recent Progress in our Understanding of Deformation and Fracture of Two-Phase and Single-Phase TiAl Alloys," Mater. Sci. Eng., A213 (1996), 25-31.

17. T.A Parthasarathy, M.G. Mendiratta, and D.M. Dimiduk, "Flow Behavior of PST and Fully Lamellar Polycrystals of Ti-48Al in the Microstrain Regime," Acta Mater., 46 (1998), 4005-4016.

18. M.H. Yoo and C.L. Fu, "Physical Constants, Deformation Twinning, and Microcracking of Titanium Aluminides," Met. Trans A, 29A (1998), 49-63.

19. N.J. Pagano, "Exact Moduli of Anisotropic Laminates," Mechanics of Composite Materials, Vol. 2, George P. Sendeckyj, ed. (New York, NY, Academic Press, 1974), 23-44.

Submitted for publication: Composites Science and Technology, October 2002

In-Plane Shear Behavior in Oxide/Oxide Ceramic Matrix Composites at Room and Elevated Temperature

Victoria A. Kramb[1], Dennis J. Buchanan[1], Reji John* and Larry P. Zawada

Materials and Manufacturing Directorate (AFRL/MLLN)
Air Force Research Laboratory
Wright-Patterson Air Force Base
OH 45433-7817
USA

[1] University of Dayton Research Institute, 300 College Park, Dayton, OH 45469-0128, USA.
* Corresponding author

Abstract

The in-plane shear behavior of an oxide/oxide ceramic matrix composite was investigated at 23 and 950°C in lab air. Tests were conducted in tension on specimens with fiber reinforcement oriented at [±45°] to the loading axis. Tensile tests were conducted on specimens 12.6, 25.4 and 38.1 mm wide to examine the effect of specimen width on the in-plane shear behavior. No effect of specimen width was observed. The failed specimen fracture surfaces were examined and the observed damage correlated with the deformation behavior. Results of the in-plane shear tests showed that at 23°C, deformation was highly nonlinear, with a gradual failure of the composite under displacement control. At 950°C, shear stress-shear strain deformation behavior was more linear, with a brittle failure mode. Examinations of the fracture surface profiles showed that at 23°C, matrix disintegration during fracture allowed entire fiber tows to be pulled from the matrix, resulting in a fibrous fracture surface. The slow fiber pullout was consistent with the nonlinear shear deformation behavior. The fracture profiles showed that at 950°C matrix had remained bonded to fiber tows during fracture resulting in short fiber lengths extending from the fracture plane. The damage observed on fracture surfaces indicated that a change in the matrix fracture behavior with temperature resulted in the change in shear deformation behavior.

Keywords: ceramic matrix composites, in-plane shear, elevated temperature, oxide/oxide

Introduction

Ceramic matrix composites (CMC) consisting of an oxide matrix and oxide fibers with no engineered fiber-matrix interphase are currently under consideration for high temperature aerospace applications due to their inherent resistance to oxidation. Oxide/oxide CMC produced with no fiber-matrix interphase utilize a weak, friable matrix which offers a low energy crack path throughout the matrix [1-3]. For this class of CMC, nearly all the load is supported by the fibers. The nearly linear stress-strain behavior exhibited by these composites in the [0°/90°] orientation is typical of fiber dominated composites [3-7]. In contrast, the notched fracture behavior is highly nonlinear due to stress redistribution around the notch during loading [6-9]. Prior studies have shown that nonlinear shear stress-shear strain behavior results in nonlinear notched fracture behavior [6-9]. However, studies that have examined the in-plane shear behavior of oxide/oxide ceramic composites are limited. Furthermore, the effect of temperature on the notched fracture behavior is highly dependent on the in-plane shear response at that temperature. In the current study, the in-plane shear response of an oxide/oxide CMC was examined at 23°C and 950°C. The effect of specimen width was also examined. The measured deformation behavior will be correlated with observed damage on the fracture surfaces.

Experimental Procedure

The Nextel610/alumina-silica (N610/AS) CMC used in this investigation was produced by General Electric Aircraft Engines (GEAE) under the product name Gen IV. The Nextel610 fibers, produced by the 3M Company [10], consisted of polycrystalline alpha alumina. The fibers were bundled into tows containing approximately 400 individual fibers, and woven into an eight harness satin weave (8HSW) cloth. The composite panel used in this study contained either 6 or 12 plies. The matrix consisted of a porous alumina-silica (AS) matrix. Fiber volume fraction was 33%. Extensive microcracking was present throughout the matrix as a result of the shrinkage that occurred during the pyrolysis processing (Fig. 1). These microcracks are distributed throughout the interior matrix as well as on the specimen surface. The resulting composite contains matrix that is weakly bonded to the fibers, with no naturally occurring or engineered interphase. Further details of the composite processing and microstructure are discussed in [4,5,9].

In-plane shear response was measured on straight sided specimens with the fiber orientation [±45°] relative to the loading axis. The specimen ends were rigidly clamped using friction grips, thus resulting in rotationally constrained end conditions. During the room temperature tests, longitudinal strain was measured using a high resolution, knife edge extensometer, or foil type strain gages (Fig. 2a). Transverse strains were measured using transversely mounted strain gages. The standard foil strain gages used were 8 mm in gage length and 4 mm in width. At 950°C a high temperature extensometer, with quartz rods, was used to measure longitudinal strains (Fig. 2b). Transverse strains were measured using a high temperature extensometer modified to measure lateral contraction of the specimen during loading. Accuracy of the modified extensometer was checked at room temperature using foil strain gages.

All mechanical testing was conducted in lab air, using a servo-controlled, hydraulic, horizontal test system [11,12]. Elevated temperature tests were conducted using closed-loop controlled, four zone quartz lamps to heat the specimen. Further details of the test equipment have been described elsewhere [11,12].

In-plane shear tests were conducted under load-line displacement control at a rate of 0.001 mm/s. Applied axial stress, axial and transverse strain gage output and load-line displacement (δ) were recorded continuously as a function of time during all tests. Shear stress was calculated from the applied axial stress (σ_a) as $\tau = \sigma_a/2$. Shear strain (γ) was calculated from the longitudinal strain (ε_L) and transverse strains (ε_T) as $\gamma = \varepsilon_L - \varepsilon_T$. Poisson's ratio was calculated from the measured longitudinal and transverse strains as $\nu_{45} = -\varepsilon_T/\varepsilon_L$. Shear modulus ($G_{12}$) was calculated from the initial loading behavior, up to approximately $\sigma_a = 5$ MPa.

Results and Discussion

In-Plane Shear Behavior at 23°C

The longitudinal stress versus longitudinal strain behavior for a specimen 12.6 mm in width is shown in Fig. 3. Several loading-unloading loops were measured during the tension test to examine the accumulation of residual strains. As shown in the figure, the highly nonlinear loading behavior resulted in residual strains after unloading prior to and after the peak load. Nonlinear shear deformation in oxide/oxide CMC with a [±45°] orientation is consistent with the results previously reported by Zawada et al. [4], Heathcote et al. [13] and Carelli et al. [14]. The nonlinear deformation behavior continued under increasing load-line displacement control as the fiber tows were gradually pulled from the matrix. After reaching the peak load, the specimen slowly separated into two pieces as the load bearing capacity decreased.

A comparison of the longitudinal stress-longitudinal strain behavior for specimens with various widths is shown without unloading loops in Fig. 4. The in-plane shear behavior for each specimen is nearly identical indicating negligible effect of specimen width on the overall shear behavior of the composite. Using the initial linear region of the loading behavior the shear modulus was calculated for each specimen as shown in Table 1. Similar values for the shear modulus and peak shear stress for the three specimen widths indicated that the observed shear behavior is not a function of width over the range of specimen sizes examined. The average shear modulus for all specimens tested was 16 GPa.

The specimen widths can also be compared to the repeat unit of the fiber architecture for the N610/AS composite. The fiber tows in the composite are approximately 1 mm wide; therefore, a repeat unit for the 8HSW composite would be approximately 8 mm wide. All specimen widths used in the current study exceed the minimum repeat unit width. These results indicate that the in-plane shear behavior is independent of specimen width for widths at least 1.5 times the repeat distance.

The room temperature deformation behavior of the N610/AS composite examined in the current study was also compared to that of two other oxide/oxide CMC. Using the same experimental procedures discussed above, an in-plane shear test was conducted on an oxide/oxide CMC produced by COI Ceramics, Inc. (COIC). The COIC composite consisted of a porous alumina-silica matrix and an 8HSW Nextel720 fiber reinforcement (N720/AS-1). Further details of the COI composite can be found in [15]. The [±45°] stress-strain behavior for the N720/AS-1 and the N610/AS composites are compared in Fig. 5. The plot shows that the overall deformation behavior for the two oxide/oxide CMC is nearly identical. Thus, as expected the effect of fiber reinforcement on the shear behavior is minimal. A comparison is also made in the figure to the results of Heathcote et al. [13] on another porous matrix oxide/oxide CMC. The composite tested by Heathcote et al. contained an 80% mullite, 20% alumina matrix reinforced with an 8HSW Nextel 610 fiber cloth (N610/AM). The results of that study showed similar nonlinear in-plane shear behavior with significant shear strain accumulation prior to failure. Very similar shear deformation behavior for all 3 brittle matrix oxide/oxide CMC indicates that the deformation behavior is controlled by the matrix behavior.

The results of the room temperature [±45°] tension tests are summarized in Table 1. A comparison of the shear modulus and peak shear stress for all tests shows that there was very little variation in the measured values independent of fiber reinforcement and specimen width. As previously discussed, the composite properties in the fiber direction are controlled by the fiber elastic modulus and strength distribution. In contrast, off-axis properties such as in-plane shear are controlled by the matrix properties. Oxide/oxide CMC consisting of a weak porous matrix offer little resistance to deformation away from the fiber direction. Thus, any loading condition that results in off-axis stresses, such as around notches and attachment points, will be affected by the shear properties of the composite. Hence, reliable design of oxide/oxide CMC components requires an understanding of the effect of temperature and environment on matrix properties becomes critical.

In-Plane Shear Behavior at 950°C

The [±45°] in-plane stress-strain response of the N610/AS composite at 950°C is shown in Fig. 6. In comparison to the room temperature behavior, the shear deformation behavior at 950°C was nearly linear prior to the maximum stress. Unloading the specimen from a stress below the peak further emphasized the linear deformation behavior as the unloading loops exhibited no significant hysteresis or residual strain. A comparison between the longitudinal and transverse [±45°] deformation behavior at 23°C and 950°C is shown without the unloading loops in Fig. 7. The nearly linear stress-strain behavior observed at 950°C is in contrast to the highly nonlinear behavior observed at 23°C. The change in deformation behavior with temperature was reflected by the increase in the shear modulus from 16 at 23°C to 23 GPa at 950°C (Table 1). The increase in peak shear stress indicates that the matrix strength increased with temperature. An increase in peak shear strength of 27 to 36 MPa with temperature from 23-1100°C was also observed by Zawada et al. [4]. In Ref. [4], interlaminar shear strength was also measured as a function of temperature and found to increase from 12 MPa at 23°C to ≈ 20 MPa at 1100°C, respectively. Interlaminar shear is a good measure of the matrix strength and clearly indicates the AS matrix in this CMC has undergone an increase in shear strength.

The effect of temperature on the deformation behavior was also examined by comparing the change in Poisson's ratio as a function of applied stress. Figure 8a shows that at room temperature the Poisson's ratio was approximately 0.3 in the initial linear loading region. With further loading, inelastic strains accumulated in both the longitudinal and transverse directions as the fibers twist to align with the loading direction. The increasing inelastic strains resulted in an increase in the measured Poisson's ratio up to a maximum value ≈ 0.65 at the peak stress. In contrast, Fig. 8b shows that at 950°C Poisson's ratio was more nearly constant at a value of ≈ 0.5, independent of applied stress. The constant value of Poisson's ratio further supports the more linear deformation behavior at 950°C and indicates a change in the failure mode of the composite between the two temperatures.

The more linear deformation behavior at 950°C was due to a change in the failure mode of the composite. Abrupt failure occurred at a maximum shear stress of 32 MPa with no post peak deformation. Brittle failure of the composite at 950°C is in sharp contrast to the gradual failure that occurred at 23°C. The differences in deformation behavior with temperature are also reflected by differences that were observed on the failed fracture surfaces as discussed below.

A comparison of the fracture surface profiles shows the differences in matrix cracking behavior at 950°C and 23°C (Fig. 9). At 23°C, multiple matrix cracking within the plies and between fiber tows allowed the fiber tows to be pulled from the composite without breaking (Fig. 9a,c). Brittle failure of the weak friable matrix is critical in this class of CMC to allow for redistribution of stresses along the fiber length. This type of damage mode resulted in long exposed fiber lengths, with little matrix remaining attached to the fibers. In contrast, at 950°C, the matrix did not readily break away from the individual fibers or tows, suggesting an increase in clamping stress of the matrix around the fiber. As a result of the change in matrix behavior at temperature, individual fibers and tows remained bonded to the matrix and fibers were broken in groups of fibers (Fig. 9b,d). The growth of a localized fracture plane at 950°C, resulted in a less fibrous failure mode. Thus, the lack of distributed matrix cracking between fibers within the tows, and between tows at 950°C resulted in a change in damage mechanism from that observed at 23°C. The difference in matrix cracking behavior resulted in the change in the shear deformation behavior. Some additional discussion of the damage progression for on axis N610/AS composites at 23°C and 950°C can be found in [8,9,16].

The change in composite failure mode, and hence off axis composite properties, at elevated temperature is significant. Although uniaxial tension, fatigue and sustained loading tests conducted on specimens in a [0°/90°] orientation provide valuable information regarding ultimate strength and long term durability, real world component applications inevitably result in off-axis loading conditions. Similarly, performance of the composite with the introduction of attachments, often including notches or holes, will depend on the in-plane shear response at temperature. The detrimental effect of temperature on the notched properties was previously examined in N610/AS by Kramb et al. [8,9,16] and in N720/AS by Antti et al. [17]. A complete understanding of the effect of temperature on the matrix fracture properties, and hence off-axis composite properties will require further studies, such as those conducted by Mattoni et al. [18] and Carelli et al. [19].

Summary and Conclusion

The results of the in-plane shear tests showed that the shear response and matrix damage in Nextel610/AS CMC were temperature dependent. At 23°C, shear modulus was ≈ 16 GPa, with a peak shear stress ≈ 28 GPa. The shear stress-shear strain behavior was highly nonlinear at 23°C, with extensive fiber pullout along the fracture surfaces. Examination of the fracture surfaces showed that extensive matrix cracking within the plies resulted in a graceful failure mode under load-line displacement control. A comparison of the in-plane shear response for three different porous matrix oxide/oxide CMC showed no significant differences in shear modulus, shear strength or deformation behavior. Similar shear properties between all three oxide/oxide CMC further indicated that the brittle matrix properties control the in-plane shear behavior.

At 950°C the in-plane shear modulus was 28 GPa, with a shear strength of 32 GPa. The shear stress-shear strain deformation behavior at 950°C was nearly linear, with a brittle failure after reaching the peak stress. Examinations of the fracture surface profiles showed that the fibers failed in groups along a single plane. The fiber failure within a tow is in contrast to in contrast to the individual fiber failure behavior observed at 23°C. The failure of fibers as groups rather than individually at temperature indicated a change in the matrix-fiber clamping stress from 23°C to 950°C. This change in matrix behavior resulted in a change in the overall composite shear deformation and fracture behavior.

Acknowledgments: This research was conducted at the Materials and Manufacturing Directorate, Air Force Research Laboratory (AFRL/MLLMN), Wright-Patterson Air Force Base, OH 45433-7817. V. A. Kramb was supported in part by the Dayton Area Graduate Studies Institute (DAGSI) and in part by AFOSR/AASERT Program (Contract No. F49620-95-1-0500). Mr. Buchanan was supported under an onsite contract number F33615-98-C-5214.

References

1. Lu TJ, Crack branching in all-oxide ceramic composites. J Am Ceram Soc 1996;79(1): 266-74.
2. Tu WC, Lange FF, Evans AG, Concept for a damage-tolerant ceramic composite with "strong" interfaces. J Am Ceram Soc 1996;79(2): 417-24.
3. Levi CG, Yang JY, Dalgleish BJ, Zok FW, Evans AG, Processing and performance of an all-oxide ceramic composite, J Am Ceram Soc 1998;81(8): 2077-86.
4. Zawada, LP, Hay RS, Lee SS, Staehler J, Characterization and high temperature mechanical behavior of an Oxide/Oxide composite. submitted for publication J Am Ceram. Soc 2002.
5. Zawada LP, Lee SS. Evaluation of four CMCs for aerospace turbine engine divergent flaps and seals. Ceram Eng Sci Proc 1995;16(4): 337-39.
6. Heredia FE, Spearing SM, Mackin TJ, He MY, Evans AG. Notch effects in carbon matrix composites. J Am Ceram Soc 1994;77(11): 2817-27.
7. Mackin TJ, Purcell TE, He MY, Evans AG. Notch sensitivity and stress redistribution in three ceramic-matrix composites. J Am Ceram Soc 1995;78(7): 1719-28.
8. Kramb VA, John R, Zawada LP. Notched fracture behavior of an oxide/oxide ceramic matrix composite. J Am Ceram Soc 1999;82(11): 3087-96.
9. Kramb VA. Notched fracture behavior of an oxide/oxide ceramic matrix composite. PhD Thesis, University of Dayton, Department of Materials Engineering, 1999.
10. 3M Company Product Data Sheet, 3M Ceramic Fibers Products, 3M Center-Building 207-1W-11, St. Paul, MN 55144-1000.
11. Hartman GA, Buchanan DJ. Methodologies for thermal and mechanical testing of TMC materials. In: Characterization of fibre reinforced titanium matrix composites. 77th Meeting of the AGARD Structures and Materials Panel, AGARD Report 796, Bordeaux, France, 27-28 September 1993.
12. Hartman DA, Russ SM. Techniques for mechanical and thermal testing of Ti3Al/SCS-6 metal matrix composites. In: Johnson WS, editor. Metal matrix composites: testing, analysis, and failure modes, ASTM STP 1032, American Society for Testing and Materials, Philadelphia, PA, 1989.
13. Heathcote JA, Gong XY, Yang J, Ramamurty U, Zok FW, In-plane mechanical properties of an all-oxide ceramic composite. J Am Ceram Soc 1999;82(10): 2721-30.
14. Carelli, EAV, Fujita H, Yang JY, Zok FW, Effects of thermal aging on the mechanical properties of a porous-matrix ceramic composite. Accepted for publication J Am Ceram Soc 2001.
15. Buchanan DJ, Kramb VA, John R, Zawada LP, Effect of small effusion holes on creep rupture behavior of oxide/oxide Nextel™720/AS composite. The 25th Annual Cocoa Beach Conference and Exposition, The American Ceramic Society, January 2001.
16. Kramb VA, John R, Stubbs DA, A study of the damage progression from notches in an oxide/oxide ceramic-matrix composite using ultrasonic C-scans, Comp Sci Tech 2001;61:1561-1570.
17. Antti M-L, Lara-Curzio E, Effect of notches, specimen size, and fiber orientation on the monotonic tensile behavior of composites at ambient and elevated temperatures. The 25th Annual Cocoa Beach Conference and Exposition, The American Ceramic Society, January 2001.
18. Mattoni MA, Yang JY, Levi CG, Zok FW, Effects of matrix porosioty on the mechanical properties of a porous-matrix, all-oxide ceramic composite. J Am Ceram Soc 2001;84(11): 2594-602.

19. Donaldson KY, Venkateswaran A, Hasselman DPH, Observations on the crack-enhanced creep-fracture of a polycrystalline alumina with a glassy grain-boundry phase, J. Mat. Sci. 1991;27(16): 4501-10.
20. Choi SR, Tikare V, Crack healing of alumina with a residual glassy phase: strength, fracture toughness and fatigue, Mat. Sci. Eng. 1993;A171 77-83.

Table Captions

Table 1. In-plane shear properties at 23°C.

Figure Captions

Figure 1. Nextel610/AS composite polished cross section optical micrograph.

Figure 2. Test specimens schematic [±45°] tensile test specimen at 23°C specimens were mounted with foil strain gages, (lines within the gages indicate the direction of strain measurement) at 950°C specimens were tested with high temperature extensometers only.

Figure 3. In-plane longitudinal stress-longitudinal strain behavior of N610/AS [±45°] at 23°C. W = 12.6 mm.

Figure 4. Effect of specimen width on tensile stress-strain behavior of N610/AS [±45°] at 23°C. Unloading data is not shown in the plot.

Figure 5. [±45°] tensile stress-strain behavior at 23°C for three different brittle matrix composites. Unloading data is not shown in the plot.

Figure 6. Longitudinal stress-longitudinal strain behavior of N610/AS [±45°] at 950°C. W = 12.6 mm.

Figure 7. Effect of temperature on the longitudinal and transverse deformation behavior on N610/AS [±45°]. Unloading data is not shown in the figure. W = 12.6 mm.

Figure 8. Effect of temperature on Poisson’s ratio of N610/AS [±45°] at (a) 23°C and (b) 950°C.

Figure 9. N610/AS [±45º] tension: fracture surfaces (a) 23°C (b) 1000°C and details of matrix and 0° fiber behavior (c) 23°C (d) 1000°C. W=12.6mm.

Table 1.
[±45] in-plane properties at 23 and 950°C.

Material	Manufacturer	Temperature (°C)	Width (mm)	G_{12} (GPa)	τ_{peak} (MPa)
N610/AS	GEAE	23	12.6	15.3	28
N610/AS	GEAE	23	25.4*	16.9±1.4	27±1.5
N610/AS	GEAE	23	38.1	16.0	32
N720/AS-1	COIC	23	38.1	17.9	32
N610/AM	Heathcote et al. [13]	23	4.9-19.5	16.0	30
N610/AS	GEAE	950	12.6	23	32

*****average of 3 specimens

Figure 1. Nextel610/AS composite polished cross section optical micrograph.

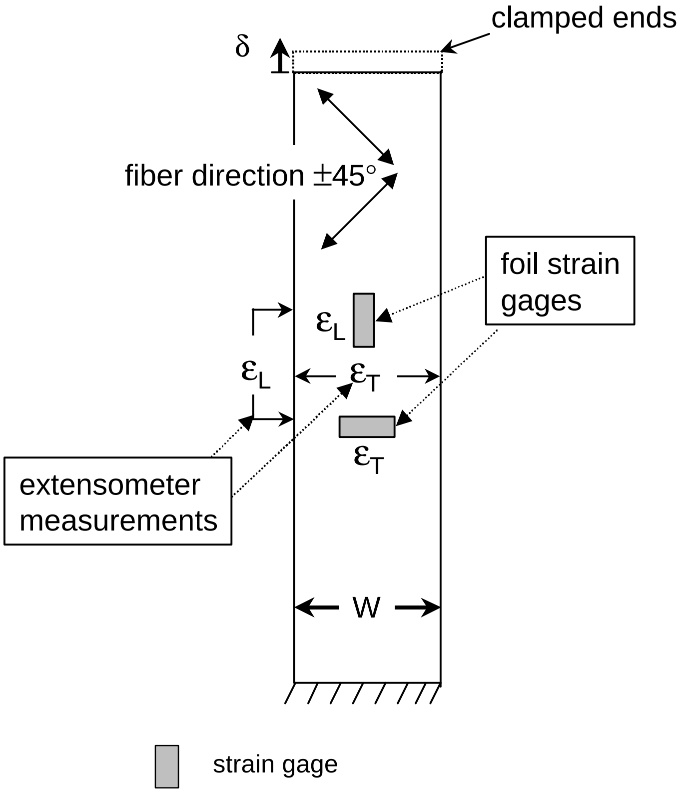

Figure 2. Test specimens schematic [±45°] tensile test specimen at 23°C specimens were mounted with foil strain gages, (lines within the gages indicate the direction of strain measurement) at 950°C specimens were tested with high temperature extensometers only.

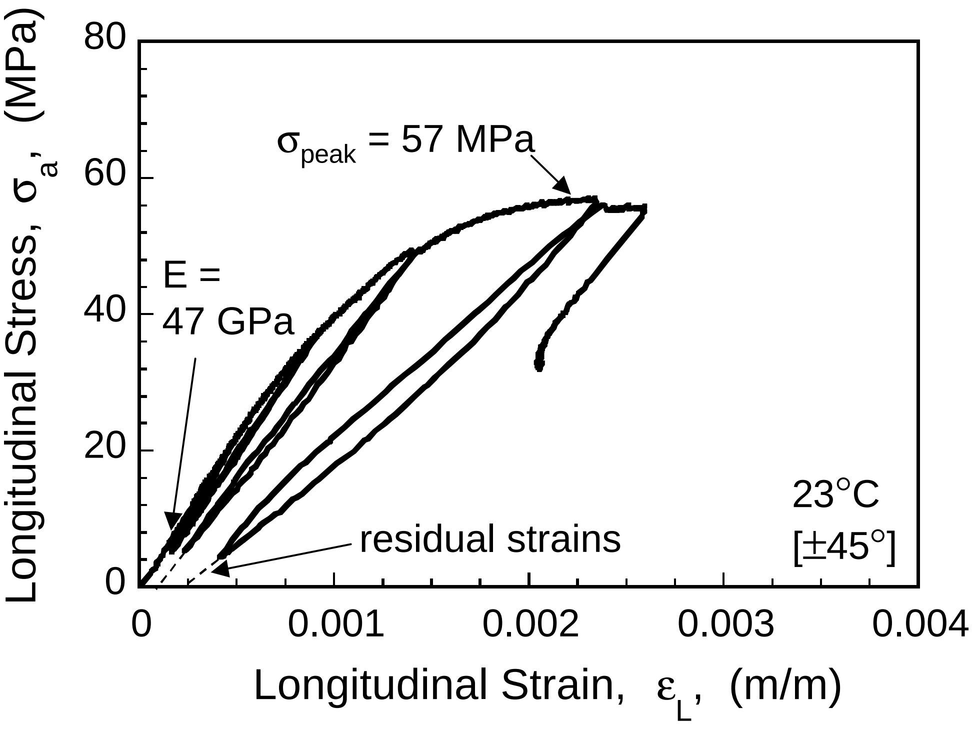

Figure 3. In-plane longitudinal stress-longitudinal strain behavior of N610/AS [±45°] at 23°C. W = 12.6 mm.

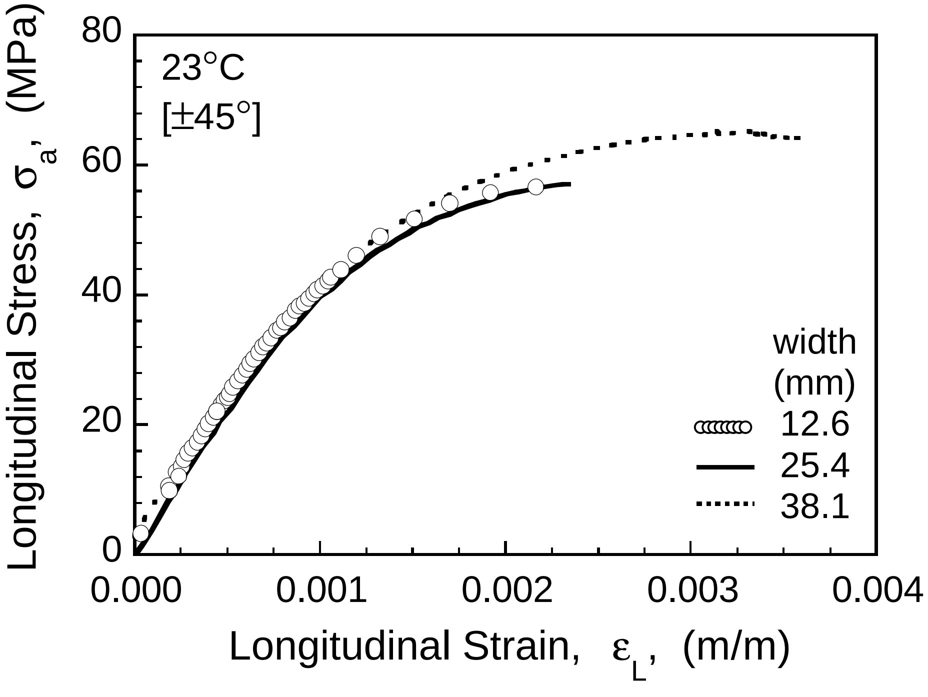

Figure 4. Effect of specimen width on tensile stress-strain behavior of N610/AS [±45°] at 23°C. Unloading data is not shown in the plot.

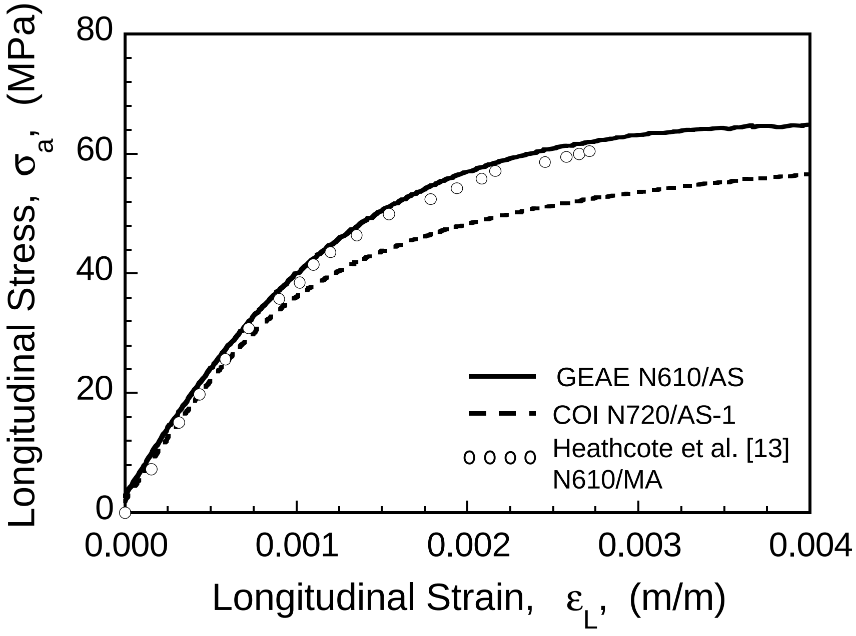

Figure 5. [±45°] tensile stress-strain behavior at 23°C for three oxide/oxide CMC. Unloading data is not shown in the plot.

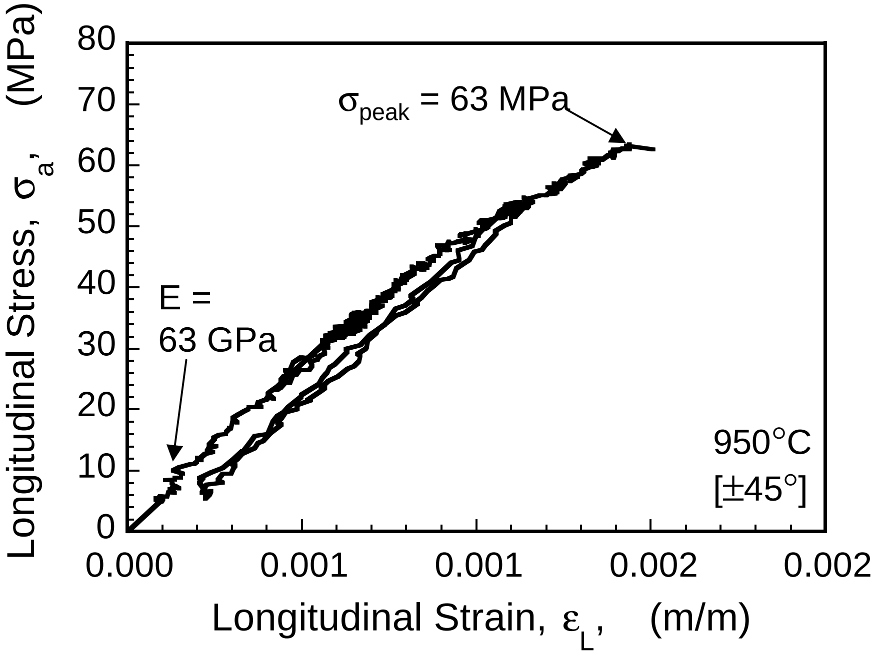

Figure 6. Longitudinal stress-longitudinal strain behavior of N610/AS [±45°] at 950°C. W = 12.6 mm.

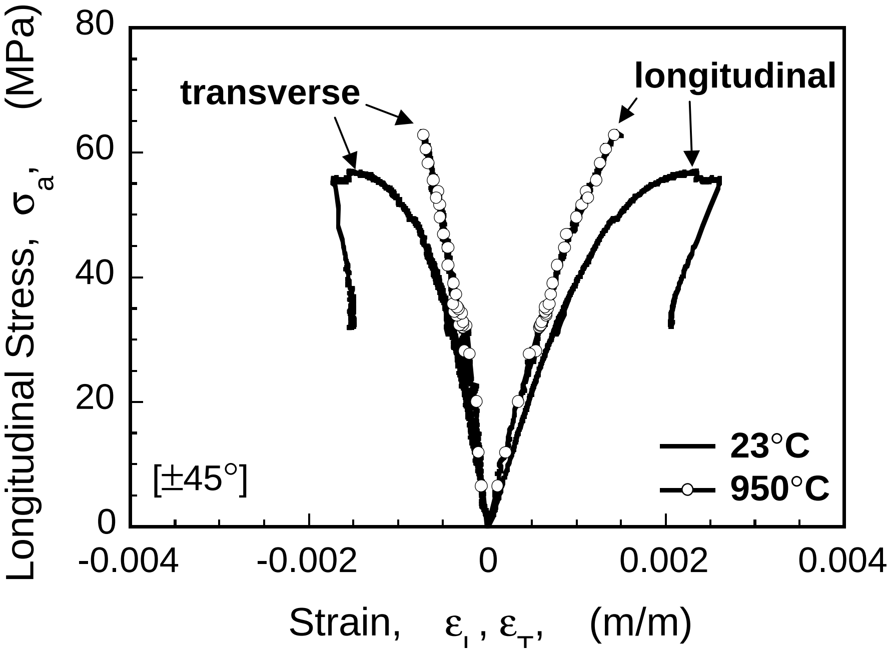

Figure 7. Effect of temperature on the longitudinal and transverse deformation behavior on N610/AS [±45°]. Unloading data is not shown in the figure. W = 12.6 mm.

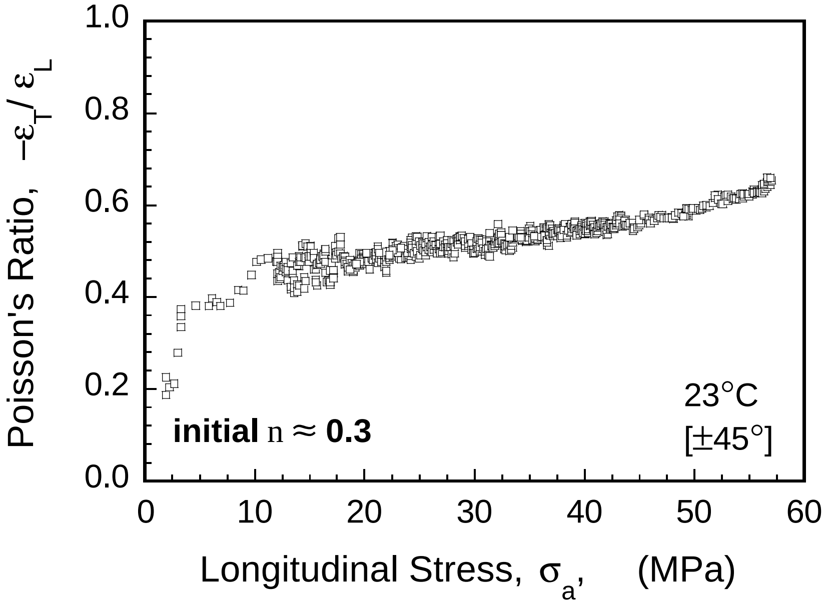

(a)

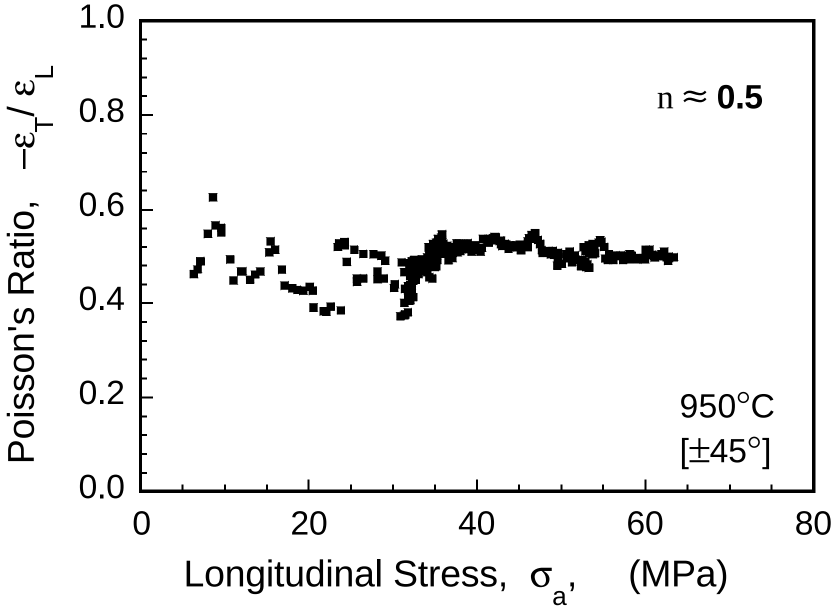

(b)

Figure 8. Effect of temperature on Poisson's ratio of N610/AS [±45°] at (a) 23°C and (b) 950°C.

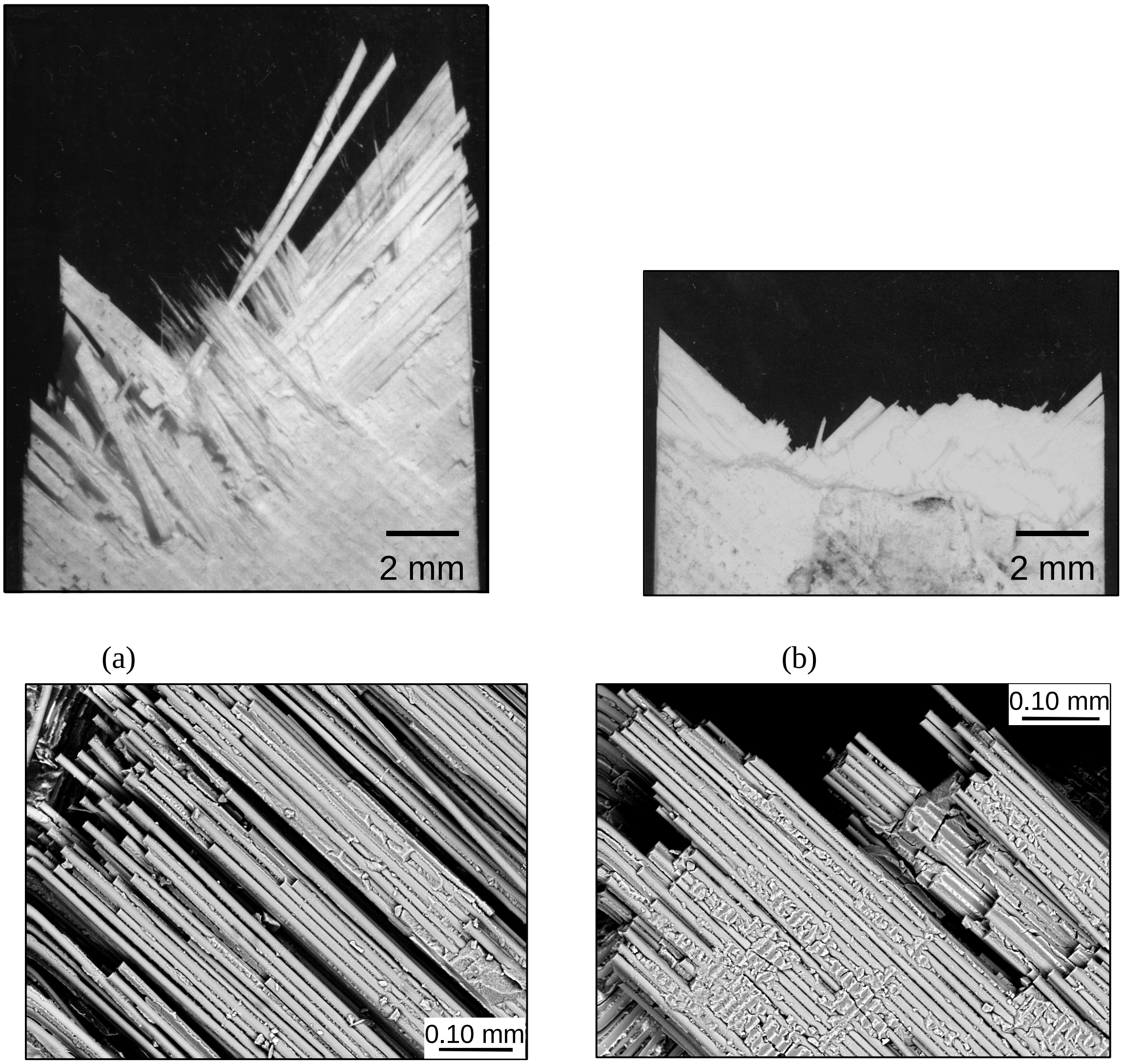

(a) (b)

(c) (d)

Figure 9. N610/AS [±45º] tension: fracture surfaces (a) 23°C (b) 950°C and details of matrix and 45° fiber fracture behavior (c) 23°C (d) 950°C. W=12.6mm.

Proceedings, 10th International Congress of Fracture (ICF10), Honolulu, Hawaii, 3-7 December 2001
Oral Reference: ICF100964OR

FRACTURE AND CREEP RUPTURE BEHAVIOR OF NOTCHED OXIDE/OXIDE AND SiC/SiC CMC

Reji John[1], Dennis J. Buchanan[2] and Larry P. Zawada[1]

[1] Air Force Research Laboratory, Materials and Manufacturing Directorate (AFRL/MLLMN)
Wright-Patterson AFB, OH 45433-7817, USA
[2] University of Dayton Research Institute
Dayton, OH 45419, USA

ABSTRACT

Woven Oxide/Oxide and SiC/SiC ceramic matrix composites (CMC) are targeted for high-temperature aerospace applications such as combustors, combustor liners, exhaust washed structures, exhaust nozzle flaps and seals, and blade outer air seals. Some of these components contain stress concentration sites such as holes and attachment points. During service, these locations will be subjected to long-term exposures. Hence, the knowledge of the effect of sustained (creep) loading on the deformation and rupture of notched Oxide/Oxide and SiC/SiC composites is required for durability assessment. The results from creep tests of unnotched and notched Nextel™720/Alumina-Silica (Nextel™720/AS-0) and Melt Infiltrated (MI) HI-NICALON-Type-S/SiC (MI HI-NICALON-S/SiC) are discussed in this paper. Nextel™720/AS-0 was evaluated at 1100°C and MI HI-NICALON-S/SiC at 1200°C in laboratory air. In the case of large notches, i.e., notch length greater than the average tow size, the notch-sensitivity increased significantly under sustained loading for both composites. Nextel™720/AS-0 specimens with straight-through effusion holes (hole diameter = 0.5 mm) were also subjected to sustained loading at 100MPa/1100°C. In this case, the presence of effusion holes did not affect the overall creep response.

KEYWORDS

ceramic matrix composite, creep, effusion holes, fracture, notch-sensitivity, oxide/oxide, sic/sic, woven cmc

INTRODUCTION

Woven Oxide/Oxide and SiC/SiC ceramic matrix composites are being demonstrated for high-temperature aerospace applications with temperature requirements in the range of 1000-1300°C [1-4]. Current targeted aerospace turbine engine components, such as combustors, combustor liners, divergent flaps and seals, contain bolted attachment points and cooling holes. Local stresses in these regions often exceed the proportional limit of the composite, resulting in damage and crack initiation. Hence, component design using CMC will require knowledge of the notched fracture behavior and damage progression under service thermomechanical loading conditions. Most of the results on the notched behavior of Oxide/Oxide and MI SiC/SiC CMC correspond to monotonic tensile loading [5-14]. Recently, John et al. [8,9] and McNulty et al. [12] studied the effects of long-term loading on notched Oxide/Oxide at 1100°C and MI SiC/SiC at 815°C, respectively. Based on specimens with large notches (i.e., notch length greater than tow size), these studies [8,9,12] reported an increase in notch-sensitivity when exposed to temperature for 100+ hours.

Components such as combustors are designed to contain effusion holes, which are used to lay down a film of cooling air on the hot wall to create a boundary layer effect and to cool the component by providing more internal surface area. The effusion holes are typically of the order of 0.50 mm diameter, which is approximately half the average fiber tow size. This paper summarizes the results of a recent study [10] on the creep behavior of Oxide/Oxide at 1100°C. The results are compared to the creep behavior of specimens with large notches. In addition, the creep behavior of notched MI SiC/SiC at 1200°C is also discussed.

MATERIAL AND EXPERIMENTAL PROCEDURE

The Oxide/Oxide CMC used in this study was Nextel™720/AS-0, which was manufactured by COI Ceramics, Inc., San Diego, CA. Figure 1(a) shows the microstructure of Nextel™720/AS-0. The matrix consists of a porous alumina-silica (AS) that is weakly bonded to the fibers without an engineered interphase. Approximately 400 Nextel™720 fibers were bundled together in tows and woven into a balanced eight-harness-satin weave (8HSW) cloth. The fiber mat had a (0/90) layup with final CMC volume fraction ≈ 0.46.

The SiC/SiC CMC used in this study was HI-NICALON-S/SiC, which was manufactured by Honeywell Advanced Composites, Inc, Newark, DE. Figure 1(b) shows the microstructure of MI HI-NICALON-S/SiC. The matrix is described as Melt-Infiltrated (MI) SiC. The HI-NICALON-Type-S (HI-NICALON-S) fibers were bundled together in tows and woven into a balanced five-harness-satin weave (5HSW) cloth. The fiber mat had a (0/90) layup with final CMC volume fraction ≈ 0.33.

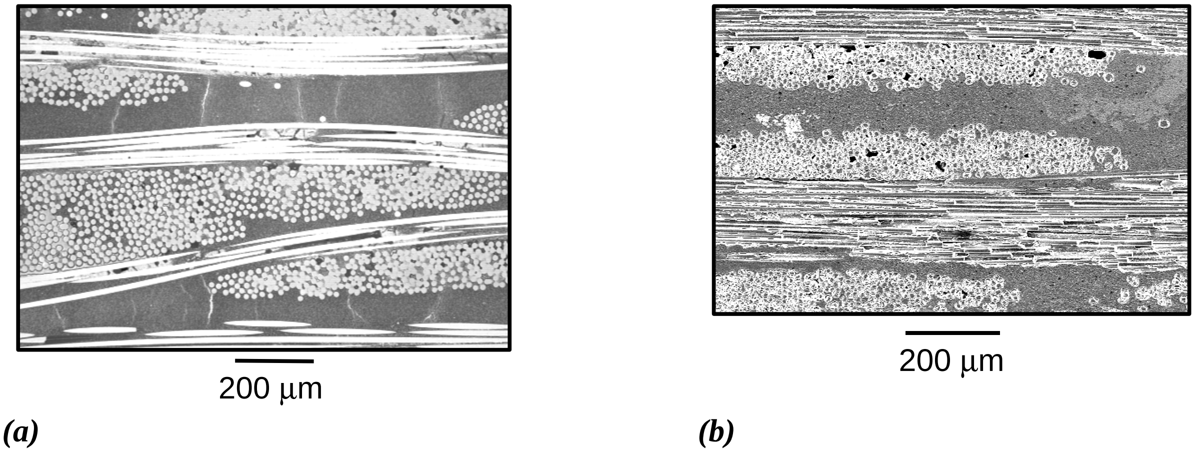

(a) *(b)*

Figure 1: Microstructure of (a) Nextel720/AS-0 and (b) Melt Infiltrated HI-NICALON-S/SiC.

During this study, baseline tensile tests were conducted using dogbone specimens. For the conventional notch sensitivity tests, straight-sided specimens with large notches (notch length greater than the average tow size) were used. Semi-circular notches, DEH(T) and sharp notches, DE(T) were used during this study, Figure 2(a). The semi-circular and sharp notches were machined using a drill and a thin diamond saw (≈ 0.1 mm thick), respectively. In all these tests, the notch mouth opening displacement (NMOD) was measured. Figure 2(b) shows the effusion hole patterns used for this study. The nominal dimensions of the specimens were, width (W) = 10.0 mm in gage section, thickness (B) ≈ 2.5 mm and gage length ≈ 12.5 mm. All effusion holes were 0.5 mm in diameter with the hole axis perpendicular to the loading axis. The hole density studied in this investigation was ≈ 8 holes/cm^2 (≈ 50 holes/in^2).

The specimens were measured and photographed to document the condition of the holes prior to testing. The specimen ends were tabbed with fiberglass tabs to provide a flat uniform surface for the smooth grip surfaces and to minimize the possibility of grip failure. The specimens were mounted in a precisely aligned, rigid grip system that minimized specimen bending and rotation. A clamshell furnace with SiC heating elements and four-zone control were used for the elevated temperature creep tests. Thermal profile maps on the specimen showed that the specimen was uniformly heated, ± 0.6%, over the entire gage section of the specimen. All creep tests were loaded to the maximum stress at a loading rate of 20 MPa/s.

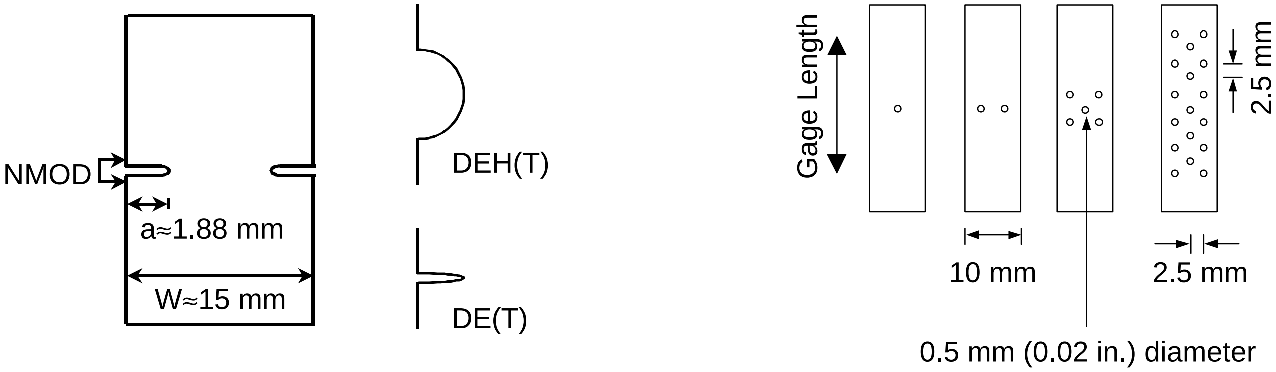

(a) CMC: Nextel™720/AS-0 & MI HI-NICALON-S/SiC

(b) CMC: Nextel™720/AS-0

Figure 2: Schematic of (a) double edge notched, and (b) effusion hole specimens.

RESULTS AND DISCUSSION

The unnotched tensile behaviors of Nextel™720/AS-0 and MI HI-NICALON-S/SiC are shown in Figures 3(a) and 3(b), respectively. Nextel™720/AS-0 exhibits nearly linear behavior until failure at 23 and 1100°C with insignificant temperature dependence. The proportional limit (PL), defined as deviation from initial linear response, for Nextel™720/AS-0 was ≈ 75 and 80 MPa at 23°C and 1100°C, respectively. In contrast, MI HI-NICALON-S/SiC exhibits bi-linear response at 23°C and 1200°C with significantly higher ultimate tensile strength (UTS) than that of Nextel™720/AS-0. The PL for MI HI-NICALON-S/SiC was ≈ 145 and 150 MPa at 23°C and 1200°C, respectively.

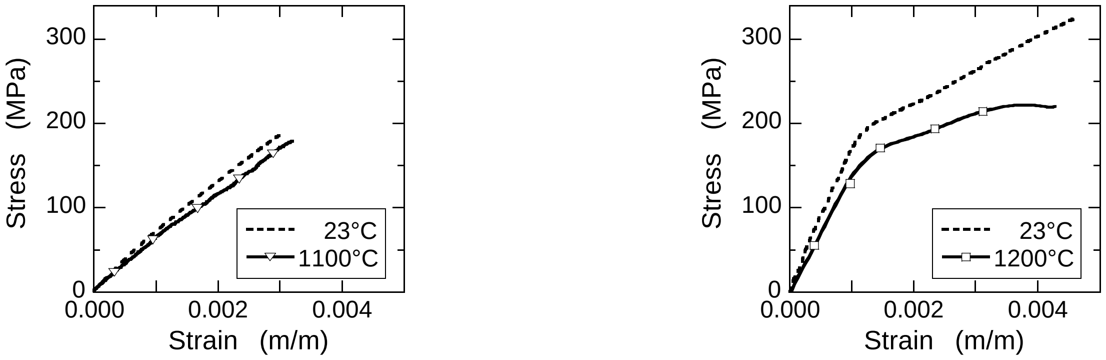

(a) *(b)*

Figure 3: Tensile behavior of (a) Nextel™720/AS-0 and (b) Melt Infiltrated HI-NICALON-S/SiC.

The net-section strength normalized with respect to the corresponding unnotched UTS versus notch length is plotted in Figures 4(a) and 4(b) for Oxide/Oxide and MI SiC/SiC systems, respectively. At room temperature, Nextel™720/AS-0 [This study, 11] is notch-insensitive while Nextel™610/MA [5] is notch-sensitive. At 1100°C, Nextel™720/AS-0 exhibits mild notch-sensitivity (≈15%) at notch length (2a) ≈ 4.5 mm. At room temperature, MI HI-NICALON-S/SiC from this study exhibits slight notch-sensitivity, similar to that reported by McNulty et al. [12,13] and Morscher et al. [14] for other SiC/SiC composites. At 815°C, MI Sylramic/SiC exhibited notch-sensitivity similar to that at room temperature [12]. In contrast, MI HI-NICALON-S/SiC was notch-insensitive at 1200°C.

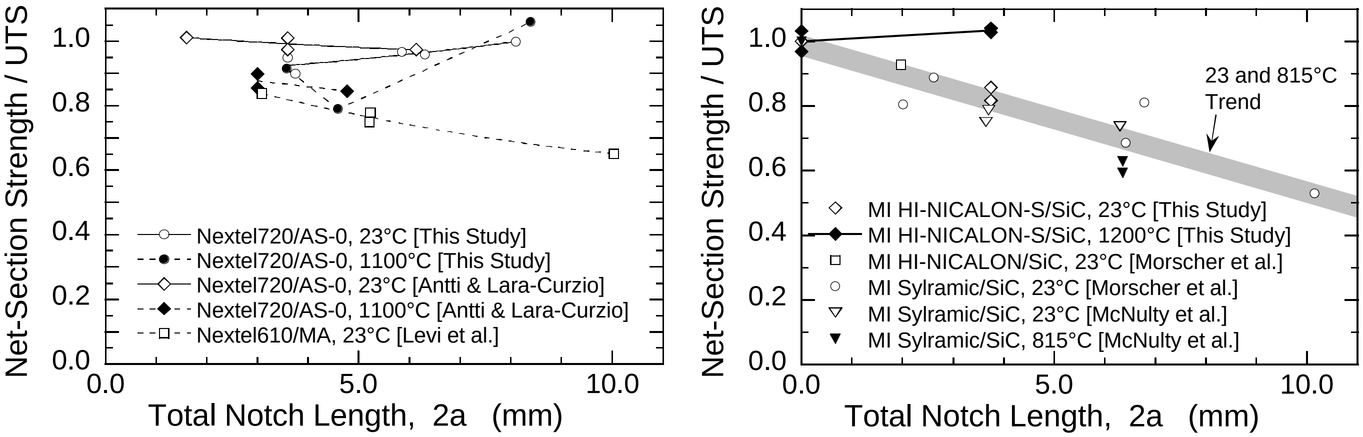

(a) *(b)*

Figure 4: Notch sensitivity of (a) Nextel™720/AS-0 and (b) MI HI-NICALON-S/SiC under tensile loading.

The notched strength data shown in Figure 4 for Oxide/Oxide and MI SiC/SiC systems correspond to short-duration tensile tests. During service, the CMC components will be subjected to long-term thermomechanical loading. Hence, durability assessment of such long-life components require knowledge of the notched behavior under long-duration test conditions. Sustained loading (creep) ***tests*** were conducted on unnotched and notched Nextel™720/AS-0 and MI HI-NICALON-S/SiC specimens at 1100°C and 1200°C, respectively, Figure 5.

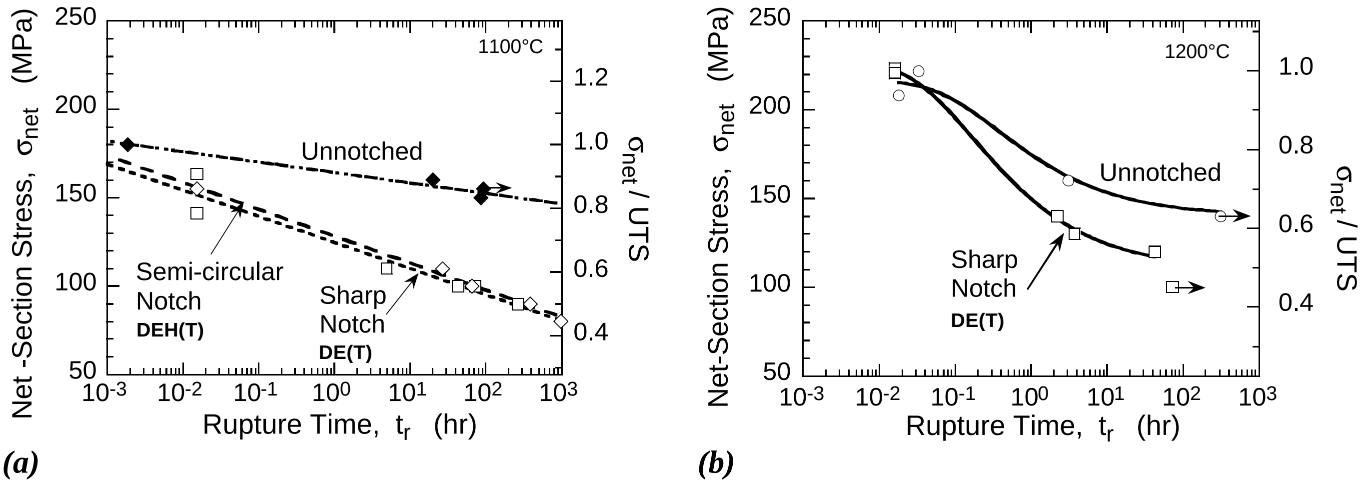

Figure 5: Notch effects on creep rupture behavior of (a) Nextel™720/AS-0 and (b) MI HI-NICALON-S/SiC.

The unnotched Nextel™720/AS-0 shows excellent creep strength of ≈ 150 MPa which is ≈80% of UTS and well above the PL≈80 MPa. Unnotched MI HI-NICALON-S/SiC also shows similar creep strength (≈150 MPa) which is close to the PL. Hence, the maximum design stress for long-life components (with no notches) is similar for both Nextel™720/AS-0 and MI HI-NICALON-S/SiC. When large notches (notch length ≈ 2 mm) are introduced, the net-section stress that can be sustained by the composite at 100+ hours decreases significantly. For Nextel™720/AS-0, the notch strength decreased to ≈ 85 MPa, which is close to the unnotched proportional limit. This decrease is independent of the type of notch. For MI HI-NICALON-S/SiC, the notch strength decreased to 110 MPa, which is ≈ 73% of PL. These results are summarized in Table 1. Also shown in Table 1 are the 815°C results from McNulty et al. [12] based on low-cycle fatigue tests with a 2 hour dwell time. At 815°C, the reduction in notch strength is greater than that observed at 1200°C. These results show that design of long-life components with stress concentration sites should be based on careful detailed durability assessment studies with sub-elements simulating the actual features.

TABLE 1
CREEP STRENGTH OF NEXTEL™720/AS-0 AND MI HI-NICALON-S/SiC

Creep Strength at rupture time = 100+ hr [This study]			LCF Threshold [McNulty et al.]
Geometry	Nextel™720/AS-0 at 1100°C	MI HI-NICALON-S/SiC at 1200°C	MI Sylramic/SiC at 815°C
Unnotched	≈ 150 MPa	≈ 150 MPa	165 MPa
Notched	≈ 85 MPa	≈ 110 MPa	60-85 MPa

Since the large notch specimens exhibited significantly increased notch-sensitivity under sustained loading in contrast to the short-duration tensile loading, a program was initiated to evaluate the performance of specimens with effusion holes under creep loading. The creep behavior of Nextel™720/AS-0 with effusion holes (8 holes/cm^2) is shown in Figure 6. The overall creep deformation is similar to that of the unnotched specimen. Following the creep tests, retained strength tests were conducted at room temperature and compared with the unnotched tensile behavior in Figure 7. The stress-strain response of specimens with effusion holes is identical to that of unnotched material. The decrease in UTS is similar to that observed for unnotched specimens. Hence, under creep loading conditions, Nextel™720/AS-0 with effusion holes @ 8 holes/cm^2 could be expected to respond similar to the unnotched composite. Additional tests are in progress to understand the effect of higher stress levels on the creep behavior of specimens with effusion holes and the relationship between hole size and notch-sensitivity.

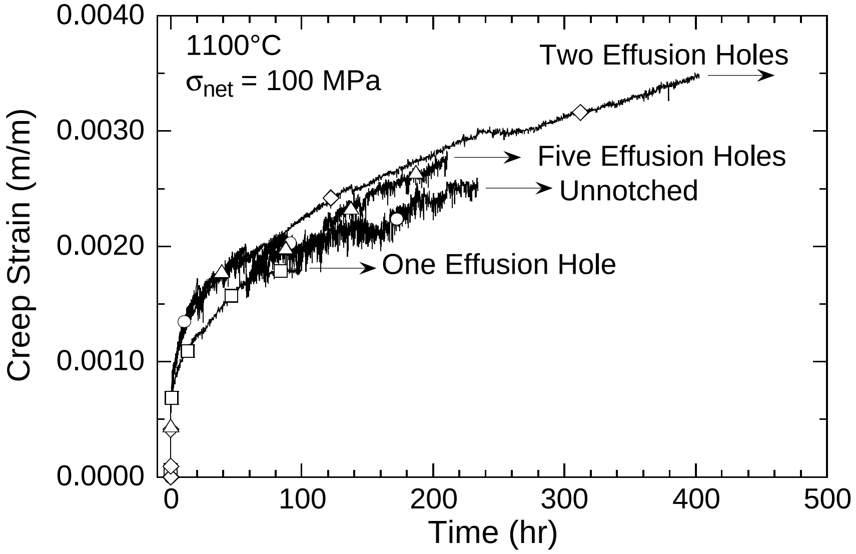

Figure 6: Creep deformation of Nextel™720/AS-0 specimens with effusion holes.

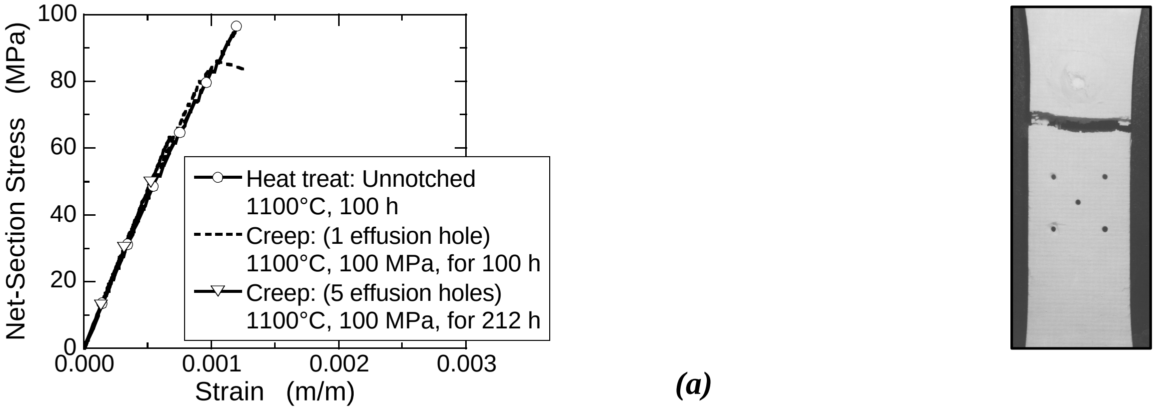

(a) *(b)*

Figure 7: (a) Retained strength (@23°C) of creep-tested Nextel™720/AS-0 specimens with effusion holes. (b) Fracture profile of effusion hole specimen after retained strength test.

CONCLUSIONS

Notch-sensitivity of woven Nextel™720/AS-0 and MI HI-NICALON-S/SiC with (0/90) layup increases significantly under sustained (creep) loading conditions. The creep strength (in terms of net-section stress) decreases ≈ 40% and 27% for Nextel™720/AS-0 and MI HI-NICALON-S/SiC, respectively. The creep behavior of Nextel™720/AS-0 with effusion holes (8 holes/cm^2) was similar to that of the unnotched composite.

ACKNOWLEDGMENTS

This research was conducted at the Air Force Research Laboratory, Materials and Manufacturing Directorate (AFRL/MLLMN), Wright-Patterson Air Force Base, OH 45433-7817 and was supported in part by the Air Force Office of Scientific Research under task 23061P10 (Program Manager: Dr. Craig Hartley). Mr. Buchanan was supported under an onsite contract number F33615-98-C-5214.

REFERENCES

[1] IHPTET Brochure, Turbine Engine Division, Propulsion Directorate (AFRL/PRT), Air Force Research Laboratory, Wright-Patterson Air Force Base, OH, USA.
[2] Brewer D. (1999) *Materials Science and Engineering A* 261, 284.
[3] Ohnabe, H., Masaki, S., Onozuka, M., Miyahara, K., and Sasa, T. (1999) *Composites: Part A* 30, 489.
[4] Zawada, L.P. and Lee, S.S. (1995) *Ceramic Engineering and Science Proceedings* 16, 337.
[5] Levi, C.G., Yang, J.Y., Dalgleish, B.J., Zok, F.W. and Evans, A.G. (1998) *Journal of the American Ceramic Society*, 81, 2077.
[6] Heathcote, J.A., Gong, X.-Y, Yang, J., Ramamurty, U., and Zok, F.W. (1999) *Journal of the American Ceramic Society*, 82, 2721.
[7] Kramb, V.A., John, R., and Zawada, L.P. (1999) *Journal of the American Ceramic Society* 82, 3087.
[8] John, R., Buchanan, D.J., and Zawada, L.P. (2000) *Ceramic Eng. and Science Proceedings* 21, 567.
[9] John, R., Buchanan, D.J. and Zawada, L.P. (2000) *STP 1392 ASTM* 172.
[10] Buchanan, D.J., Kramb, V.A., John, R., and Zawada, L.P. (2001) *Ceramic Engineering and Science Proceedings* Accepted.
[11] Antti, M-L. and Lara-Curzio, E. (2001) *Ceramic Engineering and Science Proceedings* Accepted.
[12] McNulty, J.C., He, M.Y., Zok, F.W. (2001) *Composites Science and Technology* Accepted.
[13] McNulty, J.C., Zok, F.W., Genin, G.M., and Evans, A.G., (1999) *J. of the Am. Cer. Soc.* 82, 1217.
[14] Morscher, G., Gyekenyesi, J.Z., and Gyekenyesi, A.L., (2001) *Proceedings of 46th ASME IGTI.*

Ceramic Engineering & Science Proceedings, 26th Annual Conf. on Composites, Advanced Ceramics, Matls., and Structures:A, The American Ceramic Society, Westerville, OH, 2002. Paper No.ECD2-L-02.

CREEP RUPTURE BEHAVIOR OF OXIDE/OXIDE NEXTEL™720/AS AND MI SiC/SiC COMPOSITES WITH EFFUSION HOLES

Reji John[1], Dennis J. Buchanan[2], Victoria A. Kramb[2] and Larry P. Zawada[1]

1 Air Force Research Laboratory, Materials and Manufacturing Directorate (AFRL/MLLMN), Wright-Patterson AFB, OH 45433-7817, USA

2 University of Dayton Research Institute, Dayton, OH 45419, USA

ABSTRACT

Woven Oxide/Oxide and SiC/SiC ceramic matrix composites (CMC) are targeted for high-temperature aerospace applications such as combustors, combustor liners, exhaust washed structures, exhaust nozzle flaps and seals, and blade outer air seals. Some of these components contain stress concentration sites such as holes and attachment points. Components such as combustors may also include effusion holes, which are used to lay down a film of cooling air on the hot wall to create a boundary layer effect and to cool the component by providing more internal surface area. During service, these locations will be subjected to long-term exposures and thermal stresses. Hence, the knowledge of the effect of sustained (creep) loading on the deformation and rupture of notched oxide/oxide and SiC/SiC composites is required for durability assessment. The results from creep tests of unnotched and notched Nextel™720/Alumina-Silica (Nextel™720/AS-0) and Melt Infiltrated (MI) SiC/SiC are discussed in this paper. Nextel™720/AS-0 was evaluated at 1100°C and SiC/SiC at 982°C and 1200°C in laboratory air. In the case of large notches, i.e., notch length greater than average tow size, the notch-sensitivity increased significantly under sustained loading for both composite. Under sustained loading, the effusion hole (diameter less than tow size) specimens also exhibited notch-sensitivity comparable to that of specimens with large notches.

INTRODUCTION

Woven oxide/oxide and SiC/SiC ceramic matrix composites are being demonstrated for high-temperature aerospace applications with temperature requirements in the range of 1000-1300°C [1-4]. Current targeted aerospace turbine engine components, such as combustors, combustor liners, divergent flaps and seals, contain bolted attachment points and cooling holes. Local stresses in these regions often exceed the proportional limit of the composite, resulting in damage and crack initiation. Hence, component design using CMC will require knowledge of the notched fracture behavior and damage progression under service thermomechanical loading conditions. Most of the results on the notched behavior of Oxide/Oxide and MI SiC/SiC CMC correspond to monotonic tensile loading [5-14]. Recently, John et al. [8,9] and McNulty et al. [12] studied the effects of long-term loading on notched Oxide/Oxide at 1100°C and Melt Infiltrated SiC/SiC at 815°C, respectively. Based on specimens with large notches (i.e., notch length greater than tow size), these studies [8,9,12] reported an increase in notch-sensitivity when exposed to temperature for 100+ hours.

Components such as combustors are designed to contain effusion holes, which are used to lay down a film of cooling air on the hot wall to create a boundary layer effect and to cool the component by providing more internal surface area. The effusion holes are typically of the order of 0.50 mm diameter, which is approximately half the average fiber tow size. This paper discusses the results of an investigation of the creep behavior of Oxide/Oxide and SiC/SiC composites with effusion holes. The results are compared to the creep behavior of specimens with large notches.

MATERIAL AND EXPERIMENTAL PROCEDURE

The Oxide/Oxide CMC used in this study was Nextel™720/AS-0, which was manufactured by COI Ceramics, Inc., San Diego, CA. Figure 1(a) shows the microstructure of Nextel™720/AS-0. The matrix consists of a porous alumina-silica (AS) that is weakly bonded to the fibers without an engineered interphase. Approximately 400 Nextel™720 fibers were bundled together in tows and woven into a balanced eight-harness-satin weave (8HSW) cloth. The fiber mat had a (0/90) layup with final fiber volume fraction ≈ 0.46.

The SiC/SiC CMC used in this study was Sylramic/BN/SiC, which was manufactured by Honeywell Advanced Composites, Inc, Newark, DE. Figure 1(b) shows the microstructure of MI Sylramic/BN/SiC. The matrix is described as Melt-Infiltrated (MI) SiC. The Sylramic fibers were bundled together in tows, woven into a balanced five-harness-satin weave (5HSW) cloth, and coated with BN. The fiber mat had a (0/90) layup with final CMC volume fraction ≈ 0.35.

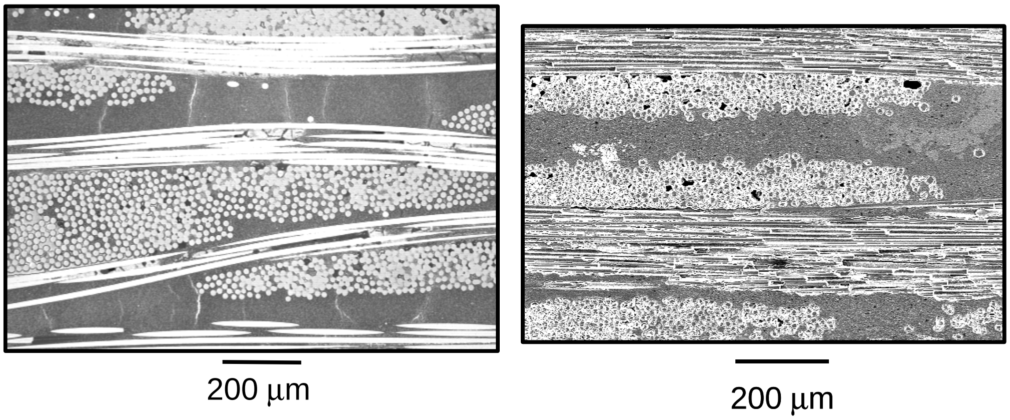

(a) Nextel720™/AS-0 ***(b) MI Hi-Nicalon-S/SiC***

Fig. 1. Microstructure of Oxide/Oxide (Nextel™720/AS) and MI SiC/SiC (MI Hi-Nicalon-S/SiC) composites studied in this investigation.

During this study, baseline tensile tests were conducted using dogbone specimens. For the conventional notch sensitivity tests, straight-sided specimens with large notches were used. These notches were larger than the average tow size, which is typically 1 mm. Semi-circular notches, DEH(T), and sharp notches, DE(T), were used during this study, Figure 2. The semi-circular and sharp notches were machined using a drill and a thin diamond saw (≈ 0.1 mm thick), respectively. In all these tests, the notch mouth opening displacement (NMOD) was measured.

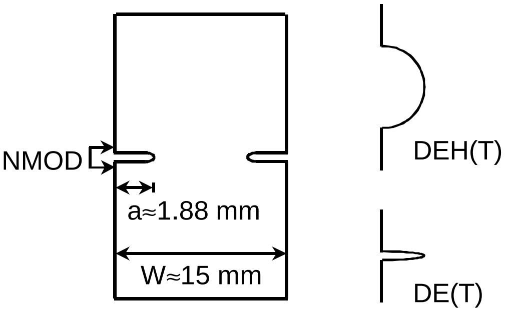

Fig. 2. Schematic of large notch geometry specimens.

Figure 3 shows the effusion hole patterns used for this study. The nominal dimensions of the specimens were, width (W) = 10.0 mm in the gage section, thickness (B) ≈ 2.5 mm and gage length ≈ 12.5 mm. The diameter of the effusion holes was 0.5 mm. Two orientations of the hole-axis were evaluated, i.e. 90° and 20° to the specimen (or fiber mat) plane. The hole-density studied in this investigation was ≈ 8 holes/cm^2 (≈ 50 holes/in^2).

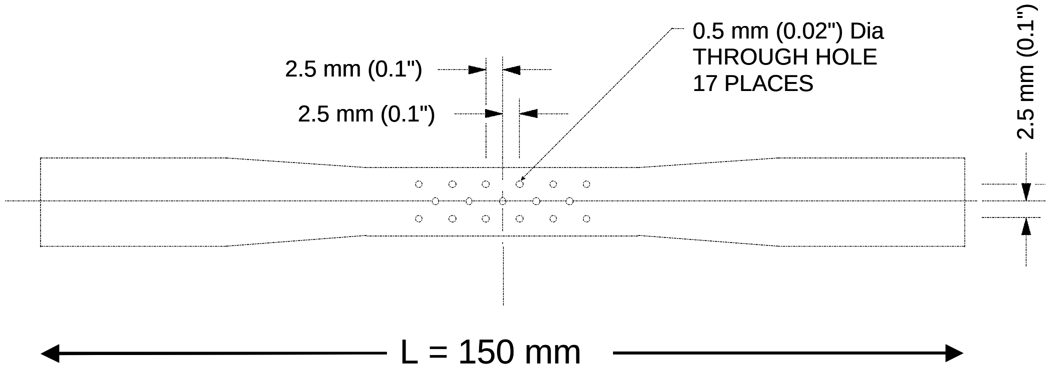

(a) 90° Effusion Hole Geometry

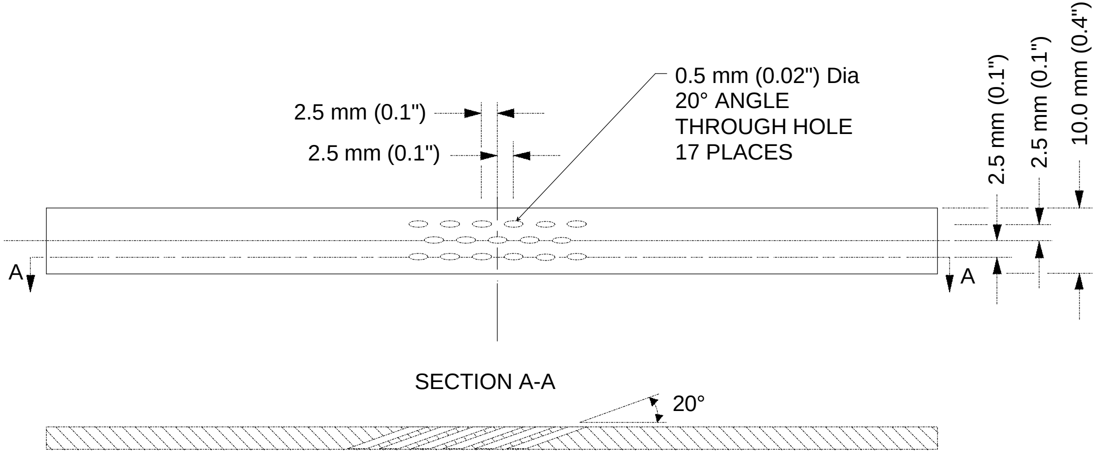

(b) 20° Effusion Hole Geometry

Fig. 3. Schematic of effusion hole geometry specimens.

Figure 4 shows the effusion holes drilled in Nextel™720/AS-0 using two techniques. The twist drilled effusion hole resulted in tear out at the back surface. The laser drilled effusion hole had near-uniform diameter, however a significant recast layer is formed around the hole. This recast layer is ≈ 50 – 100 μm thick and extensively cracked. Further investigation is required to determine the extent of the embrittled zone created during the laser drilling process.

The specimen ends were tabbed with fiberglass tabs to provide a flat uniform surface for the smooth grip surfaces and to minimize the possibility of grip failure. The specimens were mounted in a precisely aligned, rigid grip system that minimized specimen bending and rotation. A clamshell furnace with SiC heating elements and four-zone control were used for the elevated temperature creep tests. Thermal profile maps on the specimen showed that the specimen was uniformly heated, ± 0.6%, over the entire gage section of the specimen. All creep tests were loaded to the maximum stress at a loading rate of 20 MPa/s.

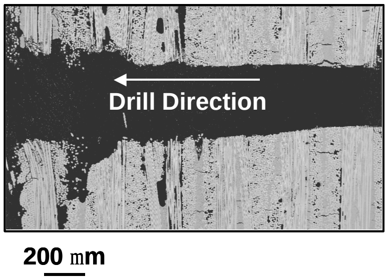

(a) Twist drilled effusion hole

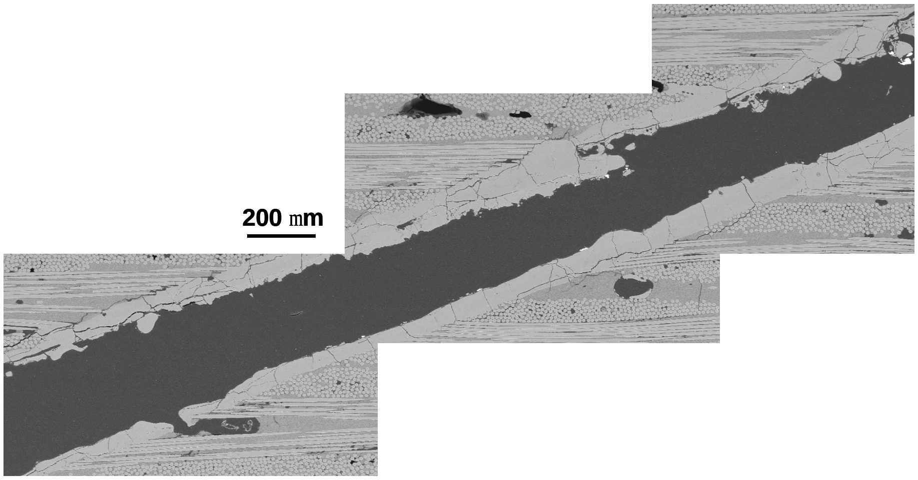

(b) Laser drilled effusion hole

Fig. 4. Effusion holes drilled in Nextel™720/AS-0.

RESULTS AND DISCUSSION

The creep behavior of unnotched and notched Nextel720™/AS-0 [8,9] and MI SiC/SiC [12,15] are summarized in Fig. 5. These notch results correspond to “large” notches, i.e. notches greater than the average tow size.

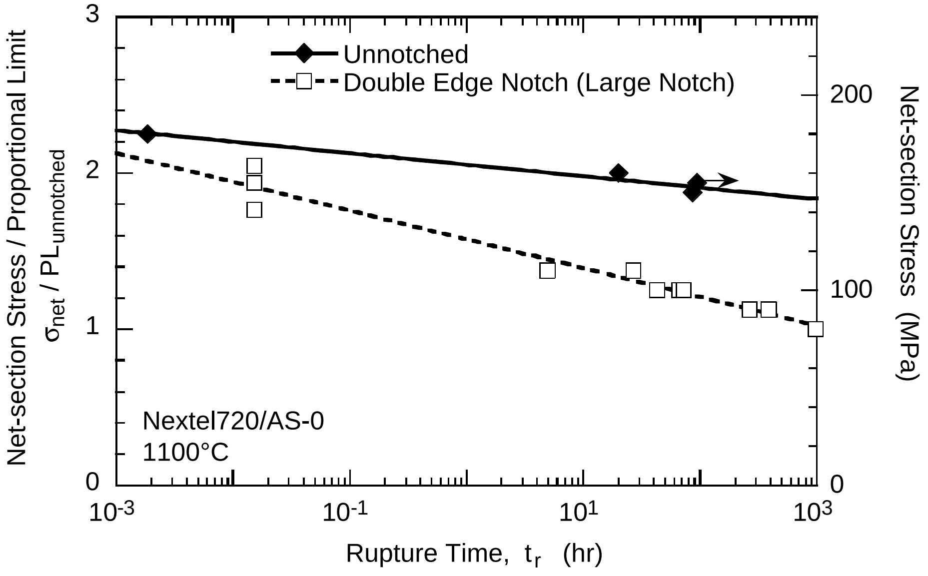

(a) Nextel™720/AS-0

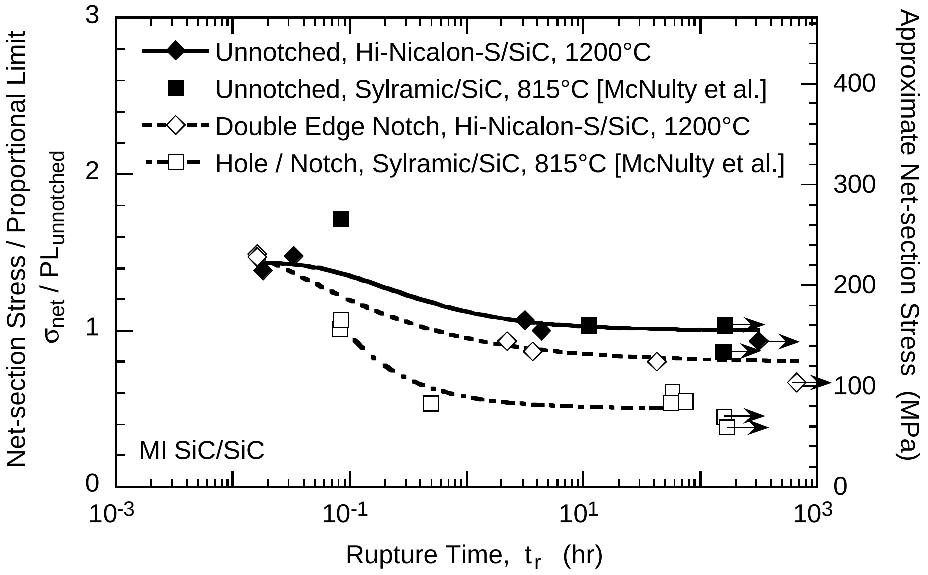

(b) MI SiC/SiC

Fig. 5. Large notch effects on creep rupture behavior of (a) Nextel™720/AS-0 and (b) MI SiC/SiC. Unnotched PL of Nextel™720/AS-0 = 80 MPa, Average PL of MI SiC/SiC » 155 MPa.

In Fig. 5, the applied stresses were normalized with respect to the Proportional Limit (PL) from unnotched tensile tests at the corresponding temperature. The Proportional Limit of Nextel™720/AS-0, MI Hi-Nicalon-S/SiC, and MI Sylramic/SiC was ≈ 80, 150 and 160 MPa, respectively. The unnotched Nextel™720/AS-0 shows excellent creep strength (100 hr run-out) of ≈ 150 MPa, which is ≈80% of UTS and about twice the PL. Unnotched MI SiC/SiC also shows similar creep strength (≈150-160 MPa), which is close to the PL. Hence, the maximum design stress for long-life components (with no notches) is similar for Nextel™720/AS-0 and MI SiC/SiC.

When large notches (notch length > tow size) are introduced, the net-section stress that can be sustained by the composite at 100+ hours decreases significantly. For Nextel™720/AS-0, the notch strength decreased to ≈ 85 MPa, which is close to the unnotched proportional limit. This decrease is independent of the type of notch. For MI SiC/SiC, the notch strength decreased to 50-80% of PL, depending on the temperature. These results show that design of long-life components with stress concentration sites should be based on careful detailed durability assessment studies with sub-elements simulating the actual features.

As discussed earlier, components such as combustors will contain effusion holes, which are 0.5 mm in diameter (< tow size ≈ 1 mm). Since the large notch specimens exhibited significantly increased notch-sensitivity under sustained loading in contrast to the short-duration tensile loading, a program was initiated to evaluate the performance of specimens with effusion holes under creep loading. The tensile response of effusion hole specimens are compared with the uunotched behavior in Figures 6 and 7 for Nextel™720/AS-0 and MI Sylramic/BN/SiC, respectively. Note that the effusion hole data for Nextel™720/AS-0 were obtained from the loading portion of creep tests. As expected, the effusion holes did not significantly alter the overall stress-strain response in the elastic regime. In MI Sylramic/BN/SiC, the PL of the specimen with effusion hole (≈150 MPa) is slightly lower than that of the unnotched specimen (≈160 MPa).

As shown in Figure 3, the effusion holes will be oriented ≤ 30° to the specimen plane. To understand the influence of the orientation of the holes, creep tests were conducted using specimens with 90° and 20° effusion holes. The creep responses of Nextel™720/AS-0 with 90° and 20° effusion holes are shown in Fig. 8. As shown by Buchanan et al. [15], the creep behavior of Nextel™720/AS-0 with twist-drilled 90°-effusion holes is similar to that of the unnotched specimens. However, the laser-drilled 20° effusion hole specimens showed significant reduction (≈90% reduction) in life, even at lower stress levels.

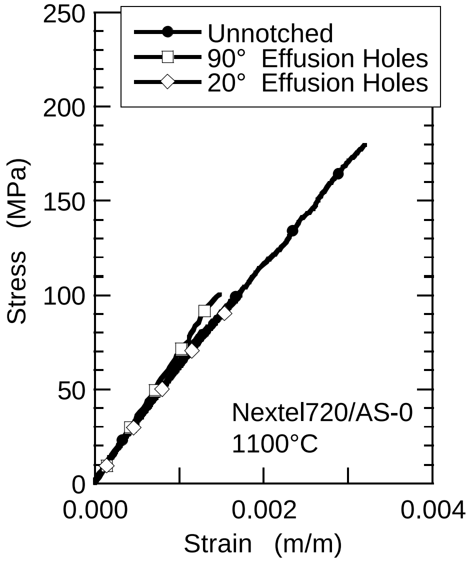

Fig. 6. Tensile behavior of Nextel™720/AS-0 at 1100°C. (Effusion hole – not tested to failure)

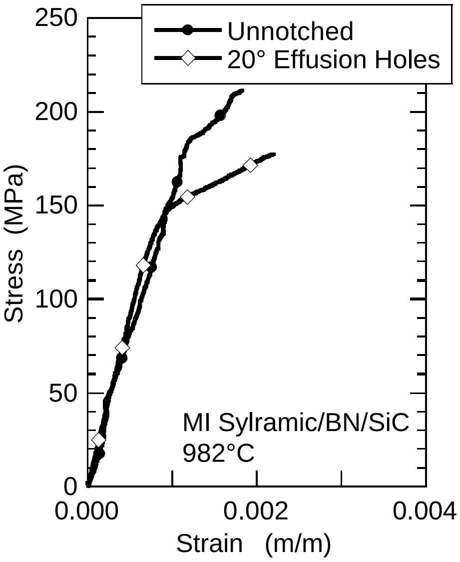

Fig. 7. Tensile behavior of MI Sylramic/BN/SiC at 982°C.

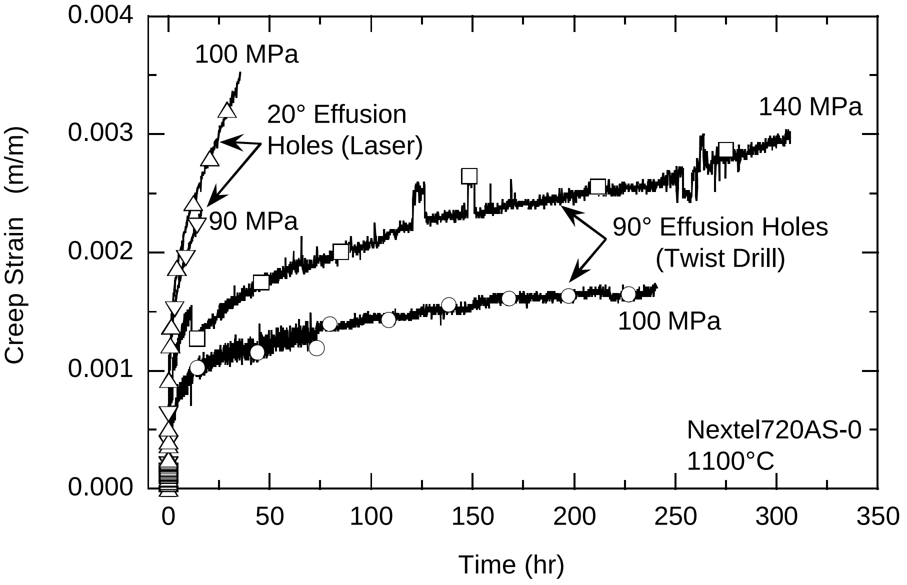

Fig. 8. Creep deformation of Nextel™720/AS-0 specimens with 20° and 90° effusion holes. Test temperature = 1100°C.

To understand the life-limiting effects of effusion holes, the creep rupture data are compared with the data for large notches for Nextel™720/AS-0 and MI Sylramic/BN/SiC in Figs. 9 and 10, respectively. In these figures, the trend lines from Fig. 5 are shown for the unnotched and large-notch behavior. In Fig. 9, we note that the specimens containing twist-drilled 90°-effusion holes behave similar to the unnotched material. However, the laser-drilled 90° effusion holes specimens showed significant reduction in life. Hence, these limited results show that the laser-drilling process used in this study could be detrimental to Nextel™720/AS-0. The similarity between the laser-drilled 90° effusion hole data and the large notch data suggests that the laser-drilling process could be generating an "affected" zone close to or larger than the tow size.

In addition, the laser-drilled 20° effusion hole specimens behave worse than the specimens with large notches at even stresses < 100 MPa. Additional tests at similar stresses are in progress to determine the differences, if any, between laser-drilled 90° and 20° effusion hole specimens. Figure 10 shows a similar effect of 20° effusion holes in MI Sylramic/BN/SiC. Additional tests are required to document the extent of the debit in strength due to effusion holes under engine loading conditions.

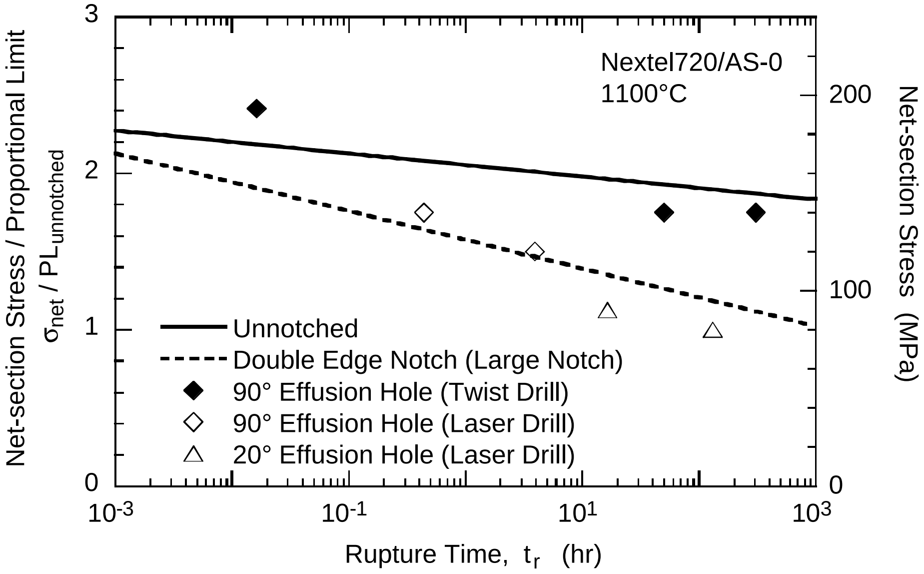

Fig. 9. Creep rupture behavior of Nextel™720/AS-0 with effusion holes. Unnotched Proportional Limit of Nextel™720/AS-0 » 80 MPa.

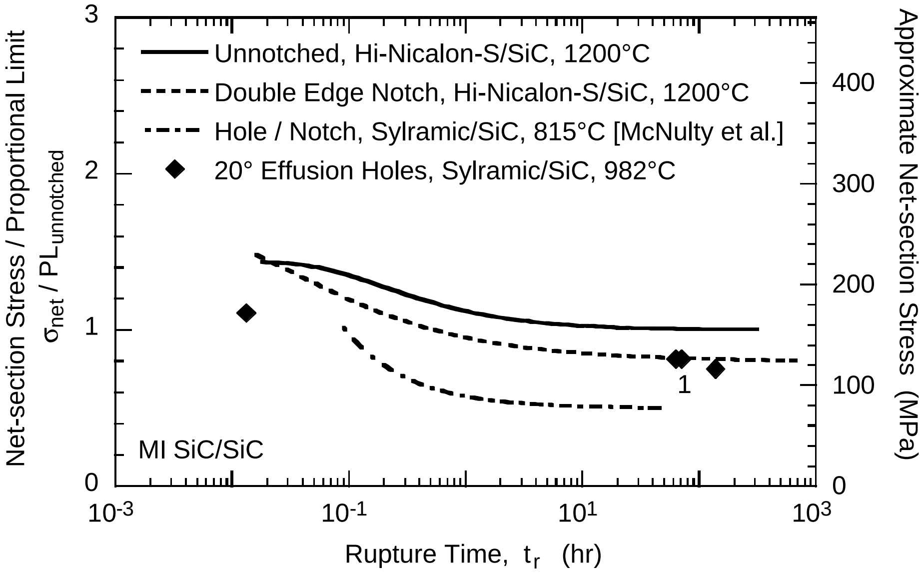

Fig. 10. Creep rupture behavior of MI Sylramic/BN/SiC with effusion holes. Average PL of MI SiC/SiC » 155 MPa. Effusion hole specimens failed away from the holes are identified as "1".

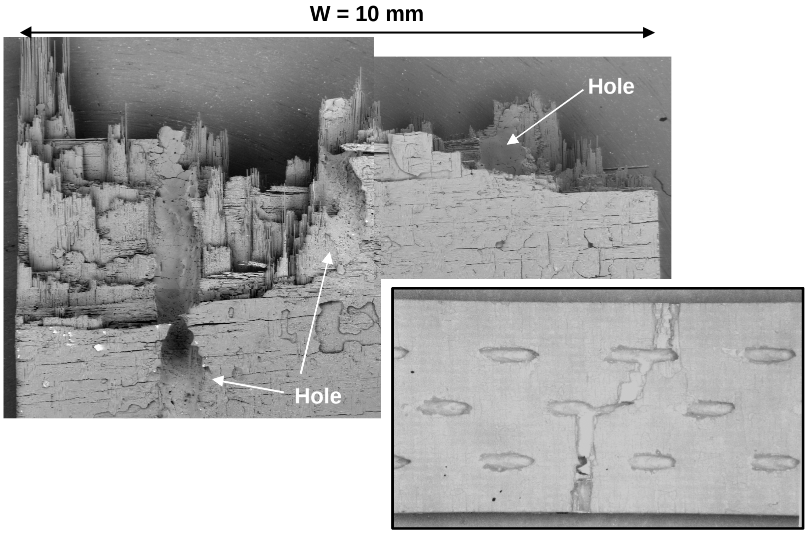

Fig. 11. Fracture profile of Nextel720™/AS-0 with 20° effusion holes.

The fracture profile of Nextel™720/AS-0 with 20° effusion holes is shown in Fig. 11. The fracture surface followed the locations of the effusion holes consistent with the notch-sensitive behavior shown in Fig. 9.

As evidenced by the tensile behavior (Figs. 6 & 7), the effusion holes do not significantly alter the overall elastic response. In Nextel™720/AS-0, the tensile strength can be expected to be insensitive to the effusion holes, similar to the large-notch data. In MI SiC/SiC, notch-sensitivity of ≈15-20% can be expected for these types of holes under tensile loading. However, under sustained loading, the notch-sensitivity of Nextel720/AS-0 and MI SiC/SiC with effusion holes is significantly increased. In this study, it was shown the effusion holes could result in loss of strength similar to that due to large notches. The limited results from this study show that the laser drilling method use to create effusion holes is detrimental to the durability of Nextel720/AS-0. Hence, further investigations into techniques for drilling effusion holes in advanced CMC are recommended. In contrast to tensile tests, loading conditions such as creep are required to better evaluate the detrimental effects, if any, of stress concentration sites such as corners and holes. Hence, design of long-life components with stress concentration sites requires careful detailed durability assessment studies with sub-elements simulating the actual features.

CONCLUSIONS

Notch-sensitivity of woven Nextel™720/AS-0 and MI SiC/SiC with (0/90) layup increases significantly under sustained (creep) loading conditions. The creep strength (in terms of net-section stress) decreases ≈ 40% and 25-50% for Nextel™720/AS-0 and MI SiC/SiC, respectively. The creep behavior of these composites with laser-drilled effusion holes is similar to the response with large notches.

ACKNOWLEDGMENTS

This research was conducted at the Air Force Research Laboratory, Materials and Manufacturing Directorate (AFRL/MLLMN), Wright-Patterson Air Force Base, OH 45433-7817 and was supported in part by the Air Force Office of Scientific Research. Mr. Buchanan and Dr. Kramb were supported under an onsite contract number F33615-98-C-5214.

REFERENCES

[1] IHPTET Brochure, Turbine Engine Division, Propulsion Directorate (AFRL/PRT), Air Force Research Laboratory, Wright-Patterson Air Force Base, OH, USA.

[2] Brewer D., *Materials Science and Engineering A*, Vol. 261, 1999, pp. 284.

[3] Ohnabe, H., Masaki, S., Onozuka, M., Miyahara, K., and Sasa, T., *Composites: Part A*, Vol. 30, 1999, pp. 489.

[4] Zawada, L.P. and Lee, S.S., *Ceramic Engineering and Science Proceedings*, Vol. 16, 1995, pp. 337.

[5] Levi, C.G., Yang, J.Y., Dalgleish, B.J., Zok, F.W. and Evans, A.G., *Journal of the American Ceramic Society*, Vol. 81, 1998, pp. 2077.

[6] Heathcote, J.A., Gong, X.-Y, Yang, J., Ramamurty, U., and Zok, F.W., *Journal of the American Ceramic Society*, Vol. 82, 1999, pp. 2721.

[7] Kramb, V.A., John, R., and Zawada, L.P., *Journal of the American Ceramic Society* Vol. 82, 1999, pp. 3087.

[8] John, R., Buchanan, D.J., and Zawada, L.P., *Ceramic Eng. and Science Proceedings*, Vol. 21, 2000, pp. 567.

[9] John, R., Buchanan, D.J. and Zawada, L.P., *STP 1392 ASTM* 172, 2000.

[10] Buchanan, D.J., Kramb, V.A., John, R., and Zawada, L.P., "Effect Of Small Effusion Holes On Creep Rupture Behavior Of Oxide/Oxide Nextel™720/AS Composite," *Ceramic Engineering and Science Proceedings,* 2001.

[11] M.-L. Antti and E. Lara-Curzio, *Ceramic Engineering and Science Proceedings,* 2001.

[12] J.C. McNulty, M.Y. He, and F.W. Zok, "Notch Sensitivity of Fatigue Life in a Sylramic/SiC Composite at Elevated Temperature," *Composites Science and Technology,* Vol. 61, 2001, pp. 1331-1338.

[13] J.C. McNulty, F.W. Zok, G.M. Genin, and A.G. Evans, *Journal of the American Ceramic Society,* Vol. 82, 1999, pp. 1217.

[14] G. Morscher, J.Z. Gyekenyesi, and A.L. Gyekenyesi, *Proceedings of 46th ASME IGTI,* 2001.

[15] R. John, D.J. Buchanan, and L.P. Zawada, "Fracture and Creep Rupture Behavior of Notched Oxide/Oxide and SiC/SiC CMC," *Proceedings, ICF10*, December 2001.

EFFECTIVE ELASTIC AND THERMAL PROPERTIES OF A DAMAGED WOVEN OXIDE-OXIDE COMPOSITE

Gyaneshwar P. Tandon*, Dennis J. Buchanan
University of Dayton Research Institute, Dayton, OH 45469
and
Nicholas J. Pagano, Reji John
Air Force Research Laboratory, WPAFB, OH 45433

ABSTRACT

We consider an oxide-oxide composite consisting of 2-D textile reinforcement (Nextel720 fibers in an eight harness satin weave (8HSW) architecture) in a matrix consisting of alumina particles, voids, inherent cracks due to processing conditions, and a silica bonding agent. Our objective is to evaluate the effective elastic and thermal properties of this multiphase woven composite, in the presence of processing-induced damage, and compare to experiments. The analytical approach follows a building-block scenario in which the microstructure is homogenized and simplified at various levels. The numerical predictions are then compared to experimental results for the composite material to assess the implications of the assumptions invoked in the model. It is demonstrated that damage modeling is essential for effective property estimation. Modeling of transverse cracking alone leads to degradation of in-plane properties, such as E_x, leaving the thickness modulus E_z unaltered from the undamaged value. We also show that it is necessary to consider additional damage mechanisms such as fiber-matrix interfacial debonding, delamination or effective matrix degradation, in order to obtain lower estimates of the Young's modulus in the thickness direction in the present composite.

Keywords: A. Oxide-oxide fabric; B. Thermomechanical; C. Micromechanics; C. Laminate mechanics

---

* Corresponding author. Tel.: +1-937-255-1393; fax: +1-937-258-8075
E-mail address: G.Tandon@afrl.af.mil

INTRODUCTION

The objectives of this effort were to support the development of a revolutionary ultra compact combustor in the areas of material selection and analytical modeling. Oxide-oxide ceramic matrix composites (CMC) consisting of oxide fibers embedded in an oxide matrix with no engineered fiber-matrix interphase are currently the subject of increased interest due to their inherent resistance to oxidation. Many investigations [1-7] have shown that oxide-oxide composites exhibit excellent tensile and fatigue properties at room and elevated temperatures. Detailed studies [2,4] have demonstrated how the fiber- matrix interphase region and matrix porosity promote a damage tolerant CMC with non-brittle fracture behavior. Nextel610 fibers and their composites are susceptible to excessive creep deformation [7-10] at temperatures greater than 1000°C. In contrast, Nextel720 fibers exhibit significant creep resistance up to 1200°C [9-10]. Hence, oxide-oxide CMC with Nextel720 fibers are under consideration for applications with temperature requirements in the range of 1000-1200°C.

In this work, we consider 2-D reinforcement of Nextel720 fibers in an 8HSW architecture in a matrix consisting of alumina particles, voids, inherent cracks due to the processing conditions, and a silica bonding agent. Predicted quantities include the effective thermal and elastic properties due to processing conditions. The effective composite properties, in turn, can serve as input parameters in a 3-D finite element analysis to analyze the stress fields in the combustor under operational conditions. A feedback loop between the finite element method (FEM) and the micromechanical model can then be established to define the evolution of the service-induced damage.

The basic research issues in mechanics include the model details for such a complex multiphase composite material, particularly, calculation of phase stresses as well as "homogenized" matrix properties, and the resulting failure initiation and fracture mechanics laws to govern crack distribution and propagation. The homogenized matrix properties are of concern from both theoretical and experimental viewpoints. For example, no experimental samples of the multiphase matrix exist. In fact, it is not known whether such specimens are even possible to manufacture in any cost-effective manner. It is therefore essential to determine the moduli and strength properties of the matrix by analysis and correlate these predictions with experimental observations of stiffness and damage in the composite material. The scale at which this modeling can be successfully accomplished is not known *a priori* and poses severe challenges to the experimentalist as well.

MATERIAL

The oxide-oxide composite used in this study was produced by COI Ceramics, Inc. The Nextel720 fibers, produced by the 3M Company, consist of fine grained (< 0.5 μm) polycrystalline alpha alumina plus mullite. The composition of the fibers included 85% Al_2O_3 and 15% silica with an average diameter of 10-12 μm. These fibers were woven into a balanced 8HSW cloth. Sections of Nextel720 cloth were prepregged with alumina powder and a silica forming polymer before stacking. The laminate was then warm molded to produce the green state ceramic tile. Sintering the green tile in air at 1000^0C removed the organic binders and produced a porous alumina-silica (AS) matrix. It was observed that majority of pores are within the size range of .01 to 2 μm. The matrix contains approximately 87 wt. % single crystal submicron alumina suspended in 13 wt. % silica. Image analysis of polished cross sections (see Fig. 1) showed that the average fiber volume fraction was 45%. Figure 2 shows extensive microcracking present throughout the matrix, presumably the result of the shrinkage which occurred during pyrolysis processing [11]. These microcracks are distributed throughout the composite with spacing ranging from 50 to 200 μm prior to machining and testing.

EXPERIMENTAL RESULTS

A dogbone specimen geometry was used for room and elevated temperature tensile tests. The typical dimensions of the specimens were: width = 15.0 mm at grip and 10.0 mm in gage section, thickness ≈ 2.5 mm and length ≈ 100 mm. All specimens were waterjet cut and diamond ground in the gage section. The specimen ends were tabbed with fiberglass tabs to provide a flat uniform surface for the smooth grip surfaces and to minimize the possibility of grip failure. The specimens were mounted in a precisely aligned, rigid grip system that minimized specimen bending and in-plane rotation. A clamshell-style furnace was used with silicon-carbide heating elements under four-zone temperature control for elevated temperature tests. The tension tests were conducted under displacement control at a rate of 0.005 mm/s in laboratory air using a computer- controlled servo-hydraulic test system. Elastic modulus for the in-plane orientation ($E_x = E_y$) was calculated from stress-strain data collected from uniaxial loading of a test coupon. Elastic modulus for the through-thickness orientation (E_z) was calculated using an ultrasonic wave propagation technique [12]. Measurements of time-of-flight for an ultrasonic signal (approximately a 1 MHz center frequency) to pass through the CMC were recorded. The longitudinal wave speed was calculated using the specimen thickness and time-of-flight data. Assuming homogeneous wave propagation through the material, the through-thickness effective stiffness coefficient, C_{zz}, is given by

$$C_{zz} = r \; v^2 \tag{1}$$

where:

ρ = bulk density,

and, v = longitudinal wavespeed.

Young's modulus in the thickness direction, E_z, was then obtained by utilizing the theoretical relations between the effective stiffness component C_{zz} and the engineering constants predicted by the analytical procedures, as discussed later.

Measurements were made on several different panels (and fabric orientations) as summarized in Table I. The fiber volume fractions were determined for each panel as shown in Table I. The bulk density measurements on the panels varied between 2.52 - 2.59 g/cm^3. The in-plane Young's modulus was found to vary between 71 to 87 GPa with an average value of 79 GPa, while the average modulus in the thickness direction was 50 GPa. Possible explanations for rather lower modulus values in the thickness directions are discussed in the next section. Poisson's ratios (ν_{xy}, $\nu_{xz} = \nu_{yz}$) were calculated from strain gage measurements mounted in the three principal material orientations of a test coupon subjected to uniaxial loading. (Note that in the convention ν_{ij}, the first index i refers to the coordinate of imposed stress or strain, and the second index j refers to the response direction). The average value of in-plane Poisson's ratio v_{xy} was 0.09, while out-of-plane Poisson's ratio was measured as 0.12. The in-plane shear modulus (G_{xy}) was calculated from the applied load, and the axial and transverse strain measurements of a test coupon with fiber tows aligned in the (±45°) direction tested under uniaxial loading. The in-plane shear modulus was measured as 17 GPa. Measurement of out-of-plane shear moduli, G_{xz} and G_{yz}, has not been made so far.

The thermal conductivity (μ) of Nextel720/AS CMC was calculated as a product of measured data: thermal diffusivity (α), specific heat (C_p) and bulk density (ρ), i.e., $\mu = \alpha \, C_p \, \rho$. Thermal diffusivity was measured by TPRL, Inc. for in-plane and through-thickness orientations. The in-plane value of thermal conductivity was approximately 25% higher than the through-thickness value. The in-plane and through-thickness thermal conductivity measurements dropped by approximately 10% from 23 to 1200°C. Lastly, the coefficient of thermal expansion (CTE) for Nextel720/AS CMC was also measured in the in-plane and through-thickness orientations by TPRL, Inc. The CTE data for the in-plane and through-thickness orientations were similar for temperatures ≤ 1000°C. Above 1100°C, the through-thickness CTE continued to increase, and the in-plane CTE started to decrease. Our own measurement of in-plane CTE's using a servohydraulic test machine resulted in slightly lower value (5.85×10^{-6}/°C) as compared to TPRL data (6.45×10^{-6}/°C).

ANALYTICAL MODELING

The approach followed a building-block scenario in which the microstructure was homogenized at various levels depending on the particular quantities being sought. Firstly, the effective properties of the multiphase matrix material were computed by use of a three-phase version of the Mori-Tanaka scheme. For the material system under consideration, the "homogenized matrix" consists of the stiff alumina particles finely dispersed in silica. Additionally, the matrix has a significant amount of porosity. An approximate theory was developed by Weng [13] to compute the overall elastic moduli for a general multiphase, anisotropic composite with arbitrarily oriented anisotropic inclusions based on Mori and Tanaka's concept of average stress in the matrix and Eshelby's solutions of an ellipsoidal inclusion. In the limiting case of a uniform dispersion of multiphase isotropic spheres in an isotropic matrix, the relations simplify to,

$$\frac{k_{\mathrm{eff}}}{k_o} = 1 + \frac{\mathrm{a}}{1 - a_{\mathrm{o}}\,\mathrm{a}}\,, \qquad \frac{\mathrm{G}_{\mathrm{eff}}}{\mathrm{G}_o} = 1 + \frac{\mathrm{b}}{1 - b_{\mathrm{o}}\,\mathrm{b}}$$

$$\textit{where} \quad a_{\mathrm{o}} = \frac{3k_0}{3k_{\mathrm{o}} + 4\,G_{\mathrm{o}}}\,, \qquad b_{\mathrm{o}} = \frac{6}{5}\,\frac{k_0 + 2G_{\mathrm{o}}}{3k_{\mathrm{o}} + 4\,G_{\mathrm{o}}} \tag{2}$$

$$a = \sum_{\mathrm{r}} \frac{\mathrm{c_r}\,(k_{\mathrm{r}} - k_{\mathrm{o}})}{a_{\mathrm{o}}\,(k_{\mathrm{r}} - k_{\mathrm{o}}) + k_{\mathrm{o}}}\,, \qquad b = \sum_{\mathrm{r}} \frac{\mathrm{c_r}\,(G_{\mathrm{r}} - G_{\mathrm{o}})}{b_{\mathrm{o}}\,(G_{\mathrm{r}} - G_{\mathrm{o}}) + G_{\mathrm{o}}}$$

while κ and G are the bulk and shear modulus, c is the volume fraction and the subscripts r, 0 and eff refer the stated quantity to the rth inclusion, unreinforced matrix, and homogenized matrix, respectively. For simplicity, we assumed that both the alumina particles and the pores were spherical in shape and evaluated the elastic properties of the effective matrix (i.e., alumina + voids in silica) using the expressions given by (2). Using the same Mori-Tanaka approach, Pan and Weng [14] obtained solutions to the effective coefficient of thermal expansion of the three-phase solid, while Norris [15] gave the following expressions for the effective thermal conductivity of a multiphase isotropic composite,

$$m_{\mathrm{eff}} = m_0 + \frac{\displaystyle\sum_{\mathrm{r}} \frac{3\mathrm{c_r}\, m_0\,(m_{\mathrm{r}} - m_0)}{(m_{\mathrm{r}} + 2\,m_0)}}{\mathrm{c}_0 + \displaystyle\sum_{\mathrm{r}} \frac{3\mathrm{c_r}\, m_0}{(m_{\mathrm{r}} + 2\,m_0)}} \tag{3}$$

where μ is the thermal conductivity, and the previous definition of the subscripts in (2) holds. The equations for the effective coefficient of thermal expansion are given in [14]. Using the handbook material properties of alumina (Young's modulus, E =310 GPa; Poisson's ratio, ν=0.15; coefficient of thermal expansion, α = 8.5 e-6/^{o}C; thermal conductivity, μ =10 W/m-K) and silica (E=72 GPa, ν=0.16, α=0.5 e-6/^{o}C, μ=1.75 W/m-K), the effective matrix properties were evaluated as,

$$E_{eff}= 69.8 \text{ GPa}, \nu_{eff}=0.18, \alpha_{eff}=7.44 \text{ e-6/}^oC, \mu_{eff}=2.66 \text{ W/m-K} \tag{4}$$

using particle and void contents of 0.52 and 0.34, respectively, in the matrix. These volume fractions were estimated in an earlier work by Zuiker [8]. The Mori-Tanaka method employed here considers only linear interactions between the inclusions in an average sense. In order to examine the accuracy of its predictions, we therefore compared the predictions of this approach with a more sophisticated method by Buryachenko [16] which considers binary interactions with the neighboring inclusions. This method is a homogenization theory based on multiparticle effective field method (MEFM) employing functions of random variables and Green's functions. It was found [17] that for the present material system and range of inclusion concentrations, the two methods give very similar results. We can therefore use with confidence the effective property predictions for the homogenized matrix obtained using the linear Mori-Tanaka approach.

Secondly, the effect of yarn crimp on the 3D effective moduli of a composite was determined by comparison of a fabric reinforcement model [18] with that for a cross-ply laminate and also with the straight-fiber micromechanical stiffness model NDSANDS [19]. The homogenized matrix properties were assumed in this comparison. The fabric itself is an 8-harness satin which could be approximated by a cross-ply laminate. Pagano and Tandon [19] have developed a theoretical model to approximate the thermoelastic response of multidirectional coated fiber composites. In order to employ their model, we approximated the 8-harness fabric by orienting the fiber tows in 0- and 90-degree orientations in the cross-sectional plane of the effective matrix, the properties of which were earlier determined. The geometric modeling of the 8-harness fabric architecture was performed by Naik [18] by utilizing the periodicity of the textile composite to isolate a representative unit cell (RUC), as shown in Figure 3. The yarn centerline path was discretely modeled within the RUC by assuming sinusoidal undulation and a flattened lenticular yarn cross-sectional shape. This assumption therefore establishes some relationships between the various geometric variables such as yarn spacing, crimp angle, undulating length and the unit cell thickness, defined in Figure 3. From the photomicrograph in Figure 1, we measured the crimp angle as ~10^0, while the yarn spacing was 1.19 mm and the unit cell thickness was 0.09 mm. In addition, a yarn fiber packing density, p_d, of 0.55, and a yarn filament count of 400 were reported for the 8-harness satin weave. These values, in conjunction with the yarn spacing measurement of 1.19 mm, resulted in theoretical estimates of 12.5^0 crimp angle and a unit cell thickness of 0.084 mm from the RUC. These values were considered reasonable when compared with the measured values of crimp angle and unit cell thickness, and therefore, gave us confidence in utilizing the geometric model for predicting effective properties for the textile composite. The yarn bundle properties were first estimated using E_f=262 GPa, ν_f=0.25, α_f=6.0 e-6/^{o}C, μ_f=5.9 W/m-K, for Nextel720 fiber, and a yarn packing density of 0.55 in the micromechanics model [19]. The three-dimensional effective stiffness of the fabric was then computed [18] by discretizing the yarn into slices, and using the material properties, spatial orientation and volume fraction of each yarn slice in a volume averaging technique that assumed an iso-strain state within the RUC. Figure 4 compares the prediction of the in-plane stiffness (E_x=E_y) for the 8-harness satin weave and a plain weave as a function of the crimp angle using the fabric model [18]. It is interesting to note that for small values of crimp angle, the two simulations result in very little differences. Even at a crimp angle approaching 60 degrees, the results differ by less than 4%. Thus, for the material system under consideration, the influence of fiber architecture is insignificant and can be ignored. We next compare in Table II the thermoelastic properties for the undamaged 8-harness fabric with the straight-fiber model (19). For the properties listed in Table II, x-y is the fabric plane and z is in the thickness direction. It is observed that the computed thermo-elastic constants using NDSANDS [19] are in very good agreement with the analytical results of Naik [18], where the actual fiber architecture is considered in a unit cell, thereby supporting our approximation of the 8-harness satin weave. Thus, a straight-fiber model, which neglects the fiber waviness, will henceforth be employed to model the effective response of Nextel720/AS cloth composite. The in-plane properties also agreed with the classical lamination plate theory results where the fabric composite was approximated as a $[0/90]_s$ laminate. However, comparison of these predictions in Table II with the experimental measurements in Table I indicates that these numerical predictions are much too high. As shown in Figure 2, on close examination, it was observed that the as-processed composite contained a fairly well defined distribution of cracks normal to the fiber directions. These cracks have not been accounted for in the effective property predictions so far.

In order to consider the influence of transverse cracking, due to processing at a higher temperature, we appealed to the Large Radius Axisymmetric Model (LRAM) of Schoeppner and Pagano [20]. The model employs the variational theorem by Reissner [21] to predict the stress fields and energy release rates for cracked flat laminates containing orthotropic layers. The formulation [20] employs the concept that the stress field in an axisymmetric cylinder approaches that in a long flat coupon as the radius-to-thickness ratio approaches infinity. The model has been utilized [22] to examine the initiation, propagation and interaction of damage for thermoelastic problems in flat laminates under generalized plane strain conditions. Assuming uniform transverse crack spacing in Nextel720/AS $[0/90]_S$ laminate, a two-dimensional (2-D) representative volume element (shown in Figure 5) was used to evaluate the changes in the effective thermoelastic properties as a function of crack density. Note that in Figure 5, the fabric is in the X-Y plane, while Z is in the thickness direction. For the unit or periodic cell of length L/2 (where L is the transverse crack spacing), it was assumed that the transverse crack extended the full depth of the 90° layer in the cross-ply laminate and was normal to the layer interface. It was also assumed that lamina interfaces were perfectly bonded and that the traction-free cracks were equally spaced. Furthermore, free-edge effects were neglected in this 2-D model. The volume average stresses and the composite strains in the periodic cell are related by the effective stiffness tensor of the laminate. The components of the effective stiffness tensor were therefore determined by subjecting the unit cell to a set of boundary value problems (for details see [22]), which lead to coupled equations in terms of the effective stiffness tensor. The effective engineering constants were then defined in terms of the effective stiffness tensor. This procedure [22] was utilized to predict all of the effective Young's moduli, Poisson's ratios, coefficient of thermal expansion and transverse shear modulus, G_{XZ}, of the damaged cross-ply laminate. In addition, the closed form shear-lag model of Tsai and Daniel [23] was employed for the determination of in-plane shear modulus, G_{xy}, whereas the shear modulus G_{yz} was assumed to be unaffected by 90^0 ply cracks [24]. As an illustration, we present the effective thermoelastic properties for a $[0/90]_s$ laminate for transverse crack spacing (in the 90^0 ply) of 192 microns:

$$\begin{gathered} E_x = 90.4 \text{ GPa},\ E_y = 136.18 \text{ GPa},\ E_z = 115.98 \text{ GPa} \\ \nu_{yx} = 0.1687,\ \nu_{zx} = 0.1704,\ \nu_{yz} = 0.2124 \qquad (5) \\ G_{xy} = 31.98 \text{ GPa},\ G_{xz} = 43.29 \text{ GPa},\ G_{yz} = 48.75 \text{ GPa} \\ \alpha_x = 6.41\text{ e-}6/^0\text{C},\ \alpha_y = 6.50\text{ e-}6/^0\text{C},\ \alpha_z = 6.72\text{ e-}6/^0\text{C} \end{gathered}$$

The next step in the procedure was to estimate the effective properties of the cracked ply. This was accomplished by utilizing the exact 3-D elasticity model by Pagano [25]. The exact elasticity model is capable of calculating the effective 3-D laminate properties of a composite for known 3-D ply level properties. Thus, knowing the effective properties of the laminate containing a crack in the 90^o ply, and assuming that the properties of the uncracked ply are not affected by the cracked ply, we could use the exact elasticity model [25] to back out the 3-D effective properties of the transversely cracked 90^o ply. Using the example of transverse crack spacing (in the 90^0 ply) of 192 microns, the cracked ply properties are given by,

$$\begin{gathered} E_T = 21.99 \text{ GPa}, E_L = 156.4 \text{ GPa}, E_Z = 115.9 \text{ GPa} \\ \nu_{LT} = 0.2185, \nu_{LZ} = 0.2185, \nu_{TZ} = 0.0391 \qquad (6) \\ G_{LZ} = 49.45 \text{ GPa}, G_{TZ} = 38.52 \text{ GPa} \\ \alpha_L = 6.33 \text{ e-}6/^0\text{C}, \alpha_T = 6.67 \text{ e-}6/^0\text{C}, \alpha_Z = 6.76 \text{ e-}6/^0\text{C} \end{gathered}$$

where L is the longitudinal fiber direction, T-Z is the transverse plane perpendicular to the fiber axis, and Z is the laminate thickness direction. This procedure therefore allowed us to calculate the effective ply properties for the 90^o ply as a function of the density of the cracks in that layer, assuming there was no damage in the 0^0 layer. However, transverse cracking occurs in both 0- and 90-degree plies due to processing. We therefore repeated the process described in the previous two steps, but with one major difference. Instead of using undamaged ply properties for the 0^0 layer, we now assigned to it the damaged ply properties (obtained by transformation of the cracked 90^0-ply properties), which had been determined in the previous step. The 2-D generalized plane strain model [22] with transverse cracking in the 90-degree ply (and damaged 0^0-ply properties) was again solved to determine the effective laminate properties. These results were then used in conjunction with the exact 3-D elasticity model [25] again to determine the effective properties of the 90^0 cracked ply in the presence of damage in the 0^0 ply. These ply properties for transverse crack spacing of 192 microns are given by,

$$\begin{gathered} E_T = 21.77 \text{ GPa}, E_L = 156.4 \text{ GPa}, E_Z = 115.9 \text{ GPa} \\ \nu_{LT} = 0.2185, \nu_{LZ} = 0.2185, \nu_{TZ} = 0.0387 \qquad (7) \\ G_{LZ} = 49.45 \text{ GPa}, G_{TZ} = 38.47 \text{ GPa} \\ \alpha_L = 6.34 \text{ e-}6/^0\text{C}, \alpha_T = 6.71 \text{ e-}6/^0\text{C}, \alpha_Z = 6.72 \text{ e-}6/^0\text{C} \end{gathered}$$

Next, the damaged ply properties were arranged in a $[0/90]_s$ orientation to obtain effective laminate properties since transverse cracking occurs in both 0- and 90-degree plies due to processing. The effective laminate properties are now given by,

$$E_x = E_y = 89.43 \text{ GPa}, \quad E_z = 115.93 \text{ GPa}$$

$$\nu_{yx} = 0.0534, \ \nu_{zx} = 0.1682, \ \nu_{yz} = 0.1297 \tag{8}$$

$$G_{xy} = 23.64 \text{ GPa}, \ G_{xz} = G_{yz} = 43.28 \text{ GPa}$$

$$\alpha_x = \alpha_y = 6.39 \text{ e-}6/^0\text{C}, \ \alpha_z = 6.72 \text{ e-}6/^0\text{C}$$

Note that in-plane shear modulus, Gxy, reported in (8) was calculated using the shear-lag model of Tsai and Daniel [23] assuming equal crack spacing in the 0- and 90-degree plies, and is listed here for completeness. This procedure of determining the effective thermo-elastic properties of a damaged 90-degree ply in the presence of damaged 0-degree ply, and assembling it to form a [0/90]s laminate with damaged ply properties, was repeated over the entire range of crack spacing measurements. The results of these calculations are shown in Figures 6a - 6d. It is these results which can now be compared to experiments and used to assess the quality of the various assumptions invoked in the calculations. It is noted that the results shown in Figures 6a - 6d approach their corresponding ply-discount limiting values for smaller crack spacing values. The predictions of effective Poisson's ratios in Figure 6b were also utilized to estimate the Young's modulus in the thickness direction using ultrasonic measurement of Czz, as mentioned previously. These calculations for Ez (reported in Table I) are not very sensitive to the transverse crack spacing ranging from 50 to 200 ? m. Overall, we find that this modeling approach which incorporates the presence of transverse cracking is seen to produce very good agreement with the experimental measurements for all of the effective thermoelastic properties, except E_Z. Since the transverse cracks are aligned in the thickness direction, the modulus in that direction is insensitive to these cracks and remains unchanged from the previously reported undamaged value in Table II.

In order to realize the smaller values of E_z which were ultrasonically measured, we once again appealed to the layer model [22] but this time considered delamination between the 0- and 90-degree plies in addition to transverse cracking. It was assumed that ply delamination simulated fiber-matrix debonding which could occur in conjunction with transverse cracking. Figure 7 is a two-dimensional (2-D) representative volume element used to simulate transverse cracking along with ply delamination. The procedure of obtaining the damaged ply properties using the 2-D variational model [22] in conjunction with the exact 3-D elasticity model [25], and assembling the damaged ply properties to form a $[0/90]_s$ laminate, was repeated for one chosen value of transverse crack spacing and some arbitrarily assumed delamination lengths. The results of these calculations are shown in Figures 8a - 8d. Figure 8a shows the predictions of the effective Young's moduli as a function of delamination length for a transverse crack spacing of 48 μm. It is seen that delamination has very little influence on E_x ($=E_y$), while E_z is strongly dependent on its length. However, the length of the delamination has to be relatively large for the predicted value of E_z to agree with the average measured value of 50 GPa. The other two elastic constants, which are affected by delamination between the 0-and 90-degree plies, are the Poisson's ratio, ν_{zx} ($= \nu_{zy}$), and the shear modulus, G_{xz} ($= G_{yz}$), as shown in Figures 8b and 8c, respectively. The effect of delamination on the remainder of the effective properties is insignificant.

Next, in order to calculate more accurate phase stresses so that the failure characteristics could be predicted, we replaced the previous layer models with a concentric cylinder model [26] in which the distinct fiber and homogenized matrix phases were recognized, along with a micromechanical representation of the damage. The latter damage mode consisted of fiber-matrix debonding (over half the fiber surface) coupled with matrix cracks emanating from the debond tips (and aligned in the thickness direction), as shown in Figure 9. This model can now be checked for consistency with the damage observations. The effective thermoelastic constants for the RVE shown in Figure 9 are given by,

$$\begin{gathered}E_{11} = 156.3\text{ GPa},\ E_{22} = 72.2\text{ GPa},\ E_{33} = 14.6\text{ GPa}\\ \nu_{12} = 0.2119,\ \nu_{13} = 0.1832,\ \nu_{23} = 0.0917 \qquad (9)\\ G_{12} = 33.1\text{ GPa},\ G_{13} = 11.6\text{ GPa},\ G_{23} = 15.7\text{ GPa}\\ \alpha_{11} = 6.35\text{e-}6/^{0}\text{C},\ \alpha_{22} = 6.89\text{e-}6/^{0}\text{C},\ \alpha_{33} = 7.64\text{e-}6/^{0}\text{C}\end{gathered}$$

where 1 is the fiber direction and 2-3 is the transverse plane. We should observe that these effective moduli have meaning here only for displacement boundary conditions applied to the RVE in Figure 9. Homogenized plies with properties given by (9) were next arranged in a $[0/90]_s$ orientation to obtain effective laminate properties since transverse cracking occurs in both 0- and 90-degree plies due to processing, and are given by

$$\begin{gathered}E_x = E_y = 85.7\text{ GPa},\ E_z = 72.2\text{ GPa}\\ \nu_{xy} = 0.0313,\ \nu_{xz} = \nu_{yz} = 0.1154 \qquad (10)\\ G_{xz} = G_{yz} = 21.3\text{ GPa},\ G_{xy} = 11.6\text{ GPa}\\ \alpha_{xx} = \alpha_{yy} = 6.47\text{e-}6/^{0}\text{C},\ \alpha_{zz} = 6.89\text{e-}6/^{0}\text{C}\end{gathered}$$

The prediction of the in-plane Young's modulus from the micromechanics model [26] agrees well with the experimental data. As opposed to straight transverse cracks only in homogeneous plies in the laminate model [22], the micromechanics model which considers 180^0 fiber-matrix debonding in conjunction with radial matrix cracking now leads to a reduced modulus in the thickness direction (as compared to the undamaged value). However, the predicted value of E_z (=72 GPa) is still higher than the average value of 50 GPa measured in the thickness direction.

Traditionally, a more simplified approach to modeling discrete damage is the property degradation model in which the stiffness of the load-carrying element is reduced to reflect the presence of damage. In the present case, we degraded the elastic modulus of the effective matrix material. The straight-fiber micromechanical stiffness model NDSANDS [19] was again used for this simulation. A parametric study revealed that a matrix elastic modulus of 20 GPa (reduced from undamaged value of 69.8 GPa) resulted in a reasonably good match with experiments for composites thermoelastic constants including Young's moduli in both the thickness and in-plane directions, as shown in Table III. Thus, if one does not want to discretely model damage in the homogenized matrix, a value of 20 GPa for the matrix elastic modulus will serve as a good estimate for the prediction of the composite properties. Of course, this method (at least at this time) is strictly based on an arbitrarily chosen value for E_{eff} and is not a mechanistic calculation. Table IV is a summary of comparison of experimental measurements with predictions simulating various failure modes. These comparisons of Young's moduli reinforce the hypothesis that some additional damage mode, such as fiber-matrix debonding or delamination, could be occurring in conjunction with transverse cracking, which in turn, leads to a lower value of E_z, and thus a better match with the measurements. This conjecture is currently under examination and will be reported elsewhere.

Lastly, Lu and Hutchinson [27] have shown that matrix cracking in combination with interfacial debonding has the potential for significantly reducing the overall longitudinal thermal conductivity of a unidirectional fiber-reinforced composite. Recently, Islam and Pramila [28] used FEM to consider combined effects of partial debonding and matrix cracking on the effective transverse thermal conductivity of fiber-reinforced composites. They concluded that the reduction of effective thermal conductivity may be as large as 50% when the interfacial conductance is reduced by two decades. In the absence of a suitable model for evaluating thermal conductivity of the damaged fabric, our analytical predictions for the undamaged fabric (reported in Table II) represent upper bound results, and are therefore higher than the measured values for the damaged fabric (reported in Table I).

CONCLUDING REMARKS

In this work, the effective thermoelastic properties of a damaged multiphase woven oxide-oxide composite were determined and compared to experiments. It is demonstrated that damage modeling is essential for effective property estimation. Modeling of transverse cracking alone leads to degradation of in-plane properties, such as E_x, leaving the thickness modulus E_z unaltered from the undamaged value. It is shown that additional damage mechanisms such as fiber-matrix interfacial debonding, delamination or effective matrix degradation, can lead to lower estimates of the Young's modulus in the thickness direction. The effective composite properties can serve as input parameters in a 3-D FEM to analyze the stress fields in the combustor under operational conditions. A feedback loop between the FEM and the micromechanical model can then be established to define the evolution of the service-induced damage.

From the mechanics viewpoint, we have provided the analytical tools and experimental protocol to enact true composite material design for high-temperature applications, and established a science-based methodology in which the development of new hot section components (ultra-compact combustor) and the enabling materials evolve through interactive studies that couple the component, structure, and material requirements. Aside from the oxide-oxide class of composites (or possibly another form of ceramic-matrix composite), the methodology is also appropriate for application to structural carbon-carbon composites which have numerous functions in thermal protection systems and other space vehicle applications.

Acknowledgement

The authors thank Dr. G. A. Schoeppner of AFRL/MLBC for considerable help with analysis, and Dr. V. A. Buryachenko of UDRI for sharing his results. This research was conducted at the Materials and Manufacturing Directorate, Air Force Research Laboratory (AFRL/MLBC and AFRL/MLLN), Wright-Patterson Air Force Base, OH 45433. This work was sponsored (in part) by the Air Force Office of Scientific Research, USAF. G. P. Tandon and D. J. Buchanan were supported under onsite contract numbers F33615-00-D-5006 and F33615-98-C-5214, respectively.

REFERENCES

(1) Zawada, L. P. and Lee, S. S., "Evaluation of Four CMC's for Aerospace Turbine Engine Divergent Flaps and Seals," Cer. Eng. Sci. Proc., 16 (1995) pp. 337-339.

(2) Mouchon, E. and Colomban, Ph., "Oxide Ceramic Matrix/Oxide Fiber Woven Fabric Composites Exhibiting Dissipative Fracture Behavior," Composites, 26 (1995) pp. 175-182.

(3) Zawada, L. P., "Longitudinal and Transverse Tensile Behavior of Several Oxide/Oxide Composites," Cer. Eng. Sci. Proc., 19 (1998) pp. 327-340.

(4) Heathcote, J. A., Gong, X-Y, Yang, J., Ramamurty, U., and Zok, F. W., "In-Plane Mechanical Properties of an All-Oxide Ceramic Composite," J. Amer. Cer. Soc., 82 (1999) pp. 2721-2730.

(5) Lundberg, R. and Eckerbom, L., "Design and Processing of All-Oxide Composites," Ceramic Transactions, 58 (1995) pp. 95-104.

(6) Lange, F.F., Tu, W.C., and Evans, A.G., "Processing of Damage-Tolerant, Oxidation- Resistant Ceramic Matrix Composites by a Precursor Infiltration and Pyrolysis Method," Materials Science and Engineering, A195 (1995) pp. 145-150.

(7) Zawada, L.P., and Lee, S. S., "The Effect of Hold Times on the Fatigue Behavior of an Oxide/Oxide Ceramic Matrix Composite," ASTM STP 1309 (1996) pp. 69-101.

(8) Zuiker, J. R., "A Model for the Creep Response of Oxide-Oxide Ceramic Matrix Composites," ASTM STP 1309 (1997) pp. 250-263.

(9) Wilson, D. M., Lieder, S. L. and Lueneburg, D. C., "Microstructure and High Temperature Properties of Nextel720 Fibers," Cer. Eng. Sci. Proc., 16 (1995) pp. 1005-1014.

(10) Yun, H.M. and DiCarlo, J. A., "Time/Temperature Dependent Tensile Strength of SiC and Al_2O_3-Based Fibers," NASA Technical Memorandum 107370, NASA Glenn Research Center, Cleveland, OH, USA (1996).

(11) John, R., Buchanan, D. J., and Zawada, L. P., "Notch-Sensitivity of a Woven Oxide/Oxide Ceramic Matrix Composite," ASTM STP 1392 (2000) pp. 172-181.

(12) Liaw, P. K., Yu, N., Hsu, D. K., Miriyala, N., Saini, V., Snead, L. L., McHargue, C. J. and Lowden, R. A., "Moduli Determination of Continuous Fiber Ceramic Composites (CFCCs)," Journal of Nuclear Materials, 219 (1995) pp. 93-100.

(13) Weng, G. J., "Some Elastic Properties of Reinforced Solids, with Special Reference to Isotropic Ones Containing Spherical Inclusions," Int. J. Engineering Science, 22 (1984) pp. 845-856.

(14) Pan, H. H. and Weng, G. J., "Thermal Stress and Volume Change During a Cooling Process Involving Phase Transformation," J. Thermal Stress, 15 (1992) pp. 1-23.

(15) Norris, A. N., "An Examination of the Mori-Tanaka Effective Medium Approximation for Multiphase Composites," J. Applied Mechanics, 56 (1989) pp. 83-88.

(16) Buryachenko, V. A., "Multiparticle Effective Field and Related Methods in Micromechanics of Composite Materials," Applied Mechanics Review, 54 (2001) pp. 1-47.

(17) Buryachenko, V. A., personal communication.

(18) Naik, R. A., "Analysis of Woven and Braided Fabric Reinforced Composites," NASA Contractor Report 194930, NASA Langley Research Center, Hampton, VA (1994).

(19) Pagano, N. J. and Tandon, G. P., "Elastic Response of Multi-Directional Coated Fiber Composites," Composites Science & Technology, 31 (1988) pp. 273-293.

(20) Schoeppner, G. A. and Pagano, N. J., "Stress Fields and Energy Release Rates in Cross-Ply Laminates," Int. J. Solids & Structures, 35 (1998) pp. 1025-1055.

(21) Reissner, E., "On a Variational Theorem in Elasticity," Journal of Mathematics and Physics, 29 (1950) pp. 90-95.

(22) Schoeppner, G. A., and Pagano, N. J., "3D Thermoelastic Moduli and Saturation Crack Density for Cross-Ply Laminates with Transverse Cracks," International Journal of Damage Mechanics, 6 (1999) pp. 273-309.

(23) Tsai, C. L. and Daniel, I. M., "The Behavior of Cracked Crossed-Ply Composite Laminates Under Shear Loading," Int. J. Solids & Structures, 29 (1992) pp. 3251-3267.

(24) Whitney, J. M., "Effective Elastic Constants of Bidirectional Laminates Containing Transverse Ply Cracks," J. Composite Materials, 34 (2000) pp. 954-978.

(25) Pagano, N. J., "Exact Moduli of Anistropic Laminates," in Composite Materials, L. J. Broutman and R. H. Krock eds., Vol. 2: Mechanics of Composite Materials. G. P. Sendeckyj, ed. (1974) pp. 23-44.

(26) N. J. Pagano and G. P. Tandon, "2-D Damage Model for Unidirectional Composites Under Transverse Tension and/or Shear," Mechanics of Composite Materials and Structures, 1 (1994) pp. 119-155.

(27) T. J. Lu and J. W. Hutchinson, "Effect of Matrix Cracking on the Overall Thermal Conductivity of Fibre-Reinforced Composites," Phil. Trans. R. Soc. Lond., A 351 (1995) pp. 595-610.

(28) MD. R. Islam and A. Pramila, "Thermal Conductivity of Fiber Reinforced Composites by the FEM," J. Composite Materials, 33 (1999) pp. 1699-1715.

LIST OF TABLES

Table I: Summary of Thermal and Elastic Property Measurements
Table II: Comparison of Effective Properties of Undamaged Cloth Composite Using Straight-Fiber and Fabric Models
Table III: Influence of Homogenized Matrix Elastic Modulus on Thermoelastic Properties of Undamaged Cloth Composite Using Straight-Fiber Model
Table IV: Summary of Comparison of Experimental Measurements with Predictions of Young's Moduli Simulating Various Failure Modes

LIST OF FIGURES

Figure 1: Microstructure of Woven Nextel720/AS
Figure 2: Magnified View of Microstructure Showing Matrix Cracks due to Processing
Figure 3: Representative Unit Cell (RUC) of an 8-Harness Satin Weave Cloth Composite
Figure 4: Variation of In-Plane Young's Modulus of 8-Harness Satin Weave Composite and Plain Weave Composite with Crimp Angle
Figure 5: A Representative Volume Element for Analyzing Transverse Cracking in Cross-Ply Laminate
Figure 6: Effective (a) Young's Moduli, (b) Poisson's Ratio, (c) Shear Moduli, and (d) Coefficient of Thermal Expansion of Nextel720/AS Composite as a Function of Transverse Crack Spacing
Figure 7: A Representative Volume Element for Analyzing Transverse Cracking and Delamination in Cross-Ply Laminate
Figure 8: Effective (a) Young's Moduli, (b) Poisson's Ratios, (c) Shear Moduli, and (d) Coefficient of Thermal Expansion of Nextel720/AS Composite as a Function of Delamination Length
Figure 9: Transverse Damage Model for Analyzing Fiber-Matrix Debonding and Radial Cracking in a Unidirectional Composite

Table I: Summary of Thermal and Elastic Property Measurements

Property	Measured	Units	Temp.	Fiber Vol. Fraction	Lay-up	Measurement Source
$E_x = E_y$	71 - 75	GPa	23°C	0.465	(0/90)	MLLN
,,	83			0.456	(0/90)	MLLN
,,	78 - 87			0.498	(0/90)	MLLN
E_z	46.2 - 48.2	GPa	23°C	0.434	(±45)	MLLN[1]
,,	51.7			na	(0/90)	MLLN[1]
ν_{xy}	0.07		23°C	0.456	(0/90)	MLLN
,,	0.11			0.456	(0/90)	MLLN
$\nu_{xz} = \nu_{yz}$	0.12		23°C	0.456	(0/90)	MLLN
G_{xy}	17	GPa	23°C	0.434	(±45)	MLLN
$\alpha_x = \alpha_y$	5.85	x 10^{-6}/°C	1100°C	0.498	(0/90)	MLLN[2]
,,	6.45			0.434	(±45)	TPRL[3]
α_z	6.99	x 10^{-6}/°C	1100°C	0.434	(±45)	TPRL[3]
$\mu_x = \mu_y$	2.15	W/(m-K)	1100°C	0.456	(0/90)	TPRL[3]
,,	1.88		1000°C	0.434	(±45)	TPRL[3]
$\mu_{45°}$	1.95		1100°C	0.434	(±45)	TPRL[3]
μ_z	1.62	W/(m-K)	1100°C	0.434	(±45)	TPRL[3]

[1] Measured using ultrasonics;
[2] Measured in servohydraulic test machine
[3] Thermophysical Properties Research Laboratory, Inc.

Table II: Comparison of Effective Properties of Undamaged Cloth Composite Using Straight-Fiber and Fabric Models

Property	Straight-Fiber Model [19]	Fabric Model [18]
E_{zz}(GPa)	116.0	120.3
E_{xx}(GPa)	136.3	138.3
E_{yy}(GPa)	136.3	138.3
ν_{xz}	0.2130	0.2149
ν_{xy}	0.1859	0.1916
ν_{yz}	0.2130	0.2149
G_{xz}(GPa)	48.75	50.45
G_{xy}(GPa)	49.42	51.03
G_{yz}(GPa)	48.75	50.45
α_{xx} (x 10^{-6}/°C)	6.502	6.477
α_{yy} (x 10^{-6}/°C)	6.502	6.477
α_{zx} (x 10^{-6}/°C)	6.719	6.661
μ_{xx} (W/m-K)	3.935	-
μ_{yy} (W/m-K)	3.935	-
μ_{zz} (W/m-K)	3.752	-

Table III: Influence of Homogenized Matrix Elastic Modulus on Thermoelastic Properties of Undamaged Cloth Composite Using Straight-Fiber Model

Property:	E_{eff}=20 GPa	E_{eff}=25GPa	E_{eff}=30 GPa	E_{eff}=69.8GPa
E_{zz}(GPa)	43.35	52.4	60.94	116.0
E_{xx}(GPa)	86.25	92.16	97.81	136.3
E_{yy}(GPa)	86.25	92.16	97.81	136.3
ν_{zx}	0.1113	0.1247	0.1357	0.1814
ν_{xy}	0.1095	0.1241	0.1362	0.1860
ν_{zy}	0.1113	0.1247	0.1357	0.1814
G_{xz}(GPa)	18.34	22.18	25.79	48.73
G_{xy}(GPa)	18.94	22.85	26.51	49.41
G_{yz}(GPa)	18.34	22.18	25.79	48.73
α_{xx}(x 10^{-6}/°C)	6.282	6.320	6.351	6.501
α_{yy}(x 10^{-6}/°C)	6.282	6.320	6.351	6.501
α_{zz}(x 10^{-6}/°C)	6.775	6.762	6.752	6.719

Table IV: Summary of Comparison of Experimental Measurements with Predictions of Young's Moduli Simulating Various Failure Modes

	$E_x = E_y$ (GPa)	E_z (GPa)
Experimental Measurements	7 1- 87	47 - 53
Laminate model {Undamaged}	136	116
Laminate model {Transverse cracking, 25 - 200 μm crack spacing}	80 - 89	116
Micromechanics model {Transverse cracking + interfacial debonding}	86	72
Laminate model {Transverse cracking (48 μm crack spacing) + delamination (42 μm length)}	78	55
Matrix Degradation {E_{eff} = 20 GPa}	86	43

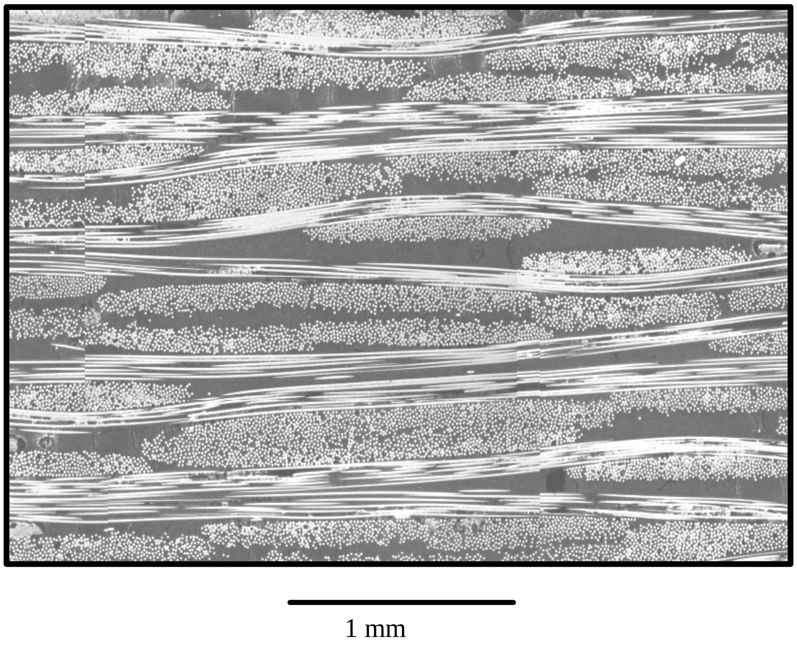

Figure 1: Microstructure of Woven Nextel720/AS

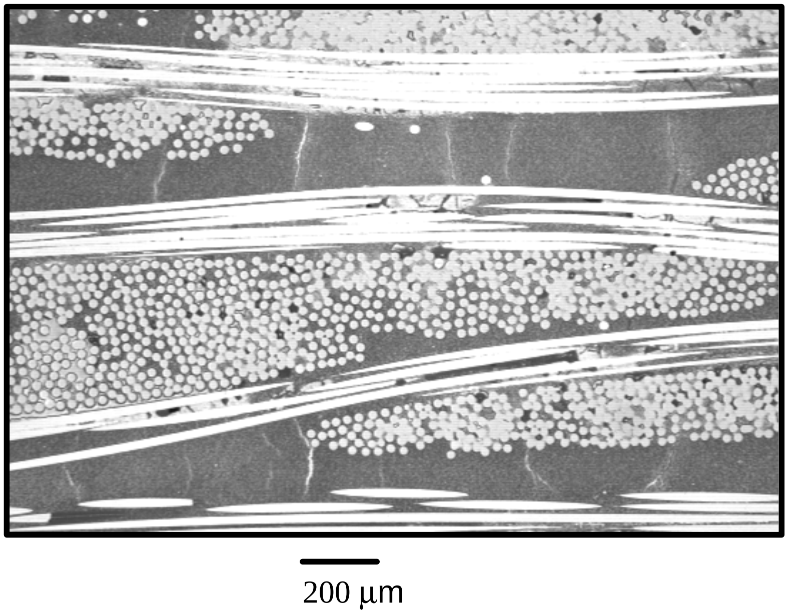

Figure 2: Magnified View of Microstructure Showing Matrix Cracks due to Processing

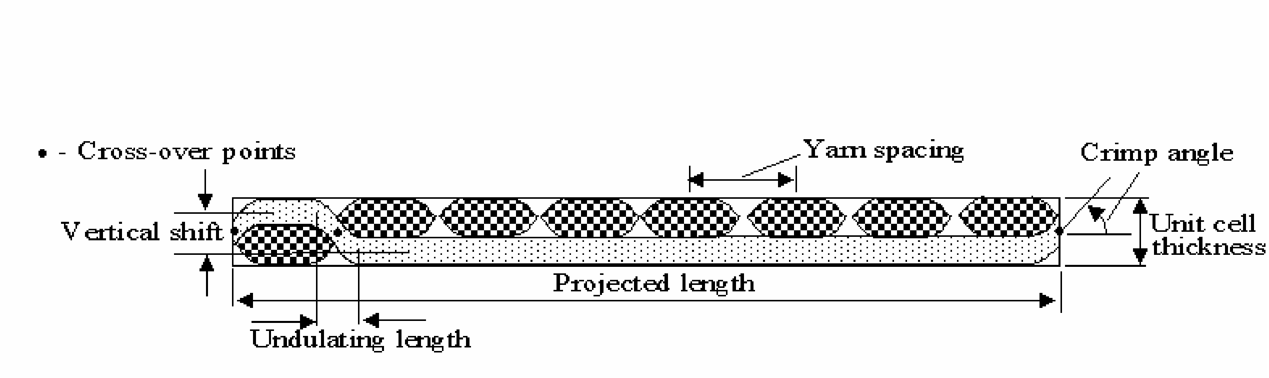

Figure 3: Representative Unit Cell (RUC) of an 8-Harness Satin Weave Cloth Composite

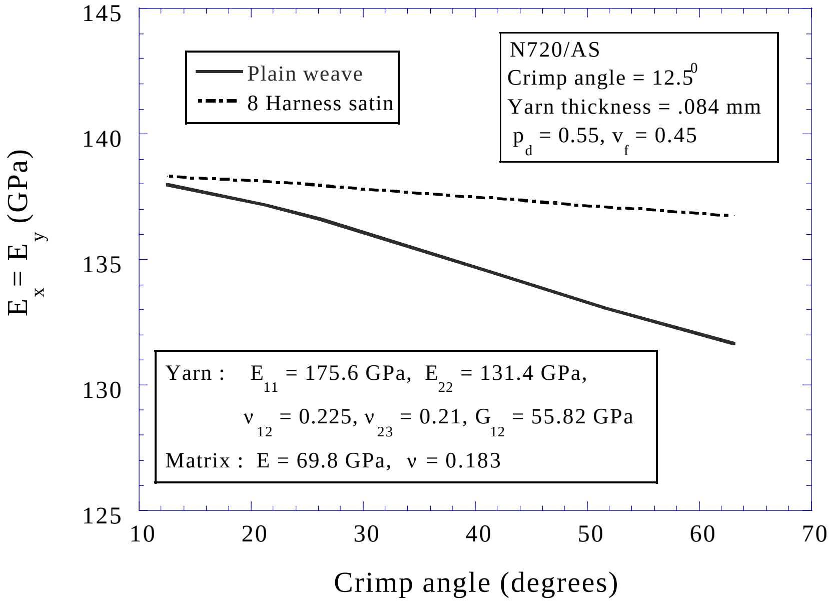

Figure 4: Variation of In-Plane Young's Modulus of 8-Harness Satin Weave Composite and Plain Weave Composite with Crimp Angle

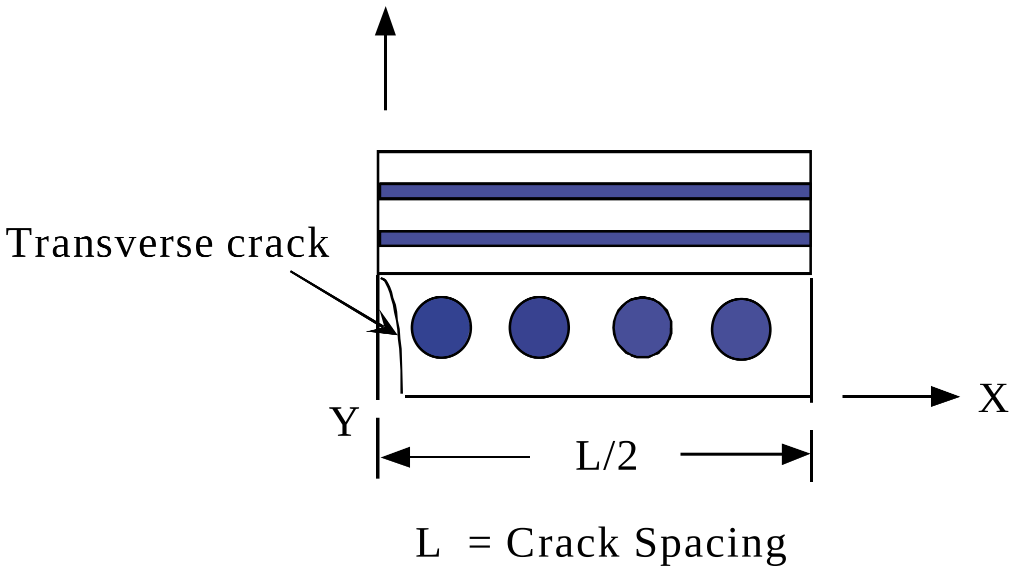

Figure 5: A Representative Volume Element for Analyzing Transverse Cracking in Cross-Ply Laminate

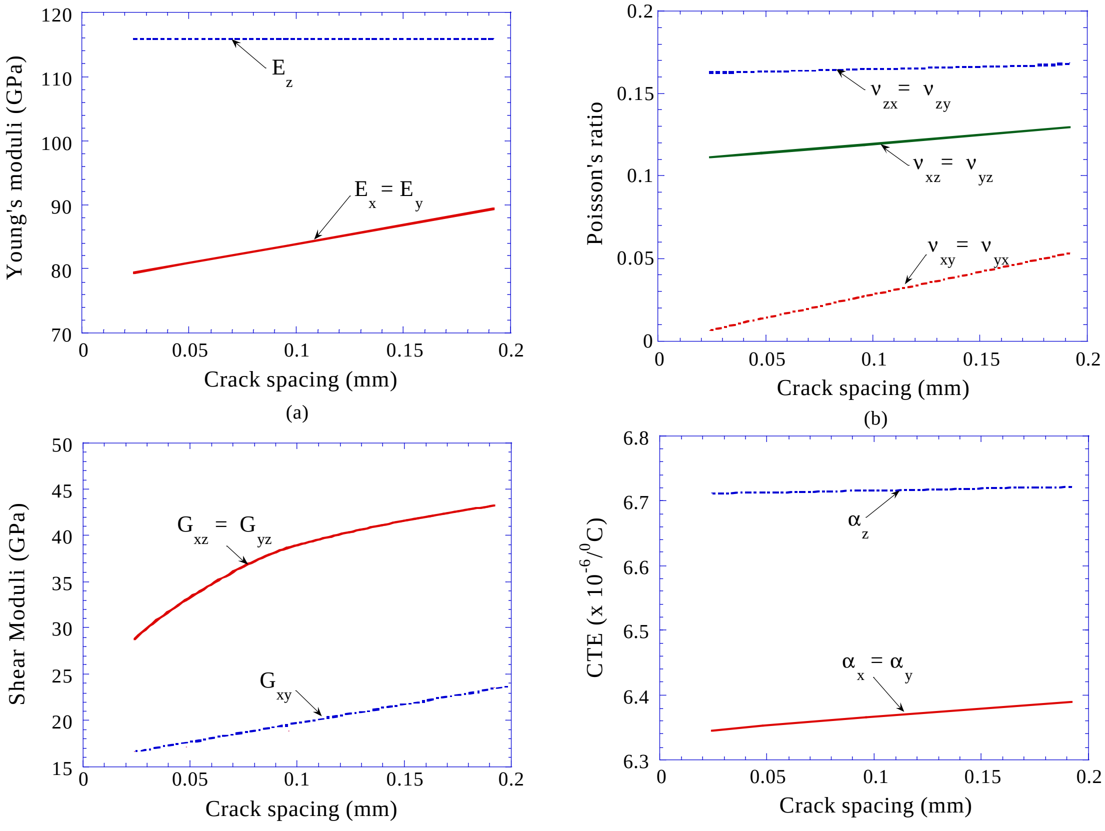

(a)

(b)

(c)

(d)

Figure 6: Effective (a) Young's Moduli, (b) Poisson's Ratios, (c) Shear Moduli, and (d) Coefficient of Thermal Expansion of Nextel720/AS Composite as a Function of Transverse Crack Spacing

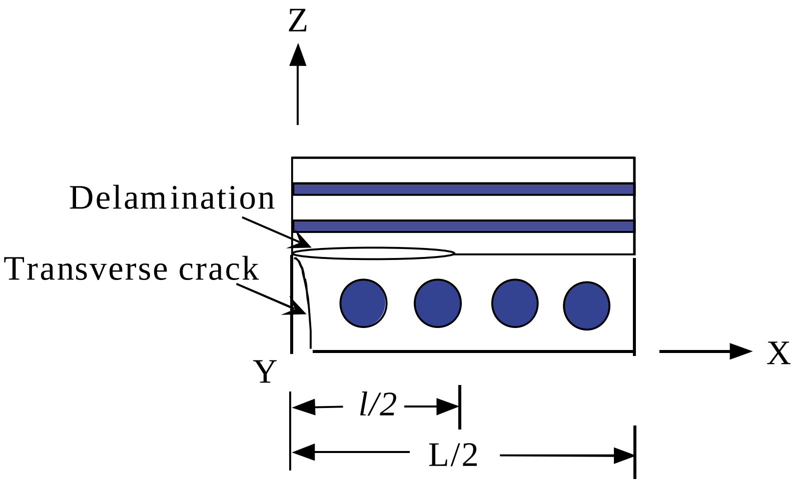

L = Crack Spacing
l = Delamination length

Figure 7: A Representative Volume Element for Analyzing Transverse Cracking and Delamination in Cross-Ply Laminate

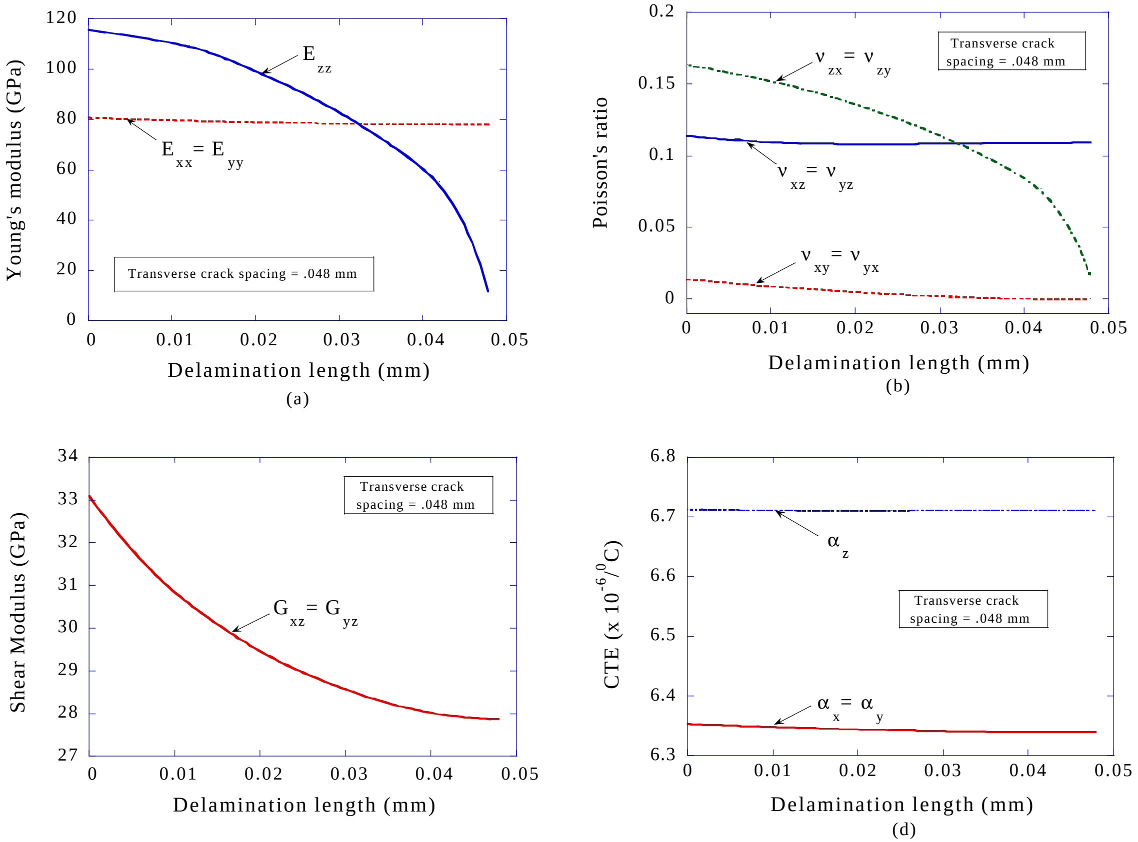

Figure 8: Effective (a) Young's Moduli, (b) Poisson's Ratios, (c) Shear Moduli, and (d) Coefficient of Thermal Expansion of Nextel720/AS Composite as a Function of Delamination Length

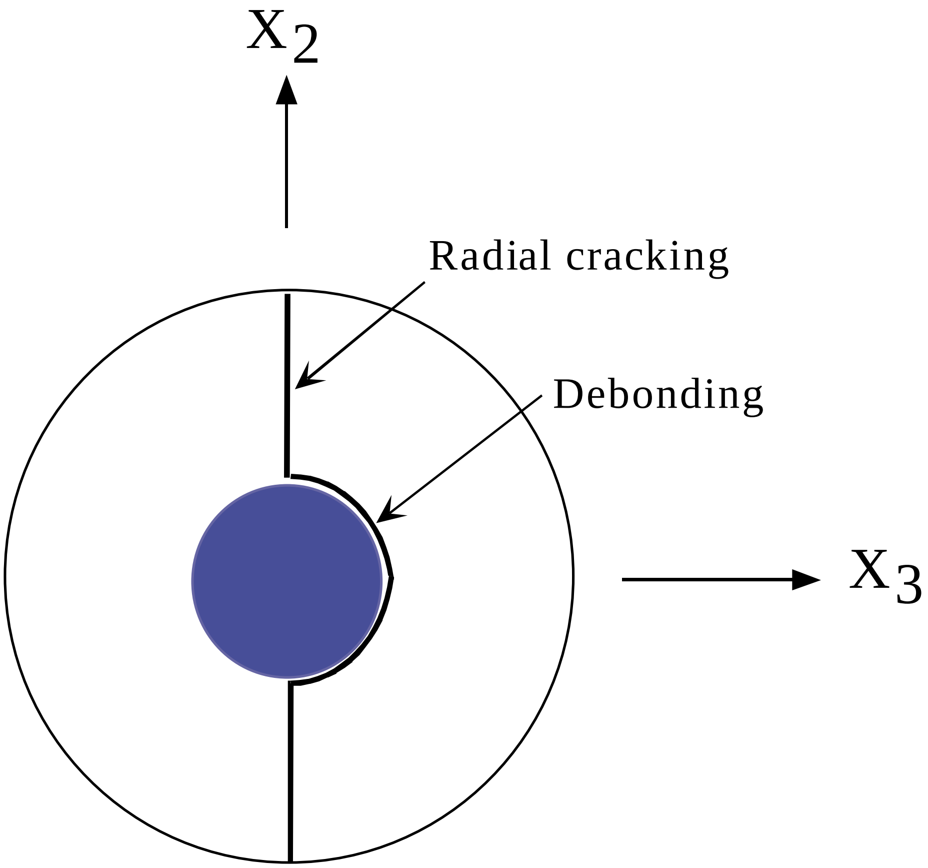

Figure 9: Transverse Damage Model for Analyzing Fiber-Matrix Debonding and Radial Cracking in a Unidirectional Composite

Characterization of Fretting Fatigue Crack Initiation Processes in Ti-6Al-4V

Alisha L. Hutson[1*], Craig Neslen, and Ted Nicholas

Air Force Research Laboratory, Materials and Manufacturing Directorate, Wright-Patterson AFB, OH 45433.

[1]University of Dayton Research Institute 300 College Park, Dayton, OH, U.S.A. 45469-0128 phone: (937) 255-2708; fax: (937) 255-1363; email: alisha.hutson@wpafb.af.mil

ABSTRACT: A study was conducted to quantify fretting fatigue damage and to evaluate the residual fatigue strength of specimens subjected to a range of fretting fatigue test conditions. Flat Ti-6Al-4V specimens were tested against flat Ti-6Al-4V fretting pads with blending radii at the edges of contact. Fretting fatigue damage for two combinations of static average clamping stress and applied axial stress were investigated for two percentages of total life. Accumulated damage was characterized using full field surface roughness evaluation and scanning electron microscopy (SEM). The effect of fretting fatigue on uniaxial fatigue strength was quantified by interrupting fretting fatigue tests, and conducting uniaxial residual fatigue strength tests at R=0.5 at 300 Hz. Results from the residual fatigue strength tests were correlated with characterization results.

While surface roughness measurements, evaluated in terms of asperity height and asperity spacing, reflected changes in the specimen surfaces as a result of fretting fatigue cycling, those changes did not correspond to decreases in residual fatigue strength. Neither means of evaluating surface roughness was able to identify cracks observed during SEM characterization. Residual fatigue strength decreased only in the presence of fretting fatigue cracks with surface lengths of 150 μm or greater, regardless of contact condition or number of applied fretting fatigue cycles. No cracks were observed on specimens tested at the lower stress condition. Threshold stress intensity factors were calculated for cracks identified during SEM characterization. The resulting values were consistent with the threshold identified for naturally initiated cracks that were stress relieved to remove load history effects.

KEYWORDS: fretting fatigue, Ti-6Al-4V, surface roughness

INTRODUCTION

In 1912 Eden, Rose & Cunningham documented findings on a newly discovered phenomenon they identified as fretting corrosion [1]. That paper is considered the first acknowledgement of damage occurring due to the presence of contact between components, and so marks the commencement of study of the effect of contact on structural components. Since that landmark publication, research has been undertaken worldwide to characterize and describe the effects of contact and to understand the sources and progression of contact-related damage [2,3]. During this time, different regimes, characterized mainly by the magnitude of displacement between the components, have been identified experimentally. These regimes, identified as gross slip (fretting wear or galling), mixed slip-stick (fretting fatigue), and stick, have been associated with different damage mechanisms, namely, wear (material removal), cracking and "no damage", of which cracking is considered the most detrimental [4,5].

---

[*] Corresponding author

Identifying these regimes in service components is an extremely difficult task that is not, as yet, totally resolved. In service, the regimes may overlap, causing damage from one regime to be obscured by another – and the transition from one regime to another is unclear, causing further confusion. Thus, the result has been efforts to identify detrimental surface conditions resulting from the contact using criteria whose validity has yet to be proven.

Currently, ultrasonic crack detection and surface features are used to identify fretted components for retirement in the aircraft industry. Existing ultrasonic crack detection technology is hampered by the presence of fretting fatigue roughened surfaces, which may themselves indicate underlying component damage, particularly for blade disk attachments in turbine engines. While this criterion is widely accepted and used to retire costly components, almost no research has been conducted to verify it.

Some efforts have been made to quantify surface features for fretting fatigue [6-9]. The United States Air Force has sponsored work to document surface roughnesses of retired engine components, although no efforts have yet been made to determine the remaining life of those components [10]. The effects of surface roughness on predicted stress profiles have been used to predict fatigue lives of laboratory specimens [8]. Shell and Eylon reported a technique to quantify surface roughnesses of fretted laboratory specimens [9]. The technique was capable of distinguishing between slip, stick and non-contacted regions on those specimens, but the results were never related to underlying damage.

The work discussed in this paper attempts to correlate the surface features quantified using the technique reported by Shell and Eylon with residual fatigue strength of Ti-6Al-4V laboratory specimens. A novel test geometry that simulates the essential loading and geometry features of a turbine engine blade root attachment while maintaining the simplicity of a more generalized geometry is employed [11,12]. Normal and shear loads similar to those present in the dovetail blade attachment during steady state operation are applied to the specimen, as shown in Figure 1. The bending moment indicated on the specimen has been shown to be relatively small and may be neglected [13]. This apparatus also produces the same type of damage as one of the types investigated in the work by Shell and Eylon.

EXPERIMENTAL APPROACH

Two objectives were defined for the current investigation: quantify the reduction of fatigue strength caused by fretting fatigue damage accumulated at two levels of fretting fatigue life, and verify the viability of surface roughness to quantify fretting fatigue damage. To achieve these objectives two series of tests were conducted: one in which the fretting fatigue portion of the experiment was interrupted at a predetermined portion of fretting fatigue life (referred to as 10%-of-life tests), and one in which the specimen was tested until fracture (referred to as 100%-of-life tests). Details on how these tests were conducted are discussed below. These tests were conducted for two combinations of axial and clamping stress. Each series of tests involved application of fretting fatigue cycles, followed by characterization of the fretting damage, heat-tinting to mark the size and location of fretting fatigue-generated cracks, and finally fracture of each specimen under uniaxial fatigue cycling.

Material and Machining Parameters

Fretting fatigue specimens and pads were machined from forged Ti-6Al-4V plates with a $\alpha+\beta$ duplex microstructure. Axial specimens were machined with the fatigue axis oriented in the longitudinal direction. Orientation of the pads was not specified or identified. The material yield strength is 930 MPa; the tensile strength is 980 MPa, and the modulus is 120 GPa. Microstructure details can be found in reference [14]. Specimens and pads were low stress ground and polished to a

RMS 8 μinch surface finish.

Fretting Fatigue Apparatus and Test Conditions

In the apparatus used for this investigation and in related investigations by the authors [11-13,15], a relatively thin, flat specimen was tested against flat pads with a specified blending radius at both edges of contact (see Figure 2). Unlike many typical fretting fatigue test systems, the fretting pads were contained in what is usually considered the grip region, and all of the load applied to the specimen was transferred to the fretting pads through shear. Hence, gross sliding is eliminated for all valid tests and damage is accumulated in a relatively small slip region that occurs at the edge of contact (Figure 2). In this unique configuration the fretting fatigue conditions in each grip are applied independently. For this study, nominally identical fretting fatigue conditions were applied to both ends of the specimen (Figure 3). For specimens that were tested to fracture, one end would fail leaving the other end intact for further characterization. These were identified as “100%-of-life” tests. For specimens that were tested to some fraction of expected total life, two fretting regions were available for characterization – the region indicated by “A” at one end of the specimen, and the region indicated by “B” at the other end of the specimen in Figure 3.

Two fretting fatigue conditions were selected, based on earlier work by some of the authors [13]. Nominal fretting pad lengths were 12.7 mm and 25.4 mm. A blending radius of 3.18 mm was used, resulting in undeformed contact lengths of 6.35 mm and 19.05 mm. A constant average clamping stress of ~200 MPa was obtained using the longer contact length; an average clamping stress of ~620 MPa was obtained using the shorter contact length.

In earlier work, the cyclic axial fretting fatigue limit stress for a 10^7 cycle fatigue life was determined to be ~350 MPa for the lower clamping stress (mean value from six tests – maximum = 405 MPa; minimum = 300 MPa) and ~250 MPa for the higher clamping stress (mean value from six tests – maximum = 276 MPa; minimum = 235 MPa) [13]. These values may be compared to the Haigh stresses, identified in column 3 of Tables 1 and 2 for the fretting fatigue portion of the 100%-of-life tests. Relative slip values for these two combinations of axial fatigue and clamping stress have been calculated using finite elements in prior work and are of the order of tens of microns at the Edge of Contact (EOC), with the value for the ~200 MPa clamping stress condition being higher than the value for the ~650 MPa condition [13,15]. The clamping stresses represent the approximate range of stresses calculated for the blade root region in some stages of the fan and compressor section in aircraft turbine engines. These conditions were identified for an axial stress ratio, R, of 0.5 for tests conducted at 300 Hz under ambient laboratory conditions. Control of clamping conditions was achieved with the use of instrumented bolts so the clamping load could be monitored *in situ* while it was being applied. Details of the test machine and the fretting fatigue fixturing can be found in reference [11].

A unique specimen design, shown in Figure 4, was used to facilitate the residual fatigue strength testing. This twin dogbone specimen was designed to allow fretting fatigue damage to be applied to a specimen suitable for subsequent uniaxial testing with a minimum of post-fretting test modification. For these experiments the fretting fatigue cycles were applied to the specimen, then the specimen was bisected, as indicated by the dashed line in Figure 4, and rectangular Ti-6Al-4V tabs of the same microstructure were laser welded to both ends to create a suitable grip section. Three fretting fatigue specimens were tested for each condition, thus producing three 100%-of-life dogbone specimens and six 10%-of-life dogbone specimens on which residual fatigue strength tests could be conducted for each clamping stress. This quantity of tests was determined to provide sufficient data from which to draw conclusions regarding trends in behavior. Width and thickness of the dogbone gage section was specified as 10 mm and 2 mm, respectively.

Fretting Fatigue Test Procedures

For the 10%-of-life fretting fatigue experiments fretting damage was applied based on the number of cycles. One million fretting cycles were applied at predetermined fretting fatigue limit stresses identified for a 10^7 cycle fatigue life for each clamping condition in the earlier work [13] (see Tables 1 and 2). Then the contact was removed and the specimens were bisected to create dogbone specimens suitable for residual fatigue strength testing. The 10%-of-life damage level was selected, in part, to allow comparison to work in the literature [2,3,16,17], where significant damage evolution up to 10% of life has been reported.

For the 100%-of-life tests, each specimen was tested until fracture using the same clamping conditions as those selected for the 10%-of-life tests. A step loading technique was used in applying the axial fatigue cycles, for which the specimen was loaded in fatigue at a selected load level (different from that used in the 10%-of-life tests) for 10^7 cycles. Then the stress was increased by five percent and the test was continued for another 10^7 cycles. The load steps were continued until fracture of one end of the specimen. The stress at the final block, the prior stress and the number of cycles applied at the final stress were then used to calculate a limit stress for the 10^7 cycle fatigue life, also known as a Haigh stress [18]. Failure of the specimen during the first loading block can occur, in which case the results correspond to a point on an S-N curve. Initial stress levels were selected based on the expected material fretting fatigue strength. After fracture, one dogbone section from each specimen was still intact, and bore damage accumulated at conditions nearly identical to the conditions that fractured the other end of the specimen. The fracture portion of the specimen was removed to allow characterization and uniaxial fatigue testing of the intact portion.

Characterization of Fretting Fatigue Damage

Fretting fatigue damage was characterized using two independent techniques: Scanning Electron Microscopy and surface roughness measurement. Characterization in the Scanning Electron Microscope (SEM) was conducted using a small bend fixture designed to fit in the SEM chamber. By using this fixture, the specimens could be inspected in the SEM while under a small bend load that would open cracks to improve visibility. All of the imaging conducted in the SEM was done using backscatter emission that enhances variations in grain structure and elemental content. In the context of this study, the backscatter imaging augmented the wear product imaging to allow qualitative analysis of wear debris.

The second characterization technique, that of surface roughness quantification, was facilitated by a white light interferometer designed to make full field measurements of surface topography with transverse resolution of 0.1 μm and vertical resolution of 3 nm [9]. All of the scans were performed at 100X magnification. Four fretting regions (two on each side), 60 μm x 45 μm, were scanned on each dogbone specimen (see inset in Figure 5). Regions along the EOC near the free edges of the specimens were selected based on optical assessments of where the worst fretting damage was located and based on results from previous work [12,19] indicating the edges as the locations most likely to nucleate fretting fatigue cracks. Details of how these locations were tracked are discussed below. Additional scans of non-fretted regions were performed to provide a baseline for comparison with the data from fretted regions. Note that surface scans to measure roughness were made in the direction of the machining texture (that is parallel to the fatigue loading axis of the specimens) to factor out machining roughness as much as possible, since the fretting induced roughnesses are of the order of the machining roughness.

The data acquisition software for the white light interferometer includes the capability to calculate average roughness values by several methods and to perform a Fourier transform of the surface profile to allow the data to be viewed in the frequency domain. By transforming the data from the spatial domain to the frequency domain, the user can view 3-dimensional data on a 2-dimensional plot of Power Spectral Density (PSD) vs. spatial frequency. These curves allow quantification of changes in surface roughness in a systematic fashion by quantifying the peak-to-peak asperity spacing population. The largest PSD values occur near zero spatial frequency, because the samples are nominally flat. Smaller PSD values occur for higher spatial frequencies, which correspond to closely spaced asperities. A prior investigation has indicated that the occurrence of smaller asperity spacing will increase as a function of fretting wear, thus providing a potential indicator of underlying fretting fatigue damage. [9]

Residual Fatigue Strength Tests

Following the fretting fatigue damage characterization, the dogbone specimens were heat tinted at 420°C for 4 hours in air to mark the location and size of any cracks, and were then tested to fracture in uniaxial fatigue to quantify the remaining specimen strength. The effect of this process on crack growth behavior has been shown to be negligible [20]. As with the fretting fatigue portion of the 100%-of-life tests, these tests were completed using a step loading technique to obtain fatigue limit stresses for a 10^7 cycle fatigue life. The dogbone specimen design, which incorporates a Kt = 1.1, allowed quantification of residual fatigue strength reductions of 10% or more from the baseline fatigue strength of 660 MPa (for a 10^7 cycle fatigue life at R = 0.5) determined for this material in an earlier study [18]. Uniaxial tests were conducted at room temperature at 300 Hz and R = 0.5, using the same test system as that used to apply fretting fatigue cycles to retain similarity to the fretting fatigue portion of the test. In a number of cases, the estimated fatigue strength of the specimen was lower than expected. In these cases, failure occurred within the first block of the step test, and the datum became a point on an S-N curve corresponding to a life less than 10^7.

RESULTS & DISCUSSION

Characterization Results

The results of the characterization techniques incorporated in this study reflected changes in the surface of each specimen that might be considered fretting fatigue damage. Those changes are discussed below for surface roughness, PSD curves and SEM inspection, respectively.

Results from the surface roughness measurements are shown in Figures 5 and 6. Figure 5 includes roughness data for specimens that failed within the gage section. Figure 6 includes data for specimens that failed outside of the gage section. Tables 1 and 2 indicate which specimens fractured at the fretted region. Specimen numbers are given on the X-axis of each plot and correspond to the specimen numbers listed in the tables. Specimens with numbers beginning in “01” are 10%-of-life specimens; those beginning in “02” are 100%-of-life specimens.

A single average roughness value is shown for each of four regions that were inspected using the white light interferometer. The regions are numbered from one to four with respect to the orientation of the specimen during fretting fatigue application (see inset in Figure 5 – note black arrow indicates top, right, front of specimen). In Figures 5 and 6, the measurements from the fretting fatigue regions are shown with data taken from as-machined surfaces (note horizontal lines – bold line indicates average of 12 measurements, “Max.” line indicates maximum as-received roughness measurement, “Min.” line indicates minimum as-received roughness measurement). Some of the measurements reflect considerable increase in surface roughness with respect to the unfretted surfaces; however, most of the roughness values are within the scatter of measurements taken from the as-received surfaces.

The data from the full field roughness profiles were also reduced by performing a Fourier transform resulting in PSD vs. spatial frequency curves. Twelve surface profiles were recorded in uncontacted regions of several samples to quantify the level of scatter in the measurement technique for the test specimens used in this investigation. The results of the unfretted scans are shown in Figure 7, which includes the highest and lowest curves and the average curve calculated for all twelve measurements. PSD values at the higher spatial frequencies vary by about an order of magnitude. Note that the curves shown in Figures 7 through 9 show only a few data points. Cubic spline curve fits were used to represent the remaining data.

Scans of fretted regions were taken near the edges of each specimen, where fretting fatigue cracks have been identified in previous studies [12,19] and where fretting damage appeared to be the worst. For each of these scans, the Fourier transform was performed, the PSD values were normalized with average unfretted PSD values to calculate the FFDP (Fretting Fatigue Damage Parameter) discussed below, and the PSD results were plotted against spatial frequency. The four PSD data sets from each specimen were also averaged to provide data on the general trend of damage for each specimen. Individual curves are not shown here due to space limitations. Typical average PSD curves from the four experimental conditions are shown in Figure 8, along with the average unfretted PSD curve included in Figure 7. (note: the hollow diamonds in Figure 7 correspond to the solid triangles in Figure 8.) In general, a higher population of larger spatial frequency (and thus smaller asperity spacing) can be observed for all of the fretting damage levels, but particularly for the 10%-of-life + low clamping stress and the 100%-of-life + high clamping stress conditions. An increase in the population of other spatial frequencies is also present, reflecting the level of wear on the surface compared to the as-received surface.

The FFDP, which quantifies the fretted PSD deviation from the as-received condition, is shown in Figure 9 for the same four cases shown in Figure 8. Results for the low clamping stress condition are higher than for the high clamping stress condition. This finding is not entirely unexpected, since lower clamping stresses allow greater freedom of motion, and with greater motion comes greater wear [4,21,22]. At low clamping stress and 100%-of-life, however, the data coincide with the high clamping stress data for high spatial frequencies (>3 μm). The data for all conditions seem to peak between spatial frequency values of 1 and 2, corresponding to 1.0 and 0.5 μm asperity spacing, respectively. In the original work with this technique, the FFDP vs. spatial frequency curves were, more or less, monotonically increasing with increasing spatial frequency, but data were not recorded beyond a spatial frequency value of 1.2. Peaks, such as the ones observed here, might be expected for surfaces with initial asperity spacing of ~1.0 μm. Without considerable breakdown and embrittlement of wear debris, no particles capable of inducing smaller topographical features would be present. Such breakdown of wear debris is not typically observed under contact conditions such as these.

Each specimen was also characterized in the SEM after application of fretting damage to provide qualitative information on the level of damage generated in each test, and to identify the presence of cracks, if any. In general, wear debris was minimal, particularly for the higher clamping stress condition (see Figures 10 and 11). None of the specimens showed sufficient wear damage to indicate a decrease in fatigue strength due to wear mechanisms. In some cases at the higher clamping stress, the edge of contact where debris usually builds up was almost indistinguishable from the as-received surface (see Figure 11). Wear damage was worst within 1 mm of the edges of the specimens, and diminished toward the center.

Cracks were identified for approximately half of the specimens subjected to fretting fatigue under the higher clamping stress condition, indicated in Table 1. In the low clamping stress condition, however, no cracks were identified in any of the specimens on which uniaxial fatigue strength tests were to be conducted, either at the 10%-of-life or the 100%-of-life damage levels. This observation is interesting in light of findings in the literature that fretting fatigue cracks nucleate very early in life.

Assuming the observations made here are an accurate representation of this particular contact condition, the findings would suggest that stress or strain criteria are a predominating factor in the nucleation of fretting fatigue cracks.

Residual Fatigue Strength Results and Correlation with Characterization Results

Results of the uniaxial fatigue tests are shown in Figures 12 and 13. In Figure 12 cycles to failure are plotted against maximum fatigue limit stress. Baseline data from earlier work on the same alloy are included for comparison [18]. Note that the cycle count for all of the data at or beyond 10^7 cycles is intended as 10^7 cycles, but some have been plotted at slightly higher cycle counts for clarity. The data from the fretted specimens are grouped by level of applied fretting fatigue damage (10% or 100%-of-life) and type of failure (Fretting Fatigue or non-Fretting Fatigue), although no apparent trend is in evidence based on these criteria. In general, the scatter in the tests that resulted in non-fretting fatigue related failures is approximately what would be expected for fatigue lives of this magnitude. The surface length of the crack is noted at the result for each specimen on which a crack was observed.

Fatigue limit stress data corresponding to 10^7 cycles from Figure 12 are re-plotted in Figure 13 for all specimens on which cracks were observed after fretting fatigue testing. The plot of stress as a function of crack depth, a, is in the form of a Kitagawa type diagram [23], which shows how small cracks cannot follow long crack fracture mechanics analysis because the endurance limit stress provides an upper limit for the stress corresponding to no crack. The intersection of the long crack fracture mechanics solution, corresponding to ? K=2.9MPavm, is defined as a_0. For cracks below a_0 (51.6 μm), it can be seen that there is essentially no debit in fatigue strength. In fact, for one specimen shown with an upward arrow, the fatigue failure was in a region away from the observed crack.

Of specific interest in this study is the correlation of the characterization results, discussed above, and the residual fatigue properties of each specimen. The results of each characterization technique, surface roughness, PSD vs. spatial frequency, and SEM inspection, have been described. The efficacy of each technique to quantify fretting fatigue damage will be discussed in light of the uniaxial fatigue results.

Most of the results of surface roughness measurements were determined to be within the level of scatter expected for the as-received surface, although a few were higher. As indicated in Figure 5, higher roughness values do not always reflect the presence of cracks. Two specimens reported in the chart (01-457 and 02-004) had regions with higher roughness values than the roughness measured in the vicinity of the crack. Also, measured roughness values were very high for one specimen (01-452) on which no cracks were found. So, average surface roughness measurements do not adequately quantify fretting fatigue damage.

Asperity spacing, quantified by the PSD vs. Spatial Frequency curves, did not effectively identify reductions in fatigue strength either. The specimen with the highest roughness values (01-452) is represented by the curve with the hollow circles in Figure 8. As one might expect, it also has the highest population of closely spaced asperities, but failure of this specimen occurred away from the fretting damage and at a stress consistent with the as-received material strength of ~660 MPa. On the specimen with the largest observed crack (01-449), the highest average roughness measurements occurred in the region of the crack, but the PSD vs. Spatial frequency curve is only slightly higher than the average curve for unfretted measurements. It must be concluded, therefore, that for the contact geometry used in this investigation no correlation exists between surface roughness, as quantified either by asperity height (average surface roughness) or asperity spacing (PSD vs. spatial frequency), and underlying fretting fatigue damage.

The one correlation that stands out is that between crack presence, identified in the SEM, and residual fatigue strength. All but one of the specimens on which measurable cracks were identified failed at those cracks during the uniaxial fatigue tests. The size of the crack was an important factor in the remaining strength of the specimen, as might be expected (see Figure 13). Measurable reductions in strength are indicated for specimens with cracks with surface lengths as small as 150 μm (see Figures 12 and 13 and Table 3). However, no reduction in strength was identified for the specimen with a very small crack, 25 μm, an observation also noted in other studies for cracks nucleated under either uniaxial fatigue or fretting fatigue conditions [20,24].

After the uniaxial fatigue tests were completed, the resulting fracture surfaces were inspected, either optically or in the SEM, for all samples that fractured in the gage section. Fractography was particularly important to determine crack shape and type for the specimens determined to have fretting fatigue nucleated cracks. Fretting fatigue cracks are generally thought to be shallow compared to the surface length due to the concentration of stresses on the surface of the specimen in the vicinity of the contact. This assumption is supported by observations for the 750 μm crack (see Figure 14) identified on 01-455. The longer crack (1.2 mm, see Figure 15) was also shallow compared to the total surface length; however, the fracture surface revealed three smaller cracks propagating in tandem, rather than a single crack. The authors have hypothesized on the likelihood of multiple simultaneous cracks in previous work [13], but have not been able to show such irrefutable evidence before this. Aspect ratios closer to unity were observed for the smaller cracks, which might be expected considering the nature of the stress distribution. Previous work in which the stress distributions were calculated using finite elements indicated that the increases in stress generated by the presence of the clamping load on the contact tend to diminish within 100 μm or less, depending on the applied stresses [15]. Observations of the semi-elliptical crack shape for smaller cracks are consistent with the stress distributions reported in that work.

Stress Intensity Factors

Another important piece of information obtained from these experiments relates to the behavior of fretting fatigue nucleated cracks. It is well known that crack behavior can be affected by load history effects, and fretting fatigue cracks, which nucleate under multi-axial loading in mixed-mode in the presence of contacting components, are no exception. These load history effects include biasing the threshold stress intensity factor below which crack propagation does not take place, or $\Delta K_{threshold}$, an important factor in damage tolerant component design. Because fretting fatigue loading conditions are so complex, the exact load history of the region in which the cracks nucleate is seldom known, except in the case of Hertzian contacts where local stress distributions may be calculated.

For the experiments conducted in this study, the stress to propagate a fretting fatigue crack was effectively measured via the step loading approach used to determine the residual fatigue strength of the specimens. The $\Delta K_{threshold}$ values from specimens bearing fretting fatigue cracks were calculated from this stress and the crack size measurements taken from fracture surfaces (see Table 3 and Figures 14 and 15).

The results for each specimen compare favorably with the $\Delta K_{threshold}$ determined for this material (~2.9 MPavm) for R = 0.5 on specimens with naturally initiated cracks that were stress relieved to remove load history effects [20]. The long, shallow crack from 01-455 seemed likely to propagate into the depth, as would be expected. The corner crack from 01-449 seemed more likely to propagate than the adjacent surface cracks, assuming no interaction between the cracks. The point corresponding to the 01-449 result on the Kitegawa diagram (Figure 13) indicates the largest deviation from the long crack model. This result that suggests that interaction between the cracks does occur and that assumptions related to crack geometry may be difficult to apply to fretting fatigue nucleated cracks. However, the authors can conclude from these results that the residual stresses expected from the fretting fatigue portion of the test did not affect resulting $\Delta K_{threshold}$ values at this stress ratio. The effect of residual stresses for lower stress ratios was not determined.

CONCLUSIONS

1. No correlation between surface roughness and underlying fretting fatigue damage was identified for the mixed slip-stick conditions and relative displacements of the order of tens of microns of the type produced in this test apparatus.
2. Fretting fatigue cracks having surface lengths of 100 μm or less nucleated under the conditions discussed above do not reduce the fatigue strength of the material, as shown in the Kitegawa type diagram.
3. Crack growth threshold behavior of the fretting fatigue nucleated cracks was consistent with uniaxial long crack behavior, and was not affected by any residual stresses which might develop under the conditions used in this study.

ACKNOWLEDGEMENTS

This work was performed at Air Force Research Laboratory in the Materials and Manufacturing Directorate (AFRL/MLLMN) under the National Turbine Engine High Cycle Fatigue Program and was funded under contract to the University of Dayton Research Institute, Air Force Contract No. 33615-98-C-5214.

REFERENCES

1. Eden, E. M., Rose, W. N. and Cunningham, F. L., “Endurance of Metals,” Proceedings of the Institute of Mechanical Engineers, Vol.4, 1911, pp. 839-974.

2. *Fretting Fatigue, ESIS 18*, R.B. Waterhouse and T.C. Lindley, Eds., Mechanical Engineering Publications, London, 1994, pp. 219-238.

3. *Standardization of Fretting Fatigue Test Methods and Equipment, ASTM STP 1159*, M. Helmi Attia, and R. B. Waterhouse, Eds., American Society for Testing and Materials, Philadelphia, 1992, pp. 153-169.

4. Bryggman, U. and Söderberg, S., “Contact Conditions and Surface Degradation Mechanisms in Low Amplitude Fretting”, *Wear*, Vol. 125, 1988, pp. 39-52.

5. Zhou, Z. R. and Vincent, L., “Mixed Fretting Regime,” *Wear*, Vol. 181-183, 1995, pp. 551-536.

6. Ruiz, C., Wang, Z. P. and Webb, P. H., “Techniques for the Characterization of Fretting Fatigue Damage,” *Standardization of Fretting Fatigue Test Methods and Equipment, ASTM STP 1159*, M. Helmi Attia, and R. B. Waterhouse, Eds., American Society for Testing and Materials, Philadelphia, 1992, pp. 170-177.

7. Fouvry, S., Kapsa, P. and Vincent, L., “Quantification of Fretting Damage,” *Wear,* Vol. 200 (1996), pp. 186-205.

8. Murthy, H., Farris, T. N. and Slavik, D. C., "Fretting Fatigue of Ti-6Al-4V Subjected to Blade/Disk Type Contacts," *Developments in Fracture Mechanics for the New Century, 50th Anniversary of Japan Society of Materials Science*, Osaka, Japan, 2001.

9. Shell, E. and Eylon, D., " A New Method for Detection and Quantification of Fretting Fatigue Damage," *Light Materials for Transport Systems 2001 (LiMAT 2001)*, Kim, N. J., Lee, C. S. and Eylon, D., eds., Center for Advanced Aerospace Materials, Pohang, Korea, 2001, pp. 133-140.

10. Braun, T., unpublished work, Veridian Engineering, Dayton, OH.

11. Hutson, A., Nicholas, T., and Goodman, R., "Fretting Fatigue of Ti-6Al-4V Under Flat-on-Flat Contact", *International Journal of Fatigue*, Vol. 21, No 7, 1999, pp. 663 – 670.

12. Hutson, A. L., Ashbaugh, N. E., and Nicholas, T., "An Investigation of Fretting Fatigue Crack Nucleation Life of Ti-6Al-4V Under Flat-on-Flat Contact," *Fretting Fatigue: Experimental and Analytical Results, ASTM STP 1425*, S. E. Kinyon, D. H. Hoeppner and Y. Mutoh, Eds., American Society for Testing and Materials, West Conshohocken, PA, 2002. (submitted July 2001).

13. Hutson, A. L., "Fretting Fatigue of Ti-6Al-4V under a Flat-on-Flat Contact with Blending Radii," *Masters Thesis*, University of Dayton, Dayton, OH, August 2000.

14. Haritos, G.K., Nicholas, T. and Lanning, D., "Notch Size Effects in HCF Behavior of Ti-6Al-4V," *International Journal of Fatigue*, Vol. 21, No 7, 1999, pp. 643 – 652.

15. Hutson, A. L., Nicholas, T., Olson, S. E. and Ashbaugh, N. E., "Effect of Sample Thickness on Local Contact Behavior in a Flat-on-Flat Fretting Fatigue Apparatus," *International Journal of Fatigue*, Vol. 23, 2001, pp. S445-S453.

16. Endo, K. and Goto, H., "Initiation and Propagation of Fretting Fatigue Cracks," *Wear*, Vol. 38, 1976, pp. 311-324.

17. Nix, K.J. and Lindley, T.C., "The Application of Fracture Mechanics to Fretting Fatigue," *Fatigue and Fracture of Engineering Materials Structures*, Vol. 8, No. 2, 1985, pp. 143-160.

18. Maxwell, D.C. and Nicholas, T., "A Rapid Method for Generation of a Haigh Diagram for High Cycle Fatigue," *Fatigue and Fracture Mechanics: 29th Volume, ASTM STP 1321*, T.L. Panotin and S.D. Sheppard, Eds., American Society for Testing and Materials, West Conshohocken, PA, 1999, pp. 626-641.

19. Hutson, A. and Nicholas, T., "Fretting Fatigue Behavior of Ti-6Al-4V against Ti-6Al-4V under Flat-on-Flat Contact with Blending Radii," *Fretting Fatigue: Current Technologies and Practices, ASTM STP 1367*, D.W. Hoeppner, V. Chandrasekaran, and C.B. Elliot, Eds., American Society for Testing and Materials, West Conshohocken, PA, 1999, pp. 308 - 321.

20. Moshier, M.A., Nicholas, T. and Hillberry, B.M., "High Cycle Fatigue Threshold in the Presence of Naturally Initiated Small Surface Cracks," *Fatigue and Fracture Mechanics: 33rd Volume, ASTM STP 1417*, W.G. Reuter and R.S. Piascik, Eds., American Society for Testing and Materials, West Conshohocken, PA, 2002. (submitted June 2001).

21. Blanchard, P., Colombie, C., Pellerin, V., Fayeulle, S. and Vincent, L. "Material Effects in Fretting Wear - Application to Iron, Titanium, and Aluminum Alloys," *Metallurgical Transactions*, Vol. 22A, 1991, pp. 1535-1544.

22. Fouvry, S., Kapsa, Ph. and Vincent, L., "Analysis of Sliding Behavior for Fretting Loadings: Determination of Transition Criteria," *Wear*, Vol. 185, 1995, pp. 35-46.

23. Kitagawa, H. and Takahashi, S., "Applicability of Fracture Mechanics to Very Small Cracks or the Cracks in the Early Stage," Proc. of Second International Conference on Mechanical Behaviour of Materials (Boston, MA: 1976) 627-631.

24. Nicholas, T., "Step Loading, Coaxing and Small Crack Thresholds in Ti-6Al-4V under High Cycle Fatigue," *Fatigue – David L Davidson Symposium*, K.S. Chan, P.K. Liaw, R.S. Bellows, T.C. Zogas and W.O. Soboyejo, Eds., TMS (The Minerals, Metals & Materials Society), Warrendale, 2002, pp. 91-106.

FIGURE CAPTIONS

Figure 1. Blade/Disk attachment and experimental apparatus load schematic.

Figure 2. Test fixture schematic indicating pad lengths, distance from center of specimen to lower edge of pad, and blending radius at edge of contact.

Figure 3. Test load train schematic. Letters indicate regions of the specimen subject to fretting fatigue.

Figure 4. Twin dogbone specimen schematic. Note: dashed line indicates bisecting line for post-fretting fatigue characterization and testing.

Figure 5. Roughness results for specimens that failed in the gage section. Inset diagram indicates the scan locations that correspond to the numbers in the legend. Asterisks indicate specimens with fretting fatigue-nucleated cracks.

Figure 6. Roughness results for specimens that weren't tested or failed outside of the gage section. See inset on Figure 3 for definition of legend.

Figure 7. Representation of scatter in roughness measurements in terms of Unfretted PSD vs. spatial frequency.

Figure 8. Comparison of fretted and unfretted PSD data. Note "unfretted" data is the same curve as the "Average PSD" shown in Figure 5.

Figure 9. Comparison of FFDP for fretted conditions shown in Figure 6.

Figure 10. Fretting damage at 10%-of-life for lower clamping stress. Average Roughness ˜ 500 nm.

Figure 11. Fretting damage at 10%-of-life for higher clamping stress. Average Roughness ˜ 275 nm.

Figure 12. Residual fatigue results for fretting-fatigue damaged specimens compared with baseline fatigue results.

Figure 13. Kitagawa-Takahashi type representation of residual fatigue strength results for fretting-fatigue damaged specimens exhibiting cracks.

Figure 14. SEM image of 700 μm fretting fatigue crack (above – contact region is on the top half of the image) and corresponding fracture surface (below). Specimen edge is shown to the left of the images. The dark region on the fracture surface indicates the depth of the crack at the time the contact was removed.

Figure 15. SEM image of 1.2 mm fretting fatigue crack (above – contact region is on the top half of the image) and corresponding fracture surface (below). Specimen edge is shown to the right of the images. The three separate dark region on the fracture surface indicate the size of the cracks at the time the contact was removed.

Table #1 – Residual fatigue strength test results for high clamping stress fretting condition
* no surface roughness measurements taken
# fatigue limit stress reported for 10^7 cycle fatigue life – not actual applied cycles
(one 100%-of-life test for this condition is not reported because the specimen was damaged during uniaxial test setup)

	Fretting Test Conditions			**Uniaxial Fatigue Results**		
Specimen number	**Normal stress (MPa)**	**FF Failure stress or Haigh Stress**	**Nf or Nfret**	**Stress @ failure point**	**Nf**	**failure point**
01-449	638	260	1,000,000	277	10,000,000#	crack; 1.2 mm
01-450	645	260	1,000,000	840	5,778,513	blend radius
01-455*	651	260	1,000,000	319	10,000,000#	crack; 750 micron
01-456	649	260	1,000,000	605	3,675,872	blend radius
01-457	652	260	1,000,000	620	252,524	crack; 200 micron
01-458*	643	260	1,000,000	669	10,000,000#	fretting; 25 micron
02-004	616	302.2	10,000,000#	483	10,000,000#	crack; 150 micron
02-006	632	276.3	10,000,000#	663	10,000,000#	blend radius

Table #2 – Residual fatigue strength test results for low clamping stress fretting condition
* no surface roughness measurements taken
# fatigue limit stress reported for 10^7 cycle fatigue life – not actual applied cycles

	Fretting Test Conditions			**Uniaxial Fatigue Results**		
Specimen number	**Normal stress (MPa)**	**FF Failure stress or Haigh Stress**	**Nf or Nfret**	**Stress @ failure point**	**Nf**	**failure point**
01-447	238	350	1,000,000	600	1,418,744	grip
01-448	240	350	1,000,000	538	10,000,000#	grip
01-451	239	350	1,000,000	840	2,903,377	blend radius
01-452	239	350	1,000,000	557	10,000,000#	gage, non-FF
01-453*	238	350	1,000,000	664	10,000,000#	gage, non-FF
01-454	239	350	1,000,000	550	1,900,172	gage, non-FF
01-460*	234	338.7	10,000,000#	567	10,000,000#	blend radius
02-001	212	368.3	10,000,000#	579	10,000,000#	gage, non-FF
02-002	210	403.5	10,000,000#	602	10,000,000#	gage, non-FF

Table #3 – Stress Intensity factor results calculated for fretting fatigue cracks

Specimen number	Crack Type	c (μm)	a (μm)	final stress (MPa)	ΔKa	ΔKc
01-455	surface	350	160	324	3.9	1.9
01-457	surface	90	50	620	3.4	2.8
02-004	corner	125	110	496	3.5	3.3
01-449a	surface	265	170	280	2.7	2.3
01-449b	surface	235	160	280	2.5	2.3
01-449c	corner	290	295	280	3.0	3.1
baseline					2.9	2.9

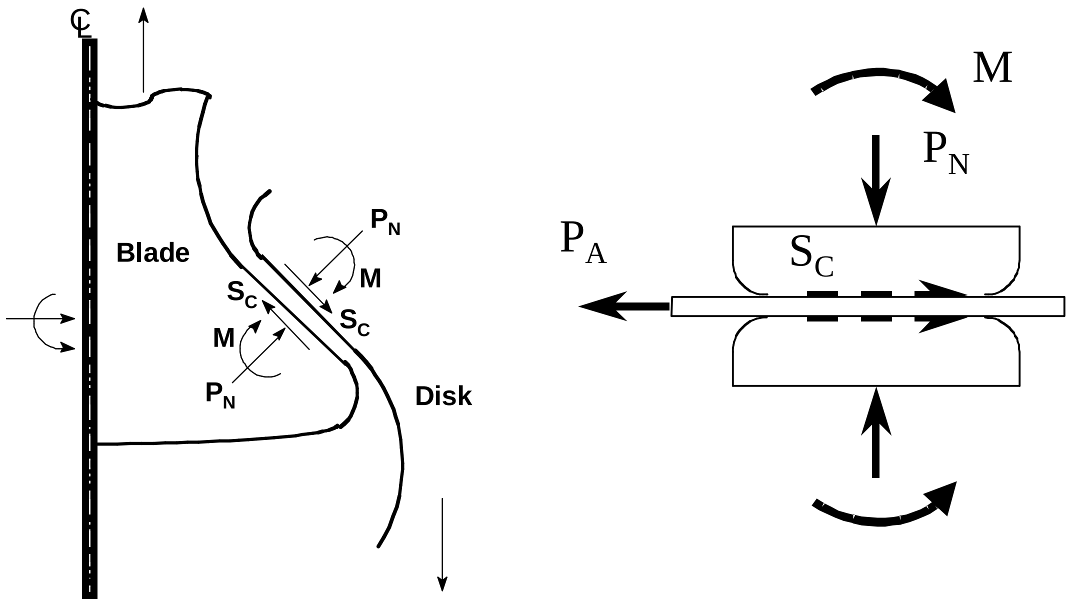

Figure 1. Blade/Disk attachment and experimental apparatus load schematic.

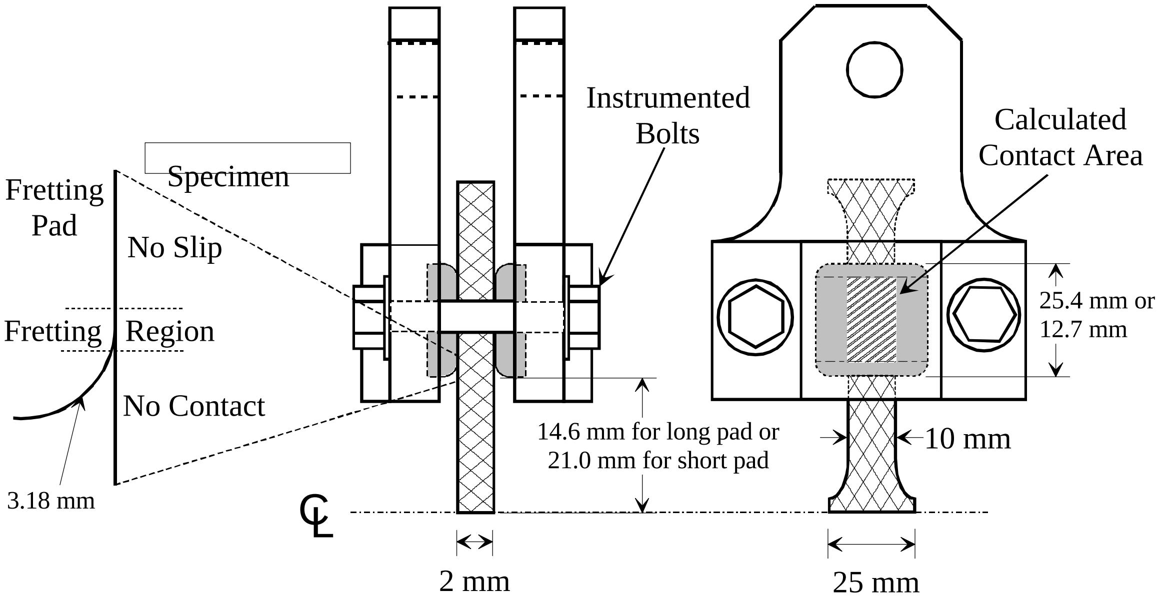

Figure 2. Test fixture schematic indicating pad lengths, distance from center of specimen to lower edge of pad, and blending radius at edge of contact.

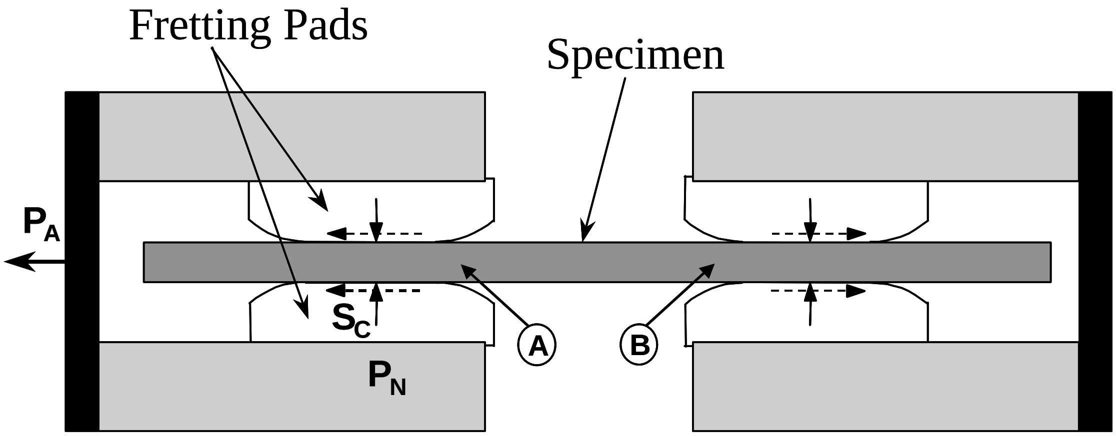

Figure 3. Test load train schematic. Letters indicate regions of the specimen subject to fretting fatigue.

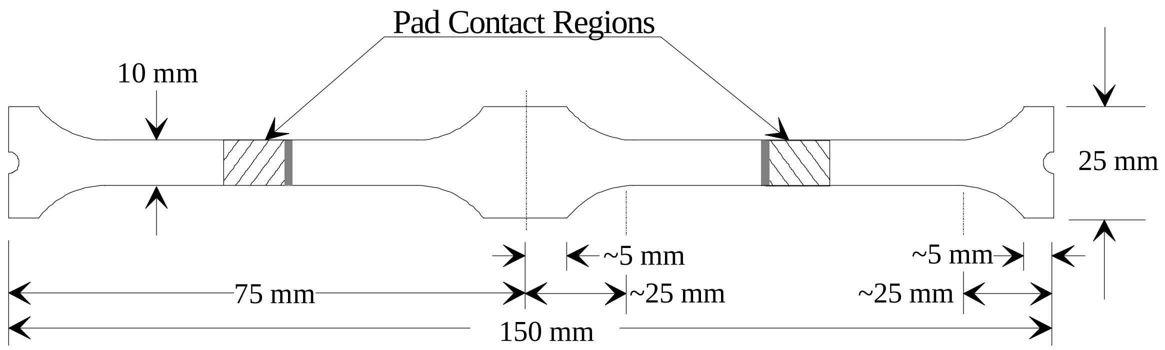

Figure 4. Twin dogbone specimen schematic. Note: dashed line indicates bisecting line for post-fretting fatigue characterization and testing.

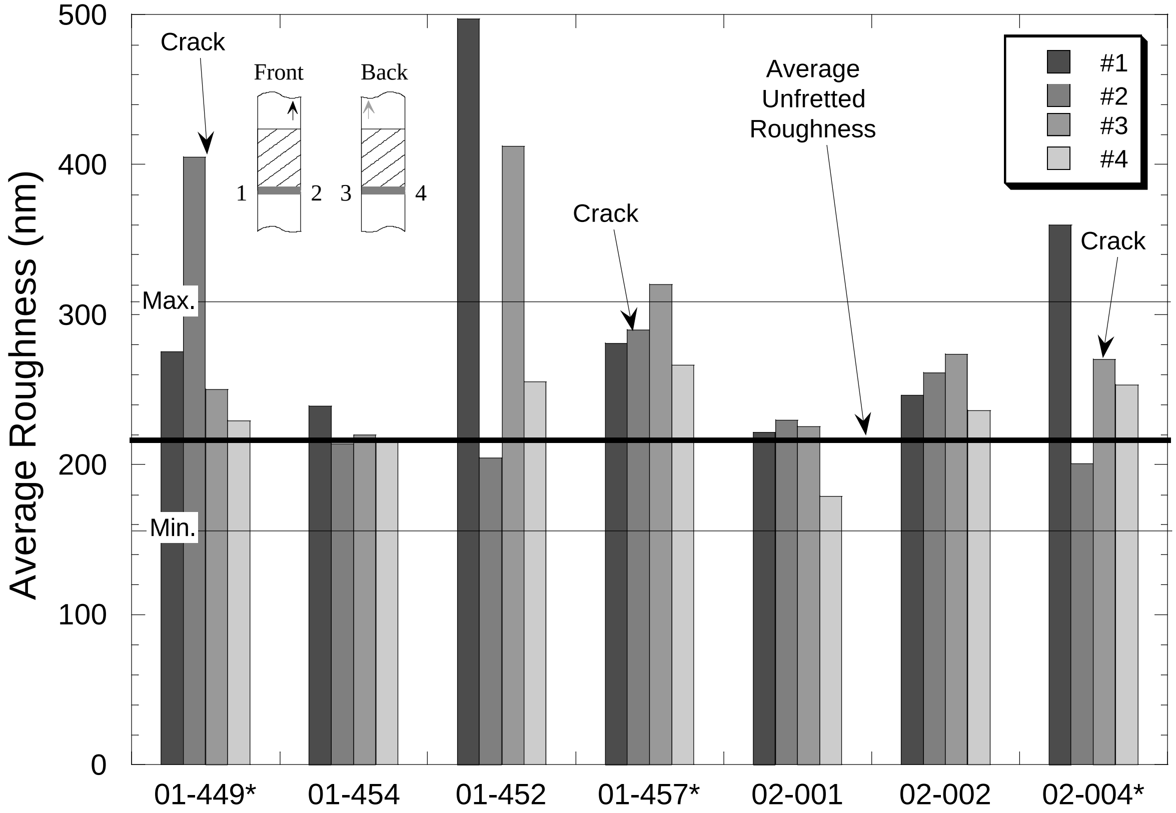

Figure 5. Roughness results for specimens that failed in the gage section. Inset diagram indicates the scan locations that correspond to the numbers in the legend. Asterisks indicate specimens with fretting fatigue-nucleated cracks.

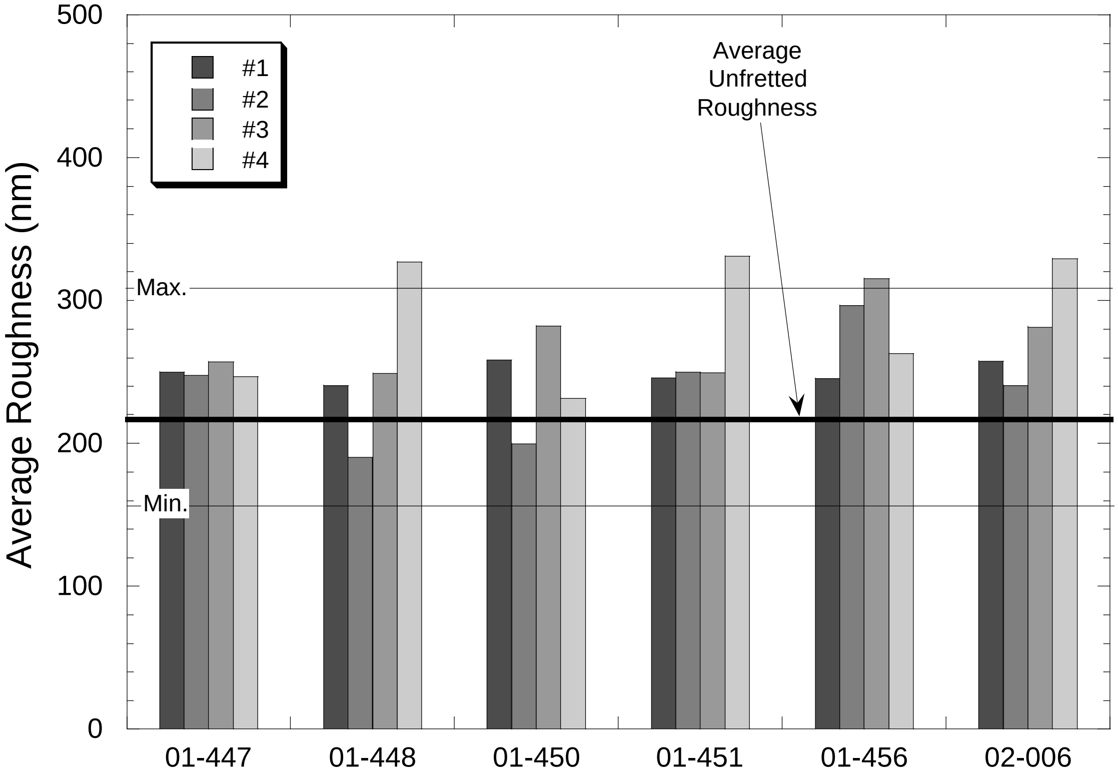

Figure 6. Roughness results for specimens that weren't tested or failed outside of the gage section. See inset on Figure 3 for definition of legend.

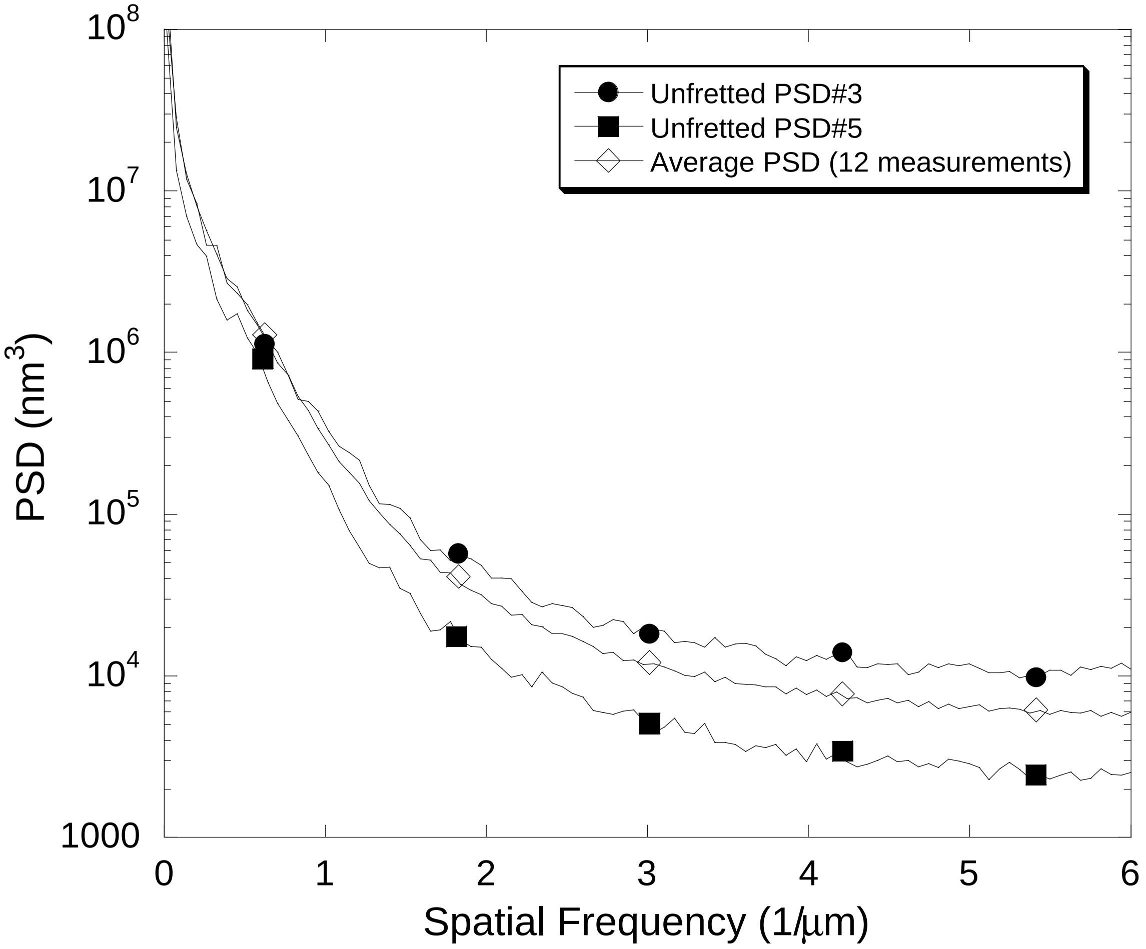

Figure 7. Representation of scatter in roughness measurements in terms of Unfretted PSD vs. spatial frequency.

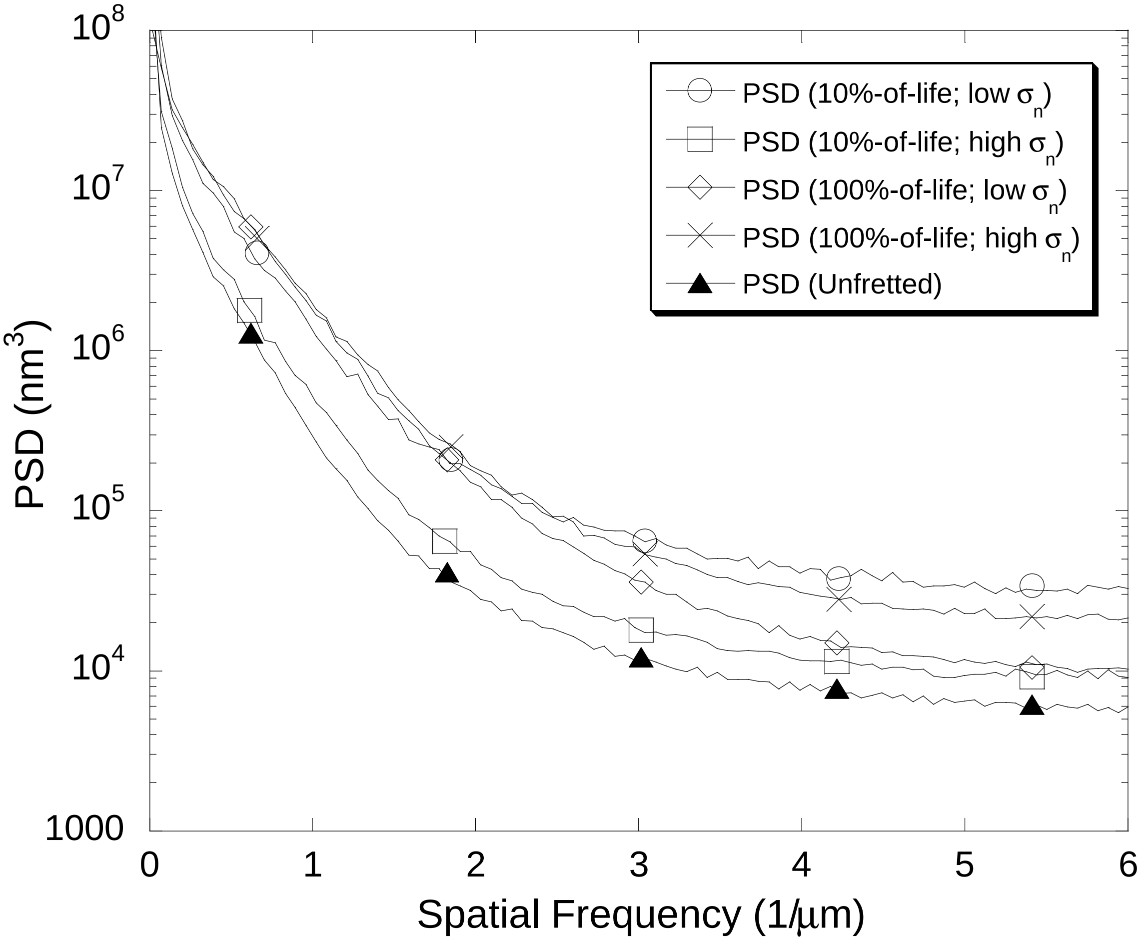

Figure 8. Comparison of fretted and unfretted PSD data. Note "unfretted" data is the same curve as the "Average PSD" shown in Figure 5.

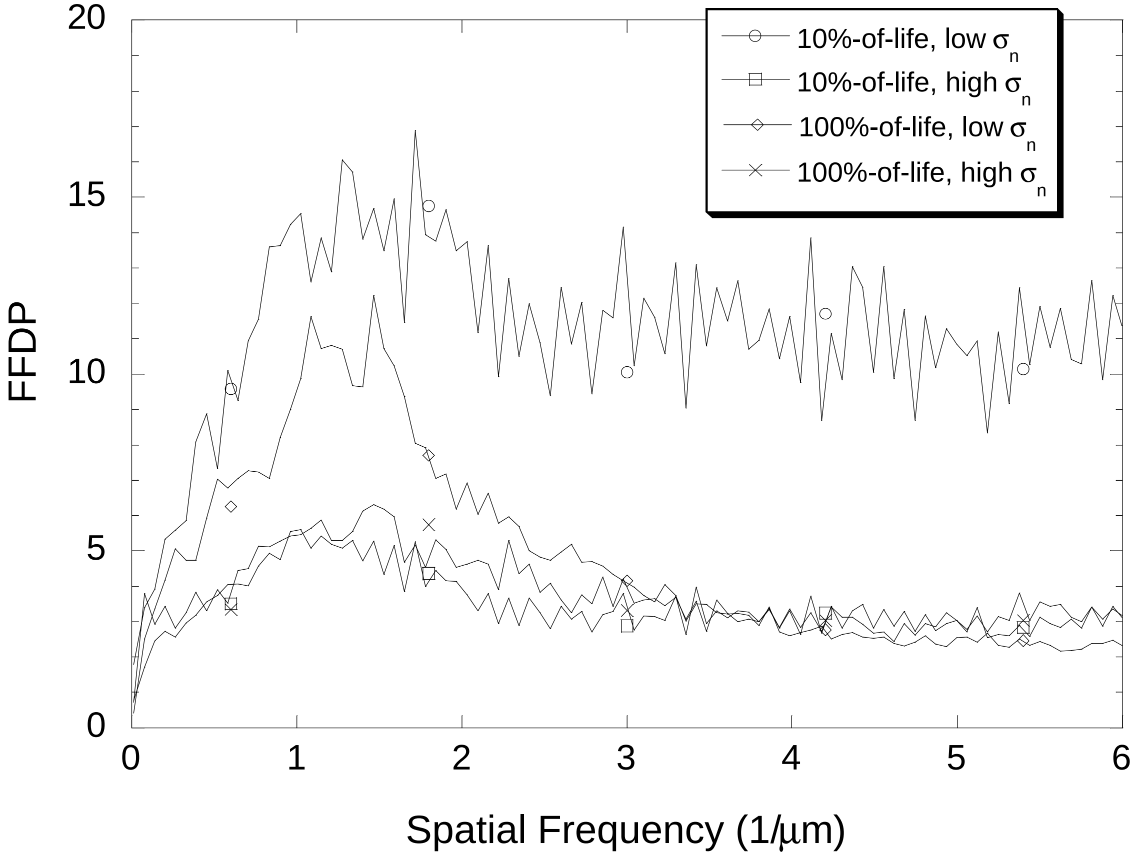

Figure 9. Comparison of FFDP for fretted conditions shown in Figure 6.

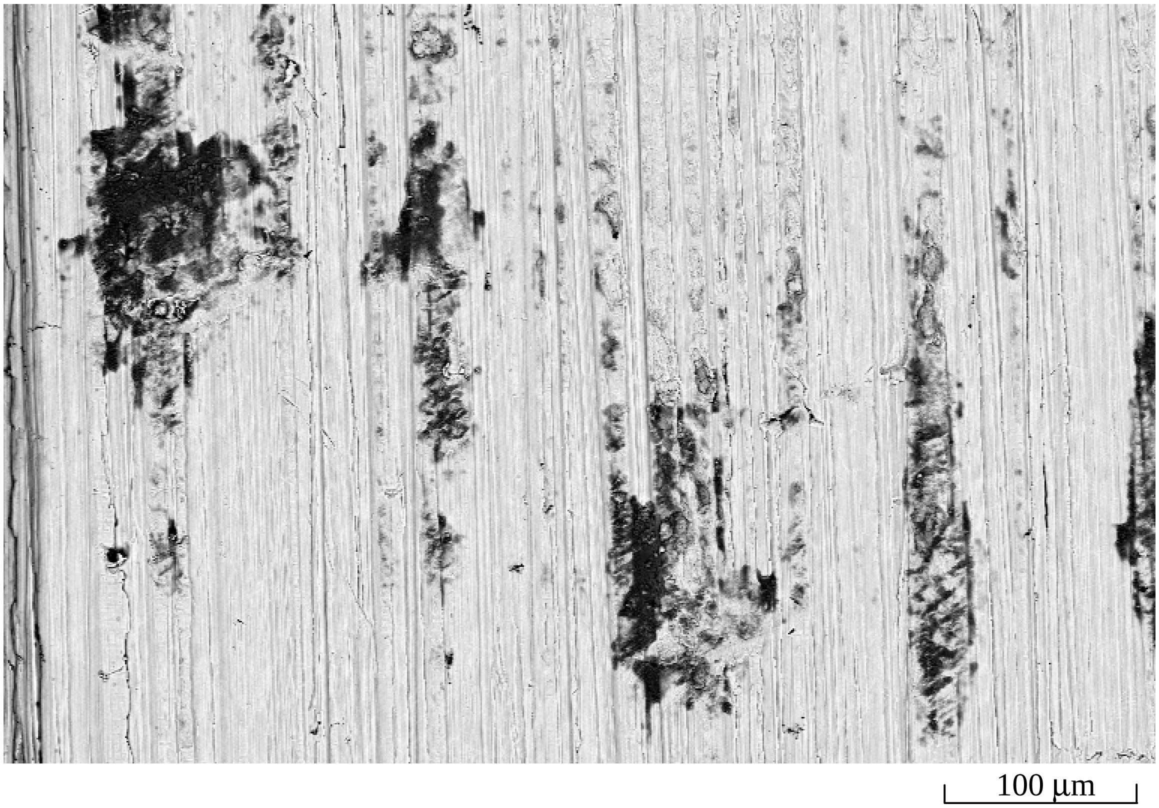

Figure 10. Fretting damage at 10%-of-life for lower clamping stress. Average Roughness ˜ 500 nm

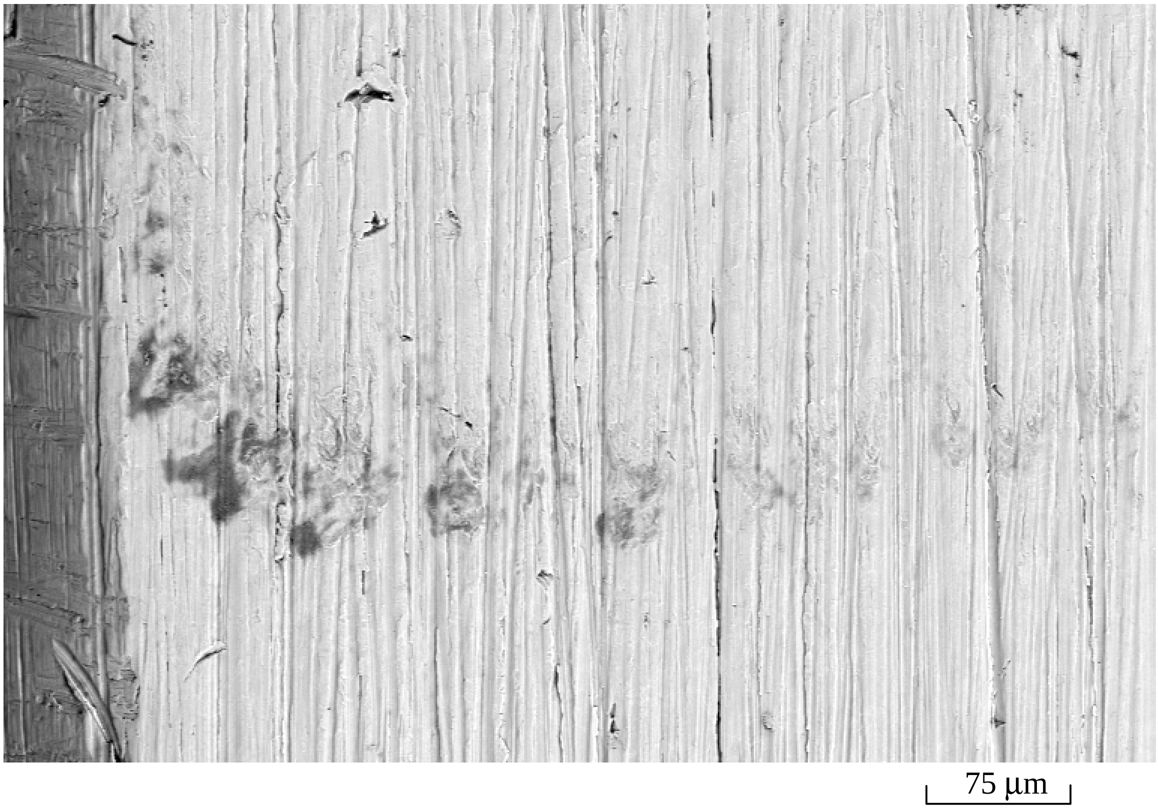

Figure 11. Fretting damage at 10%-of-life for higher clamping stress. Average Roughness ˜ 275 nm

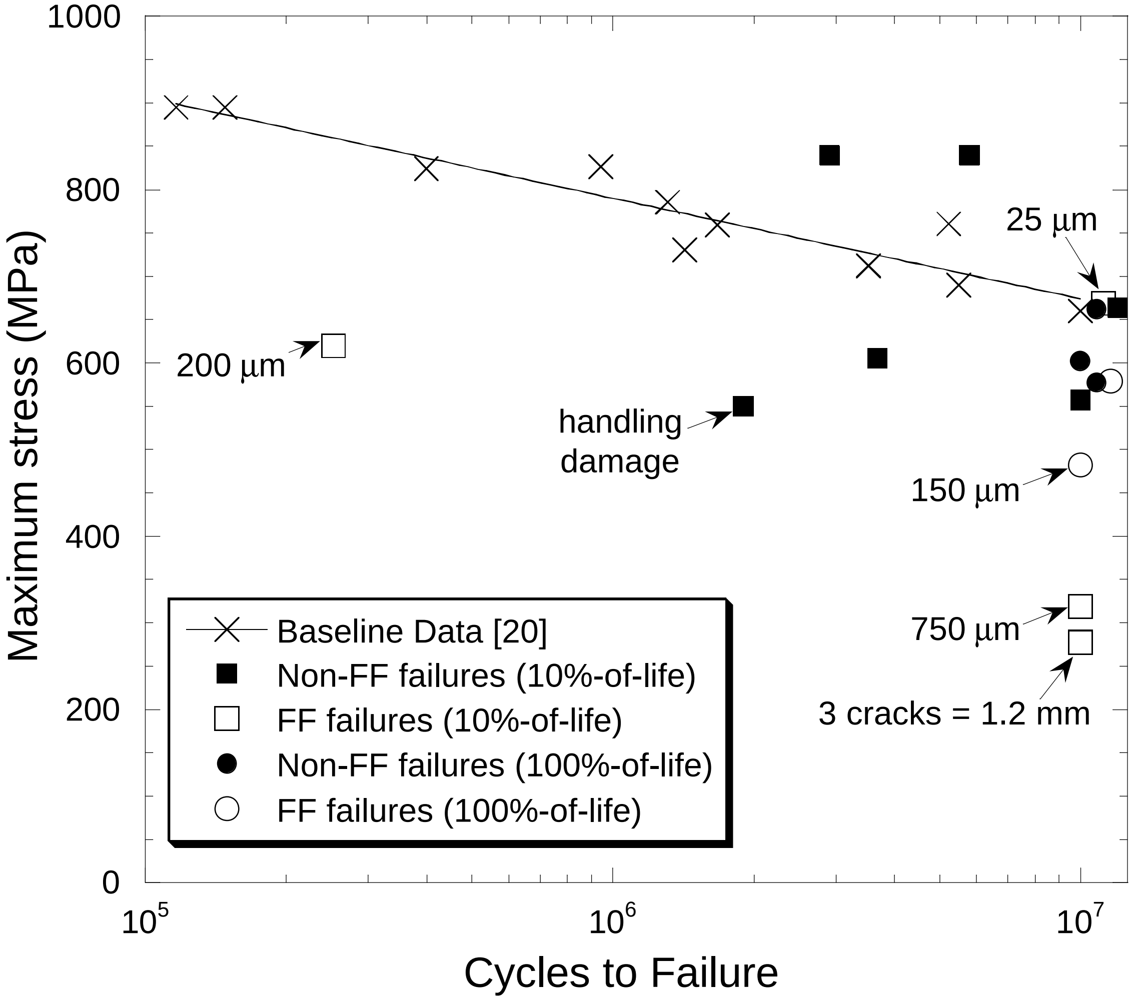

Figure 12. Residual fatigue results for fretting-fatigue damaged specimens compared with baseline fatigue results.

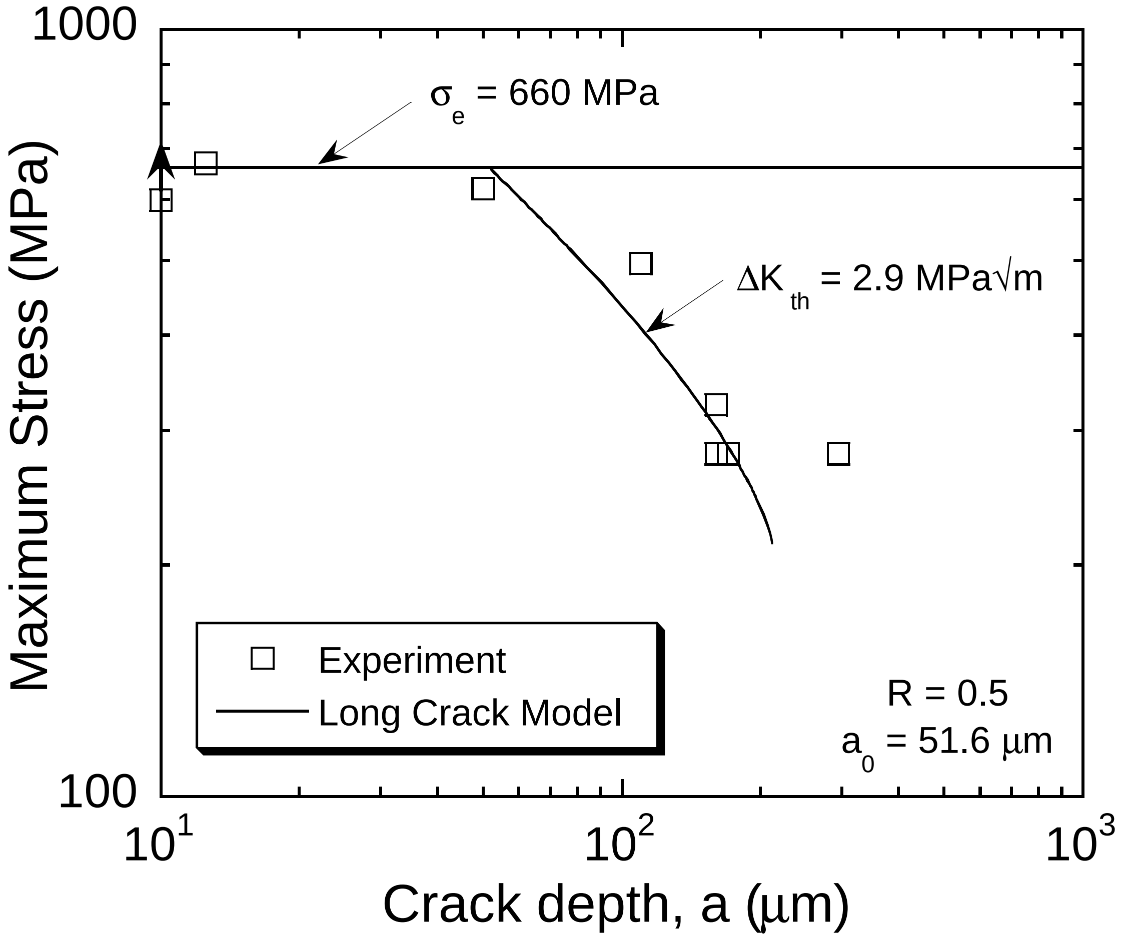

Figure 13. Kitagawa-Takahashi type representation of residual fatigue strength results for fretting-fatigue damaged specimens exhibiting cracks.

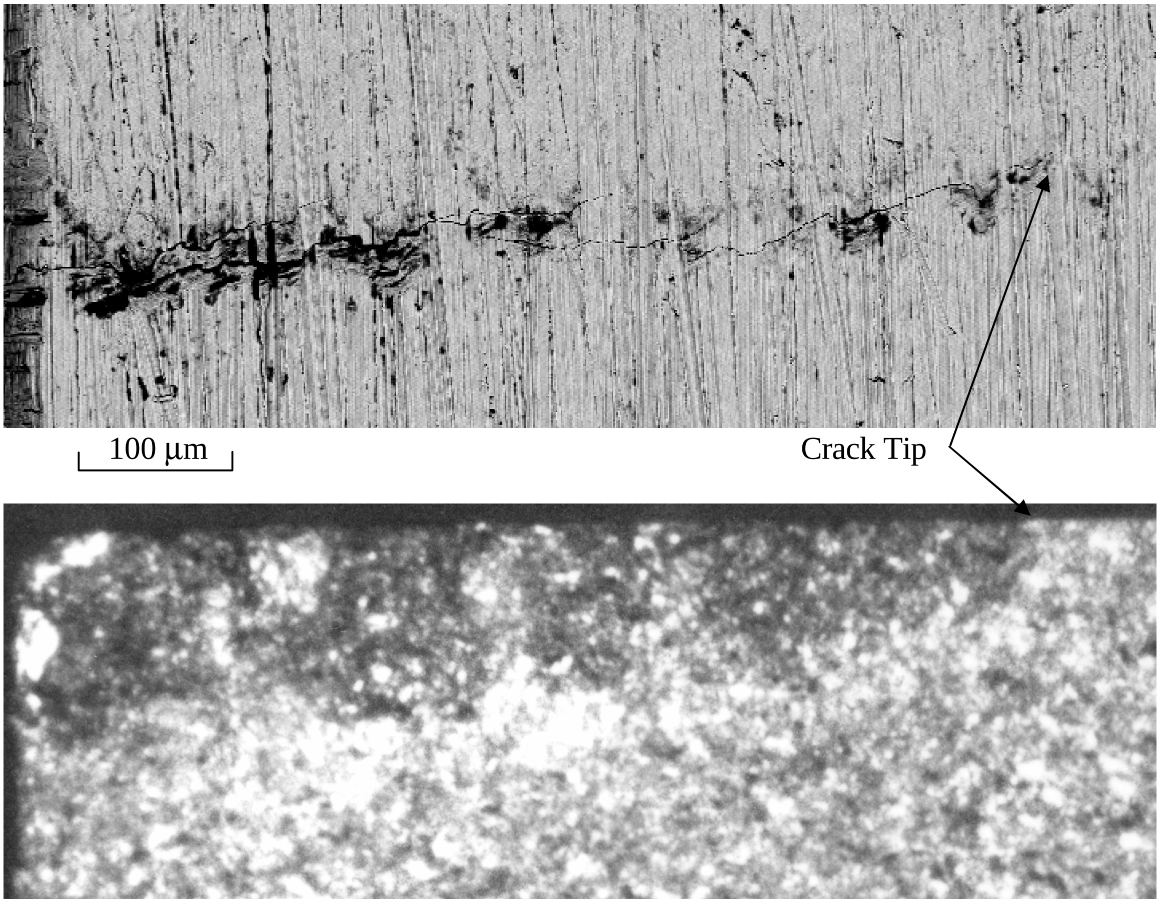

Figure 14. SEM image of 700 mm fretting fatigue crack (above – contact region is on the top half of the image) and corresponding fracture surface (below). Specimen edge is shown to the left of the images. The dark region on the fracture surface indicates the depth of the crack at the time the contact was removed.

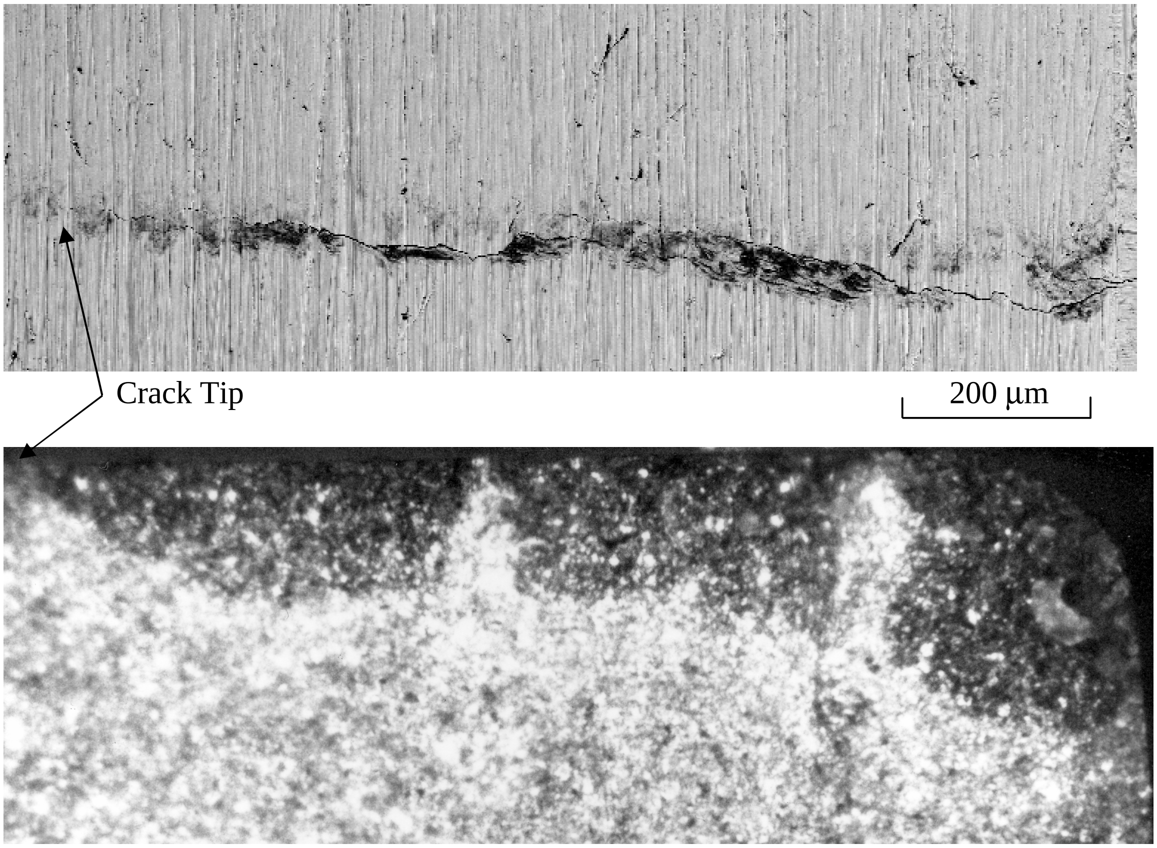

Figure 15. SEM image of 1.2 mm fretting fatigue crack (above – contact region is on the top half of the image) and corresponding fracture surface (below). Specimen edge is shown to the right of the images. The three separate dark region on the fracture surface indicate the size of the cracks at the time the contact was removed.

This page intentionally left blank

Fretting Fatigue of Dissimilar Metals

Mrs. A. L. Hutson[1], Dr. S. E. Olson[1] and Dr. T. Nicholas[2]

[1]University of Dayton Research Institute, Dayton, OH, 45469
Tel: 937-255-2708, FAX: 937-255-1363, E-mail: alisha.hutson@afrl.af.mil
[2]Air Force Research Laboratory (AFRL/MLLN), Wright-Patterson AFB, OH 45433-7817
Tel: 937-255-1347, FAX: 937-656-4840, E-mail: theodore.nicolas@afrl.af.mil

INTRODUCTION

While fretting fatigue has been studied extensively, there are so many aspects to the problem [1] that it is still not a well understood phenomenon. Fretting fatigue, as described here, refers to the cyclic loading of a material that is subjected to clamping stresses normal to the direction of loading. What distinguishes fretting fatigue from wear or galling is rather subjective, but fretting fatigue is normally associated with small magnitudes of localized relative slip on the order of tens of microns and little if any material removal. Such damage has been indicated as the cause of many unanticipated disk and blade failures in turbine engines.

The majority of such failures have occurred under fretting wear conditions where both components are made of the same material type, if not the same alloy. In addition, most fretting research has focused on the contact between like materials, since the worst fretting wear damage occurs where like materials are in contact, most likely because of local adhesion. However, fretting fatigue also occurs between dissimilar materials, such as the blade attachment regions in higher stage compressor and turbine applications, and so an investigation addressing the role of material composition in fretting fatigue behavior is critical to developing a comprehensive life prediction methodology for fretting.

The purpose of the present investigation is to elucidate some of the issues regarding the role of contact material on fretting fatigue behavior. An experimental determination of the conditions under fretting fatigue which are analogous to the fatigue limit stress under uniaxial fatigue loading corresponding to a 10^7 cycle fatigue life is presented for three contact pad materials. Details of the stress distributions in the test apparatus, calculated using finite element analysis, are included for representative experimental conditions. Characterization results from surface roughness measurement, spectral analysis (EDS), and Scanning Electron Microscopy (SEM) are presented for the resulting wear scars.

EXPERIMENTS

A unique, high frequency test system was used to conduct tests simulating the fretting fatigue damage that occurs in turbine engine blade attachments [2-4]. The apparatus uses flat fretting pads, with a radius at the edge of contact, against a flat specimen. Normal and shear loads are applied to the specimen as shown in Figure 1. The test geometry restricts the maximum nominal shear stress to that which can be reached for a given nominal clamping stress before total slip occurs. A previous study has shown that the bending moment present in the apparatus is negligible relative to other parameters, and may be disregarded when designing the tests [5]. Therefore, the reported experimental data will only include the applied normal load and shear load.

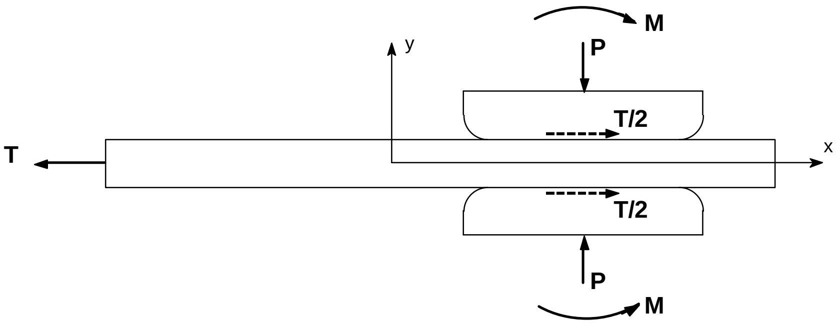

Figure 1: Test geometry and loading schematic (half specimen shown).

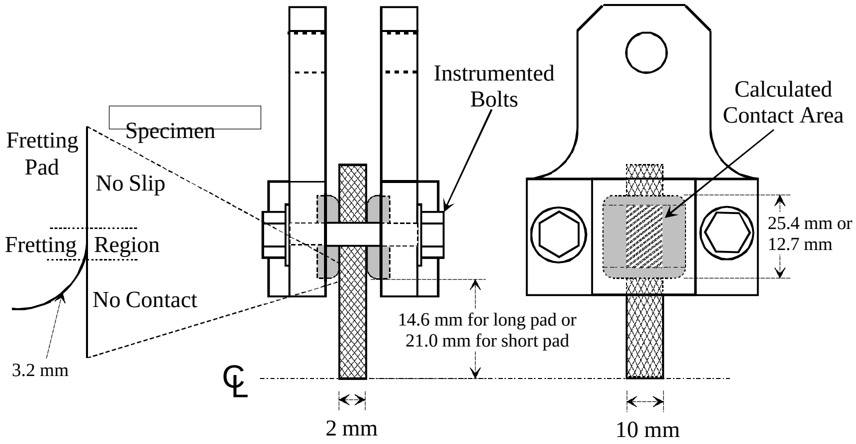

Figure 2: Test fixture schematic indicating pad lengths, distance from center of specimen to lower edge of pad, and blending radius at edge of contact.

The test geometry differs from conventional fretting fatigue tests [6,7] in two fundamental ways. First, the axial stress is transferred entirely to the fixture through shear (Figure 2). Resulting stresses in the specimen are zero on one end of the pad, thus the shear force into the pad is determined from the load applied to the specimen. Second, symmetry of the apparatus provides a specimen which breaks on one end, leaving the other end with a fretting scar and damage obtained under nominally identical conditions. As with a conventional fretting fatigue apparatus, the clamping force is constant and only the axial and shear loads are oscillatory.

All tests were conducted at 300 Hz at R = 0.5 under ambient lab conditions. Specimens were taken from forged Ti-6Al-4V plates used in a series of investigations under a U.S. Air Force sponsored high cycle fatigue program. The processing details are reviewed in previous work [8,9]. Fretting pads were manufactured from one of three materials: 7075 T6 aluminum, IN 100 (of unknown pedigree), or the Ti-6Al-4V used in the specimen manufacture. The moduli for the three pad materials are 72, 200 and 120 GPa; the Poisson's ratios are 0.33, 0.312 and 0.3, respectively.

Each specimen was subjected to uniaxial fatigue using a step-loading procedure [10] to determine a fatigue limit stress corresponding to 10^7 cycle fatigue life. Tests were conducted by incrementing the maximum axial stress by five percent of the initial value until specimen fracture. The step loading technique was validated in earlier fretting fatigue studies using the same apparatus [2]. Two clamping stresses (~240 MPa and ~650 MPa) were selected for the experiments with the IN 100 and aluminum pads, and were produced by varying pad length and clamping force. The pad lengths used were 12.7 mm and 25.4 mm. When combined with a 3.175 mm blending radius, the resulting contact lengths were 6.35 mm and 19.05 mm. These pad geometries were used in tests with the Ti-6Al-4V pads to produce a broad range of clamping stresses, including 240 and 650 MPa.

ANALYSIS

Analyses were conducted to determine the state of stress and the magnitude of relative slip of the pad with respect to the specimen at the edge of contact. ABAQUS was selected as the finite element modeling package. Eight node quadrilateral elements were used, with mesh refinement down to sizes of ~ 6.5 μm near the edges of contact. Quasi-static linear elastic behavior under plane stress was assumed. Additional details of the finite element methods are presented in [5].

The geometry for the pads and specimen was treated as two-dimensional and, because of symmetry, only one pad and half the specimen thickness was modeled. A line of symmetry, defined along the x-axis corresponding to the middle of the specimen, limited translation n the y direction. In addition, the pad was prevented from rotation as shown in Figure 3, and the back of the pad was limited so that all of the nodes would translate as a single entity. The clamping stress was applied by imposing the desired force on the back of the pad, which resulted in a uniform displacement of the pad. A similar technique was used to impose the axial stress on the specimen. Contact was defined for the entire top region of the specimen and the pad bottom including the full radius. The

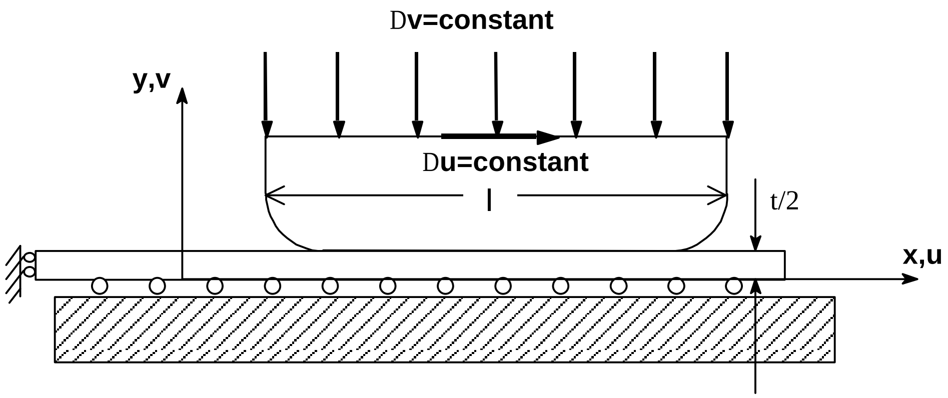

Figure 3: Finite Element Analysis geometry and loading schematic.

TABLE 1

SUMMARY OF TEST CONDITIONS AND RESULTS FOR FINITE ELEMENT ANALYSIS.

Pad Material	Applied σ_{axial} (MPa)	Average σ_y (MPa)	Peak τ_{xy} (MPa)	Peak σ_x (MPa)	Slip length (mm)	% of CL in partial slip	Max. Relative Displacement (μm)
Ti-6Al-4V	250	650	410	1250	0.63	9%	3.9
Ti-6Al-4V	330	240	230	825	2.91	15%	7.9
Ti-6Al-4V (μ = 0.7)	330	240	460	1360	0.26	1%	2.4
IN 100	300	650	420	1330	1.22	18%	4.3
IN 100	360	240	230	750	3.89	20%	9.7
7075 T6 Al	256	650	380	1200	0.42	6%	4.9
7075 T6 Al	300	240	215	750	1.87	10%	6.3

material was modeled as a Ti-6Al-4V specimen against a pad of one of the three materials indicated above. For most of the conditions simulated numerically [2,4,5], the coefficient of friction, μ, was taken as 0.3. In one case μ was increased to 0.7, the value measured for Ti-6Al-4V against Ti-6Al-4V using this test apparatus in a previous investigation, to allow comparison of resulting stresses and relative displacements. Only the first half of the initial fatigue cycle was modeled.

Clamping loads were taken as those used in the experiments; axial stress in the specimen was taken from experimental observations. The specimen was modeled as 2 mm thick by 10 mm wide. The two pad geometries described above for the experiments were incorporated into the models. The clamping loads on the pads were either 45.7 kN for the long pad (σ_N = 240 MPa) or 41.275 kN for the short pad (σ_N = 650 MPa). A summary of the test conditions simulated with the FEM analysis and indicating maximum stresses is given in Table 1.

RESULTS & DISCUSSION

Experimental Results:

The results for the experiments conducted for this investigation are shown in Figure 4. In this figure the fretting fatigue limit stresses (σ_{FF}) for a 10^7 cycle fatigue life are plotted as a function of average applied clamping stress, or "Normal σ". A subtle decrease in fatigue limit stress with increasing average clamping stress is evident. The results for the 7075 T6 aluminum pads fall within the scatter of the results reported for the tests against the Ti-6Al-4V pads, thus indicating no effect as a function of contact material. At the lower clamping stresses, the IN 100 data also fall within the scatter of Ti-6Al-4V pad test results. However, at the higher clamping stresses, the results for the IN 100 pad tests are slightly higher than the results for either the Ti-6Al-4V pads or the aluminum pads. Some overlap with the Ti-6Al-4V results is indicated by the S-N test, which is denoted by downward pointing arrows. These data should be considered an upper bound for the fatigue limit stress for that specimen.

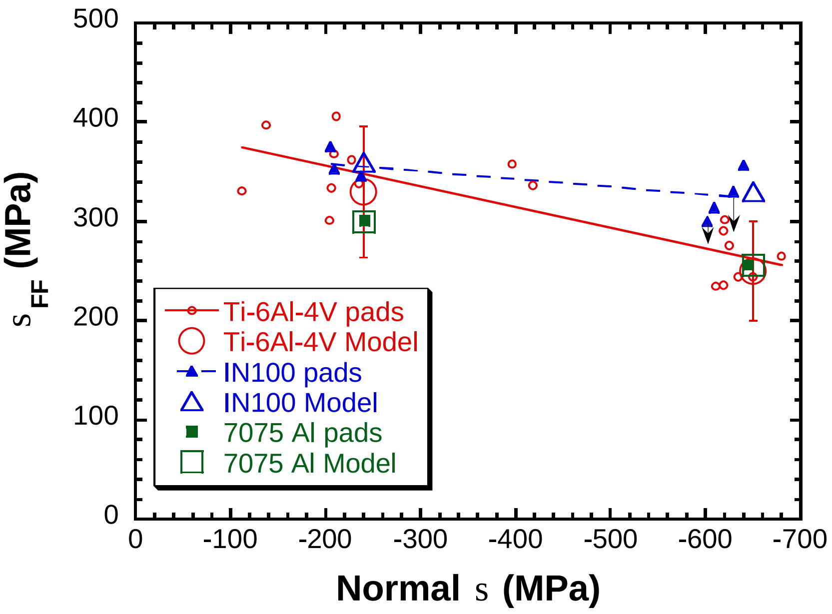

Figure 4. Fretting fatigue limit stress results shown as a function of average applied clamping stress. Analytical conditions are indicated with large hollow symbols. Data points with down-pointing arrows are S-N tests.

These findings are significant in light of the popular opinion that fretting fatigue behavior is quite sensitive to contact material. This opinion originated from investigations on fretting wear, in which the tribological properties of the contact dramatically affected the wear behavior of the contact pair. It has long been assumed that fretting fatigue and fretting wear mechanisms were the same, and so the effect of certain variables, like contact material, would also be the same. That assumption does not seem valid in light of the results documented in Figure 4. Possible differences in damage mechanisms between the two contact phenomena will be discussed below.

Analytical Results:

Analytical results are shown in Figures 5–12. In these figures, the loaded end of the specimen is to the left of the chart while the right end of the specimen is stress free outside the right edge of contact. Also, the coefficient of friction, μ, was assumed to be 0.3, except as discussed toward the end of this section.

The distribution of stresses along the length of the pad for the Ti-6Al-4V long pad model is shown in Figure 5, where x is normalized with respect to the half-length of the pad between the center and the position of undeformed contact (UEC). The stress concentrations at the edges of contact are included in a subsequent figure. The σ_y stresses are approximately equal to the average applied clamping stress for this condition, dropping off toward the edges of contact. Slight increases in τ_{xy} and σ_x stresses are observed in the region undergoing slip.

For the models with the different pad materials, the τ_{xy} and σ_y stresses distributions were very similar. Significant differences in stress distribution were observed only for the σ_x stress, so the τ_{xy} and σ_y stresses are omitted in the subsequent plots. The σ_x stresses between the UEC regions for the long pad models are shown in Figure 6. The trends are essentially the same, with the only real difference being the magnitude of the peak located in the slip region. This value seems to vary as a function of the applied axial stress.

The edge of contact (EOC) stresses for the three different long pad models are shown in Figure 7. For the EOC plots (Figures 7, 9 and 11), -1 corresponds to the left EOC and is the same location as –1 in the plots on which stresses under the pad are presented (Figures 5, 6, 8 and 12).

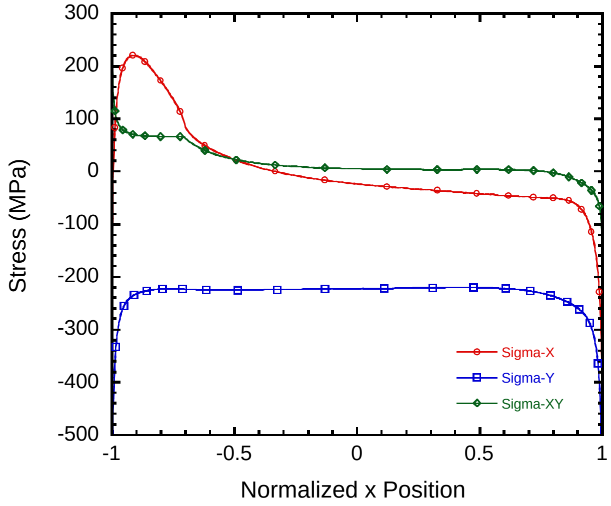

Figure 5. Stress distribution between the undeformed edges of contact for the Ti-6Al-4V long pad model. m = 0.3, s_N = 240 MPa

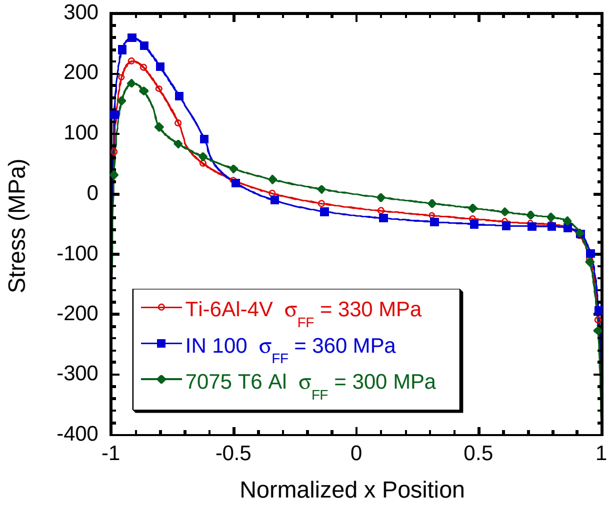

Figure 6. Comparison of σ_x stresses between the undeformed edges of contact for the three different pad materials. m = 0.3, s_N = 240 MPa (long pad models)

Again, the magnitudes of the stresses are slightly different, but the general shape of the stress distribution is the same and shows that peak stresses are very localized near the EOC. The exact location of the peak seems be a function of material modulus and/or applied axial stress.

Figures 8 and 9 contain similar data obtained for the short pad models. In Figure 8, the σ_X stress distributions are shown for the three models. In these cases, the σ_X stresses are dominated by the applied clamping stress, and all fall below zero, except for a small portion of the curve for the IN 100 pad model. Also, the trends for the IN 100 model under the pad follow the trends observed for the lower clamping stress model. The peak under the pad is not present for the short pad models with either the Ti-6Al-4V or the aluminum pads, indicating shorter slip lengths and smaller relative slip for these two conditions.

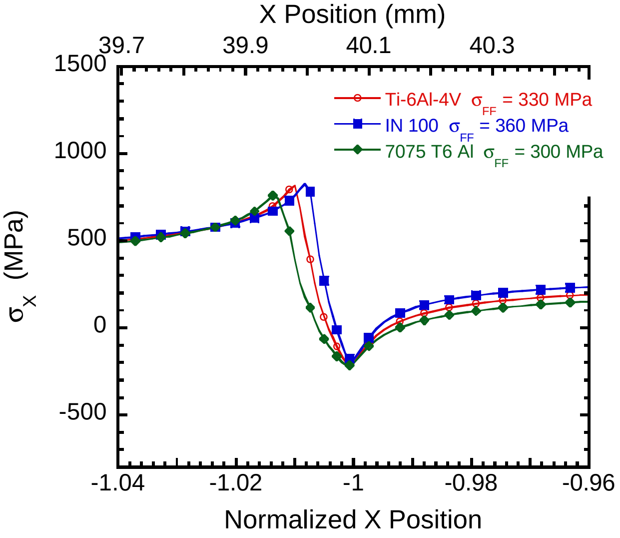

Figure 7. Comparison of σ_X stresses at the edge of contact for the three different pad materials. $m = 0.3$, $s_N = 240$ MPa (long pad models)

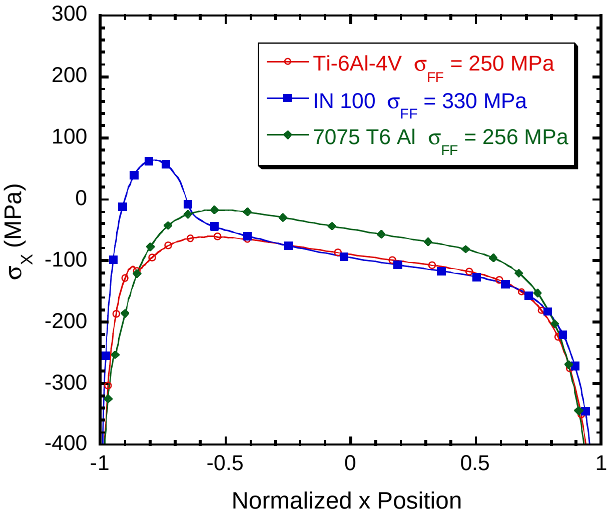

Figure 8. Comparison of σ_X stresses between the undeformed edges of contact for the three different pad materials. $m = 0.3$, $s_N = 650$ MPa (short pad models)

Stress distributions for the short pad models at the EOC are shown in Figure 9. Note that the y-scale in this chart is the same as that in Figure 7, to allow comparison of peak σ_X stress values between the short and long pad models; however, the x-scale had to be adapted to incorporate the peaks at the EOC. Note that the actual model dimensions have been included in the upper x-axis for comparison. Peak tensile stresses in this region are all greater than 1200 MPa, due to the higher applied clamping stress. The locations of the respective peaks are governed by the pad modulus. Models that incorporated aluminum or Ti-6Al-4V pads imposed nominally identical applied loads for the short pad geometry, but the lower modulus of the aluminum allowed for greater deformation of the pad. This deformation changed the location of the peak σ_X stress.

The stress gradients along the contact length have been shown in Figures 7 and 9 to be very steep for the contact geometry under investigation. It stands to reason that the gradients into the specimen thickness will be localized in the same manner. Representative σ_X curves are shown in Figure 10 for the six models that have been discussed. In this figure, the coordinate y=1 corresponds to the surface of the specimen in contact with the pad and lower numbers correspond to locations within the specimen thickness. Solid lines indicate data for the long pad models (σ_A = 240 MPa). Dashed lines indicate data for the short pad model (σ_A = 650 MPa). Data for each curve was taken at the model undeformed edge of contact location at the loaded end of the specimen. The stress profiles show that the σ_x stresses decay rapidly, with stresses at 100μm below the surface (y=0.9) being almost the same as those much deeper. Thus, stress gradients into the thickness are of the same order of magnitude as those along the surface. Similar observations were made for the other cases, which are not shown here.

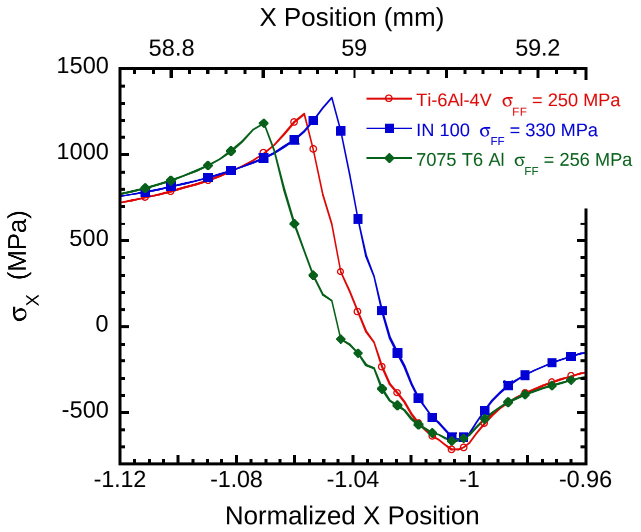

Figure 9. Comparison of σ_x stresses at the edge of contact for the three different pad materials. m = 0.3, s_N = 650 MPa (short pad models)

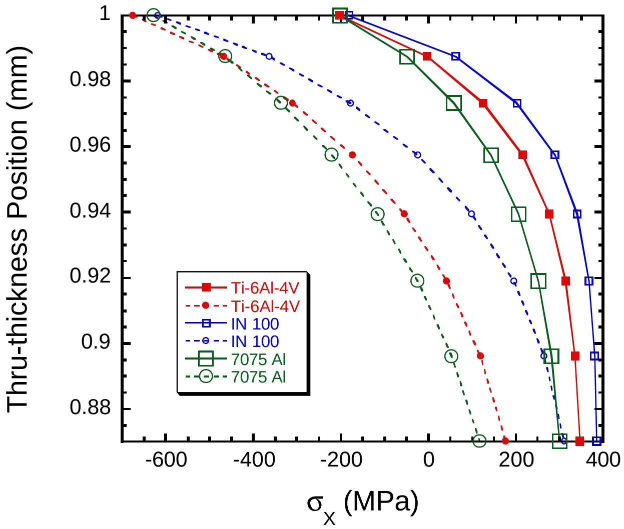

Figure 10. σ_x stress gradients. Dashed lines indicate short pad model (s_N = 650 MPa). Solid lines indicate long pad model (s_N = 240 MPa). y=1 corresponds to specimen surface, m = 0.3.

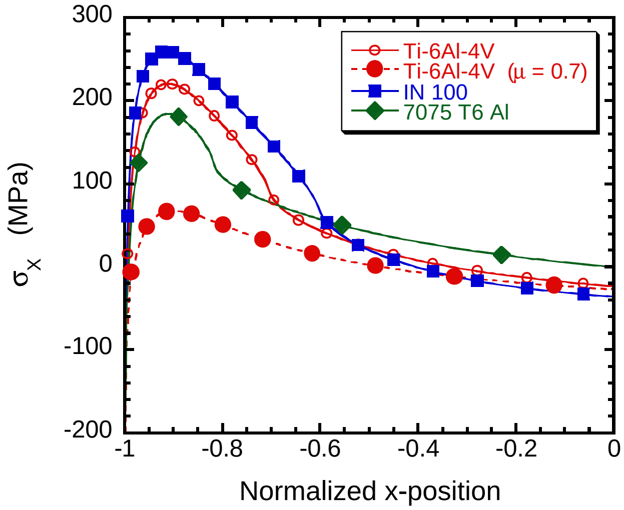

Figure 11. Comparison of σ_x stresses between the undeformed edges of contact for the three different pad materials. s_N = 240 MPa (long pad models) m = 0.3, except as noted.

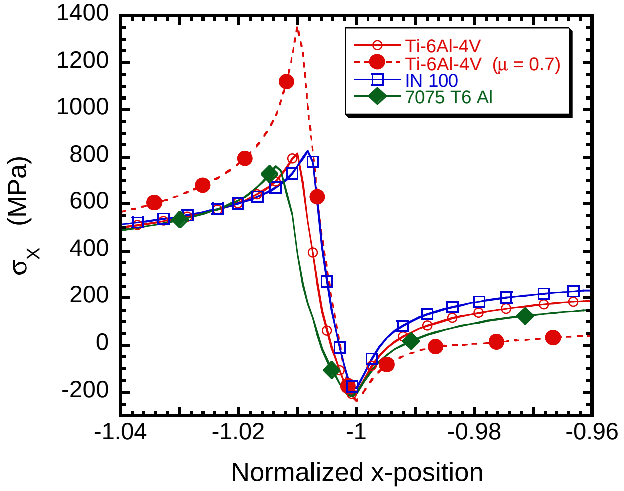

Figure 12. Comparison of σ_x stresses at the edge of contact for the three different pad materials. s_N = 240 MPa (long pad models) m = 0.3, except as noted.

Throughout the analyses conducted for this investigation, μ has been assumed to be 0.3, although it was not measured during the experiments for the dissimilar metal contacts. A value of 0.7 was measured for μ between Ti-6Al-4V on Ti-6Al-4V in a prior investigation [11] using the fretting fatigue apparatus described above, and it is well known that fretting fatigue behavior is very sensitive to μ. So, the Ti-6Al-4V long pad model was reanalyzed with $\mu = 0.7$ to provide a basis on which to evaluate trends in fretting fatigue behavior as a function of μ.

The data from Figures 6 and 7 are shown again in Figure 11 and 12, respectively, with data from the $\mu = 0.7$ Ti-6Al-4V long pad model. In Figure 11, the region from the center of the pad to the UEC at the loaded end of the specimen is shown. Note that the peak for the μ=0.7 model is much lower than the other three models. In Figure 12, the EOC stress peak is nearly twice as high as the corresponding peak for μ=0.3, indicating a predicted load transfer over a much smaller area than would be achieved with a lower μ. Accordingly, the relative slip and the slip length are much smaller (see Table 1) for the model with the higher μ value. Thus, the role of μ on the experimental data cannot be evaluated without knowing μ for the dissimilar metal contacts.

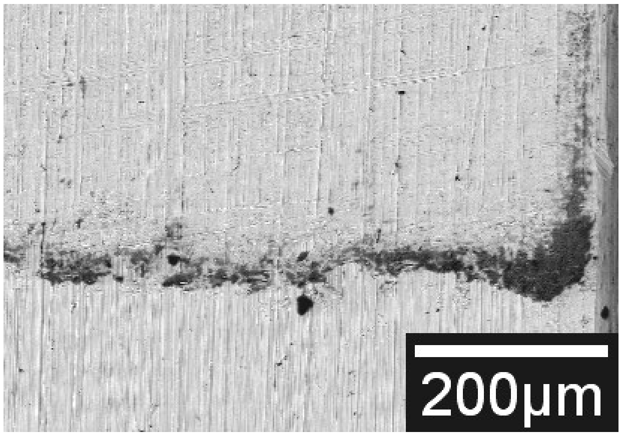

Figure 13. Fretting scar from specimen tested under a 650 MPa clamping stress (s_{FF} = 250 MPa) using Ti-6Al-4V pads.

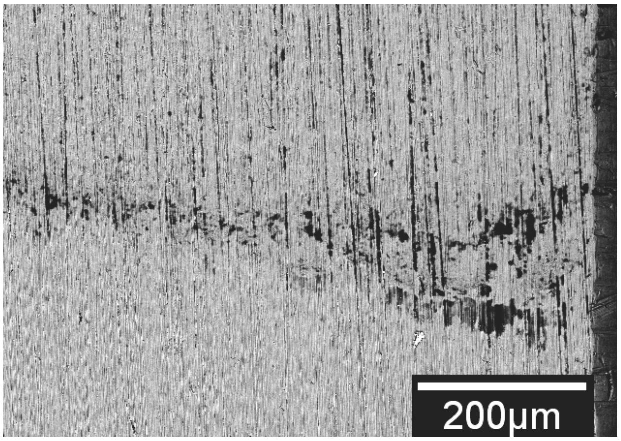

Figure 14. Fretting scar from specimen tested under a 650 MPa clamping stress (s_{FF} = 256 MPa) using 7075 T6 Al pads.

Characterization Results:

Several techniques were used to evaluate the specimens after testing: Scanning Electron Microscopy (SEM), surface roughness and spectral analysis (EDS). The first of these techniques was used to evaluate fretting debris and to identify cracks on the unfractured end of each specimen. Representative micrographs are shown in Figures 13 – 15, which include fretting scars in the region of fretting crack nucleation for specimens tested against Ti-6Al-4V, aluminum and IN 100 pads, respectively. Each of the specimens shown was subjected to a clamping stress of approximately 650 MPa. The aluminum pads left less debris on the specimen than the IN 100 pads. This evidence supports the analytical results that indicated smaller slip lengths for the aluminum pad contacts.

The higher relative slip and slip length resulting from the IN 100 contact produced greater amounts of debris than either the aluminum or Ti-6Al-4V pad contacts. In specimens subjected to the lower clamping stress condition (not shown) layers of brittle debris products were generated that spalled off in places. As in fretting wear, these layers may have served to protect the underlying

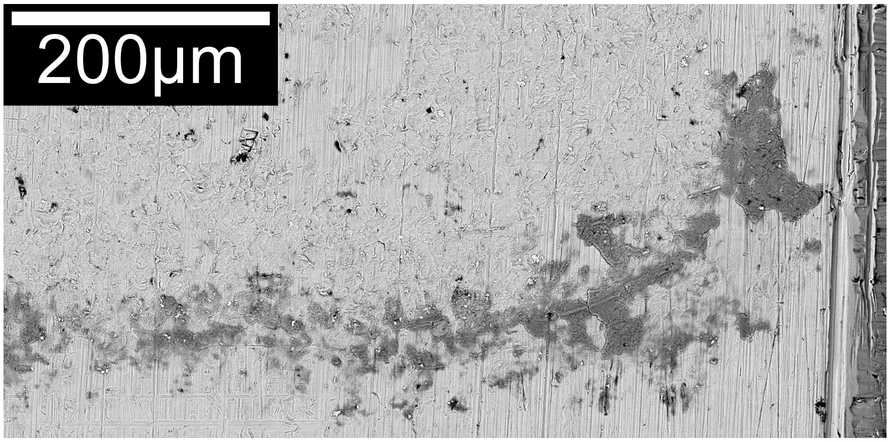

Figure 15. Fretting scar from specimen tested under a 650 MPa clamping stress (s_{FF} = 300 MPa) using IN 100 pads.

specimen from wear damage through the introduction of a third-body particle bed and from fretting fatigue damage through modification of the stress field near the EOC.

Surface roughness of the pads and specimens were also evaluated using a white light interferometer with vertical resolution of ~3 nm and spatial resolution of ~0.1 μm. The results of this evaluation are shown in Figure 16 in which red hatching (x-hatch or upper-left to lower-right hatch) indicates specimen roughnesses and blue hatching (lower-left to upper right hatch) indicates pad roughnesses. The height of each column represents the average of several measurements, and the error bars indicate the maximum and minimum measurement values for the respective column.

Little variation was observed in the surface roughnesses (see Figure 16), except for the IN 100 pads. These pads were two to three times rougher than the Ti-6Al-4V or aluminum pads, and produced rougher fretting scars on the specimens as a result. In a prior investigation, pad roughness was linked with higher fretting fatigue limit stresses [11]. The difference in pad surface topography of the IN 100 pads may be responsible for the higher fretting fatigue limit stresses noted for the IN 100 tests at the higher clamping stress condition.

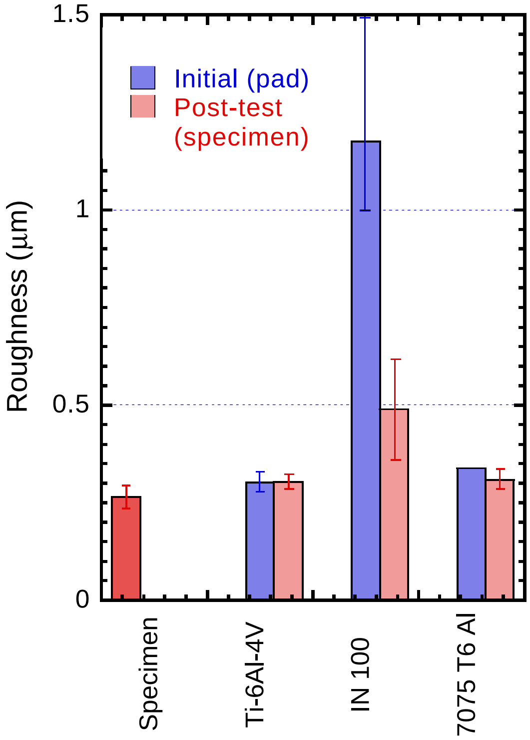

Figure 16. Comparison of pre- and post-test specimen roughness, and pre-test pad roughness.

The improvement in fretting fatigue limit stress was not observed for the lower clamping stress condition, as one might expect if pad roughness is responsible for the improvement at the higher clamping stress. While it is known that surface roughness affects both fretting fatigue and fretting wear behavior, no studies have been conducted linking fretting fatigue behavior, surface roughness and applied clamping stress. Prior work by the authors addressed only the higher clamping stress condition. Thus, it is impossible to say conclusively that roughness is the mechanism responsible for the higher fretting fatigue limit stresses produced with the IN 100 pads.

Elemental content of the as-received specimen surfaces and post-test fretting debris was characterized using Energy Dispersive technique. The results are shown in Table 2, below. For the Ti-6Al-4V pads, oxidation of the alloying elements took place during the generation of debris products. In the aluminum on Ti-6Al-4V contact, aluminum was transferred to the specimen surface and oxidized debris products were created. Trace amounts of titanium were noted on the aluminum pad, probably due to an alumina particle wearing at the titanium surface.

The most significant differences to note are in the IN 100 on Ti-6Al-4V contact. For this material pair, relatively large amounts of debris were observed and higher relative slip values were predicted by the analysis. These two observations point toward potentially higher temperatures at the EOC, although temperature was neither measured nor controlled during the experiments. Analysis of debris on the specimen would support such a conclusion. A marked increase in oxygen was noted in the specimen debris. Since oxygen is relatively small, large amounts are required to produce peaks of the order of those observed here, which were approximately as tall as those for titanium or nickel. Also, significant amounts of nickel, chromium and cobalt were identified in the debris on the specimen, indicating material transfer from the pad to the specimen. The authors suggest this transfer of material was caused by TiO_2 produced by fretting wear mechanisms.

The dominance of such mechanisms can improve fretting fatigue behavior by wearing away small cracks before they have a chance to propagate, and might better explain why the IN 100 pads produced improved fretting fatigue behavior in the Ti-6Al-4V specimens, but only for the higher clamping stress condition. Crack nucleation has been observed to occur in the first 10% of life for high clamping stresses. These cracks tend to propagate slowly once they extend beyond the localized stress peaks produced by the EOC, and might easily be removed before they would propagate to fracture. On the other hand, cracks tend to nucleate late in life at lower clamping stresses, and although the stress peaks are lower, the remote bulk stresses are higher – possibly high enough to propagate a crack to failure before wear mechanisms would dominate.

TABLE 2

SUMMARY OF ELEMENTAL ANALYSIS RESULTS

7075 T6 Al	AR	Al	Mg	Na	O	Si	Zn	Cu	C	
	Debris (pad)	Al	Na	Mg	Si	O	(Ti)			
	Debris (specimen)	Al	Ti	O	V	Si	Mg	Na	C	
IN 100	AR	Ni	Al	Cr	Co	Ti	Mo	Fe	C	
	Debris (pad)	Ti	Al	V	Ni	C				
	Debris (specimen)	Ti	O	Ni	Al	V	Cr	Co	Si	C
Ti-6Al-4V	AR	Ti	Al	V	C					
	Debris (pad)	Ti	Al	O	V	C				
	Debris (specimen)	Ti	Al	O	V	C				

CONCLUSIONS

1. Fretting fatigue behavior of Ti-6Al-4V is relatively insensitive to the contact pad material, as indicated by both experimental & analytical results.
2. Slight improvement in σ_{FF} in tests with IN 100 pads is probably related to the dominance of wear mechanisms present at the higher clamping stress condition coupled with higher roughness of the pad surface.
3. Material transfer between the pad and specimen is dependent on the material properties (transfer of softer material to the harder one generally occurs).
4. Coefficient of friction and material hardness should be evaluated for aluminum-on-Ti-6Al-4V and IN 100-on-Ti-6Al-4V contacts to fully explain fretting fatigue behavior.

REFERENCES

1. Dobromirski, J.M., *Fretting Fatigue, ESIS 18*, R.B. Waterhouse and T.C. Lindley, Eds., Mechanical Engineering Publications, London, 1994, pp. 60-66.
2. Hutson, A., Nicholas, T., and Goodman, R., *Int. J. Fatigue*, 21, 7, 1999, pp. 663 – 670.
3. Hutson, A. and Nicholas, T., *Fretting Fatigue Current Technologies and Practices, ASTM STP 1367*, D.W. Hoeppner, V. Chandrasekaran, and C.B. Elliot, Eds., American Society for Testing and Materials, West Conshohocken, PA, 1999, pp. 308-321.
4. Hutson, A.L., Nicholas, T., Olson, S.E., and Ashbaugh, N.E., *Int. J. Fatigue*, 23, 2001, pp. S445-S453.
5. Hutson, A.L., "Fretting Fatigue of Ti-6Al-4V Under Flat-on-Flat Contact with Blending Radii," M.S. Thesis, School of Engineering, University of Dayton, Dayton, OH, August, 2000.
6. *Fretting Fatigue, ESIS 18,* R.B. Waterhouse and T.C. Lindley, Eds., Mechanical Engineering Publications, London, 1994, pp. 171-182.
7. *Standardization of Fretting Fatigue Test Methods and Equipment, ASTM STP 1159*, M. H. Attia, and R. B. Waterhouse, Eds., American Society for Testing and Materials, Philadelphia, 1992.
8. Peters, J.O. and Ritchie, R. O., *Int. J. Fatigue*, 23, 2001, pp. S413-S421.
9. Moshier, M.A., Nicholas, T. and Hillberry, B.M., *Int. J. Fatigue*, 23, 2001, pp. S253-S258.
10. Maxwell, D., and Nicholas, T., *Fatigue and Fracture Mechanics: 29th Vol., ASTM STP 1321*, T. L. Panotin and S. D. Sheppard, Eds. American Society for Testing and Materials, 1999, pp. 626-641.
11. Hutson, A. L., Niinomi, M., Nicholas, T. and Eylon, D., “Effect of Various Surface Conditions on Fretting Fatigue Behavior of Ti-6Al-4V,” *accepted for publication by Int. J. Fatigue* April 2002.

Observations of fretting fatigue micro-damage of Ti–6Al–4V

B.P. Conner[a], A.L. Hutson[b], L. Chambon[c]
[a] Air Force Research Laboratory, Materials and Manufacturing Directorate, AFB, Wright-Patterson, OH 45433, USA
[b] University of Dayton Research Institute, 300 College Park, Dayton, OH 45469-0128, USA
[c] Massachusetts Institute of Technology, 77 Massachusetts Avenue, Cambridge, MA 02139, USA

Abstract

Small displacement contact fatigue below the threshold of sliding produces micro-slip near the edges of contact. The damage that results is known as fretting fatigue, and includes large surface stresses, wear in the regions of slip and crack nucleation, all of which contribute to drastic reductions in fatigue capability. Damage of this type that was generated using three independent test systems on four different contact geometries is compared. Characterization of the damage was conducted using scanning electron microscopy (SEM), semi-quantitative elemental analysis and metallographic cross-sectioning to identify damage micro-mechanisms. The evidence presented indicates the near simultaneous nucleation of multiple cracks, some of which will propagate if subjected to a sufficient bulk stress. While most cracks nucleated in regions of slip, cracks were observed outside of the slip regions under certain conditions. In regions of wear, micro-notches that can lead to the formation of fretting fatigue cracks were observed and appeared to have been the result of local plasticity induced by shot peening. Wear particles were observed in the mouths of cracks as small as 3μm in depth. The implications of these observations on the development of life prediction models for fretting fatigue are discussed.

Keywords: Fretting fatigue; Damage mechanisms; Titanium

1. Introduction

Contact related damage, first identified in steel components as fretting corrosion [1], has been the focus of numerous investigations over the years. During that time many different experimental and analytical approaches have been attempted with varying degrees of success. Part of the difficulty in developing a comprehensive model of contact-related damage lies in the many different conditions under which fretting wear and fretting fatigue behavior may appear. Analytical techniques to model behavior of laboratory specimens have focused on stress-life [2], stress/strain/displacement, [3] and fracture mechanics based approaches [4–6]. Experimental techniques have interrogated as many as fifty different parameters including, applied stresses, materials, contact geometry, time dependent contact interactions and environmental factors [7]. Considerable difficulty has been encountered in applying the results of these investigations to service components, or even to other test geometries due to the interdependence and time dependence of many of the critical parameters, and due to the localized nature of the phenomenon.

The results of various efforts to model, predict or correct for contact related damage have ranged from application of knockdown factors to determination of fretting fatigue limit stresses and methods to evaluate the local state of stress in components using hybrid finite element/closed form analysis. Knockdown factors must be determined empirically, and are therefore, limited to specific contact and material conditions. The stress-based approach to fretting fatigue life prediction based on maximum stresses at the surface generally under-predicts fretting fatigue life and is also limited to given contact conditions [8]. While each technique has its merits, few show promise of being applicable to service components, because of the complexity of the component geometry as well as the wide range of loading conditions to which the components are subject.

Despite the monumental difficulties presented by contact fatigue in its various forms, many behavioral commonalties have been identified and investigated. Highly localized stress concentrations at the edges of contact are assumed. Various material interactions, such as adhesion and diffusion, as well as environmental interactions, such as oxidation or corrosion, have been identified [6,9–13]. Relative motion between the components, resulting from differences in material moduli, or from bulk loads applied to one or more of the contact members, has been calculated or measured for a wide range of conditions.

Similarities in contact related damage have also been observed. For contacts subjected to partial sliding, in which one of the contact edges moves relative to the mating component, premature nucleation of cracks that propagate to fracture the component have been identified. All contacts subject to relative motion have been observed to produce wear debris to some extent. The synergistic interaction of loading and environmental factors has also been reported [14]. However, very few efforts have addressed fretting fatigue damage mechanisms outside of the context of a specific experimental investigation [15,16].

The purpose of the following discussion is to present observations from several test systems using varied contact geometries over a range of test conditions. From these observations, conclusions about fretting fatigue behavior are presented and the implications of the observations and conclusions on life prediction efforts are discussed. Ti–6Al–4V has been selected as the material of focus for this work due to its numerous aerospace and biomedical applications.

2. Experimental background

2.1. Experimental fretting fixtures

Three experimental fixtures and four contact pad geometries were included for comparison in this work. The test fixtures and pad geometries tested in each are summarized in Table 1. Each fixture was selected because of the unique features offered by each to allow investigation of different regimes in fretting fatigue. The first was a system developed at Massachusetts Institute of Technology (MIT) in which a flat dogbone specimen was contacted on both sides by spherical fretting pads, as indicated in Fig. 1 [17]. This fixture, which we will refer to as the "MIT rig", is typical of many fretting fatigue fixtures reported in the literature. It produces partial transfer of load through the fretting pads to a nominally rigid fixturing device that controls the applied clamping load and pad alignment. Gross sliding occurred early in each test until surface interactions changed the local friction behavior, after which slip–stick conditions prevailed.

The second system was developed at the Air Force Research Laboratory Materials and Manufacturing Directorate (AFRL/MLLMN—henceforth referred to as the "AFRL rig") and was used to test thin flat specimens against flat pads with blending radii at the edges of contact (see Fig. 2) [18]. Unlike the MIT rig, all of the load applied to the specimen in the AFRL rig was transferred to the fixture through the fretting pads. Thus, the portion of the specimen that was beyond the contact area and not subject to the bulk fatigue load was stress free, similar to a dovetail slot. Also, gross sliding was eliminated throughout each test (for all valid tests) thereby simplifying quantification of the shear stress on the contact and minimizing the fretting wear component of damage that tends to obscure small cracks.

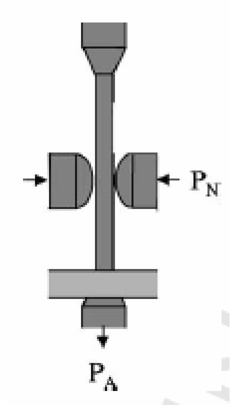

Fig. 1. Schematic of the MIT fretting fixture.

The third fixture was a simplified dovetail fixture (Fig. 3) whose primary feature was cyclic clamping loads. A flank angle of 45. had been incorporated in this fixture and in-phase fatigue loading of both the shear and clamping loads was achieved. Cylindrical pads and flat pads with blending radii were used in tests with this fixture. Gross sliding and slip–stick conditions occurred within each fatigue cycle for this test fixture, since both P and Q vary as a function of time.

2.2. Material

The material used throughout all of the tests reported in this study was Ti–6Al–4V, a common alloy in aerospace and biomedical applications, with a solution treatment and over-aging producing a bimodal microstructure and a re- sulting grain size of approximately 15 µm. This material has been extensively studied as part of the National Turbine Engine High Cycle Fatigue Program. Literature values for the mechanical properties are E = 116 GPa, ? =0.3, s_y = 930MPa under the ambient laboratory conditions used throughout the experimentation [19]. In all cases shown, both the contact pads and the specimen are made of Ti–6Al–4V.

3. Experimental observations

In the following section, observations of several types of damage are presented. The observations were taken from tests conducted in the three test fixtures for a broad range of conditions. First, plastic deformation resulting in generation of both debris particles and cracks or crack precursors is described. Then, crack nucleation locations and the significance of those sites in relation to stress state in the relevant test geometries, as well as the crack nucleation angles are discussed. Finally, observations of wear debris in combination with cracks and the potential impact of such debris on crack propagation is reported.

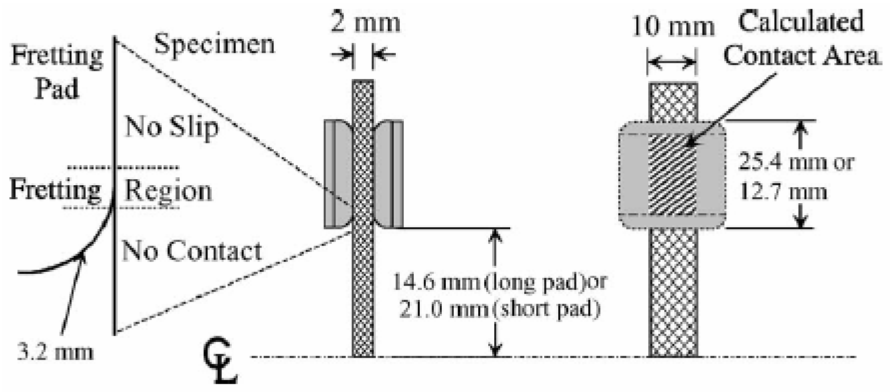

Fig. 2. Schematic of AFRL flat-on-flat fretting fixture.

Fig. 2. Schematic of AFRL flat-on-flat fretting fixture.

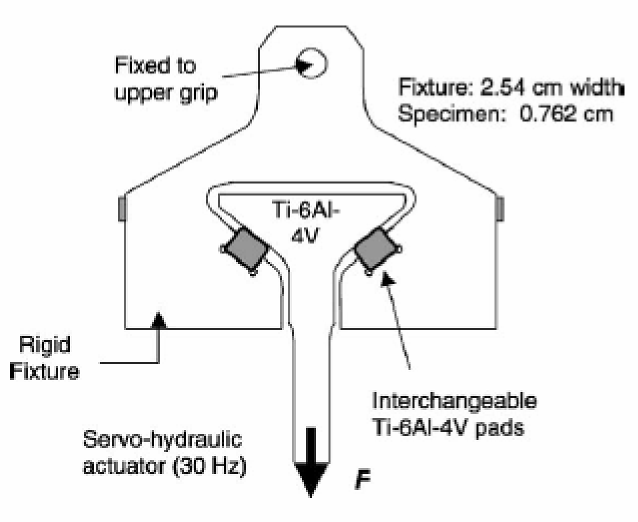

Fig. 3. Schematic of the dovetail fretting fixture and specimen.

3.1. Plasticity

While the overall stresses from the contact fatigue are elastic or elastic via shakedown [20], plastic deformation near the surface occurs, usually in asperity tips as the local stresses exceed yield. Wear typically accompanies this deformation since asperities harden under the fatigue load, become brittle and finally fracture from one of the two main bodies. Observations made of such a region on a specimen contacted by a rounded flat pad (Figs. 4 and 5) indicate removal of asperities in this manner and the presence of resulting craters that contribute to increased roughness. This image also demonstrates that wear pits serve as stress concentrators where cracks can develop.

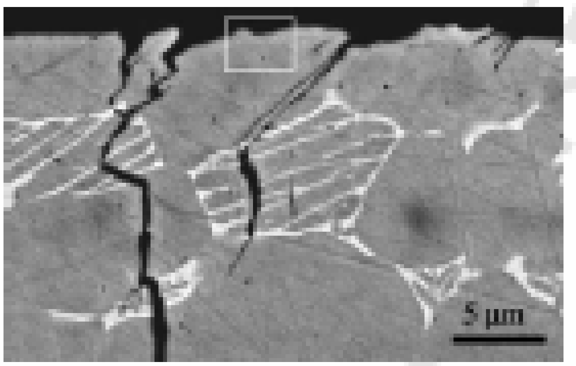

Fig. 4. Cross-section of fretting fatigue crack in the AFRL rig. $s_{n,ave}$ = 610MPa, s_a = 260MPa at $R = 0.5$, N = 4,130,000 cycles; fatigue loading axis is horizontal.

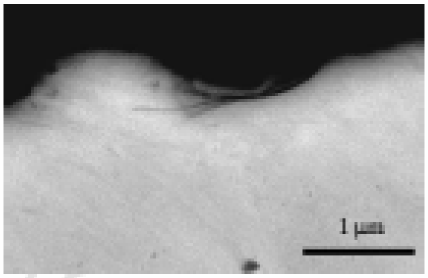

Fig. 5. Magnified view of the region indicated by the white box in Fig. 4. A crack growing from a wear crater into an asperity indicates debris production mechanism.

Under contacts subject to even greater levels of plasticity, micro-sized notches may develop in the slip zone, which may in turn, contribute to the initiation of cracks and further development of wear particles, assuming the continued effects of the contact. Such notches have been observed on specimens, tested in the MIT rig, that were shot-peened prior to testing (see Figs. 6 and 7). Surface treatments such as shot peening are often used to extend the fatigue life of a component subject to cyclic contact loads. However, the impact of shot pellets can result in surface damage that could become nucleation sites for fatigue cracks, particularly if the residual stresses are either thermally or mechanically relieved [21]. Note the significant plastic deformation due to wear in the slip region in Fig. 6.

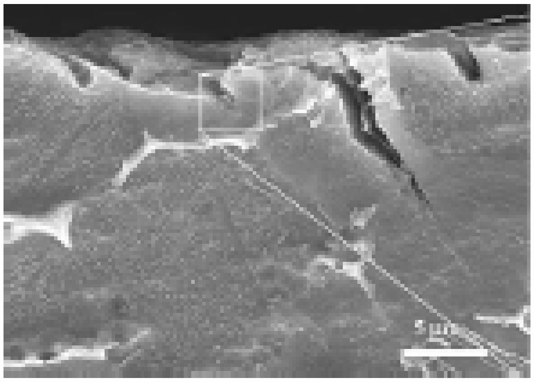

Fig. 6. SEM image of surface damage showing delamination and theformation of small notches developing into cracks (MIT rig: P = 50 N,Q = 27.5N, N = 300,000 cycles, s_{axial} = 270MPa, $R = 0.1$, r = 12.7 mm; fatigue loading axis is horizontal).

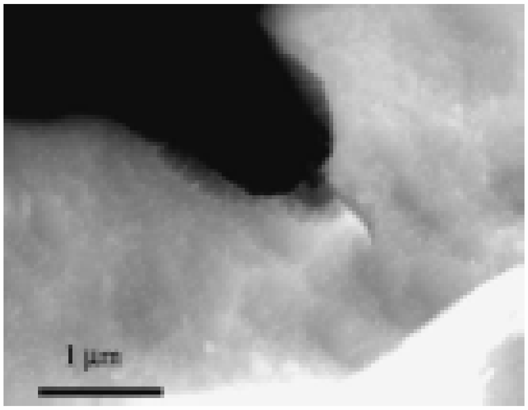

Fig. 7. Magnified view of the region indicated by the white box in Fig. 6. A small crack (0.5 µm) growing out of a notch points to notches as a potential crack initiation mechanism.

Contact pressure superimposed on the compressive residual stresses produced by shot peening could result in a stress state where the compressive yield strength of the material is exceeded at the surface at the leading edge of contact, thus mechanically relieving the residual stresses [22]. Effects of local sliding in the form of localized heating may further relieve the residual stresses, depending on material, heat treatment, and related factors. The surface yielding impacts fretting fatigue damage in two ways. First, surface wear depth increases. Fig. 6 is a picture of a fretting fatigue damage near the edge of contact for a specimen tested under contact conditions of $P = 50$ N, $Q = 27.5$N, $s_{\mathrm{amp}} = 270$MPa, $R = 0.1$, and a pad radius of 12.7 mm. Note that cracks are formed in a severe wear region. The depth of wear was observed to be two to three times greater than that of unpeened specimens, perhaps a result of the higher stresses or longer lives supported on the shot peened specimens. Second, wear pits may become micro-notches before nucleating fatigue cracks as seen in Figs. 6 and 7. One 20 µm crack and three small notches are clearly visible. Notches such as these served as initiation sites for fatigue cracks under these conditions, as indicated by an image taken at higher magnification (Fig. 7), in which a small crack can be seen growing out of one of the notches. The damage in Fig. 6, which was only identified in the shot peened specimens, looks similar to what would be expected by crystal plasticity modeling of fretting in Ti–6Al–4V [23].

Although wear pits provide sites favorable for crack nucleation, the related mechanisms are not responsible for crack propagation and not all cracks will nucleate in wear regions. Evidence of this statement can be seen in Fig. 8 in which a crack that nucleated ~ 60µm from the edge of the specimen (just beyond the left edge of the image) can be seen propagating toward the middle of the specimen away from the local wear scar. Such a crack might be expected to propagate by the dislocation movement mechanisms documented for uniaxial fatigue. Accordingly, persistent slip bands can be observed in Figs. 9 and 10 on a specimen that was highly polished prior to testing. The existence of these slip bands, which were found adjacent to a sizeable crack nucleated on a flat specimen tested in the AFRL rig (Fig. 11), suggests that fretting fatigue cracks do propagate by the mechanisms responsible for fatigue crack propagation in metals subjected to uniaxial loading.

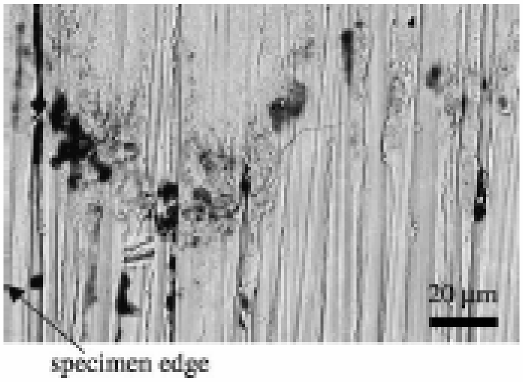

Fig. 8. A fretting fatigue crack nucleated on a flat specimen from the AFRL rig ($s_{n,ave}$ = 650MPa, s_a = 260MPa at R = 0.5, N = 1,000,000 cycles; fatigue loading axis is vertical). Note direction of crack propagation away from wear damage.

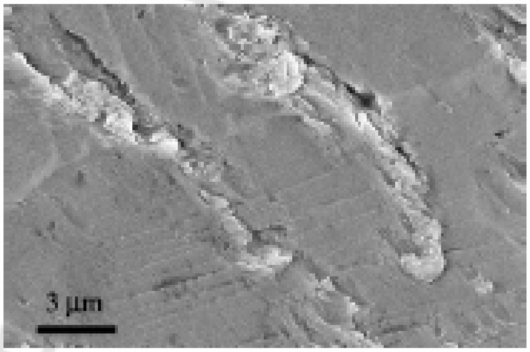

Fig. 9. Slip bands identified in the slip zone on a polished specimen. See left-hand box in Fig. 11 (rotated 90. clock-wise).

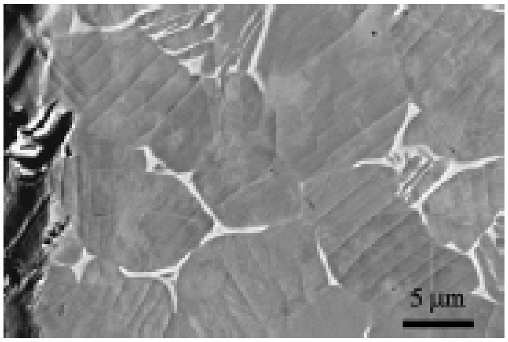

Fig. 10. Slip bands identified adjacent to the slip zone on a polished specimen. See right-hand box in Fig. 11 (rotated 90. clock-wise).

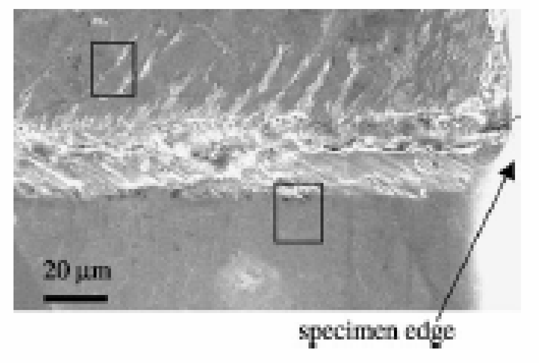

Fig. 11. Fretting fatigue crack nucleated on a highly polished specimen from the AFRL rig ($s_{n,ave}$. 420MPa, s_a = 300MPa at R = 0.5, N = 4,830,000 cycles; fatigue loading axis is vertical).

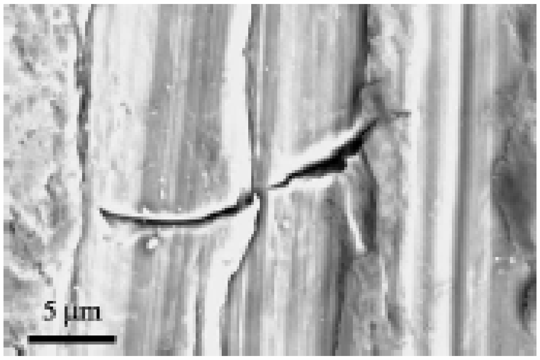

Fig. 12. Magnified view of the fretting fatigue crack indicated by the left-hand box in Fig. 14. Minimal wear debris indicates crack nucleation due to stress concentration.

In some specimens, cracks have been observed in the absence of any significant fretting wear. In Figs. 12 and 13, two cracks are shown that nucleated in the bottom of grooves created during specimen fabrication. These cracks were found on a single flat specimen tested in the AFRL rig, within the relative slip region at the edge of contact (Fig. 14). The location of these cracks was consistent with the estimated nucleation sites of larger cracks found on other specimens that were tested under similar conditions (not shown). From this evidence, one can conclude that, at least under some conditions, local stresses are sufficient to nucleate cracks with minimal influence from the wear component of damage.

Fig. 13. Magnified view of the fretting fatigue crack indicated by the righthand box in Fig. 14.

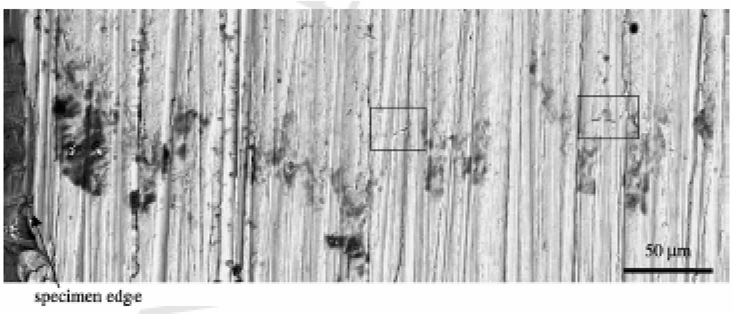

Fig. 14. Fretting scar containing cracks nucleated in the AFRL rig. Boxes indicate the location of cracks that nucleated almost simultaneously due to stress concentration at the edge of contact. $s_{n,ave}$ = 640MPa, s_a = 260MPa at R = 0.5, N = 1,000,000 cycles, fatigue loading axis is vertical.

3.2. Crack initiation behavior

The location of fretting fatigue nucleated cracks seems to further emphasize the role that strain plays in fretting fatigue damage progression. For the sphere-on-flat geometry, tested in the MIT rig, observations [24] reveal that fretting cracks initiated on the centerline of the contact region near the edge of contact closest to the actuator. Cracks initiate in this location since the edge of contact closest to the actuator is subjected to the maximum contact stresses [20] at the same time the specimen is subjected to the greatest bulk tension. Fig. 15 indicates a crack that developed within ±25µm of the edge of contact, which corresponds to the region of relative slip or the region just outside the slip zone. Crack nucleation behavior of this type is characteristic of the sphere-on-flat contact geometry.

Observations of flat specimens tested in the AFRL rig indicated that cracks typically nucleate in the slip zone, within approximately 1mm of the sample edge (Fig. 14) [25]. The actual crack location varies from specimen to specimen in this test fixture, depending on loading conditions and local variations in geometry. However, it is important to note that crack nucleation does not occur on the corner, where the least material constraint and the greatest wear are found, or near the center at the location of the highest stress.

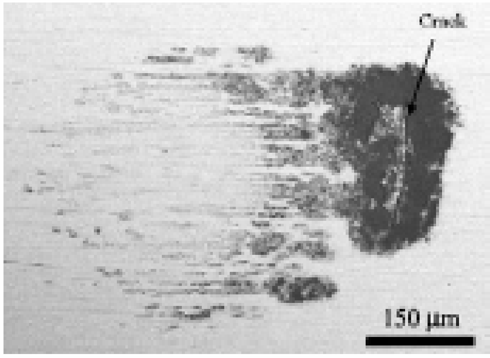

Fig. 15. Fretting scar from the sphere-on-flat geometry. Note crack at trailing edge of contact (MIT rig: P = 50 N, Q = 27.5N, N = 300,000 cycles, s_{axial} = 270MPa, R = 0.1, r = 12.7 mm; fatigue loading axis is horizontal).

Identifying cracks on the dovetail specimens was complicated by the presence of wear debris volume greater than that observed on specimens subjected to static clamping loads. Crack identification through the debris bed was finally achieved by cutting the scar from the original sample and placing it in a three-point-bend apparatus developed for the SEM. Using this technique, dominant cracks were found on the side of the dovetail scar closest to the actuator in the slip region, but not always near the edge of contact. Sectioning and polishing revealed cracks had nucleated at both edges of contact (even the side away from the actuator—see Fig. 16). The crack location with respect to the edge of contact is likely a result of the cyclical normal loading, which causes the contact width to decrease as the normal load decreases. Besides the dominant cracks, multiple cracks with surface lengths on the order of 20µm were found in the slip region. This phenomenon of nearly simultaneous multiple crack initiations is common throughout the contact geometries and fixtures.

Two different types of cracks have been identified for fretting wear in sphere-on-flat contact geometry [26]. The first type was oriented at a shallow angle to the surface. Dubourg and Lamacq postulated that this type of crack was shear initiated. The second type entered at a steeper angle and was believed to have initiated as a result of normal stresses. The type I cracks entered at angles between 15 and 40. to the surface while the type II cracks entered at angles between 60 and 85.. Similar behavior was observed in all 289 geometries and fixtures investigated here. Note in Figs. 4, 6 and 16 the fretting fatigue crack nucleation angles for the AFRL, MIT and Dovetail rigs, respectively.

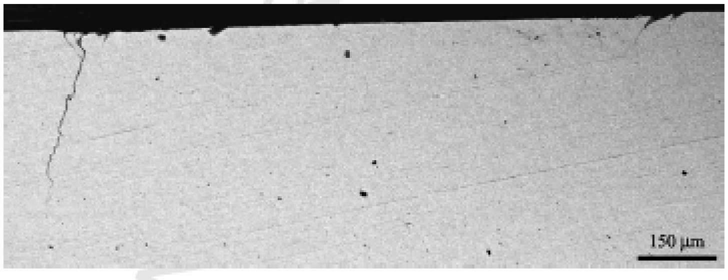

Fig. 16. Cross-section of a dovetail specimen fretting region. Fretting pad geometry was a 3mm flat with a 3mm radius blending into an 11. chamfer.Note fretting cracks at leading (right) and trailing (left) edges of contact.

The crack entrance angles may be estimated using the fretting fatigue crack analogue [6] model and the mechanics of kinked cracks [27]. Giannakopoulos et al. suggest for the case of the sphere on flat geometry that the surface tractions are asymptotically square root singular for a contact under partial-slip conditions [6]. They propose that these tractions are analogous to crack tip stress-intensity factors where the bulk normal component, p, is k_1 and the bulk shear component, q, is k_2 as x approaches the edges of contact. Using mechanics of kinked cracks, the contact stress-intensity factors are analogous to the large crack region, and the incipient fretting crack is analogous to the kinked crack with local k_1 and k_2 [27]. With the condition that the kinked crack will advance in the direction that $k_2 = 0$, the angle is predicted to be 70.5. if k_1 . 0. This result agrees well with the observations of type II cracks in general and specifically in the case of dominant cracks in sphere on flat contacts in titanium [28]. It should be noted that the presence of a bulk stress acting parallel to the surface in fretting fatigue is analogous to the asymptotically non-zero T stresses identified for the stress state at the crack tip in fracture mechanics [6]. These stresses can bias the actual angle of entrance compared to the predicted one [27]. This behavior in the presence of a bulk stress is distinctly different from the case of fretting wear. The observations noted above, namely plasticity induced wear and cracking, and the crack nucleation behavior for each of the three geometries, all seem to point to a single fact: that wear and state of stress both play a role in crack development. Whether wear or state of stress is more dominant seems to depend on local contact and material conditions. But, regardless of the actual crack nucleation mechanism, cracks are the hallmark of fretting fatigue damage and in the absence of significant levels of wear, will nucleate under the applied contact stresses with wear becoming a contributing factor as the crack presence alters the stress state and the dynamic behavior of the contact. The qualitative effect of wear on nucleated fretting fatigue cracks is noted below.

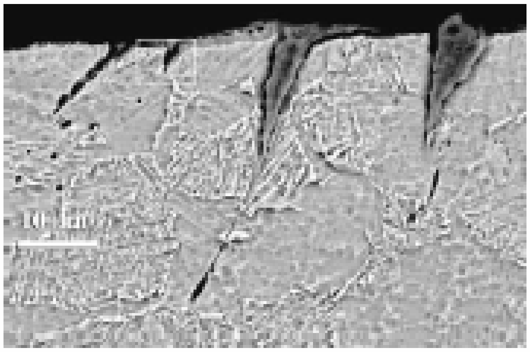

Fig. 17. Fretting cracks containing wear debris on a specimen tested in the MIT rig. Fatigue loading axis is horizontal (P = 50 N, Q = 27.5N, N = 300,000 cycles, s_a = 270MPa, R = 0.1, r = 12.7 mm; fatigue loading axis is horizontal).

3.3. Crack propagation mechanisms

Figs. 17 and 18 were taken from a specimen tested against a spherical pad in the MIT rig. Fig. 17 shows cracks that are filled with wear debris that was probably generated by wear mechanisms from the sample surface and subsequently forced into the crack mouth by the fretting pad. The smallest of these cracks is about 3 µm long (Fig. 18).

Similar observations have been recorded for tests conducted on the flat-on-flat geometry. In Fig. 19, a crack ~ 10µm long can be seen with debris filling the crack mouth. The presence of debris in the crack mouth also serves to render the crack invisible to many common inspection techniques, including optical and eddy current inspection. Much of the damage presented here was not visible even using secondary emission SEM and could only be imaged using backscatter emission techniques and three-point-bend fixtures to open the cracks.

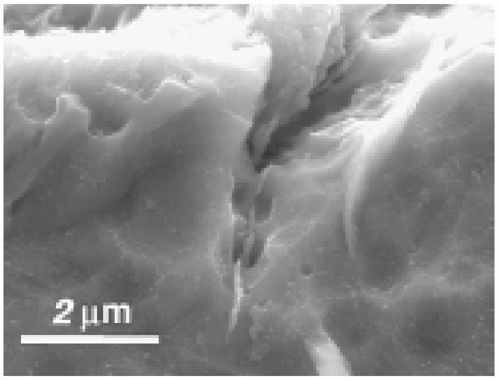

Fig. 18. Magnified view of the fretting fatigue crack indicated by the white box in Fig. 17. Note wear debris in crack mouth.

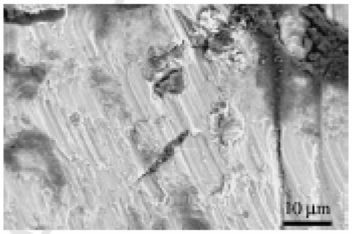

Fig. 19. Fretting fatigue crack from a specimen tested in the AFRL rig. Note wear debris in crack mouth ($s_{n,ave}$ = 240MPa; s_a = 350MPa at $R = 0.5$; N = 1,000,000 cycles, fatigue loading axis is vertical).

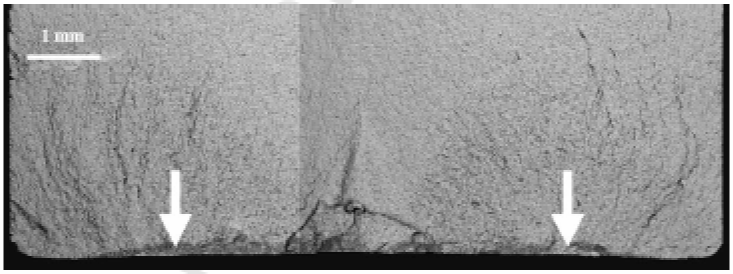

Fig. 20. Fracture surface from a specimen tested in the AFRL Dovetail rig. Note the crack initiation sites (indicated by white arrows), the propagation paths of the cracks and the location where the two crack merged in roughly the center of the specimen. Fretting pad geometry was a 3mm flat with a 3mm radius blending into an 11. chamfer.

In Fig. 20, the fracture surface from a dovetail specimen is shown on which two crack initiation sites approximately equidistant from the center of the specimen can be seen. Semi-quantitative elemental analysis near the sites of initiation (indicated by the white arrows) revealed a higher concentration of oxygen in these regions compared to other regions of the fracture surface. Based on this evidence and on the surface morphology, the presence of wear-generated oxide to a depth of 100 µm on the fracture seems the most likely conclusion. In the cross-section shown in Fig. 21 (an enlarged view of the trailing edge of contact the shown in the left half of Fig. 16), debris can be seen in the crack mouth to a depth of 25–50 µm. The location of this cross-section with respect to the center of the specimen is unknown.

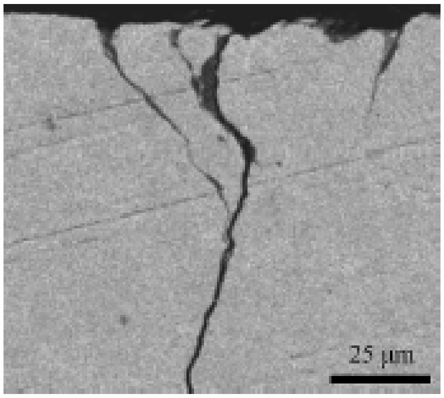

Fig. 21. Fretting fatigue crack from the trailing edge of contact in a dovetail specimen. Note presence of debris in crack mouth. Fretting pad geometry was a 3mm flat with a 3mm radius blending into an 11° chamfer.

In general, four stages of fretting fatigue crack growth are assumed. The first stage is crack nucleation. The second stage is propagation by the combination of the contact and bulk stresses. This stage lasts until the total stress asymptotically approaches the stress-state of the bulk material. The third stage is crack propagation solely by the bulk stresses. The fourth stage is that of fast fracture and can be neglected in terms of the overall fatigue life [29]. The latter three stages would seem to be controlled exclusively by the local stress field; however, a life prediction approach based on this assumption would fail to incorporate the effect of the types of damage observed here. Clearly, the growth of cracks such as the would be heavily influenced by the presence of debris in the crack wake, and the presence of this debris seems to be independent of contact geometry or loading conditions.

The propagation of such cracks would also be influenced by the presence of surface treatments, such as shot peening, intended to inhibit the nucleation and propagation of fretting fatigue cracks via the introduction of compressive residual stresses. In the previous section, peening was shown to worsen the effect of plasticity induced surface damage in some of the specimens investigated here. However, observations of shot peened-treated specimen cross-sections revealed that many cracks nucleated but most if not all cracks arrested. Thus, the combination of contact stresses, bulk stresses and residual stresses were such that the local stress intensity factor to dropped below threshold [30], which can vary as a function of depth with the stress ratio. This finding is consistent with observations in the literature on fretting fatigue of shot peened specimens of other materials and geometries [31]. Thus, the residual stresses may not necessarily prevent crack initiation but certainly inhibit growth.

4. Discussion

4.1. Impact of micro-mechanisms on life-prediction modeling

The presence of the types of damage described above, such as the presence of multiple cracks and wear debris in the crack wake, directly impact efforts at fretting fatigue life prediction. The observations of other mechanisms, such as the presence of dislocation movement and near-surface plasticity, provide information to clarify which processes are present during fretting fatigue damage progression, and help explain the transition in behavior over the domain of possible slip conditions.

Near-simultaneous nucleation of fretting fatigue cracks has been noted in specific contact geometries [9]. For a given contact plane only one or two such cracks actually propagate to specimen fracture. Our observations indicate that this phenomenon is true regardless of contact geometry or loading condition. The presence of several cracks, even in the complex stress state surrounding the contact, would result in crack shielding. Thus, fracture mechanics based modeling of cracks growing out of this region should adjust *K* to an effective *K* to account for shielding effects:

$$K \; ? \; K_{eff} \quad (1)$$

The micro-mechanism of wear debris can be expected to impact fracture-mechanics based life-prediction models. Once a crack initiates and is opened by the tensile portion of the fretting fatigue loading, wear debris at the surface may enter into and fill the crack, thus diverting energy from the crack tip. Typical modeling of short cracks is based on the absence of crack closure due to plastic wake. Often, the absence of closure leads to accelerated crack growth compared to linear elastic cracks of the same K. However, the observations in this study clearly show very small cracks ($l \sim$ 5µm) filled with debris.

From early research in steels, it has been shown that as the displacement or the ratio of Q_{max} (_P) increases, the number of cycles to failure reaches a minimum then increases [32,33]. The wear damage due to contact is a function of the displacement. Vingsbo and Söderberg postulated that increased wear damage may remove small cracks [32]. Fatigue life (represented by the solid line) and wear removal (represented by the dashed line) are shown qualitatively as functions of the displacement in Fig. 22. However, the increase in wear also results in an increase in the production of wear particles that can enter cracks and retard propagation. The ratio of crack removal and crack filling would change as a function of displacement with the former becoming more dominant in the region of global sliding. However, at some point in the partial-slip regime, the rate of change in the fatigue life as a function of displacement is reduced until the minimum fatigue life is reached. The authors hypothesize that this effect is due to the filling of cracks by wear particles, since the wear rate is still insufficient to remove small cracks. Otherwise we would expect both a constant rate of change in the fatigue life (in partial-slip) as a function of displacement as well as a sharp transition in fatigue life and mechanisms upon sliding. Therefore, the effective stress-intensity factor from above should also include the effects of the wear particle by becoming a function of displacement. Based on the foregoing, a relationship in the form (2) would be expected: K_{eff} ? K_{eff} _l, d or Q_{max} (_P)_ (2) where l is the crack length and d the displacement.

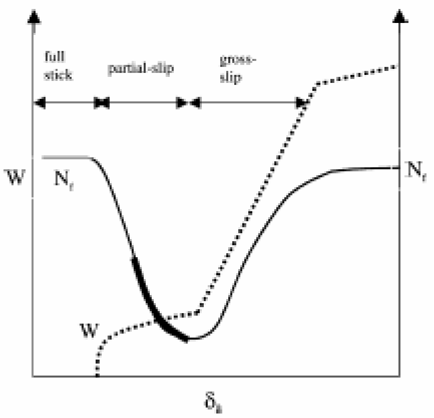

Fig. 22. Schematic indicating the dependence of fatigue life (N_f) and wear volume (W) on fretting displacement slip amplitude. The region where wear debris most impacts fatigue life is highlighted.

Crack arrest also impacts life-prediction modeling. There are several reasons why fretting fatigue cracks nucleate and then arrest. These include the combined effects of shielding, wear filling of cracks, evolution of surface interaction as characterized by coefficient of friction (μ), near surface crystal properties and the combination of contact and bulk stresses below the contact interface. Merely determining crack initiation based on local stresses has been shown to be overly conservative [34]. Such methods may predict crack initiation but fail to incorporate the effects of micro-mechanisms that would inhibit propagation. Likewise, short-crack fracture mechanics methods may be also overly conservative because of crack closure due to wear debris in cracks as that are only a few microns in length. Both initiation-based and fracture mechanics based life-prediction methods may be conservative because of the effects of the stress-state and micro-mechanisms. Stress/strain-at-a-point methods would fail to capture any of these effects. Introduction of a length-scale such as a volume-averaging technique [35] or fracture mechanics-based method would help capture the gradient in contact stresses. Fracture mechanics could be modified in light of crack shielding. Crystal plasticity modeling may reveal more information on near-surface plasticity and wear. However, none of these approaches adequately addresses the evolution of frictional properties, to which contact stresses are extremely sensitive [8]. To truly incorporate all of these micro-mechanisms would be extremely difficult and one might need to resort to a probabilistic design approach.

5. Summary

An examination of specimens and pads from three different fretting fixtures and four different contact geometries revealed several damage mechanisms that are of note. Fretting fatigue produces wear debris that can enter cracks a few microns in length and cause crack closure in very small cracks in Ti–6Al–4V. While wear debris does interact with cracks, the depth of wear or appearance of wear is a poor indicator of fretting fatigue life.

The overall contact mechanics in fretting fatigue are elastic, although localized plasticity is present. The plasticity results in wear damage at the surface and near-surface ratcheting. Micro-notches form in the wear region with lengths as small as 1 μm and root radii as small as 0.5 μm. These features, seen mainly on specimens that were shot peened prior to testing, become crack initiation sites and contribute to further wear damage through the development of small cracks that propagate until surface material is removed.

In all of the fretting geometries observed, multiple cracks initiate nearly simultaneously. The presence of multiple cracks encourages crack shielding. Also, early crack growth is affected by the crystallographic properties of near surface grains. As a result of these mechanisms, most fretting fatigue cracks that do initiate do not propagate, but arrest. Only one or two will dominate in propagation.

Acknowledgements

The portion of this work performed at MIT was supported by the Multi-University Research Initiative (MURI) on High Cycle Fatigue, which is funded by the Air Force Office of Scientific Research, Grant No. 49620-96-1-0478, through a subcontract from the University of California at Berkeley. The work at AFRL was supported by the University of Dayton Research Institute, Air Force Contact No. 33615-98-C-5214.

References

[1] E.M. Eden, W.N. Rose, F.L. Cunningham, The endurance of metals, Proc. Inst. Mech. Eng. 4 (1911) 839–974.

[2] M. Szolwinski, T.N. Farris, Observation, analysis and prediction of fretting fatigue in 2024-T351 aluminum alloy, Wear 221 (1998) 24–36.

[3] C. Ruiz, K.C. Chen, Life assessment of dovetail joints between blades and disks in aero-engines, in: Proceedings of the International Conference Fat., Sheffield, I. Mech. E., London, 1986, pp. 197–194.

[4] P.R. Edwards, The application of fracture mechanics to predicting fretting fatigue, in: R.B. Waterhouse (Ed.), Fretting Fatigue, Elsevier Applied Science, London, 1981, pp. 67–99.

[5] A.E. Giannakopoulos, T.C. Lindley, S. Suresh, Aspects of equivalence between contact mechanics and fracture mechanics: theoretical connections and life prediction methodology for fretting fatigue, Acta Mater. 46 (9) (1998) 2955–2968.

[6] A.E. Giannakopoulos, T.A. Venkatesh, T.C. Lindley, S. Suresh, The role of adhesion in contact fatigue, Acta Mater. 47 (18) (1999) 4653– 4664.

[7] J.M. Dobromirski, Variables of fretting process: are there 50 of them? in: M. Helmi Attia, R.B. Waterhouse (Eds.), Standardization of Fretting Fatigue Test Methods and Equipment, ASTM STP 1159, Am. Soc. Testing Mater., Philadelphia, PA, USA, 1992, pp. 60–66.

[8] A.L. Hutson, T. Nicholas, S.E. Olson, N.E. Ashbaugh, Effect of sample thickness on local contact behavior in a flat-on-flat fretting fatigue apparatus, Int. J. Fatigue 23 (2001) S445–S454.

[9] T.C. Lindley, Fretting fatigue in engineering alloys, Int. J. Fatigue 19 (1997) S39–S49.

[10] M.M. Hamdy, R.B. Waterhouse, The fretting fatigue behavior of Ti–6Al–4V at temperatures up to 600 .C, Wear 56 (1979) 1–8.

[11] S. Saritas, R.P.M. Procter, W.A. Grant, Effect of ion implantation on fatigue, fretting and fretting corrosion of Ti–6Al–4V, Mater. Sci. Eng. A115 (1989) 307–314.

[12] R.B. Waterhouse, The role of adhesion and delamination in the fretting ware of metallic materials, Wear 45 (1977) 355–364.

[13] R.B. Waterhouse, Fretting wear, Wear 100 (1984) 107–118.

[14] D.W. Hoeppner, Mechanisms of fretting fatigue, in: R.B. Waterhouse, T.C. Lindley (Eds.), Fretting Fatigue, ESIS 18, Mechanical Enginee- ring Publications, London, 1994, pp. 3–19.

[15] R.A. Antoniou, T.C. Radtke, Mechanisms of fretting-fatigue of titanium alloys, Mater. Sci. Eng. A (1997) 229–240.

[16] D.E. Taylor, Fretting fatigue in high temperature oxidising gases, in: R.B. Waterhouse (Ed.), Fretting Fatigue, 1981, pp. 177–202.

[17] B.U. Wittkowsky, P.R. Birch, J. Dominguez, S. Suresh, An apparatus for quantitative fretting-fatigue testing, Fat. Fract. Eng. Metal Struct. 22 (4) (1999) 307–320.

[18] A.L. Hutson, T. Nicholas, R. Goodman, Fretting fatigue of Ti–6Al–4V under flat-on-flat contact, Int. J. Fatigue 21 (7) (1999) 663–670.

[19] G.K. Haritos, T. Nicholas, D. Lanning, Notch size effects in HCF behavior of Ti–6Al–4V, Int. J. Fatigue 21 (7) (1999) 643–652.

[20] A.R.S. Pointer, A.D. Hearle, K.L. Johnson, Application of the kinematical shakedown theorem to rolling and sliding point contacts, J. Mech. Phys. Solids 33 (4) (1985) 339–362.

[21] R.B. Waterhouse, Residual stresses and fretting—crack initiation and propagation, in: Advances in Surface Treatment-Technology,Applications, Effects, vol. 4, Residual Stresses, Pergamon Press, Oxford, 1987, p. 517.

[22] G.W. Kirkpatrick, Fretting fatigue analysis and palliatives, SM Thesis, MIT, 1999.

[23] C.-H. Goh, J.M. Wallace, R.W. Neu, D.L. McDowell, Polycrystal plasticity simulations of fretting fatigue, Int. J. Fatigue 23 (2001) S423–S435.

[24] G.M. Hamilton, Explicit equations for the stresses underneath a sliding spherical contact, Proc. Inst. Mech. Eng. 197C (1983) 53–59.

[25] A.L. Hutson, C. Neslen, T. Nicholas, Characterization of fretting fatigue crack initiation processes in Ti–6Al–4V, Trib. Int. 36 (2003) 133–143.

[26] M.-C. Dubourg, V. Lamacq, Stage II crack propagation direction determination under fretting fatigue loading: a new approach with experimental observations, in: D.W. Hoeppner, V. Chandrasekaran, C.B. Elliot (Eds.), Fretting Fatigue: Current Technology and Practices, ASTM STP 1367, Am. Soc. Testing Mater., West Consho- hocken, PA, USA, 2000, pp. 436–450.

[27] B. Cotterell, J.R. Rice, Slightly curved or kinked cracks, Int. J. Fract. 16 (1980) 155–169.

[28] T.A. Venkatesh, B.P. Conner, C.S. Lee, A.E. Giannakopoulos, T.C. Lindley, S. Suresh, An experimental investigation of fretting fatigue in Ti–6Al–4V: the role of contact conditions and microstructure, Metal Trans. 32A (2001) 1131–1146.
[29] D.W. Hoeppner, Review of fretting fatigue component life estimation/ prediction: past, present and future, in: Y. Mutoh, S.E. Kinyon, D.H. Hoeppner (Eds.), Fretting Fatigue: Advances in Basic Understanding and Applications, ASTM STP 1425, ASTM International, West Conshohocken, PA, in press.
[30] L. Chambon, A unified fracture mechanics approach to fretting fatigue growth, SM Thesis, MIT, 2001. 602
[31] T.C. Lindley, K.J. Nix, Fretting fatigue in the power generation industry, in: H.A. Attia, R.B. Waterhouse (Eds.), Standardization of Fretting Fatigue Test Methods and Equipment, ASTM STP 1159, Am. Soc. Testing Mater., Philadelphia, PA, USA, 1992, pp. 153– 169.
[32] O. Vingsbo, D. Söderberg, On fretting maps, Wear 126 (1988) 131– 147.
[33] F.S. Sproles, D.J. Duquette, The mechanism of material removal in fretting, Wear 49 (1978) 339–352.
[34] H. Murthy, T.N. Farris, Fretting fatigue of Ti–6Al–4V subjected to blade/disk contact loading, in: developments in fracture mechanics for the new century, 50th Anniversary of Japan Society of Materials Science, Osaka, Japan, 2001.
[35] S. Fouvry, Ph. Kapsa, L. Vincent, Fretting-wear and fretting-fatigue: relation through mapping concept, in: D.W. Hoeppner, V. Chandrasekaran, C.B. Elliot (Eds.), Fretting fatigue: current tech- nology and practices, ASTM STP 1367, Am. Soc. Testing Mater., West Conshohocken, PA, USA, 2000, pp. 49–64.

Incorporating Residual Stresses in Life Prediction of Turbine Engine Components

Reji John[1], James M. Larsen[1], Dennis J. Buchanan[2], and Noel E. Ashbaugh[2]

The U.S. Air Force has initiated a technology development initiative known as Engine Rotor Life Extension (ERLE), which has the goal of extending the useful lifetime of major, fracture-critical components in currently fielded gas turbine engines, without increasing the risk of component failure. Full achievement of this goal will require improvements in a broad range of technologies, including life prediction and fracture mechanics, nondestructive evaluation, engine usage and health monitoring, and component repair. This paper focuses on the incorporation of residual stress effects. Beneficial surface treatments are extensively employed in the turbine engine components. However, current damage-tolerance-based life management practices do not explicitly account for the residual stresses induced by surface enhancement procedures. This paper provides an assessment of the role of residual stresses in the durability of the component and identifies critical issues to be addressed during implementation in life prediction methods.

INTRODUCTION

A technology development program known as Engine Rotor Life Extension (ERLE) [1] has been initiated by the United States Air Force. ERLE has the goal of extending the useful lifetime of major, fracture-critical components in currently fielded gas turbine engines, without increasing the risk of component failure. A broad range of related technologies such as life prediction and fracture mechanics, nondestructive evaluation, engine usage and health monitoring, and component repair have been targeted for achievement of this goal. The total life of an engine component can be determined as the sum of crack initiation life and crack propagation life. Crack propagation life typically includes the small and large crack growth regimes. Current life management practice (Engine Structural Integrity Program, ENSIP) [2,3] by the U.S. Air Force uses a damage-tolerance-based method for managing the life of safety-critical components. This approach is based on systematic inspections of critical life-limiting locations in components. The inspection intervals are determined as 50% of the predicted crack growth life from an assumed initial flaw size. Using nondestructive inspection (NDI) techniques, the components are inspected for location-specific crack sizes. The component design lifetime is based on a crack initiation criterion, but if a crack is detected prior to this mandatory component retirement lifetime, then the component is retired immediately.

The prediction of the crack length versus cycles behavior at critical locations in a component is based on the expected thermo-mechanical loading conditions and the assumed crack growth behavior of the material. Prior to insertion in service, most critical locations, such as holes, stress concentration sites, etc., are subjected to surface enhancement procedures such as shot peening. Most of the legacy engines use shot-peening to retard crack growth at critical locations. Shot-peening introduces significant near-surface (within 150-200 μm) compressive stresses. The benefits of these compressive residual stresses in improving fatigue life, retardation of crack growth and

[1] Air Force Research Laboratory, Materials and Manufacturing Directorate, AFRL/MLLMN,
2230 Tenth Street, Suite No. 1, Wright-Patterson Air Force Base, Ohio 45433-7817, U.S.A.
[2] University of Dayton Research Institute, 300 College Park, Dayton, Ohio 45469, U.S.A.

resistance to foreign object damage have been extensively demonstrated. However, current damage-tolerance-based life management practices, i.e. predictions of crack initiation life and crack propagation life, do not explicitly account for the residual stresses induced by surface enhancement procedures. In current engines, shot-peening is used as a bonus factor of safety, resulting in potentially excessive conservatism in the component life prediction. Hence, incorporating residual stresses in crack growth life prediction is a key life extension technology. This paper provides an assessment of the role of residual stresses in the durability of the component and identifies critical issues to be addressed during implementation in life prediction methods.

MATERIAL

One of the materials used in components under consideration for life extension is Ti-6Al-2Sn-4Zr-6Mo (weight %) (Ti-6246). This material was forged and heat treated to produce a fine duplex microstructure of equiaxed primary a phase (hexagonal close packed) in a matrix of Widmanstatten a + ß (body-centered cubic) phase. This material had a room temperature yield strength of 1158 MPa and a fatigue limit of ~720 MPa at stress ratio, R=0.1. The analysis of crack growth in the presence of residual stresses requires characterization of baseline crack growth behavior of the material over a wide range of stress ratios, R. Hence, experiments were conducted to describe the baseline crack growth behavior of Ti-6246 for the range $-1 \leq R \leq 0.8$.

SHOT-PEEN-INDUCED RESIDUAL STRESSES

During service, the turbine engine components are subjected to complex thermal and mechanical loading conditions. Numerous studies have shown that residual stresses relax during thermal exposure and fatigue loading [for example, 4-9]. Most of these data are based on surface residual stress measurements. However, accurate prediction of crack growth requires the knowledge of residual stress distribution as a function of depth. Figure 1(a) shows the relaxation of residual stresses in Ti-6Al-4V at 325°C [7]. Rapid and significant relaxation (≈50%) is observed near the surface during the first ten minutes and the distribution remains relatively stable beyond 10 minutes. Similar results were also reported for a Ni-base superalloy at 650°C [6]. Most of the relaxation of the residual stresses is confined to ≈ 100 µm below the surface. Recently, Vukelich et al. [10] reported the results of residual stress measurements at various locations in Ni base superalloy engine disks, as shown in Figure 1(b). Although there is significant scatter in the results, the data clearly show that, even after 8000 TACs (Total Accumulated Cycles), the minimum retained surface residual stress is ≈30-50% of the initial level.

The results from Refs. [4-10] show that a wide variation in the magnitude of retained residual stresses can be expected during service. Hence, this paper is directed towards an assessment of the influence of residual stresses on the remaining crack propagation life and the effect of various degrees of retention of residual stresses. Incorporation of residual stresses in prediction of crack growth life requires accurate models to predict the relaxation of residual stresses during service. A few relaxation models [6,9] have been developed for a limited range of temperatures and mechanical loading. Additional extensive testing and modeling are required for accurate prediction of changes in residual stresses under service conditions. Available data indicate that the most substantial residual stress relaxation occurs during the initial cycles. Hence, during this study, crack growth analysis was conducted for various levels of retained residual stresses as a percentage of the original stress distribution.

The estimated baseline residual stress distribution corresponding to shot-peen intensity of ~8A is shown in Figure 2(a). The baseline distribution is identified as "~8A, 100%". The residual stress distributions corresponding to 50% and 20% retention are also shown in Figure 2(a). The corresponding $K_{res,c}$ and $K_{res,a}$ are shown in Figure 2(b). Note that even an assumption of 50% retention of residual stresses results in K_{res} of ≈ -4 to –8 MPa√m for crack sizes of ≈ 50 to 200 μm. These K_{res} values are of the same order of magnitude as ΔK_{th}, and hence, the retained residual stresses are sufficient for significant crack growth retardation. The influence of retained residual stresses on crack propagation life is discussed next.

RESIDUAL STRESS EFFECTS ON CRACK GROWTH

The ENSIP design philosophy assumes that a 794 μm (=1/32 in.) flaw could initiate during service in 1 out of 1000 components. In addition, ENSIP requires that the remaining crack propagation life from an inspectable crack size be equal to the component design life. This life management practice relies on accurate prediction of the crack growth behavior at critical locations and the ability to define safe inspection intervals based on this prediction. Current crack growth predictions exclude the influence of beneficial compressive residual stresses. As discussed earlier, residual stresses relax, and significant scatter exists in the retained residual stresses. Hence, prior to implementation of the residual stresses in component lifing, the sensitivity of crack propagation life to various levels of residual stresses should be assessed. Extensive crack growth analyses were conducted for a semi-elliptical surface crack in an infinite geometry. In this study, the large-crack growth behavior was used for analysis of small cracks. For cracks greater than ≈ 25μm, this assumption was previously shown to be valid in Ti-6Al-2Sn-4Zr-6Mo [11]. The crack growth analyses were conducted using the code AFGROW [12].

Figures 3(a) and 3(b) show the predicted maximum stresses versus crack propagation life, N_p, for an initial flaw size = 120 μm and residual stress levels corresponding to 20% and 50% of 8A. The ratio of propagation life with residual stresses to the baseline life ranges from 2 to 50 depending on the stress level, stress ratio and the retained residual stresses. Under LCF conditions (R = 0.1), 20% retention of the residual stress was sufficient to retain 5X to 50X increase in N_p compared to the baseline. Relative life gain higher than 2X at the high stress level for flaw size of 120 μm required 50% retention of the residual stresses. Under high mean stress conditions (R=0.8), the relative gain at high stress levels is less than 2X for residual stress retention of 50%. The lower gain in N_p at R=0.8 is consistent with similar observations of crack growth in the presence of residual stresses [13].

The crack growth response (surface crack length and crack depth versus cycles) at 600 MPa, R=0.1, corresponding to s_{res} = 0 and 50% 8A is shown in Figure 4(a) and 4(b), respectively. The initial flaw size was c_i = 120 μm and the initial aspect ratio was a_i/c_i = 1.0. In the absence of residual stresses, this surface crack grows such that the aspect ratio remains nearly the same. In addition, at half-life, c has increased from 120 μm to ≈ 210 μm. Hence, the detectability of this crack has increased significantly at the end of the half-life period. In the absence of residual stresses, the crack propagation life = 11150 cycles. In contrast, as shown in Fig. 4(b), crack propagation life in the presence of residual stress = 467743 cycles, which corresponds to ~40X increase in life. The crack grows faster in the depth direction than on the surface resulting in aspect ratio (a/c) greater than 1.0. To enable comparison between baseline and residual stress behavior based on similar inspection intervals, the final 11150 cycles are shown in Figure 2(b). At 5000 cycles prior to failure, the surface and depth crack size in the presence of residual stress is approximately equal to and significantly greater than the corresponding baseline size, respectively. Hence, the development of NDI techniques, which are sensitive to the crack extension in the surface and depth directions, will significantly aid risk reduction.

REMARKS

The results of this study show that even retention of only 20-50% of the original residual stress distribution can yield greater than 2X increase in crack growth life, compared to the current baseline predictions that exclude residual stresses. Data from laboratory coupon specimens and recent field inspection studies have shown that residual stresses can be expected to relax in most components. Thus, combining data from the field with detailed laboratory experiments and analysis, a reduced level of residual stress can be established and implemented in life management practice. Monitoring residual stresses at critical locations during service can help reduce the potential increase in risk associated with disk life extension. Life management based on such threshold residual stress level will require NDI-based accurate monitoring of residual stress at critical locations. Recent depth measurements have shown that the most substantial residual stress relaxation occurs close to the surface. Sub-surface residual stress relaxation is not as severe as that observed on the surface. Hence, the NDI techniques should be capable of sub-surface residual stress measurement, preferably up to 150 μm deep. Note that such residual stress inspections are in addition to current crack inspections being conducted under the ENSIP program. Therefore, successful implementation of a life prediction methodology using residual stresses requires two critical NDI technology developments. These are: (1) accurate and reliable NDI techniques sensitive to crack extension in the surface and depth directions, and (2) NDI techniques to monitor surface and subsurface changes in residual stresses in components.

SUMMARY

Life extension of fracture critical parts is under consideration by the US Air Force. This technology development initiative is expected to significantly reduce the sustainment burden and to enable future long-life durable engines. Data from legacy engines indicate that shot-peen induced residual stresses at critical locations are retained only partially during service. This paper assessed the influence of various levels of retained residual stresses on the remaining crack propagation life in Ti-6Al-2Sn-4Zr-6Mo. The results show that retention of ≈50% of the original residual stress distribution can yield greater than 2X increase in crack growth life compared to the baseline predictions excluding residual stresses. Thus, combining data from the field with detailed experiments and analysis, a threshold level of location-specific residual stress can be established and implemented in the life management practice. The inclusion of residual stresses in life prediction of the component will require NDI-based accurate monitoring of residual stress at life-limiting critical locations, in addition to crack inspections being conducted under the ENSIP program. The NDI techniques should enable monitoring of surface and sub-surface residual stresses.

ACKNOWLEDGMENTS

This research was performed in the Air Force Research Laboratory, Materials and Manufacturing Directorate (AFRL/MLLMN), Wright-Patterson Air Force Base, OH, USA.

REFERENCES

1. Larsen, J.M. et al., "The Engine Rotor Life Extension (ERLE) Initiative and It's Opportunities to Increase Life and Reduce Maintenance Costs," presented at AeroMat 2001, Long Beach, CA, 12 June 2001.
2. Harris, J.A., AFWAL-TR-87-4069, Vol. I., Air Force Wright Aeronautical Laboratories, Wright-Patterson AFB, OH, 1987.
3. Engine Structural Integrity Program (ENSIP), MIL-STD-1783 (USAF), Nov. 2001.
4. Holzapel, H., Schulze, V., Vohringer, O., and Macherauch, E., Materials Science & Engineering, Vol. A248, 1998, pp. 9-18.
5. Berger, M.-C and Gregory, J.K., Matls. Sci. and Eng., Vol. A263, 1999, pp. 200-204.
6. Cao, W., Khadhraoui, M., Brenier, B., Guedou, J.Y., and Castex, L., Material Science and Technology, Vol. 10, 1994, pp. 947-954.
7. Prevey, P., Hornbach, D., and Mason, P., Proceedings of the 17th Heat Treating Society Conference and Exposition and the 1st International Induction Heat Treating Symposium, D.L. Milam et al., Eds., ASM, Materials Park, OH, pp. 3-12, 1998.
8. Prevey, P., Proceedings, 20th ASM Materials Solutions Conference & Exposition, St. Louis, Missouri, Oct. 10-12, 2000.
9. Ahmad, J., Chandu, S., and Prevey, P., To be submitted for publication, 2001.
10. Vukelich, S., Russ, S.M., Berkley, S., and Bradley, E.F., The 9th International Symposium on Transport Phenomena and Dynamics of Rotating Machinery, Honolulu, Hawaii, February 10-14, 2002.
11. Larsen, J.M. and Jira, J.R., Experimental Mechanics, 1991, pp. 82-87.
12. AFGROW, Harter, J., US Air Force Research Laboratory, Air Vehicles Directorate, AFRL/VASM, Wright-Patterson Air Force Base, OH, USA. Available at http://fibec.flight.wpafb.af.mil/fibec/afgrow.html.
13. Ruschau, J.J., John, R., Thompson, S.R., and Nicholas, T., Journal of Engineering Materials and Technology, Vol. 121, No.3, pp. 321-329, 1999.

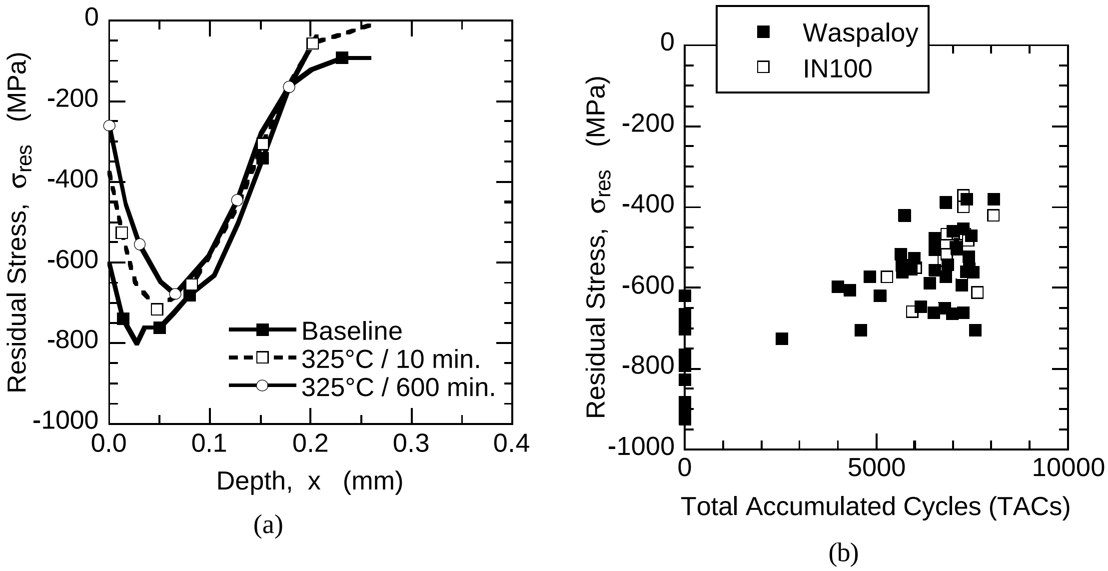

(a)

(b)

Figure 1. (a) Residual stress relaxation in Ti-6Al-4V at 325°C [Prevey et al.], and

(b) Surface residual stress relaxation in engine disks [Vukelich et al.].

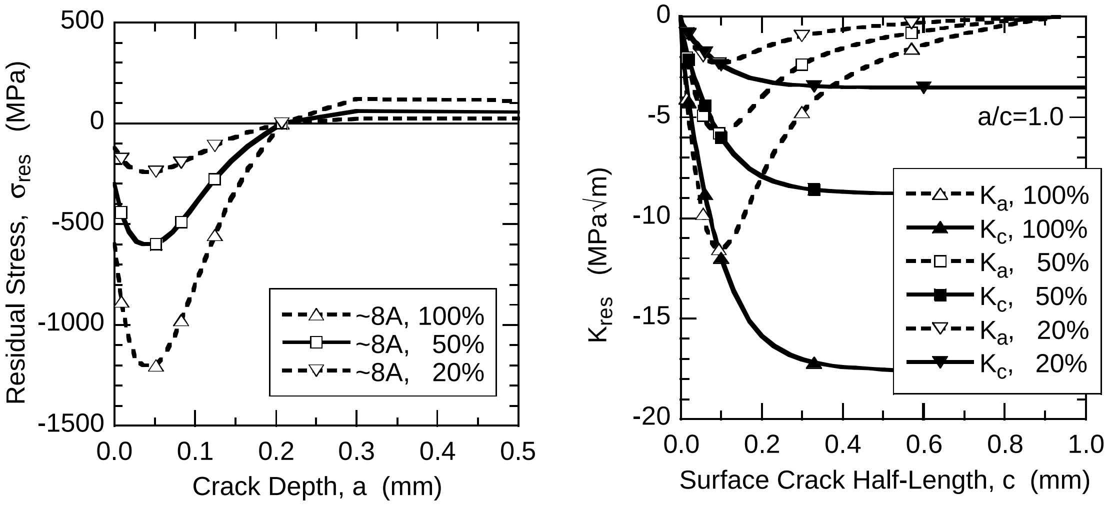

(a) (b)

Figure 2. (a) Assumed residual stress distributions to simulate relaxation during service. Baseline = 100% 8A. (b) Corresponding $K_{res,c}$ and $K_{res,a}$ for aspect ratio, a/c=1.

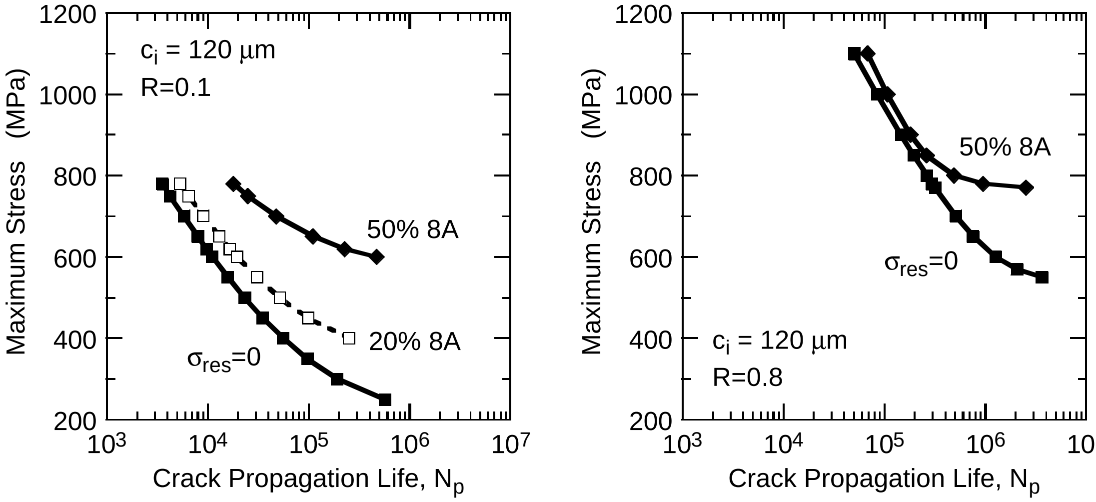

(a) R = 0.1

(b) R = 0.8

Figure 3. Predicted influence of retained residual stresses on crack propagation life. (a) Maximum stress versus propagation life (S-N_p) at R=0.1, and (b) S-N_p behavior at R=0.8. Assumed for $c_{initial}$=120 mm and $(a/c)_{initial}$=1.

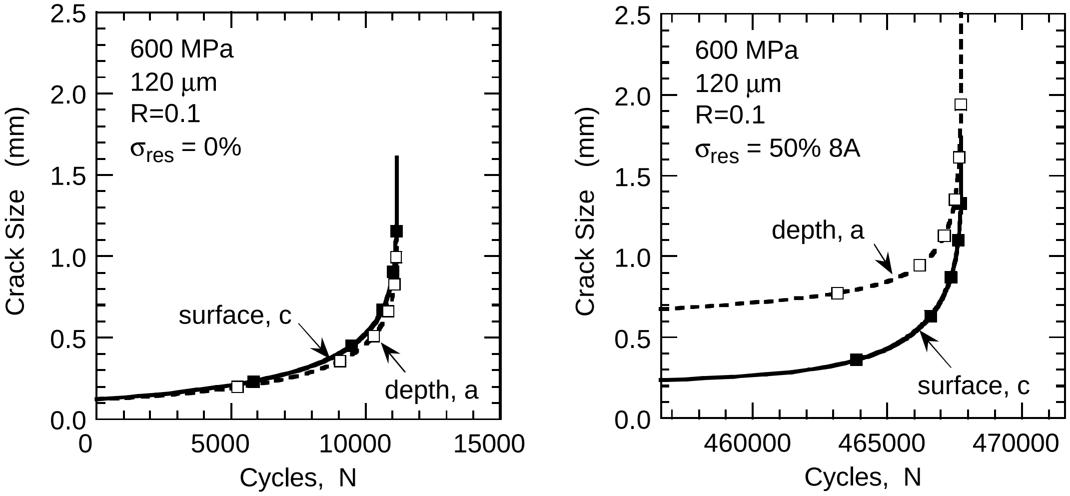

(a) $\sigma_{res} = 0$

(b) σ_{res} = 50% of 8A

Figure 4. Influence of residual stresses on crack growth behavior at R=0.1. Assumed $c_{initial}$ *= 120 mm and* $(a/c)_{initial}$ *= 1.0.*

This page intentionally left blank

NATO RTO (AVT) Symp. on Monitoring and Management of Gas Turbine Fleets for Extended Life and Reduced Costs, Oct. 8-11, 2001

INCORPORATING RESIDUAL STRESSES IN LIFE PREDICTION OF TURBINE ENGINE DISKS

Reji John[1], James M. Larsen[1], Dennis J. Buchanan[2], and Noel E. Ashbaugh[2]

[1] Air Force Research Laboratory
Materials and Manufacturing Directorate
AFRL/MLLMN, 2230 Tenth Street, Suite No. 1
Wright-Patterson Air Force Base, Ohio 45433-7817, U.S.A.
[2] University of Dayton Research Institute,
300 College Park, Dayton, Ohio 45469, U.S.A.

ABSTRACT

The U.S. Air Force has initiated a technology development initiative known as Engine Rotor Life Extension (ERLE), which has the goal of extending the useful lifetime of major, fracture-critical components in currently fielded gas turbine engines, without increasing the risk of component failure. Full achievement of this goal will require improvements in a broad range of technologies, including life prediction and fracture mechanics, nondestructive evaluation, engine usage and health monitoring, and component repair. This paper focuses on a key aspect of the life prediction process – the incorporation of residual stress effects. The benefits of compressive residual stresses in improving fatigue life, retardation of crack growth and resistance to foreign object damage have been demonstrated. Hence, these beneficial surface treatments are extensively employed in the turbine engine components. However, current damage-tolerance-based life management practices do not explicitly account for the residual stresses induced by surface enhancement procedures. Significant increase in predicted damage tolerance can be obtained if residual stresses are included in the life prediction methodology. This paper provides an assessment of the role of residual stresses in the durability of the component and identifies critical issues to be addressed during implementation in life prediction methods.

INTRODUCTION

The U.S. Air Force has initiated a technology development initiative known as Engine Rotor Life Extension (ERLE) [1], which has the goal of extending the useful lifetime of major, fracture-critical components in currently fielded gas turbine engines, without increasing the risk of component failure. A broad range of related technologies such as life prediction and fracture mechanics, nondestructive evaluation, engine usage and health monitoring, and component repair have been targeted for achievement of this goal. The total life of an engine component can be determined as the sum of crack initiation life and crack propagation life. Crack propagation life typically includes the short and long crack growth regimes. Current life management practice (Engine Structural Integrity Program, ENSIP) [2,3] by the U.S. Air Force uses a damage-tolerance-based method for managing the life of safety-critical components. This approach is based on systematic inspections of critical life-limiting locations in components. The inspection intervals are determined as 50% of the predicted crack growth life from an assumed initial crack growth size. Using nondestructive inspection (NDI) techniques, the components are inspected for location-specific crack sizes. The component design lifetime is based on a crack initiation criterion, but if a crack is detected prior to this mandatory component retirement lifetime, then the component is retired immediately.

The prediction of the crack length versus cycles behavior at critical locations in a component is based on the expected thermo-mechanical loading conditions and the assumed crack growth behavior of material. Prior to insertion in service, most critical locations, such as holes, stress concentration sites, etc., are subjected to surface enhancement procedures such as shot peening. Most of the legacy engines used shot-peening to retard crack growth at critical locations. Shot-peening introduces significant near-surface (within 150-200 μm) compressive stresses. The benefits of these compressive residual stresses in improving fatigue life, retardation of crack growth and resistance to foreign object damage have been extensively demonstrated. However, current damage-tolerance-based life management practices, i.e. predictions of crack initiation life and crack propagation life, do not explicitly account for the residual stresses induced by surface enhancement procedures. In current engines, shot-peening is used as a bonus factor of safety, resulting in potentially excessive conservatism in the component life prediction. Hence, incorporating residual stresses in crack growth life prediction is a key life extension technology. This paper provides an assessment of the role of residual stresses in the durability of the component and identifies critical issues to be addressed during implementation in life prediction methods.

MATERIAL

One of the materials used in components under consideration for life extension is Ti-6Al-2Sn-4Zr-6Mo (weight %) (Ti-6246). This material was forged and heat treated to produce a fine duplex microstructure of equiaxed primary a phase (hexagonal close packed) in a matrix of Widmanstatten a + ß (body-centered cubic) phase as shown in Figure 1.

The analysis of crack growth in the presence of residual stresses requires characterization of baseline crack growth behavior of the material over a wide range of stress ratios, R. Hence, fatigue crack growth experiments were conducted using standard compact tension, C(T) geometry and single edge cracked geometry with clamped ends, CSE(T). The C(T) specimen was used for R = 0.1, 0.2, 0.3, 0.5, 0.6, 0.7, 0.8 and 0.9, and the CSE(T) specimen was used for R=-0.5 and –1.0. The crack growth data were acquired under decreasing stress-intensity-factor-range, ΔK, fatigue followed by constant-load amplitude fatigue. The resulting fatigue crack growth rate data were fit using Eqn. (1).

$$\log\left(\frac{da}{dN}\right) = C_1 \left\{\operatorname{arctanh}\left(C_2\left[\log(\Delta K) + C_3\right]\right)\right\} + C_4 \tag{1}$$

in which,

$$C_i = A_{0i} + A_{1i}\log(1-R) + A_{2i}\left[\log(1-R)\right]^2 \ . \tag{2}$$

The baseline crack growth behavior of Ti-6246, as described by Eqn. (1), is shown in Figure 2 for the range $-1 \le R \le 0.8$. In obtaining the constants A_{0i}, A_{1i} and A_{2i}, the fracture toughness of Ti-6246 was set equal to 28

MPa√m, based on the data. Note that, in Figure 2, $\Delta K = K_{max} - K_{min}$ for all R. The threshold stress intensity factor range, ΔK_{th}, is ≈ 1.5 – 4 for all R. Hence, the near-threshold crack growth response of materials with such low values of ΔK_{th} can be expected to be influenced significantly by residual stresses, even if the magnitude of residual stress is low.

SHOT PEEN INDUCED RESIDUAL STRESSES

Shot peening induced residual stress (s_{res}) distributions for Ti-6246 were unavailable in the open literature. Hence, we estimated the residual stress distribution as a function of depth based on available data on similar materials such as Ti-6Al-4V. The magnitude of the residual stress distribution was estimated using the ratio of the yield stresses of the materials (≈1170 MPa for Ti-6246 and ≈950 MPa for Ti-6Al-4V). The estimated s_{res} for Ti-6246 is shown in Figure 3 for four shot peening intensities. Extensive data for various materials available in the literature show that the surface residual stress is typically lower than the sub-surface peak value. The magnitude of the surface residual stress depends on many factors such as shot-peening intensity, shot-peening coverage, surface finish prior to shot peening, material hardening behavior, etc. Hence, based on available data, the surface stress was conservatively assumed to be 50% of the sub-surface peak value.

Using the weight function method, the stress intensity factor due to residual stresses, K_{res} was determined for a semi-elliptical surface with surface crack length = 2c (tip-to-tip), crack depth = a, and aspect ratio, a/c=1. K_{res} at the surface crack tip (c), $K_{res,c}$, and at the deepest point in the depth direction (a), $K_{res,a}$, is shown in Figure 4 corresponding to the s_{res} distributions shown in Figure 3. Since residual stresses are compressive, the computed K_{res} is mathematically negative. While the authors recognize that a negative K_{res} has no formal meaning, negative K_{res} is used to describe the relative magnitude of the compressive stress across the crack surfaces. K_{res} is always added to the applied K, and the total K = applied K + K_{res} should be positive for crack growth to occur. The magnitude of $K_{res,c}$ and $K_{res,a}$ are in the same range or higher than ΔK_{th} for a = 50 – 300 μm. Hence, in this regime of crack growth, significant influence of s_{res} on the crack length versus cycles response can be expected. $K_{res,c}$ reaches a maximum at c ≈ 200 μm and remains constant up to c = 1000 μm. In contrast, $K_{res,a}$ reaches a maximum at c = a ≈ 100 μm and decreases to ≈0 at c = a ≈ 600-1000 μm. This difference between $K_{res,c}$ and $K_{res,a}$ implies that, in the presence of residual stresses, minimal crack extension might be observed on the surface while the crack is growing inside the specimen.

During service, the turbine engine components are subjected to complex thermal and mechanical loading conditions. Numerous studies using coupon-type specimens have shown that residual stresses relax during thermal exposure and fatigue loading [for example, 4-9]. Most of the data available are based on surface residual stress measurements. However, accurate prediction of crack growth requires the knowledge of residual stress distribution as a function of depth. Recent work by Cao et al. [6] and Prevey et al. [7,8] report residual stress distributions as a function of exposure time. Figure 5(a) shows the relaxation of residual stresses in Ti-6Al-4V at 325°C [7]. Rapid and significant relaxation (≈50%) is observed near the surface during the first ten minutes and the distribution remains relatively stable beyond 10 minutes. Similar results were also reported by Cao et al. [6] for a Ni-base superalloy (Astroloy) at 650°C. An important feature to be noted is that most of the relaxation of the residual stresses is confined to ≈ 100 μm below the surface.

Recently, Vukelich et al. [10] reported the results of residual stress measurements at various locations in Ni base superalloy engine disks, as shown in Figure 5(b). These disks had been subjected to complex thermal and mechanical loading conditions during service. These data are a compilation of measurements from numerous disks. Hence, the initial residual stresses (post shot-peen, pre-service) and the subsequent relaxation during service were not tracked at the same location and on the same component. Although there is significant scatter in the results, the data clearly show that, even after 8000 TACs (Total Accumulated Cycles), the minimum retained surface residual stress is ≈30-50% of the initial level.

The above results show that a wide variation in the magnitude of retained residual stresses can be expected during service. Hence, this paper is directed towards an assessment of the influence of residual stresses on the remaining crack propagation life and the effect of various degrees of retention of residual stresses. Incorporation of residual stresses in prediction of crack growth life requires accurate models to predict the relaxation of residual stresses during service. A few relaxation models [6,9] have been developed for a limited range of temperatures and mechanical loading. Additional extensive testing and modeling are required for accurate prediction of the true rate of decrease in the residual stresses under a wide range of thermal and mechanical loading conditions. Available data indicate that the most substantial residual stress relaxation occurs during the initial cycles. Hence, during this study, crack growth analysis was conducted for various levels of retained residual stresses as a percentage of the original stress distribution, as shown in Figure 6(a). This approach will result in conservative predictions for surface initiated cracks because as shown in Figure 5(a) most of the measured residual stress relaxation is restricted to the initial ≈100μm beneath the surface. The corresponding $K_{res,c}$ and $K_{res,a}$ are shown in Figure 6(b). Note that even an assumption of 50% retention of residual stresses results in K_{res} of ≈ -4 to –8 MPa√m for crack sizes of ≈ 50 to 200 μm. These K_{res} values are of the same order of magnitude as ΔK_{th}, and hence, the retained residual stresses are sufficient for significant crack growth retardation. The influence of retained residual stresses on fatigue limits and crack propagation life is discussed next. In the following sections, the long-crack growth behavior shown in Figure 2 was used for analysis of small cracks. For cracks greater than ≈ 25μm, this assumption was previously shown to be valid based on experiments on naturally initiated small surface cracks in Ti-6246 [11,12].

RESIDUAL STRESS EFFECTS ON THRESHOLD STRESS AND FLAW SIZE

The influence of residual stresses on the threshold crack size corresponding to no-growth conditions was studied by utilizing a Kitagawa-Takahashi [13] type plot of maximum stress versus flaw size. Such a plot corresponding to R=0.1 and R=0.8 is shown in Figure 7(a) and 7(b), respectively. These stress ratios bound the typical stress ratios experienced by some of the life extension candidate components. The maximum stress is bounded by the fatigue limit (typically 10^7-cycle fatigue limit) [14] and the stress-crack length relationship defined by the threshold stress intensity factor range, ΔK_{th}. A similar approach was used by Larsen et al. [14,15] to generate fatigue life maps and to assess the influence of residual stresses on threshold crack sizes. At R=0.1 and 0.8, if the assumed initial flaw depth exceeds 10 and 30 μm, respectively, the threshold stress (fatigue limit) decreases with increasing flaw size per LEFM equations. Figure 7 also shows the predictions for threshold stress in the presence of residual stresses corresponding to intensities of ~ 4A and ~16A. The predictions for the two shot peening intensities are nearly similar and clearly shows the substantial increase in the fatigue limit for a given flaw size. For a flaw size ≈ 100 μm, at R=0.1 and 0.8, the threshold stress ≈ 200 and 500 MPa, respectively, in the absence of residual stresses. These threshold-stresses increase to the respective upper bound fatigue limit in the presence of the residual stress. For a stress level of ≈ 200 MPa, the threshold flaw size increases from ≈ 100 μm to ≈ 400 μm. Thus, the safe region for the no-growth condition is increased substantially by the residual stresses. Although, the threshold flaw size at R=0.8 is higher than that at R=0.1 for a given stress, the subsequent benefit of the residual stresses is significantly lower than that at R=0.1. Figure 7 also shows that the benefits of the residual stresses vanish for flaw size greater than 600-700 μm. This result is consistent with the predicted near-zero $K_{res,a}$ for flaw sizes greater than 600-700 μm, as shown in Figure 4(b).

As discussed earlier, shot-peening induced residual stresses relax during service. Hence, the threshold stress for two flaw sizes were determined for various levels (0 to 100%) of the residual stress corresponding to ~8A intensity, as shown in Figure 8(a). The corresponding residual stress distribution was shown in Figure 6. Under LCF conditions (R=0.1), for a flaw size of 120 μm, the threshold stress is ≈ 250% higher than the baseline stress even at residual stress retention of only 50%. For a flaw size of 25 μm, the threshold stress at R=0.1 is ≈ 40% higher than the baseline. Therefore, the larger flaw size exhibits a higher increase of threshold stress. At R=0.8, even though the relative increase is lower than that for R=0.1, the retained threshold stress is still higher than the baseline value. The sensitivity of the threshold flaw size corresponding to stress = 500 MPa to the level of residual stress is shown in Figure 8(b). Corresponding to the baseline value, at 100% of residual stress, the threshold flaw is ≈ 10X and 2X higher at R=0.1 and 0.8, respectively. Even with only 50% retention of the residual stress, the threshold flaw size is still greater than the current NDE limit (≈ 125 μm) for some components. The results in Figure 8 clearly show that 50% retention of residual stresses is sufficient to generate substantial increases in threshold stress and flaw size. In this calculation, the entire residual stress distribution was assumed to decrease by the same percentage. As discussed earlier, Figure 5(a), the bulk of the relaxation occurs near the surface. Hence, the actual retained residual stress benefits can be expected to be higher than that predicted in Figure 8. The benefits of residual stresses on the crack propagation life are discussed next.

RESIDUAL STRESS EFFECTS ON CRACK GROWTH BEHAVIOR

The ENSIP design philosophy assumes that a 794 μm (=1/32 in.) flaw could initiate during service in 1 out of 1000 components. In addition, ENSIP requires that the remaining crack propagation life from an inspectable crack size be equal to the component design life. This life management practice relies on accurate prediction of the crack growth behavior at critical locations and the ability to define safe inspection intervals based on this prediction. Current crack growth predictions exclude the influence of beneficial compressive residual stresses. Extensive data and analyses are available in the literature highlighting the significant increase in crack propagation life due to residual stresses. As discussed earlier, residual stresses relax, and significant scatter exists in the retained residual stresses. Hence, prior to implementation of the residual stresses in component lifing, the sensitivity of crack propagation life to various levels of residual stresses should be assessed. Extensive crack growth analyses were conducted for a semi-elliptical surface crack in an infinite geometry. The crack growth analysis code AFGROW [16] was used during this study. Equations (1) and (2) were used to generate a tabular database to represent the crack growth behavior of the material in AFGROW.

Figures 9(a) to 9(c) show the predicted maximum stresses versus crack propagation life, N_p, for two initial flaw sizes (25 and 120 μm) and residual stress levels corresponding to 20 and 50% of 8A. In actual components, the amount of retained residual stresses can be expected to be dependent on the applied stresses. The relaxation occurring at locations with high stresses (close to yield) will be the maximum. In this analysis, we assumed that the extent of relaxation is independent of stress level. The results from Figures 9(a) to 9(c) are summarized in Figure 9(d), which shows the ratio of N_p to N_p corresponding to $\sigma_{res}=0$ as a function of maximum applied stress. At R=0.1, this ratio ranges from 2 to 50 depending on the stress level and initial flaw size. The smaller the initial crack size, the higher is the relative gain in N_p. For initial flaw size of 25 μm, under LCF conditions (R = 0.1), 20% retention of the residual stress was sufficient to retain 5X to 50X increase in N_p compared to the baseline. Relative life gain higher than 2X at the high stress level for flaw size of 120 μm required 50% retention of the residual stresses. Under HCF conditions (R=0.8), the relative gain at high stress levels is less than 2X for residual stress retention of 50%. The lower gain in N_p at R=0.8 is consistent with similar observations of crack growth in residual stress fields in the literature [17]. The data shown in Figure 5(b) exhibited residual stress retention of ≈ 30-50%, based on surface measurement. The calculations were conducted assuming that the entire stress distribution decreased by the same percentage, in contrast to the data. Hence, the predictions shown in Figure 9 may be considered conservative, considering observations similar to those in Figure 5(a).

The crack growth response (surface crack length and crack depth versus cycles) at 600 MPa / R=0.1 corresponding to s_{res} = 0 and 50% 8A is shown in Figure 10(a) and 10(b), respectively. The initial flaw size was c_i = 120 μm and the initial aspect ratio was a_i/c_i = 1.0. In the absence of residual stresses, this surface crack grows such that the aspect ratio nearly remains the same. In addition, at half-life, c has increased from 120 μm to ≈ 210 μm. Hence, the detectability of this crack has increased significantly at the end of the half-life period. In contrast, in the presence of residual stresses, the surface crack shows negligible crack growth almost up to 90% of total life. This response is similar to the response under HCF loading conditions. In the depth direction, there is marked increase in the rate of crack growth at ≈ 67% of life. This distinct difference in the crack growth response in the presence of σ_{res} compared to that in the absence of σ_{res} identifies a critical need for a more accurate and reliable NDI technique, which is sensitive to the crack extension in the surface and depth directions.

The influence of retained residual stresses on crack growth in the presence of combined LCF-type and HCF-type cycles is shown in Figure 11. Crack propagation life for an initial crack size of 120 μm subjected to maximum stress = 625 MPa was predicted for various ratios of number of cycles at R=0.8 to number of cycles at R=0.1. The retained residual stress distribution was assumed to be 30% of 8A. Also shown in Figure 11 is the baseline prediction (σ_{res}=0) and the trend-line corresponding to two times the baseline predictions. The crack propagation life in the presence of σ_{res} was always greater than twice that of the baseline, even for the case with high number of HCF-type cycles. Note that at stress levels close to the yield stress, the retained residual stresses may be significantly lower than 50%. In this case, the higher number of HCF-type cycles result in significantly reduced residual stress benefits on crack propagation life.

REMARKS

The properties used during this study are based on the original material prior to insertion in service. During service, the *in situ* properties of the material could change. Hence, analysis conducted to predict the remaining life should account for the current material behavior and the anticipated changes in these properties. Fractographic examinations of post-service components are in progress to assess the changes in the microstructure during service. Following these examinations, crack growth behavior will be characterized on specimens extracted from these components.

Successful incorporation of residual stresses in life management will require a good understanding of the surface and sub-surface residual stress changes. As mentioned earlier, only limited data [e.g. 6-8] are available documenting sub-surface residual stress changes. Vuckelich et al. [10] reported the first work documenting surface residual stress changes from detailed measurements on actual components. This work provided an idea of the range of relaxation of residual stresses that can be expected during service. However, accurate prediction of crack growth life requires sub-surface residual stress distributions also. Hence, additional data from destructive sub-surface measurements need to be collected.

The results of this study show that even retention of only 30% of the original residual stress distribution can yield greater than 2X increase in crack growth life, compared to the current baseline predictions, which exclude residual stresses. Data from laboratory coupon specimens and recent field inspection studies have shown that residual stresses can be expected to relax in most components. Thus, combining data from the field with detailed laboratory experiments and analysis, a reduced level of residual stress can be established and implemented in life management practice. Monitoring residual stresses at critical locations during service can help reduce the potential increase in risk associated with disk life extension. Life management based on such threshold residual stress level will require NDI-based accurate monitoring of residual stress at critical locations. Recent depth measurements have shown that the most substantial residual stress relaxation occurs close to the surface. Sub-surface residual stress relaxation is not as severe as that observed on the surface. Hence, the NDI techniques should be capable of sub-surface residual stress measurement, preferably up to 150 μm deep. Note that such residual stress inspections are in addition to current crack inspections being conducted under the ENSIP program. Therefore, successful implementation of a life prediction methodology using residual stresses requires two critical NDI technology developments. These are: (1) accurate and reliable NDI techniques sensitive to crack extension in the surface and depth directions, and (2) NDI techniques to monitor surface and subsurface changes in residual stresses in components.

Surface enhancement procedures, such as shot peening, retard or prevent surface crack growth. Hence, if the lives of some of the components are extended, at certain locations, the chances of sub-surface crack initiation and growth are increased. Additional testing and analysis are required to characterize and model this behavior. New NDE techniques for detecting sub-surface crack initiation and growth may also be required to mitigate the increased risk of failure at these locations.

The results from this study show that substantial gains in crack propagation life can be realized if residual stresses are included in the life prediction methodology. This would require: (1) adequate quality control during the surface enhancement procedure, (2) understanding of changes in the residual stress distribution (surface and depth) during service, (3) accurate life prediction with residual stresses, and (4) monitoring of surface and depth residual stress periodically during service, similar to current crack inspection procedures. The utilization of residual stresses in the engine life management practice is also a key technology necessary for developing longer life and durable engines. Introduction of residual stresses via newer procedures such as low plasticity burnishing (LPB) [18] and laser shock peening (LSP) [19] are being explored. The retention of residual stresses generated by LPB and LSP have been reported to be significantly better than that generated by shot peening because of the reduced cold work [7,8]. Hence, re-introduction of residual stresses in legacy engine components using LPB and LSP should also be explored.

SUMMARY

Life extension of fracture critical parts is under consideration by the US Air Force. This technology development initiative is expected to significantly reduce the sustainment burden and to enable future long-life durable engines. Data from legacy engines indicate that shot-peen induced residual stresses at critical locations are retained only partially during service. This paper assessed the influence of various levels of retained residual stresses on the threshold stresses, threshold crack sizes and crack propagation in Ti-6Al-2Sn-4Zr-6Mo. The results show that even retention of only 30% of the original residual stress distribution can yield greater than 2X increase in crack growth life compared to the baseline predictions excluding residual stresses. Thus, combining data from the field with detailed experiments and analysis, a threshold level of location-specific residual stress can be established and implemented in the life management practice. The inclusion of residual stresses in life prediction of the component will require NDI-based accurate monitoring of residual stress at life-limiting critical locations, in addition to crack inspections being conducted under the ENSIP program. The NDI techniques should enable monitoring of surface and sub-surface residual stresses. Improved NDI techniques, sensitive to surface and depth crack growth, are also required.

ACKNOWLEDGMENTS

This research was performed in the Air Force Research Laboratory, Materials and Manufacturing Directorate (AFRL/MLLMN), Wright-Patterson Air Force Base, OH, USA.

REFERENCES

14. Larsen, J.M. et al., “The Engine Rotor Life Extension (ERLE) Initiative and It’s Opportunities to Increase Life and Reduce Maintenance Costs,” presented at AeroMat 2001, Long Beach, CA, 12 June 2001.
15. Harris, J.A., “Engine Component Retirement for Cause, Vol. I - Executive Summary,” AFWAL-TR-87-4069, Vol. I., Air Force Wright Aeronautical Laboratories,” Wright-Patterson AFB, OH, 1987.
16. Engine Structural Integrity Program (ENSIP), MIL-STD-1783 (USAF), 30 November 2001.
17. Holzapel, H., Schulze, V., Vohringer, O., and Macherauch, E., “Residual Stress Relaxation in an AISI 4140 Stell due to Quasi-static and Cyclic Loading at Higher Temperatures,” Materials Science & Engineering, Vol. A248, pp. 9-18, 1998.
18. Berger, M.-C and Gregory, J.K., “Residual Stress Relaxation in Shot Peened Timetal®21S,” Materials Science and Engineering, Vol. A263, pp. 200-204, 1999.
19. Cao, W., Khadhraoui, M., Brenier, B., Guedou, J.Y., and Castex, L., “Thermomechanical Relaxation of Residual Stress in Shot Peened Nickel Base Superalloy,” Material Science and Technology, Vol. 10, pp. 947-954, November 1994.
20. Prevey, P., Hornbach, D., and Mason, P., “Thermal Residual Stress Relaxation and Distortion in Surface Enhanced Gas Turbine Engine Components,” Proceedings of the 17th Heat Treating Society Conference and Exposition and the 1st International Induction Heat Treating Symposium, D.L. Milam et al., Eds., ASM, Materials Park, OH, pp. 3-12, 1998.
21. Prevey, P., “The Effect of Cold Work on the Thermal Stability of Residual Compression in Surface Enhanced IN718,” Proceedings, 20th ASM Materials Solutions Conference & Exposition, St. Louis, Missouri, Oct. 10-12, 2000.
22. Ahmad, J., Chandu, S., and Prevey, P., "An Analysis of Redistribution of Surface Treatment Induced Residual Stresses", To be submitted for publication, 2001.
23. Vukelich, S., Russ, S.M., Berkley, S., and Bradley, E.F., “Residual Stress Measurement and it’s Application to Achieve Predicted Full Life Potential of Low Cycle Fatigue (LCF) Limited Engine Disks,” The 9th International Symposium on Transport Phenomena and Dynamics of Rotating Machinery, Honolulu, Hawaii, February 10-14, 2002.
24. Larsen, J.M. and Jira, J.R., Experimental Mechanics, pp. 82-87, 1991.
25. Jira, J.R., Nicholas, T., and Larsen, J.M., Fatigue 87, Vol. IV, E. Starke and R.O. Ritchie, Eds., Engineering Materials Advisory Services, Ltd., West Midlands, U.K., pp. 1851-1860, 1987.
26. Kitagawa, H. and Takahashi, S., Proceedings of the Second International Conference on Mechanical Behavior of Materials, Boston, MA, pp. 627-631, 1976.
27. Larsen, J.M., Russ, S.M., John, R., and Maxwell, D.C., “The Role of Threshold Fatigue Crack Growth in Life Prediction of Two Titanium Alloys Under High Cycle Fatigue Spectra,” To be submitted for publication, 2001.
28. Larsen, J.M., John, R., Russ, S.M., Maxwell, D.C., Worth, B.D., Rosenberger, A.H., Li, K. and Porter, W.J., “The Role of Near-Threshold Small-Crack Behavior in Life Prediction of Titanium Alloys For Use in

Advanced Turbine Engines," Small Fatigue Cracks: Mechanics and Mechanisms, K.S. Ravichandran, R.O. Ritchie, and Murakami, Y., Eds., Elsevier Science, Oxford, UK, 1999.

29. AFGROW, Harter, J., US Air Force Research Laboratory, AFRL/VASM, Wright-Patterson Air Force Base, OH, USA. Available at http://fibec.flight.wpafb.af.mil/fibec/afgrow.html.
30. Ruschau, J.J., John, R., Thompson, S.R., and Nicholas, T., "Fatigue Crack Growth Characteristics of Laser Shock Peened Ti-6Al-4V" Journal of Engineering Materials and Technology, Vol. 121, No.3, pp. 321-329, 1999.
31. Prevey, P.S. and Cammett, J., "Low Cost Corrosion Mitigation and Improved Fatigue Performance of Low Plasticity Burnished 7075-T6," Proceedings, 4th International Aircraft Corrosion Workshop, Solomons, MD, Aug 22-25, 2000.
32. Clauer, A.H., "Laser Shock Peening for Fatigue Resistance," Surface Performance of Titanium, J.K. Gregory et al., Eds., TMS, Warrendale, PA, pp. 217-230, 1996.

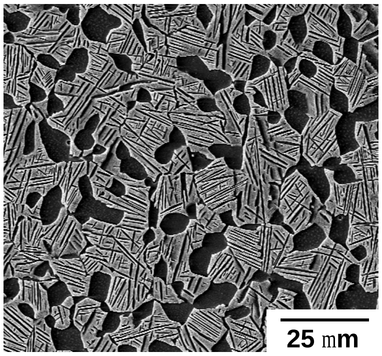

Figure 1. *Fine, equiaxed a + b microstructure of Ti-6Al-2Sn-4Zr-6Mo after heat treatment.*

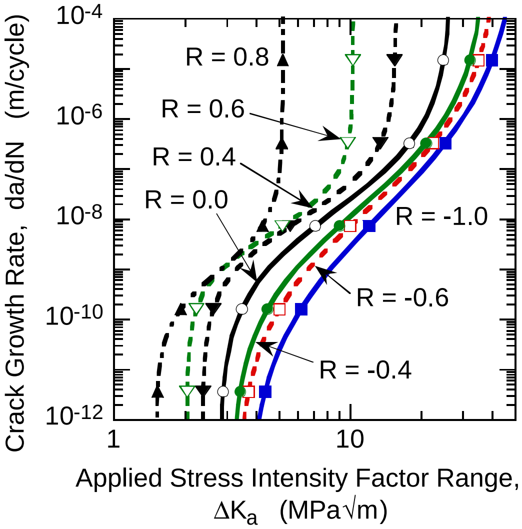

Figure 2. *Baseline long crack growth behavior of Ti-6Al-2Sn-4Zr-6Mo. These curves are from Equation (1).*

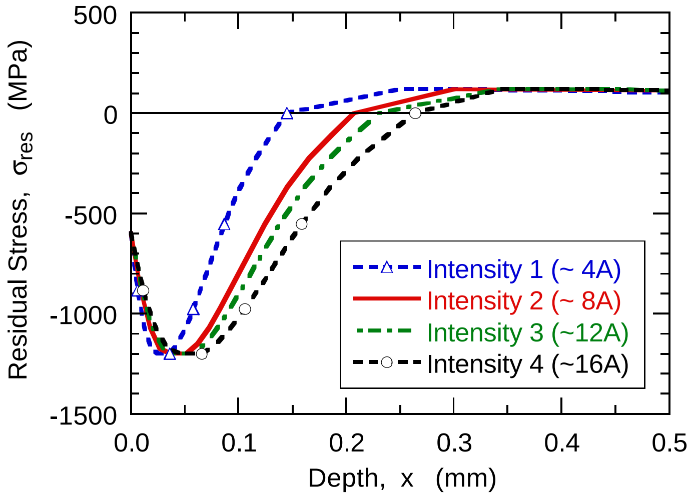

Figure 3. Estimated residual stress, s_{res}*, distributions in Ti-6Al-2Sn-4Zr-6Mo due to shot-peening.*

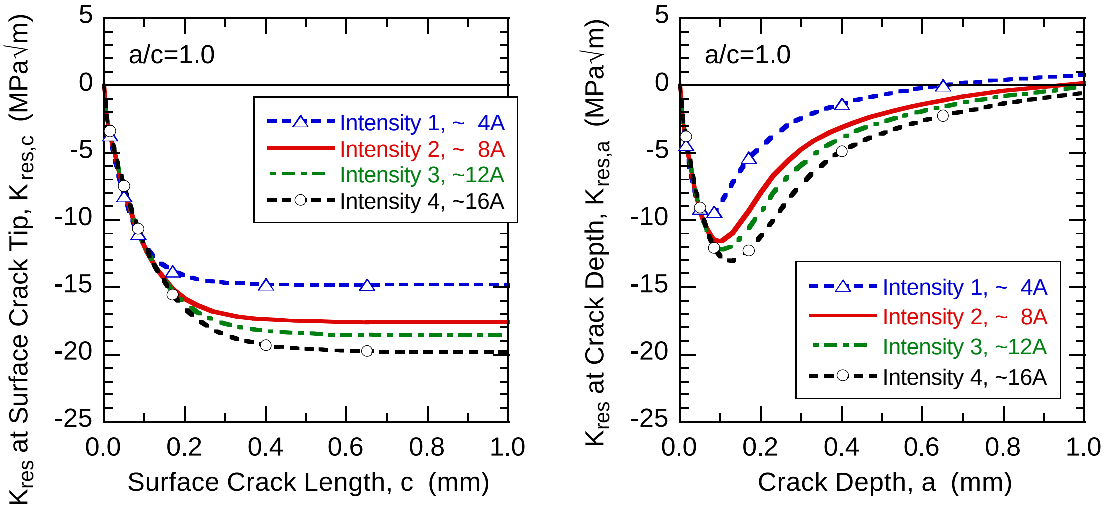

(a) (b)

Figure 4. Residual stress intensity factor, K_{res}*, for a semi-elliptical surface crack with aspect ratio (a/c) = 1, due to the residual stress distributions shown in Figure 3. (a)* K_{res} *at surface crack tip,c, and (b)* K_{res} *at crack depth, a.*

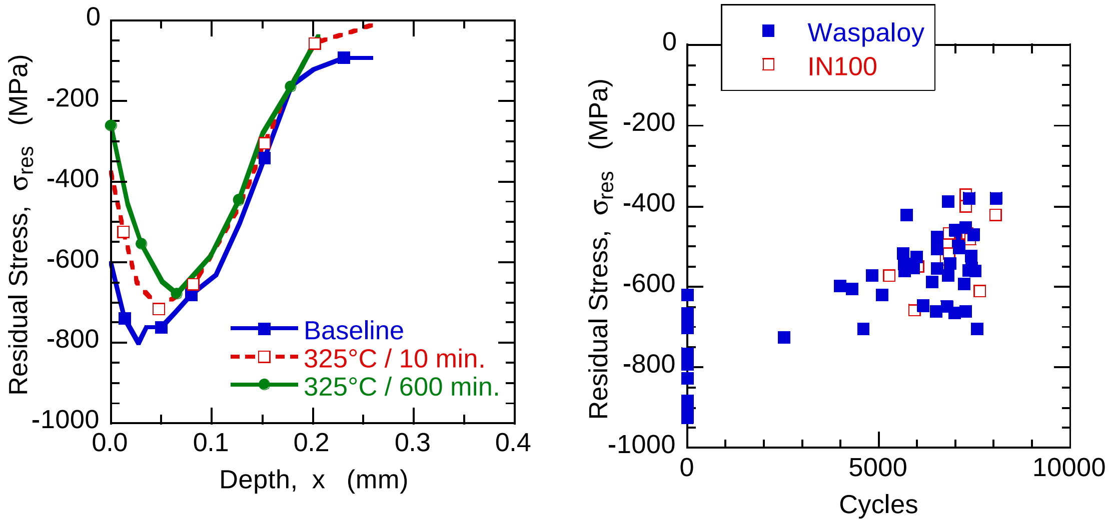

(a)

(b)

Figure 5. *(a) Residual stress relaxation in Ti-6Al-4V at 325°C [Prevey et al., 1998], and (b) Surface residual stress relaxation at notches in Ni-base superalloy engine disks [Vukelich et al., 2002].*

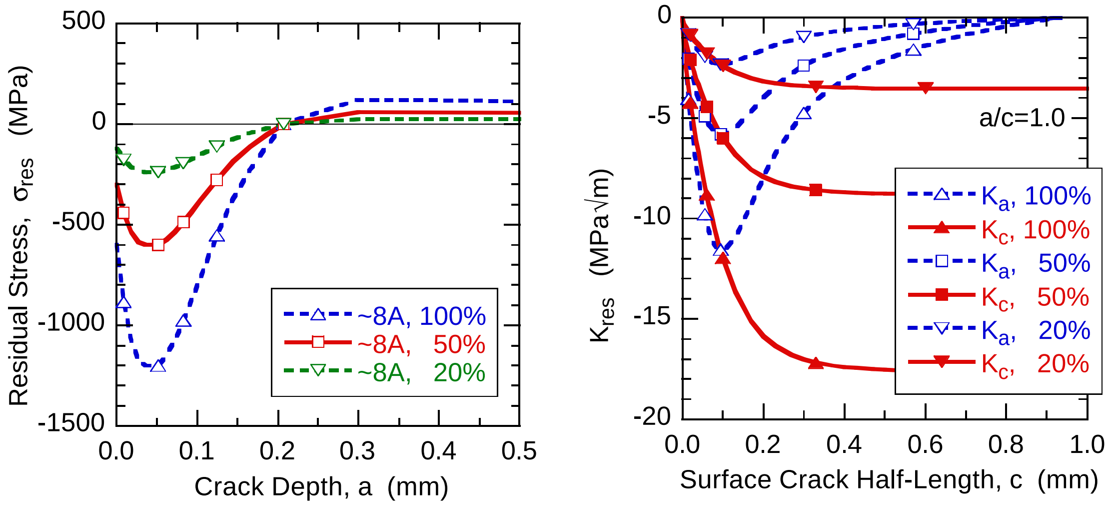

(a)

(b)

Figure 6. *(a) Assumed residual stress distributions to simulate relaxation during service. (b) Corresponding* $K_{res,c}$ *and* $K_{res,a}$ *for aspect ratio, a/c=1.*

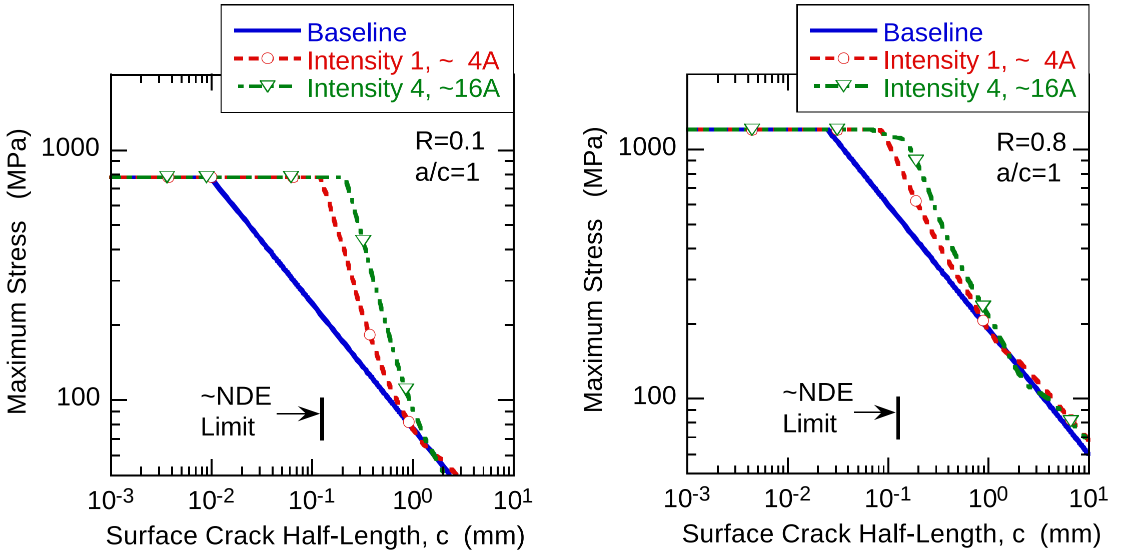

(a) (b)

Figure 7. *Predicted influence of shot-peen residual stresses on fatigue limit of Ti-6Al-2Sn-4Zr-6Mo at (a) R=0.1 and (b) R=0.8. Aspect ratio, a/c=1.*

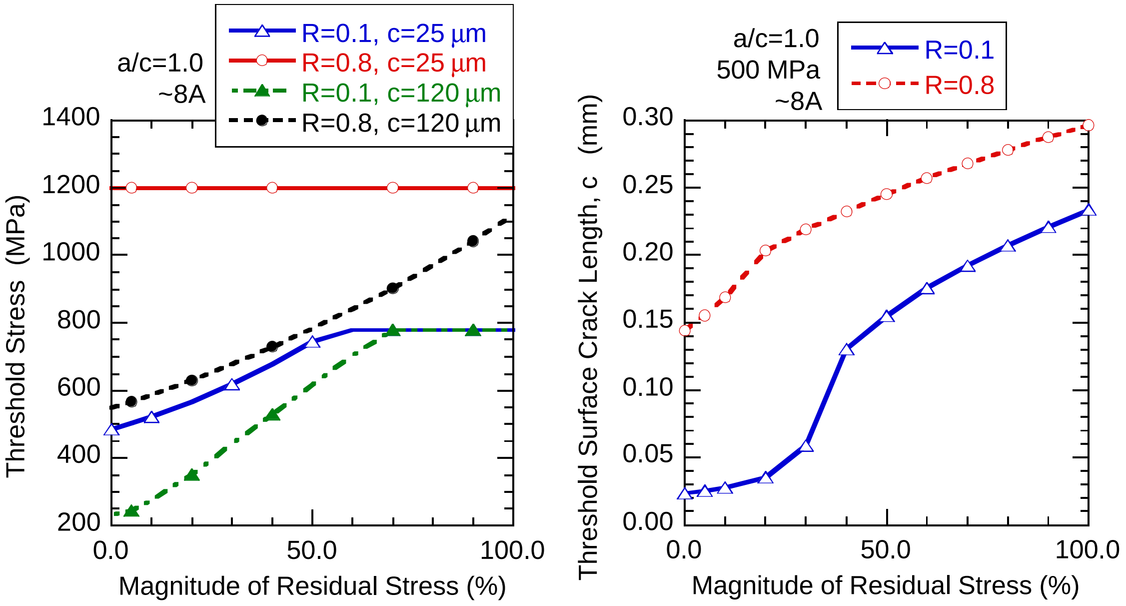

(a) (b)

Figure 8. *Influence of varying levels of residual stresses (0-100% of Intensity 2, ~8A) on (a) Threshold stress corresponding to c=25 and 120 mm, and (b) Threshold surface crack length corresponding to maximum applied stress = 500 MPa for a/c=1.0.*

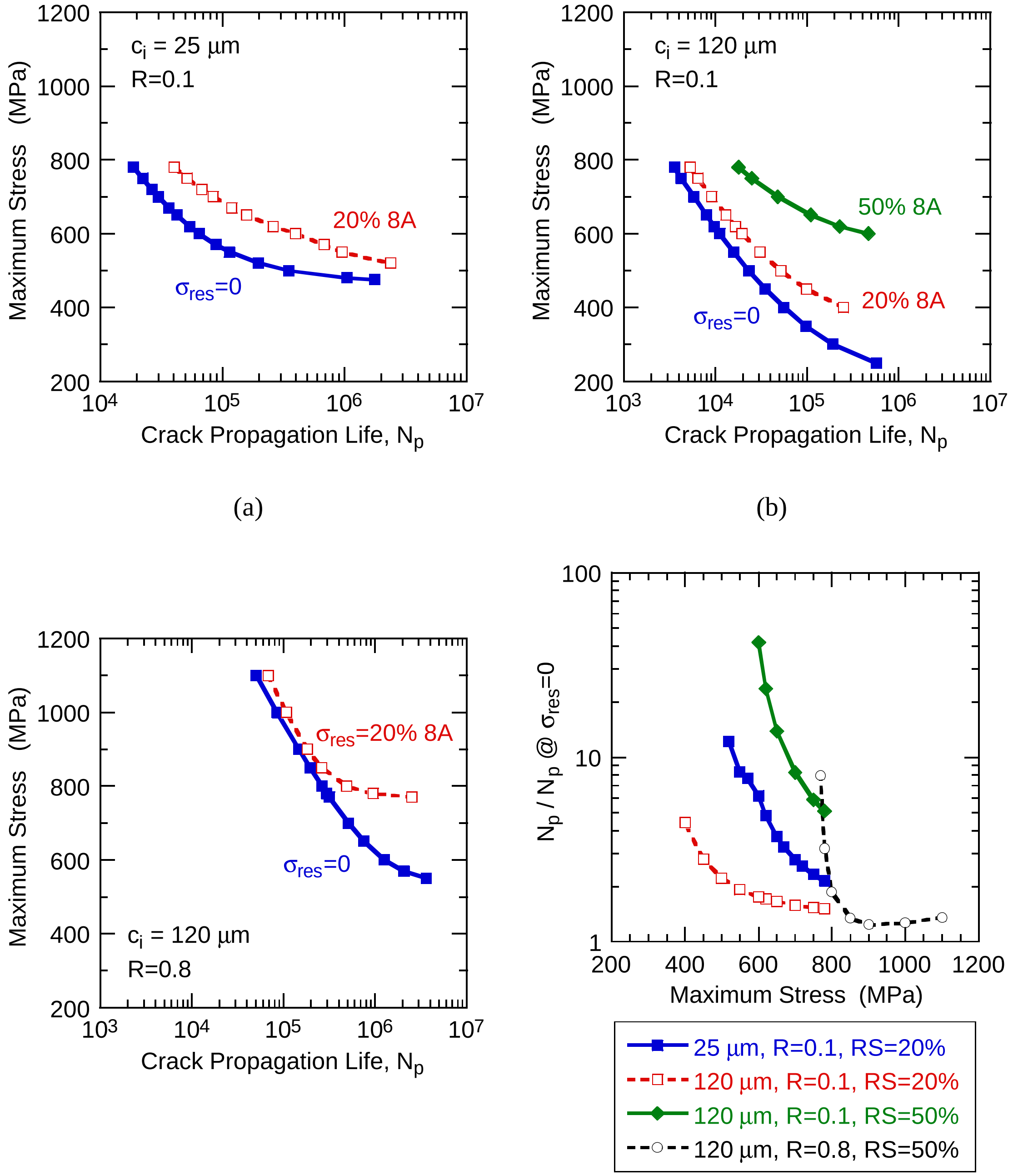

(a)

(b)

(c)

(d)

Figure 9. Predicted influence of retained residual stresses on crack propagation life (N_p). (a) Maximum stress versus propagation life (S-N_p) behavior at R=0.1 for $c_{initial}$=25 mm and a/c=1. (b) S-N_p behavior at R=0.1 for $c_{initial}$=120 mm and a/c=1. (c) S-N_p behavior at R=0.8 for $c_{initial}$=120 mm and a/c=1. (d) Ratio of N_p to baseline (s_{res}=0) Np as a function of maximum stress.

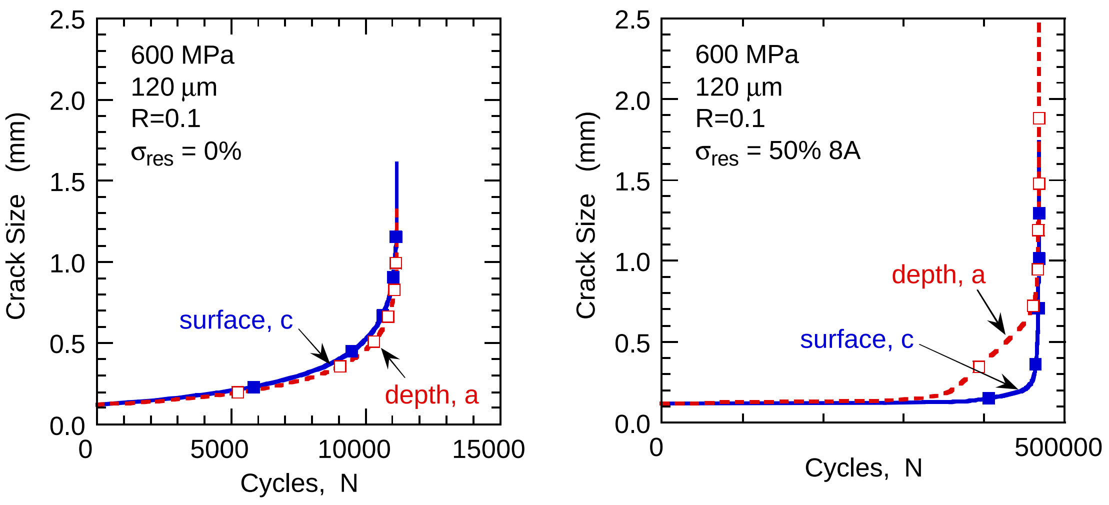

(a)

(b)

Figure 10. Crack growth behavior in the presence of residual stresses at R=0.1. (a) s_{res} = 0, and (b) s_{res} = 50% of 8A. Assumed initial crack size = 120 mm and initial a/c = 1.0.

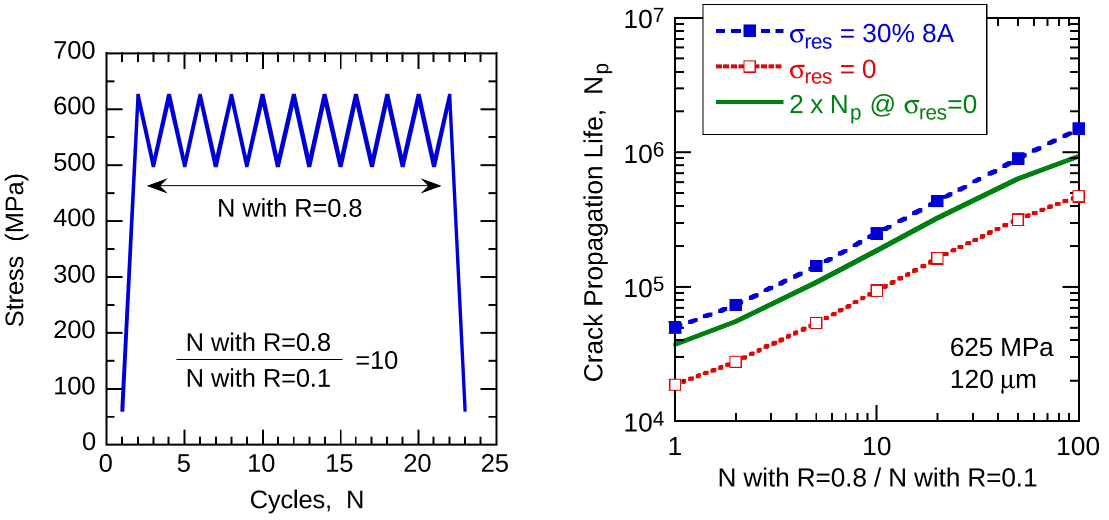

(a)

(b)

Figure 11. (a) Assumed simple mission loading sequence containing 1 R=0.1 cycle and multiple R=0.8 cycles. (b) Predicted crack propagation life, N_p. Assumed maximum stress = 625 MPa and initial crack size = 120mm.

LIST OF SYMBOLS, ABBREVIATIONS, AND ACRONYMS

ABBREVIATION	DEFINITION
γ-TiAl	Gamma Titanium Aluminide
A/D	Anolog-to-Digital
AE	Acoustic Emission
CMC	Ceramic Matrix Composites
COF	Coefficient of Friction
COTS	Commercial Off-the-Shelf
CTE	Coefficient Thermal Expansion
CVI	Chemical Vapor Infiltrated
DCPD	Direct Current Potential Difference
DE(T)	Double-notched Tension Specimen
DEH(T)	Semicircular Double-notched Tension Specimen
EBSP	Electron Back-Scattered Diffraction Patterns
ERLE	Engine Rotor Life Extension
FCC	Face-Centered Cubic
FOD	Foreign Object Damage
FY	Fiscal Year
HCF	High Cycle Fatigue
IDDS	Infrared Damage Detection System
IHPTET	Integrated High Performance Turbine Engine Technology
IPF	Intensity Pole Figure
LCF	Low Cycle Fatigue
LE	Leading Edge
LVDT	Linear Variable Differential Transformer
MH(T)	Middle Hole Tension Specimen
MI	Melt Infiltrated
MLLM	Metals Branch
MLLMN	Behavior/Life Prediction Section
MLOC	Government Computer Support
NDE	Nondestructive Evaluation
NDI	Nondestructive Inspection
NTED	National Turbine Engine Durability
OIM	Orientation Imaging Microscopy
PIN	Physically Isolated Networks
PLAT	Probabilistic Life Analysis Technique
PM	Powder Metallurgy
PST	Poly Synthetically Twinned
SBIR	Small Business Innovation Research
SE(T)	Single Edge Hole Tension Specimen
SEM	Scanning Electron Microscopy
Ti	Titanium
TMF	Thermo-mechanical Fatigue
TPRL	Thermophysical Properties Research Laboratory
USAF	United States Air Force
UMAT	User Material
WANS	WinMATE Analytical and Numerical Solutions